Abstract

Title of dissertation: NEUTRONIC EFFECTS ON TUNGSTEN-186 DOUBLE NEUTRON CAPTURE

Marc Alan Garland, Doctor of Philosophy, 2004

Dissertation directed by: Professor Mohamad I. Al-Sheikhly
Professor Gary A. Pertmer
Department of Materials Science and Engineering

Dr. Saed Mirzadeh
Nuclear Science and Technology Division
Oak Ridge National Laboratory

Rhenium-188, a daughter product of tungsten-188, is an isotope of great interest in therapeutic nuclear medicine, being used in dozens of laboratory and clinical investigations worldwide. Applications include various cancer therapy strategies, treatment of rheumatoid arthritis, prevention of restenosis following coronary artery angioplasty, and palliation of bone pain associated with cancer metastases. With its half-life of 17 hours, 2.12 MeV (maximum) beta-particle emission, chemical similarity to technetium-99m (the most widely used diagnostic radioisotope), and its availability in a convenient tungsten-188/rhenium-188 generator system, rhenium-188 is a superb candidate for a broad range of applications.

Production of ^{188}W is typically via double neutron capture by ^{186}W in a high flux nuclear reactor, predominantly the High Flux Isotope Reactor at the Oak Ridge National Laboratory in Tennessee. Experience at HFIR has shown that production yields (measured in Ci of ^{188}W produced per g of ^{186}W target) decrease considerably as target size increases. While the phenomenon of neutron resonance self-shielding would be expected to produce such an effect, temperature effects on neutron flux distribution and neutron capture rates may also be involved. Experimental investigations of these phenomena have not been previously performed.

The work presented in this thesis evaluates the factors that contribute to the decrease in ^{188}W yield from both theoretical and experimental standpoints. Neutron self-shielding and temperature effects were characterized to develop a strategy for target design that would optimize production yield, an important factor in minimizing health care costs. It was determined that decrease in yield due to neutron self-shielding can be attributed to depletion of epithermal neutrons at resonant energies, most significantly within the initial 0.4 mm depth of the target. The results from these studies further show that ^{188}W yield in the interior of the target (beyond 0.4 mm depth) does not decrease as would be expected due to neutron attenuation. This observation was explained by the fact elevated temperatures in the interior of the target result in an increase in the ^{188}W yield through Doppler broadening of cross sections, compensating for reduced yield due to neutron attenuation. Finally, this work supports earlier analyses that questioned the accuracy of the ^{187}W thermal cross section and resonance integral.

NEUTRONIC EFFECTS ON TUNGSTEN-186 DOUBLE NEUTRON CAPTURE

by

Marc Alan Garland

Dissertation submitted to the Faculty of the Graduate School of the
University of Maryland, College Park in partial fulfillment
of the requirements for the degree of
Doctor of Philosophy
2004

Advisory Committee:

Professor Mohamad I. Al-Sheikhly, Chair
Professor Gary A. Pertmer, Co-chair
Dr. Saed Mirzadeh
Professor Joseph Silverman
Professor Peter Kofinas
Professor William E. Bentley

Acknowledgements

I would like to thank the members of my advisory committee, Professors Mohamad Al-Sheikhly, Gary Pertmer, Joseph Silverman, Peter Kofinas, and William Bentley and Dr. Saed Mirzadeh, for agreeing to serve in that capacity. The guidance and assistance of the co-chairs, Mohamad Al-Sheikhly and Gary Pertmer, over the years has been greatly appreciated.

I am deeply indebted to the many fine people at the Oak Ridge National Laboratory where most of this work was conducted. In particular, Russ Knapp and Steve Kennel provided invaluable insights into the biological aspects of nuclear medicine, greatly expanding my appreciation of the field beyond the physical sciences. I am truly grateful for the assistance and advice of David Glasgow, Lou Qualls, Chuck Alexander, Greg Hirtz, Randy Hobbs, Arnold Beets, Bob Sitterson, and Nancy Larson of ORNL and also Eric Iverson of Iverson Engineering Corporation who produced materials for experiments performed at ORNL.

Collaboration with Steve Binney and Ken Krane of Oregon State University was very rewarding with the sharing of ideas while pursuing similar work.

I would also like to recognize my teachers at the University of Maryland, particularly the late Lothar Wolf, of whom I will always have fond memories.

While it seems like such a long time ago, my interest in nuclear medicine was fostered by people at the Pacific Northwest National Laboratory and I thank Bob Schenter, Darrell Fisher and Dennis Wester for putting me on the right course in life and helping me stay on it all these years. In particular, Bob Schenter was the true catalyst for my involvement in nuclear medicine and his unbounded enthusiasm and tremendous knowledge of nuclear physics have inspired me from the beginning and will keep me going for years to come.

I extend my gratitude to Greg Schenter and Frank Schmittroth for their consultation in physics and mathematics, and advice and encouragement.

I am also grateful to have been blessed with a wonderful family, whose indulgence of my pursuits will forever be appreciated.

Finally, my most sincere thanks to Saed Mirzadeh, my advisor at ORNL, who not only provided inspiration as an outstanding scientist, but also as an exceptional person.

This work was possible through the generous support of the U. S. Department of Energy. I held a fellowship in the DOE Nuclear Engineering and Health Physics Fellowship Program and received funding through a collaboration with Oregon State University in the DOE Nuclear Engineering Education Research Program (contract DE-FG07-01ID14109). All work was performed at the Oak Ridge National Laboratory, which is managed by UT-Battelle for DOE under contract DE-AC05-00OR22725.

Contents

Tables

Figures

Abbreviations

AAS	atomic absorption spectrometry
BNL	Brookhaven National Laboratory
CLSQ	[Cumming 1962]
cps	counts per second
dps	disintegrations per second
DOE	U. S. Department of Energy
ENDF	Evaluated Nuclear Data File
EOB	end of bombardment
H7	[HEATING7 1999]
HFIR	High Flux Isotope Reactor (Oak Ridge National Laboratory)
HPGe	high purity germanium gamma ray spectrometer
HT	Hydraulic Tube
IAEA	International Atomic Energy Agency
ID	inner diameter
LAURA	[Mirzadeh and Walsh 1998]
LCS	limiting control setting
MCA	multi-channel analyzer
NAA	neutron activation analysis
NIST	National Institute of Standards and Technology
NNDC	National Nuclear Data Center (Brookhaven National Laboratory)
OD	outer diameter
ORNL	Oak Ridge National Laboratory
PTP	Peripheral Target Position
RHS	right hand side
RRD	Research Reactors Division (Oak Ridge National Laboratory)

Symbols

A^0	activity at end of bombardment
E_C	cadmium cutoff energy
E_{kT}	neutron energy at temperature T
E_n	neutron energy
E_β	beta particle energy
$<E_\beta>$	average beta particle energy
E_γ	gamma ray energy
$<E_\gamma>$	average gamma ray energy
f_a	gamma ray self-absorption factor
g	Westcott factor
k	Boltzmann's constant
I_0	neutron resonance integral above E_C
I'_0	neutron resonance integral above $5E_{kT}$
I_a	neutron absorption resonance integral
I_β	beta particle intensity
I_γ	gamma ray intensity
r	neutron flux ratio, ϕ_0/ϕ_{ep}
S	radioactive source strength
$t_{1/2}$	radioactive half-life
t_{irr}	irradiation duration

ε	gamma ray detector efficiency
Λ	total nuclide depletion constant
Λ^*	nuclide formation constant
λ	radioactive decay constant
μ	attenuation coefficient
μ/ρ	mass attenuation coefficient
ρ	density
σ	neutron cross section
σ_0	2200 m/s neutron cross section
σ_a	neutron absorption cross section
σ_{eff}	effective neutron cross section (Equation 2.4)
σ_{mxw}	thermal (Maxwellian) neutron cross section
σ_{th}	neutron cross section below E_C
$\overline{\sigma}/\overline{x}$	error of the mean
ϕ	neutron flux
ϕ_0	2200 m/s neutron flux
ϕ_{ep}	epithermal neutron flux
ϕ_T	thermal neutron flux with a temperature-dependent distribution

[n,n′] neutron inelastic scattering reaction
[n,p] neutron-proton reaction
[n,γ] neutron radiative capture reaction

1 Scope of Work

Tungsten-188 has been produced at the Oak Ridge National Laboratory (ORNL) and distributed globally to support laboratory and clinical investigations in nuclear medicine. Production involves the irradiation of ^{186}W in the High Flux Isotope Reactor (HFIR) and subsequent radiochemical processing at ORNL. Analysis of many tungsten irradiations has shown that production yields decrease significantly with increasing tungsten target size.

Neutron self-shielding is one phenomenon that would account for the decreasing yields, but it has also been suspected that elevated temperatures experienced by the tungsten during irradiation impact yields. This work will investigate phenomena that could contribute to the lower than theoretically calculated yields.

1.1 Importance of ^{188}W Production

Rhenium-188 is of great interest in therapeutic nuclear medicine due to its radioactive decay properties, chemistry, and the fact that it has a long-lived parent, ^{188}W. Its half-life of 17 hours and high energy (2.12 MeV maximum) beta particle emission are desirable for dose delivery in many therapeutic applications. Its 155 keV gamma ray emission also provides good imaging capabilities. Since it is chemically similar to ^{99m}Tc, the most widely used diagnostic radioisotope, much of the radiochemistry developed for

diagnostic applications involving ^{99m}Tc can be applied to ^{188}Re. It shares another similarity with ^{99m}Tc in that it can be made available in a generator system. Like ^{99m}Tc ($t_{1/2}$ = 6.01 h) which has a longer-lived parent ^{99}Mo ($t_{1/2}$ = 2.75 d), ^{188}Re has a relatively longer-lived parent ^{188}W ($t_{1/2}$ = 69.78 d). The advantage of such systems is that short-lived isotopes desirable for medical applications can be provided without essentially continuous production, purification and transportation to replenish the rapidly decaying short-lived isotopes. Instead, the long-lived parent isotope is loaded on a column from which the short-lived daughter can be eluted. Figure 1.1 is a photograph of a ^{188}W/^{188}Re generator, courtesy of Russ Knapp of ORNL. Tungsten-188 is loaded on the column shown inside a cutaway of a lead pig used for shipping and shielding. A syringe of saline is used to elute ^{188}Re from the column.

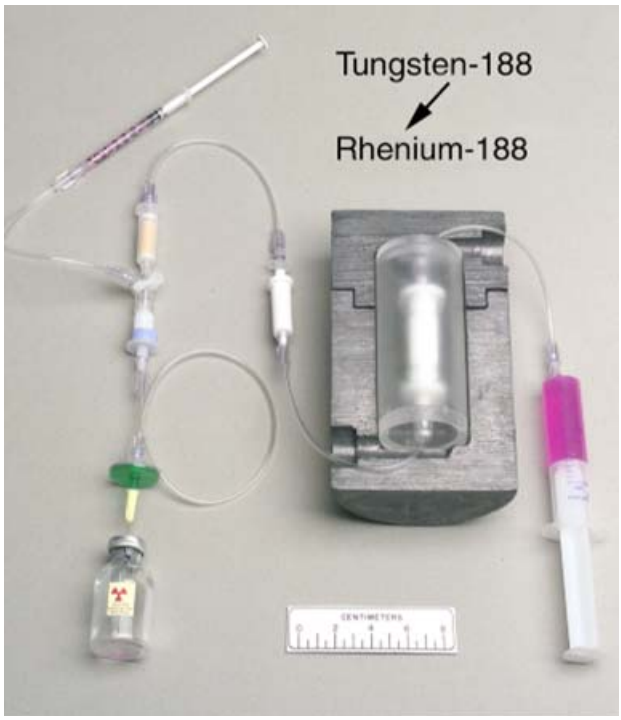

Figure 1.1 ^{188}W/^{188}Re Generator

Medical applications involving ^{188}Re under investigation include various cancer therapy strategies (such as radioimmunotherapy and labeled peptides for tumor targeting and microparticles for liver cancer treatment), treatment of rheumatoid arthritis by radiation synovectomy, prevention of restenosis following coronary artery angioplasty (using liquid-filled balloons and radioactive stents), bone marrow ablation, and palliation of bone pain associated with cancer metastases. With such potential in the field of medicine, it is important to provide ^{188}Re in sufficient quantities and at a cost that can be borne by the health care system.

1.2 ^{188}W Production

Production of ^{188}W is typically via double neutron capture by ^{186}W in a high flux nuclear reactor, predominantly the High Flux Isotope Reactor at the Oak Ridge National Laboratory in Tennessee. Figure 1.2 depicts this production scheme.

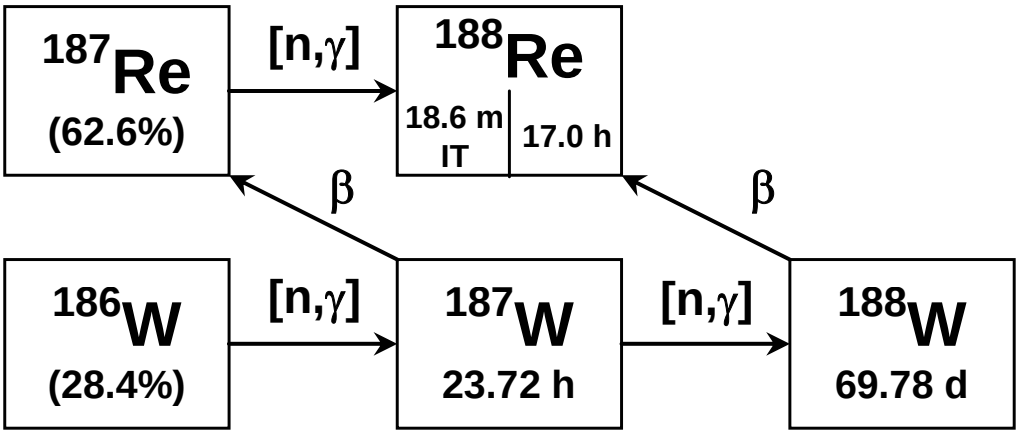

Figure 1.2 ^{188}W Production via ^{186}W Double Neutron Capture

Experience at HFIR has shown that production yields (measured in Ci of ^{188}W produced per g of ^{186}W target) decrease considerably as target size increases. Figure 1.3 displays production data, the filled data points representing irradiations of tungsten metal and the hollow data points representing tungsten oxide irradiations. These actual yields are well below predicted yields since these irradiations were mostly performed in locations with flux levels between 1.5 x 10^{15} and 2.0 x 10^{15} n cm^{-2} s^{-1}.

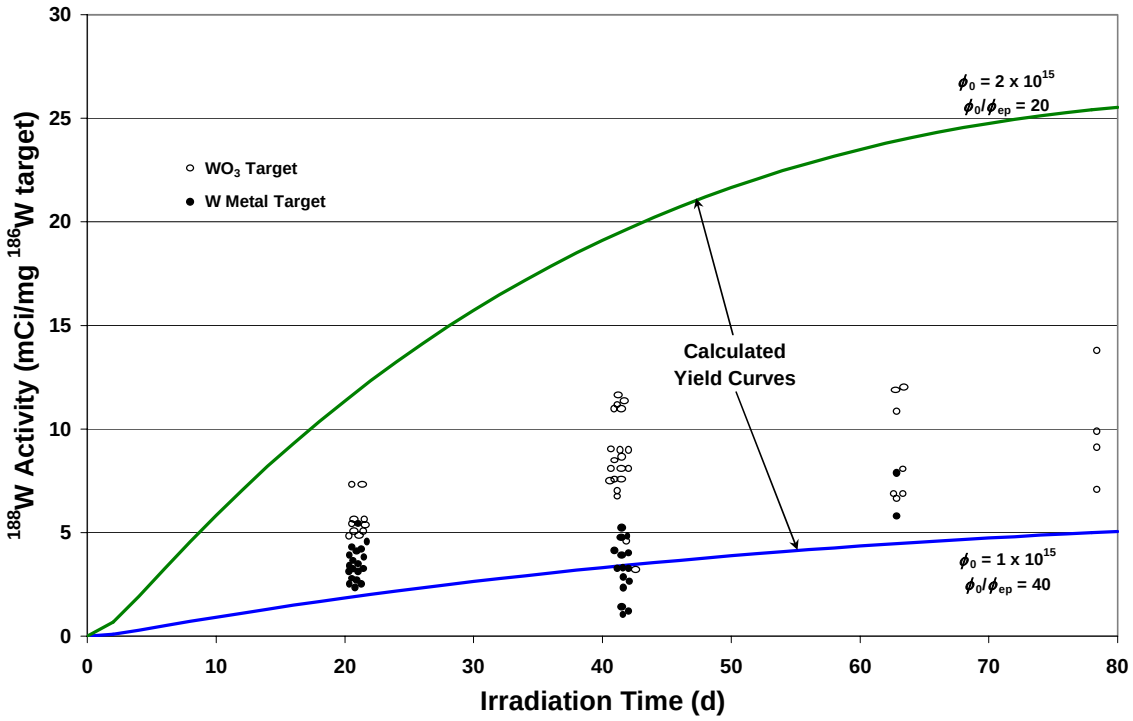

Figure 1.3 ^{188}W Production Yields

1.3 Postulated Phenomena Affecting ^{188}W Production

While the phenomenon of neutron resonance self-shielding would be expected to produce such an effect, temperature effects on neutron flux distribution and neutron capture rates

may also be involved. Experimental investigations of these phenomena have not been previously performed.

It is also possible that actual yields are lower than theoretical calculations because the fundamental physical quantities used in those calculations are in error.

1.4 Scope of Work

This work analyzes the factors that could contribute to low ^{188}W product yields from theoretical and experimental standpoints.

In Chapter 2, measurements are made of the neutron flux in a peripheral target position of the HFIR flux trap region, the present location of most ^{188}W production. An evaluation is performed of the neutron flux in the hydraulic tube, also located in the flux trap and used for the irradiation of previous ^{188}W targets. The hydraulic tube is also used for experiments that are described in Chapter 5. Knowledge of flux levels is necessary to accurately predict transmutation of target isotopes.

Chapter 3 evaluates neutron cross section information and performs cross section measurements to confirm the values used in ^{188}W production calculations.

In Chapter 4, an assessment of tungsten temperatures during irradiation is performed. Primarily due to gamma heating, tungsten targets can reach very high temperatures. A

theoretical prediction of temperature is used to evaluate what, if any, thermally-induced phenomena impact production of ^{188}W.

Experiments conducted to study neutron self-shielding are described in Chapter 5.

Chapter 6 draws conclusions and suggests further work to reach the goal of characterizing neutron self-shielding and temperature effects to develop a strategy for target design that would optimize production yield, an important factor in minimizing health care costs.

2 Neutron Flux Characterization

In order to evaluate tungsten-188 yields, it was necessary to characterize the neutron flux in locations used for isotope production. The High Flux Isotope Reactor hydraulic tube (HT) facility has been characterized experimentally [Mahmood *et al*. 1995]. This chapter presents experimental results for a peripheral target position (PTP) and evaluates the HT and PTP experimental results in conjunction with design flux data to produce recommended flux data for isotope production calculations.

2.1 Introduction

The High Flux Isotope Reactor (HFIR) is a versatile 85 MW radioisotope production and test reactor with the capability and facilities for performing a wide variety of irradiations. HFIR is a beryllium-reflected, flux trap-type reactor. It is cooled and moderated by light water and uses highly enriched uranium (93% ^{235}U) fuel.

The flux trap is a 12.7 x 50.8 cm (diameter x height) cylindrical cavity centered inside the reactor fuel elements [Cheverton and Sims 1971; Mirzadeh *et al*. 1992]. It provides the highest steady-state thermal neutron flux available in the reactor. A bundle (Figure 2.1) containing force-cooled target rods is loaded in the flux trap and is accessible only during refueling. Of thirty positions in the bundle, 12-16 typically contain Cm targets for the production of transuranic isotopes, although other targets can be irradiated in these positions. Solid aluminum targets are used to fill any vacancies. Six peripheral target

positions (PTP) are evenly spaced along the outer radial edge of the bundle. Due to their close proximity to fuel, PTP positions are expected to have the highest accessible fast neutron fluxes in the reactor.

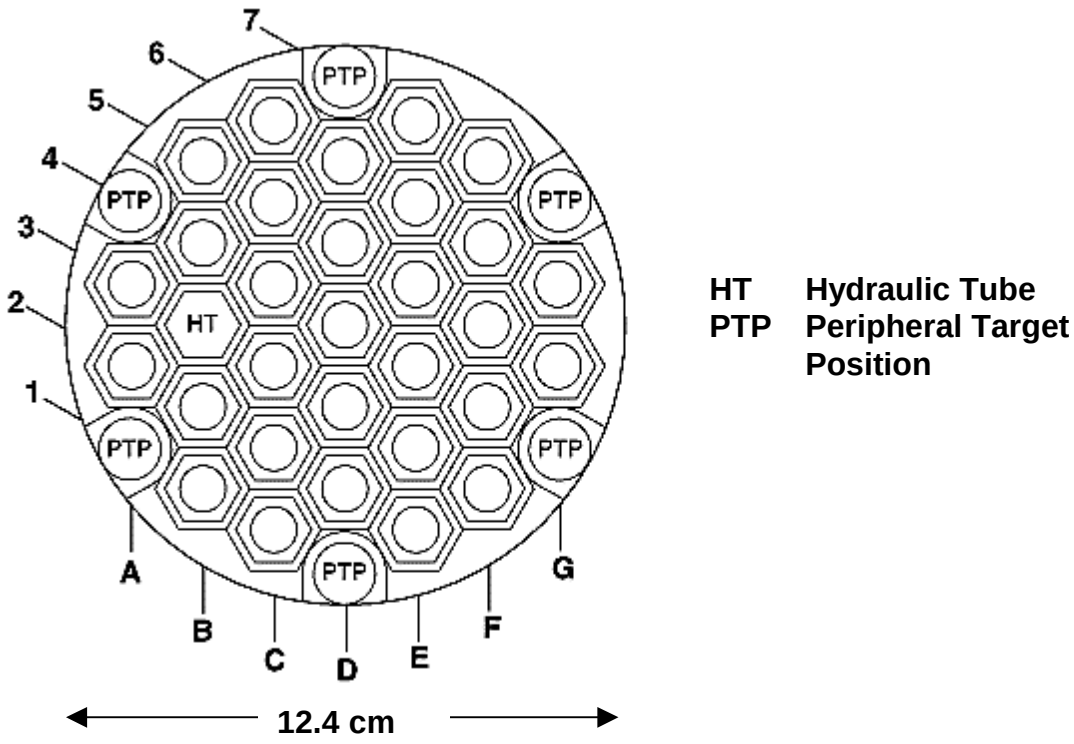

Figure 2.1 HFIR Flux Trap Target Bundle

2.1.1 Hydraulic Tube

The flux trap target bundle also accommodates the hydraulic tube (HT), which is a single tube that inserts into the bundle and exits the reactor through a special vessel head adaptation. The HT is in a very high flux region of the flux trap and is allocated for research and production of short-lived medical and industrial radioisotopes. A

hydraulically driven train of nine vertically stacked capsules can be inserted and removed while the reactor is operating.

Normally, the heat flux at the surface of a capsule due to neutron and gamma heating of the capsule and its contents is limited to 2.5×10^5 W m^{-2}. Furthermore, the neutron poison content of the HT facility load is limited such that the reactor is not subjected to a significant reactivity change during the insertion or removal of capsules.

Four additional HTs are currently under consideration. Detailed information with regard to HT neutron flux measurement and neutron spectra unfolding is given in Mahmood *et al*. [1995]. In addition to the central flux trap, there are several other irradiation facilities, all of which are located in the beryllium reflector. A detailed description of these facilities can be found in Mirzadeh *et al*. [1992].

2.1.2 Peripheral Target Positions

Six peripheral target positions are located at the outer radial edge of the flux trap (Figure 2.1). The fast neutron flux values in these positions are expected to be the highest accessible in the reactor. Design calculations indicate that at this location there exists a steep radial gradient in the thermal neutron flux which is affected by the degree of moderation [Mirzadeh *et al*. 1992]. A typical experiment contains a neutron poison load equivalent to that associated with 200 g of aluminum and 35 g of stainless steel distributed uniformly over a 50.8 cm length. PTP experiments containing significant

neutron poison loads are discouraged due to their adverse effects on fuel cycle length, fuel element power distribution, and transuranium production rates. All PTP experiments are non-instrumented. At normal full system flow, a pressure drop of 36 psi (0.25 MPa) is available to provide coolant for the targets. The irradiation target tubes (Figure 2.2) used in the PTP facilities are typically 1.27 x 61.0 cm (diameter x length) and in the newest design, described below, accept seven HT target capsules.

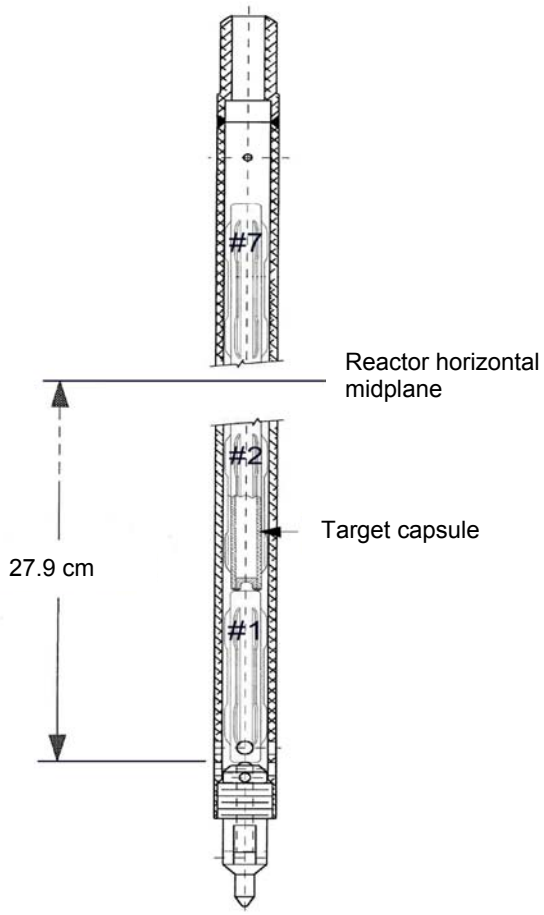

Figure 2.2 PTP Target Tube

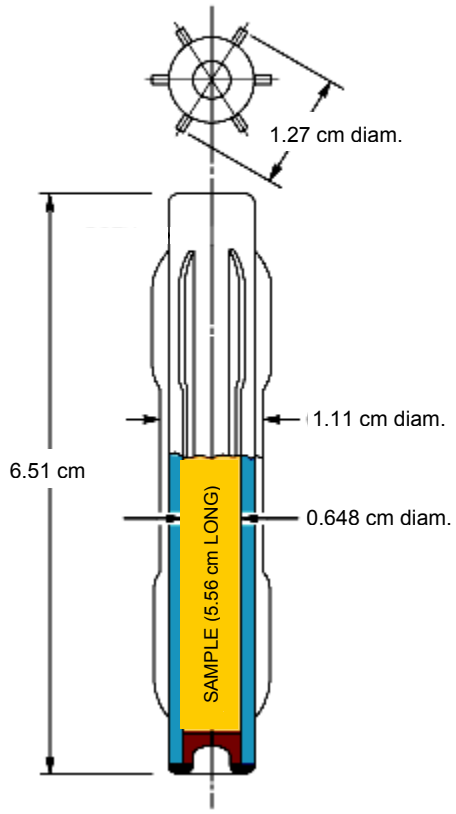

Figure 2.3 Target Capsule

The six PTP experiment facilities support independent target tubes containing target capsules (Figure 2.3). The purpose of a target tube is to position the target capsules and to passively meter coolant to the capsules by directing flow from the orifice at the top of the tube across the target capsules to perforations near the bottom end of the tube. The bottom of the stack of target capsules is 27.9 cm below the core centerline and the overall capsule height is nominally 6.67 cm (the capsule housing and welded end caps). Thus, the stack of seven capsules extends from –27.9 cm to +18.7 cm with respect to the core centerline which intersects capsule #5 below its centerline (capsule #1 is at the bottom of the stack, capsule #7 is at the top).

2.1.3 Neutron Flux Conventions

This chapter describes the measurement of flux spectra in a peripheral target position located at the radial outer edge of the flux trap and compares the results with previous experimental and design data. A variety of flux monitors, covering single and double radiative capture reactions, inelastic scattering and threshold reactions were used for mapping the flux spectrum. In this chapter, the term "thermal flux" refers to the 2200 m/s flux (ϕ_0, a pseudoflux that assumes all thermal neutrons have a single energy of 0.0253 eV) rather than the thermal flux with a temperature–dependent distribution (ϕ_T). Also, values for epithermal flux are given per unit lethargy, $\ln\Delta E$ [definition in Stoughton and Halperin 1959]. These conventions were used because those quantities are the direct result of flux monitor analyses and are the quantities that are used in isotope production calculations. Whenever necessary, ϕ_T (e.g., as provided in Cheverton and Sims 1971)

was converted to ϕ_0 by dividing ϕ_T by a factor of 1.2, reflecting the HFIR operating temperature of 60 ºC [Lamarsh 1993, Eq. 5.63]:

$$\frac{\phi_0}{\phi_T} = \frac{\sqrt{\pi}}{2}\left(\frac{T_0}{T}\right)^{\frac{1}{2}} \tag{2.1}$$

where T_0 and T are 295 and 333 K, respectively. Likewise, total epithermal flux values were converted to flux per unit lethargy by dividing by 12.2, the natural log of the epithermal energy range (0.5 eV ≤ E_n ≤ 100 keV) [Stoughton and Halperin 1959].

2.2 Experiment Design

Since PTP flux monitors remain in the reactor for the entire HFIR operating cycle (~24 days), target materials were chosen with relatively small cross sections in order to limit induced radioactivity and also to minimize target burn-up. Many of the monitors chosen have additional interest for evaluating production yields. The high PTP fluence also prevents the direct measurement of epithermal flux using cadmium covers due to significant burnout of the Cd. Monitors were also chosen based on a variety of reactions: single and double neutron radiative capture, [n,γ] and [n,γ][n,γ], inelastic neutron scattering [n,n′], and threshold reactions such as neutron-proton [n,p] reactions.

The flux monitors consisted of Co/Al (0.082%), In/Al (0.02%) and Ag/Al (0.092%) wires (Reactor Experiments, Inc., Sunnyvale, CA), high purity (99.99%) natural W and Fe metal wires (Alfa Aesar, Ward Hill, MA), enriched ^{116}Sn (95.75%) and ^{117}Sn (89.21%) metal, and ^{122}Te (96.45%) metal powder (ORNL Isotope Production and Distribution

Office). Monitors were prepared in pairs and sealed in high purity synthetic quartz ampoules (3 mm OD, 2 mm ID, ~20 mm length, Suprasil, Heraeus Amersil, Duluth, GA). Seven irradiation capsules (referred to as rabbits) each containing two flux monitors, one loaded in the top of the capsule and one in the bottom, were then prepared (Table 2.1). Capsules were welded in ambient atmosphere and subjected to a helium leak test to ensure weld integrity. The capsules were loaded into the PTP target tube such that the positions of the monitors were mirror imaged with respect to the reactor horizontal midplane (about position #5). Irradiation was conducted during HFIR Cycle 362 in PTP position G4 (Figure 2.1) for 581 hours (2058 MWD).

After irradiation, the capsules were removed, transported to a hot cell and cut open. The quartz ampoules containing monitor samples were removed and transported to a laboratory where the ampoules were soaked in concentrated HNO_3 for a few minutes, then rinsed with water to remove surface contamination, dried and mounted on counting cards. The γ-ray spectra of the irradiated samples were taken with no chemical processing. Gamma spectrometry was performed using a well-calibrated intrinsic Ge detector (50 cm^3, EG&G Ortec, Oak Ridge, TN) and PC-based MCA (Canberra Industries, Inc., Meriden, CT). The detector has a resolution of 1.0 keV at 123 keV and 1.8 keV at 1332 keV. Energy and efficiency calibrations were performed with γ-ray sources traceable to the National Institute of Standards and Technology. Samples were counted with dead times not exceeding 15%, at 10 to 60 cm distance from the surface of the Ge detector. The time interval between the end of irradiation and beginning of counting ranged from a few months to about two years depending on the radioisotope

Table 2.1 Flux Monitors and Their Positions in the PTP Array

Array Position	Position in Capsule	Flux Monitor	Mass (mg)	Nuclear Reaction	Target Isotope Enrichment (%)[a]	Target Isotope Mass (mg)
1 (bottom)	Top	In (0.02%)/Al wire	5.8	^{113}In [n,γ] ^{114m}In	4.29	5.0×10^{-5}
	Bottom	Ag (0.092%)/Al wire	9.1	^{109}Ag [n,γ] ^{110m}Ag	48.161	4.0×10^{-3}
2	Top	Co (0.082%)/Al wire	0.565	^{59}Co [n,γ] ^{60}Co	100	4.6×10^{-4}
	Bottom	natural W wire	13.4	^{186}W 2[n,γ] ^{188}W	28.426	3.81
3	Top	enriched ^{122}Te powder	1.5	^{122}Te [n,γ] ^{123m}Te	96.45	1.4
	Bottom	natural Fe wire	1.8	^{54}Fe [n,p] ^{54}Mn ^{58}Fe [n,γ] ^{59}Fe	5.845 0.282	0.11 5.1×10^{-3}
4	Top	enriched ^{116}Sn metal	2.5	^{116}Sn [n,γ] ^{117m}Sn ^{112}Sn [n,γ] ^{113}Sn	95.75 < 0.05	2.4 $< 1.3 \times 10^{-3}$
	Bottom	enriched ^{117}Sn metal	4.2	^{117}Sn [n,n′] ^{117m}Sn ^{112}Sn [n,γ] ^{113}Sn	89.21 0.052	3.8 2.2×10^{-3}
5	Top	enriched ^{117}Sn metal	4.6	^{117}Sn [n,n′] ^{117m}Sn ^{112}Sn [n,γ] ^{113}Sn	89.21 0.052	4.1 2.4×10^{-3}
	Bottom	enriched ^{116}Sn metal	4.2	^{116}Sn [n,γ] ^{117m}Sn ^{112}Sn [n,γ] ^{113}Sn	95.75 < 0.05	4.0 $< 2.1 \times 10^{-3}$
6	Top	natural Fe wire	2.7	^{54}Fe [n,p] ^{54}Mn ^{58}Fe [n,γ] ^{59}Fe	5.845 0.282	0.16 7.6×10^{-3}
	Bottom	enriched ^{122}Te powder	3.0	^{122}Te [n,γ] ^{123m}Te	96.45	2.9
7 (top)	Top	natural W wire	9.6	^{186}W 2[n,γ] ^{188}W	28.426	2.7
	Bottom	Co (0.082%)/Al wire	0.86	^{59}Co [n,γ] ^{60}Co	100	7.1×10^{-4}

[a] natural abundance or enrichment

Table 2.2 Gamma Rays, Half-lives, and Neutron Cross Sections Used in Analyses

Nuclide Used for Analysis	Gamma Ray Used for Analysis [a]		Production and Burnup Reactions	Product Half-life [a]	Neutron Cross Section (barns)		
	Energy (keV)	Intensity (%)			Thermal	Resonance Integral	Reference
^{110m}Ag	657.8	94.3 ± 0.3	^{109}Ag [n,γ] ^{110m}Ag	249.79 d	4.7 ± 0.2	72.3 ± 4.0	NNDC 2002a
	884.7	72.7 ± 0.4	^{109}Ag [n,γ] ^{110}Ag	24.6 s	86.3 ± 3.0	1328 ± 48	NNDC 2002a
	937.5	34.2 ± 0.6	^{110m}Ag [n,γ] ^{111}Ag	7.45 d [b]	82 ± 11	93.88	NNDC 2002a, BNL 2002
^{60}Co	1173.2	99.97 ± 0.01	^{59}Co [n,γ] ^{60}Co	5.2714 y	16.78 ± 0.66	35 ± 2	NNDC 2002a
	1332.5	99.99 ± 0.01	^{59}Co [n,γ] ^{60m}Co	10.467 m	20.4 ± 0.8	39 ± 2	
			^{60}Co [n,γ] ^{61}Co	1.65 h [b]	2.0 ± 0.66	4.3 ± 0.9	
^{54}Mn	834.8	99.98 ± 0.01	^{54}Fe [n,p] ^{54}Mn	312.11 d	(82.5 ± 5) x 10^{-3} [c]	—	IAEA 1974
			^{54}Fe [n,γ] ^{55}Fe	2.74 y [b]	2.25 ± 0.18	1.2 ± 0.2	NNDC 2002a
			^{54}Mn [n,γ] ^{55}Mn	stable [b]	10	1	Parrington *et al*. 1996, d
^{59}Fe	1099.3	56.5 ± 1.9	^{58}Fe [n,γ] ^{59}Fe	44.472 d	1.28 ± 0.05	1.7 ± 0.1	NNDC 2002a
	1291.6	43.2 ± 1.4	^{59}Fe [n,γ] ^{60}Fe	1.5x10^{6} y [b]	1.5	2	NNDC 2002b [e]
^{114m}In	190.3	15.56 ± 0.16	^{113}In [n,γ] ^{114m}In	49.51 d	8.1 ± 0.8	220 ± 15	NNDC 2002a
			^{114m}In [n,γ] ^{115}In	stable [b]	1	1	d
^{113}Sn	391.7[f]	64.97 ± 0.17	^{112}Sn [n,γ] ^{113}Sn	115.09 d	0.393 ± 0.019	20.6 ± 2	DeCorte *et al*. 1985, NNDC 2002a
			^{112}Sn [n,γ] ^{113m}Sn	21.4 m	0.161 ± 0.025	8.4 ± 2	DeCorte *et al*. 1985, NNDC 2002a
			^{113}Sn [n,γ] ^{114}Sn	stable [b]	9	200	Parrington *et al*. 1996
^{117m}Sn	158.6	86.4 ± 0.4	^{116}Sn [n,γ] ^{117m}Sn	13.60 d	(5.8 ± 1.2) x 10^{-3}	(350 ± 53) x 10^{-3}	Mirzadeh *et al*. 1997a
			^{116}Sn [n,γ] ^{117}Sn	stable	0.134 ± 0.03	10.81 ± 2.0	NNDC 2002a
			^{117m}Sn [n,γ] ^{118}Sn	stable [b]	1	1	d
^{117m}Sn	158.6	86.4 ± 0.4	^{117}Sn [n,n′] ^{117m}Sn	13.60 d	(222 ± 16) x 10^{-3} [c]	—	Mirzadeh *et al*. 1997a
			^{117}Sn [n,γ] ^{118}Sn	stable [b]	2.3 ± 0.5	16 ± 5	NNDC 2002a
^{188}W	155.0[h]	15.1 ± 0.9	^{186}W [n,γ] ^{187}W	23.72 h	36.5 ± 4.2	290.3	g
			^{187}W [n,γ] ^{188}W	69.78 d	14.5	398	g
			^{188}W [n,γ] ^{189}W	10.7 m [b]	12 ± 2.5	1	Mirzadeh *et al*. 1997b, d

[a] [NNDC 2002a]
[b] half-life not used in calculations
[c] fission-neutron-averaged cross section
[d] default value of 1 b used for reactions having no reported cross sections
[e] estimated from curves of ^{58}Fe and ^{59}Fe [n,γ] cross sections vs. neutron energy
[f] from daughter ^{113m}In
[g] see Section 2.3 for discussion of ^{186}W [n,γ] ^{187}W [n,γ] ^{188}W cross sections
[h] from daughter ^{188}Re

half-life, level of radioactivity, and intensity and energy of γ-rays. When possible, all activities were measured over several half-lives and the activities at the end of bombardment (A^0) were calculated using the CLSQ code [Cumming 1962]. Table 1.2 summarizes the radioisotopes analyzed to determine flux spectra. Neutron cross sections and relevant nuclear data were obtained from the National Nuclear Data Center [NNDC 2002a] or BNL325 [Mughabghab *et al*. 1984], except as noted in Table 1.2.

Radioactivity ($\boldsymbol{A^0}$, counts per second, cps) at the end of bombardment (EOB) was converted to absolute disintegrations per second (A^0, dps) by appropriate corrections for gamma ray intensity (I_γ) and detector efficiency (ε_γ), $A^0 = \boldsymbol{A^0}/I_\gamma\varepsilon_\gamma$. The general equations governing the reactor production of radionuclides are complex, and hence neutron flux can only be determined numerically. The radionuclide transmutation and decay code LAURA [Mirzadeh and Walsh 1998] was used to calculate fluxes, accounting for both target depletion and product nuclei burn-up. LAURA is based on the well-known Bateman [1910] equations which govern transmutation of nuclei by neutron capture in addition to spontaneous decay. In a generalized form, the Bateman equations can be written as:

$$N_n(t) = \left(\prod_{i=1}^{n-1} c_i\right) N_1^0 \sum_{i=1}^{n} a_i e^{-\Lambda_i t}$$
$$a_i = \prod_{j \neq i} \left(\Lambda_j - \Lambda_i\right)^{-1} \quad (j = 1, 2, ..., n) \tag{2.2}$$

where $N_n(t)$ is the number of atoms of the n^{th} species at time t, and N_1^0 is the number of target atoms (which includes appropriate corrections for isotopic mass and enrichment).

c_n is the formation constant (λ_{n-1} or $\sigma_{n-1}\phi$) of the n^{th} species from $(n\text{-}1)^{th}$ species. σ_n is the cross section for a specific reaction (cm^2), ϕ is the neutron flux (n cm^{-2} s^{-1}), and λ_n is the decay constant of the n^{th} nuclide (s^{-1}). Λ_n is the total depletion constant, defined as $\lambda_n + \sigma_n\phi$, and t is the irradiation time (s). In the simplest form, however, when the irradiation time is very short and the product nuclei burn-up cross section and target depletion cross section are not very large, the neutron flux (ϕ) can be calculated using the equation:

$$\phi = A^0 \left[N_1^0 \sigma_n \left(1 - e^{-\lambda t}\right)\right]^{-1} \tag{2.3}$$

where A^0 is the activity of the product radionuclide (dps).

In the case of neutron capture reactions, σ_n represents the effective cross section,

$$\sigma_{\text{eff}} = \sigma_0 + \left(\frac{1}{r}\right) I_0 \tag{2.4}$$

where σ_0 is the 2200 m/s cross section, I_0 is the resonance integral, and $r = \phi_0/\phi_{ep}$ (ϕ_0 is the thermal neutron flux and ϕ_{ep} is the epithermal neutron flux per unit ln ΔE, lethargy [Stoughton and Halperin 1959]). Since direct measurement of PTP epithermal flux by the Cd cover technique was not possible, thermal to epithermal flux ratios were derived from HFIR hydraulic tube flux ratio measurements [Mahmood *et al*. 1995] and theoretical predictions of the relationship between hydraulic tube and PTP fluxes [Cheverton and Sims 1971].

For neutron inelastic and threshold reactions, σ_n represents the fission-neutron-averaged cross section (from threshold up to 20 MeV).

For a reaction involving two successive neutron captures (i.e., transformation of ^{186}W to ^{188}W), a high burn-up cross section of the product nucleus (e.g., burn-up of ^{60}Co), or a high cross section for target depletion (e.g., depletion of ^{113}In in the ^{113}In[n,γ]^{114g}In reaction), the thermal neutron flux was determined numerically using LAURA. For a given set of cross section values, irradiation time and other relevant nuclear data, LAURA is used to calculate the activity at the end of bombardment, A^0, as a function of neutron flux. The measured A^0 can then be used to arrive at the corresponding thermal flux. In the case of neutron transmutation of ^{186}W to ^{188}W, the following cross sections were used: ^{186}W: σ_0 = 36.5 b, I_0 = 290.3 b; ^{187}W: σ_0 = 14.5 b, I_0 = 398 b (unpublished HFIR measurements). Note that the recent HFIR measurements have indicated significantly lower cross sections than reported values for the ^{187}W[n,γ]^{188}W reaction (the corresponding cross sections from the Evaluated Nuclear Data File [NNDC 2002a] are: ^{186}W: σ_0 = 37.9 b, I_0 = 485 b; ^{187}W: σ_0 = 64 b, I_0 = 2760 b), but are consistent with experience from the routine production of this medical radioisotope [Callahan *et al*. 1992]. Since the γ-rays of ^{188}W are exceedingly weak, ^{188}W radioactivity was determined by measuring the intensity of 155 keV γ-rays from its daughter, ^{188}Re ($t_{1/2}$ = 17.0 h), at equilibrium (Table 2.2). Similarly, ^{113}Sn radioactivity was determined by measuring the intensity of 392 keV γ-rays from its daughter, ^{113m}In ($t_{1/2}$ = 1.658 h), at equilibrium (Table 2.2).

The actual mass of Co/Al monitors in positions 2 and 7 (Table 2.1) were 6.4 mg and 7.5 mg, respectively, and a year after irradiation, these monitors were still too active for

direct gamma ray analysis. To conserve time, small portions of these monitors (~10%) were cut, weighed and subjected to gamma ray analysis.

Systematic error was calculated based on the errors associated with cross sections, activity rates and detector efficiencies. The error propagation throughout the flux calculations was based on the sum of squares of the systematic errors (one sigma, one standard deviation) or the deviation from mean of the data points, whichever was greater. Some uncertainty is also introduced by assuming a fission neutron spectrum for threshold reactions (i.e., [n,p] and [n,n′]) flux calculations, but that error was not quantifiable (i.e., data is not available to quantify the deviation of neutron flux spectra in PTP positions from a fission spectrum).

2.3 Experimental Results

2.3.1 Thermal Neutron Flux

The single and double radiative capture reactions were used to determine the axial flux profile at one of the six peripheral target positions (G4, Figure 2.1). The results for the various reactions in each capsule were averaged to produce a single value for thermal flux for each array position (Table 2.3). The flux monitors involving a single radiative capture reaction included: $^{113}In[n,\gamma]^{114m}In$, $^{109}Ag[n,\gamma]^{110m}Ag$, $^{58}Fe[n,\gamma]^{59}Fe$, $^{116}Sn[n,\gamma]^{117m}Sn$, $^{112}Sn[n,\gamma]^{113}Sn$, and $^{122}Te[n,\gamma]^{123}Te$. The measured thermal neutron flux values ranged from 1.11×10^{15} to 1.49×10^{15} n cm^{-2} s^{-1}.

Table 2.3 PTP Thermal and Epithermal Neutron Flux Spectra

Array Position	Nuclear Reaction	Saturation Activity at EOB (Bq mg^{-1})	ϕ_0 Ave. (n cm^{-2} s^{-1})	ϕ_0/ϕ_{ep} [a]	ϕ_{ep} (n cm^{-2} s^{-1})
1 (bottom)	^{113}In [n,γ] ^{114m}In ^{109}Ag [n,γ] ^{110m}Ag	2.36×10^{10} 2.29×10^{9}	$(1.14 \pm 0.08) \times 10^{15}$	33	$(3.5 \pm 0.3) \times 10^{13}$
2	^{59}Co [n,γ] ^{60}Co ^{186}W 2[n,γ] ^{188}W	3.65×10^{9} 1.29×10^{8}	$(1.11 \pm 0.08) \times 10^{15}$	28	$(4.0 \pm 0.3) \times 10^{13}$
3	^{58}Fe [n,γ] ^{59}Fe	5.70×10^{9}	$(1.30 \pm 0.06) \times 10^{15}$	24	$(5.4 \pm 0.2) \times 10^{13}$
4	^{116}Sn [n,γ] ^{117m}Sn ^{112}Sn [n,γ] ^{113}Sn	1.33×10^{8} 2.12×10^{9}	$(1.49 \pm 0.16) \times 10^{15}$	20	$(7.5 \pm 0.8) \times 10^{13}$
5	^{116}Sn [n,γ] ^{117m}Sn ^{112}Sn [n,γ] ^{113}Sn	1.18×10^{8} 2.19×10^{9}	$(1.35 \pm 0.15) \times 10^{15}$	18	$(7.5 \pm 0.8) \times 10^{13}$
6	^{58}Fe [n,γ] ^{59}Fe	5.94×10^{9}	$(1.35 \pm 0.06) \times 10^{15}$	23	$(5.9 \pm 0.3) \times 10^{13}$
7 (top)	^{186}W 2[n,γ] ^{188}W ^{59}Co [n,γ] ^{60}Co	1.54×10^{8} 3.83×10^{9}	$(1.18 \pm 0.08) \times 10^{15}$	27	$(4.4 \pm 0.3) \times 10^{13}$

[a] derived from hydraulic tube measurements

The neutron flux values obtained from the ^{122}Te monitors were consistently lower than other monitors and were not included in the average. It is suspected that the reported cross sections for the ^{122}Te[n,γ]^{123}Te reaction [NNDC 2002a] are inaccurate. The cross sections reported for the transformation of ^{122}Te to the metastable (1.1 b) and ground (2.3 b) states of ^{123}Te are inconsistent with what would be expected based on quantum mechanics. The thermal cross section for production of ^{123m}Te, with a spin of -11/2, should be much smaller than the cross section for production of ^{123g}Te, which has a spin of +1/2. The calculated effective cross section for the ^{122}Te[n,γ]^{123m}Te reaction (which includes ^{123m}Te production via both ^{122}Te[n,γ]^{123m}Te and ^{122}Te[n,γ]^{123g}Te[n,n′]^{123m}Te) based on the thermal flux calculated from the ^{58}Fe monitor in the same capsule (position 3, Table 2.1) was 7.7 mb, much lower than the reported value of 1.1 b for the direct production reaction (^{122}Te[n,γ]^{123m}Te) alone.

The double radiative capture reaction, ^{186}W[n,γ]^{187}W[n,γ]^{188}W, gave values of 1.13 x 10^{15} and 1.22 x 10^{15} n cm^{-2} s^{-1} for neutron flux at positions 2 and 7, respectively. As stated earlier, an estimate of the epithermal flux (0.5 eV ≤ E_n ≤ 100 keV) profile was made using thermal to epithermal flux ratios extrapolated from HFIR hydraulic tube data [Mahmood *et al*. 1995].

The epithermal flux values, derived by dividing the thermal flux by the associated flux ratio in Table 2.3, ranged from 3.5 x 10^{13} to 7.5 x 10^{13} n cm^{-2} s^{-1}. Thermal and epithermal flux profiles of the HFIR PTP are plotted in Figure 2.4 along with hydraulic tube thermal and epithermal flux curves for comparison.

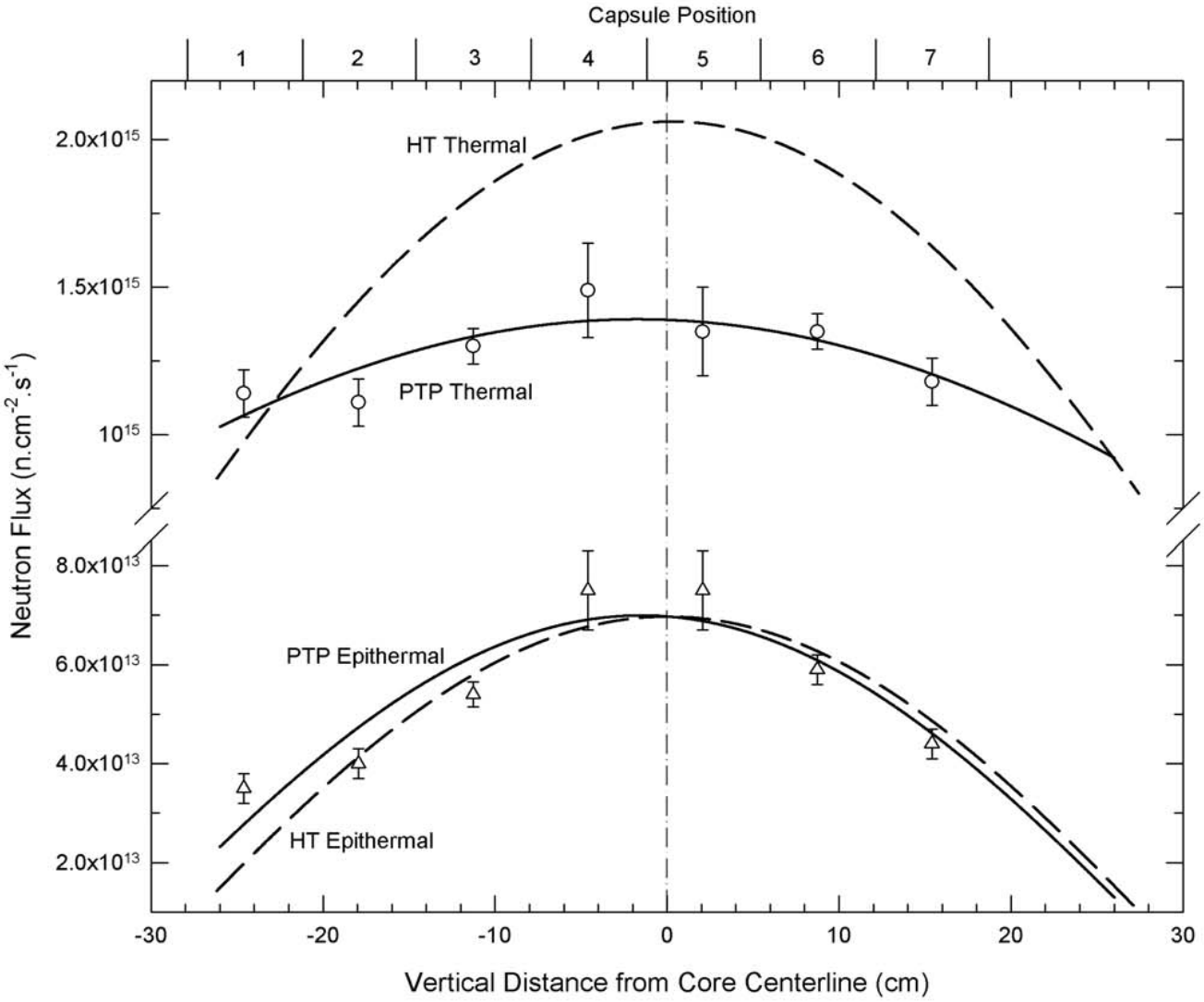

Figure 2.4 Peripheral Target Position and Hydraulic Tube Neutron Flux Profiles

2.3.2 Fast Neutron Flux

A neutron inelastic reaction, ^{117}Sn[n,n′]^{117m}Sn, was used to determine the integrated neutron flux above 0.318 MeV, the calculated threshold [Evans 1955] for this reaction. The flux values for neutrons with $E_n \geq 0.318$ MeV were 5.87 x 10^{14} and 5.99 x 10^{14} n cm^{-2} s^{-1} for positions 4 and 5 of the PTP, respectively (Table 2.4). These flux values were based on a 222 ± 16 mb cross section for the ^{117}Sn[n,n′]^{117m}Sn reaction which was previously measured in the HFIR hydraulic tube [Mirzadeh *et al*. 1997a], and a value of 0.60 for the ratio of fast ($E_n \geq 0.318$ MeV) to thermal flux obtained from PTP design data (see Section 2.4).

The data from the ^{54}Fe[n,p]^{54}Mn reaction provided information for the total flux above ~1.5 MeV, the threshold energy for this reaction (determined graphically from a BNL325-type plot [NNDC 2002b] because the Q value is positive and thus the effective threshold is due to the Coulomb barrier of the compound nucleus). The integrated flux values for fast neutrons with $E_n \geq 1.5$ MeV were 5.94 x 10^{14} and 6.10 x 10^{14} n cm^{-2} s^{-1} for positions 3 and 6, respectively (Table 2.4). A spectrum-averaged cross section of 82.5 ± 5.0 mb was used for the ^{54}Fe[n,p]^{54}Mn reaction [IAEA 1974]. Similar to the ^{117}Sn[n,n′]^{117m}Sn reaction, a fast ($E_n \geq 1.5$ MeV) to thermal flux ratio of 0.40, obtained from design data, was used in the calculations to account for target depletion and product burn-up during irradiation.

Table 2.4 PTP Fast Neutron Flux Measurements [a]

Array Position	Nuclear Reaction	$\phi_{(n,n')}$ (n cm^{-2} s^{-1})	$\phi_{(n,p)}$ (n cm^{-2} s^{-1})
3	^{54}Fe [n,p] ^{54}Mn	—	$(5.94 \pm 0.47) \times 10^{14}$
4	^{117}Sn [n,n′] ^{117m}Sn	$(5.87 \pm 0.51) \times 10^{14}$	—
5	^{117}Sn [n,n′] ^{117m}Sn	$(5.99 \pm 0.53) \times 10^{14}$	—
6	^{54}Fe [n,p] ^{54}Mn	—	$(6.10 \pm 0.48) \times 10^{14}$

[a] reported neutron flux values are based on the fission-neutron-averaged cross sections for the corresponding reactions

2.4 Design Calculation of Neutron Fluxes

Design neutron flux values reported by Cheverton and Sims [1971, Appendix C] were used to help evaluate the experimental results. The calculations by Cheverton and Sims were based on one-dimensional 33-group diffusion theory. Relevant data from these multi-group calculations were converted to 2200 m/s flux (thermal group) and flux per unit lethargy (epithermal groups) and adjusted to 85 MW (the current HFIR operation power level). This data is presented in Table 2.5. Group 33 is the thermal neutron group with neutron energy < 0.414 eV and groups 8 through 32 represent the epithermal range with energies from 0.414 eV to 111 keV. Note that single values given for epithermal flux represent an arithmetic mean of groups 8 through 32.

Table 2.5 PTP and HT Neutron Flux Design Values

Flux Group	Computer Output Group Flux [a]		Group Energy Boundary (eV) [b]		Group Flux (n cm^{-2} s^{-1}) [c,d]	
	Mesh Point 7 [e]	Mesh Point 13 [f]	Lower	Upper	Hydraulic Tube	Peripheral Target Position
33 (Thermal)	14.71	13.09	0	4.14×10^{-1}	2.00×10^{15}	1.78×10^{15}
32	0.486	0.517	4.14×10^{-1}	6.83×10^{-1}	7.93×10^{13}	8.43×10^{13}
31	0.505	0.542	6.83×10^{-1}	1.13	8.26×10^{13}	8.87×10^{13}
30	0.515	0.559	1.13	1.86	8.36×10^{13}	9.08×10^{13}
29	0.516	0.568	1.86	3.06	8.46×10^{13}	9.31×10^{13}
28	0.495	0.571	3.06	5.04	8.09×10^{13}	9.34×10^{13}
27	0.423	0.567	5.04	8.32	6.89×10^{13}	9.22×10^{13}
26	0.604	0.622	8.32	1.37×10^{1}	9.88×10^{13}	1.02×10^{14}
25	0.607	0.631	1.37×10^{1}	2.26×10^{1}	9.89×10^{13}	1.03×10^{14}
24	0.606	0.636	2.26×10^{1}	3.73×10^{1}	9.87×10^{13}	1.04×10^{14}
23	0.607	0.642	3.73×10^{1}	6.14×10^{1}	9.94×10^{13}	1.05×10^{14}
22	0.612	0.650	6.14×10^{1}	1.01×10^{2}	1.00×10^{14}	1.07×10^{14}
21	0.612	0.653	1.01×10^{2}	1.67×10^{2}	9.93×10^{13}	1.06×10^{14}
20	0.610	0.653	1.67×10^{2}	2.75×10^{2}	9.97×10^{13}	1.07×10^{14}
19	0.607	0.654	2.75×10^{2}	4.54×10^{2}	9.88×10^{13}	1.06×10^{14}
18	0.603	0.653	4.54×10^{2}	7.48×10^{2}	9.86×10^{13}	1.07×10^{14}
17	0.599	0.652	7.48×10^{2}	1.23×10^{3}	9.82×10^{13}	1.07×10^{14}
16	0.595	0.651	1.23×10^{3}	2.04×10^{3}	9.59×10^{13}	1.05×10^{14}
15	0.589	0.648	2.04×10^{3}	3.36×10^{3}	9.64×10^{13}	1.06×10^{14}
14	0.589	0.651	3.36×10^{3}	5.53×10^{3}	9.65×10^{13}	1.07×10^{14}
13	0.593	0.659	5.53×10^{3}	9.12×10^{3}	9.67×10^{13}	1.08×10^{14}
12	0.611	0.682	9.12×10^{3}	1.50×10^{4}	1.00×10^{14}	1.12×10^{14}
11	0.639	0.717	1.50×10^{4}	2.48×10^{4}	1.04×10^{14}	1.16×10^{14}
10	0.659	0.742	2.48×10^{4}	4.09×10^{4}	1.07×10^{14}	1.21×10^{14}
9	0.742	0.839	4.09×10^{4}	6.74×10^{4}	1.21×10^{14}	1.37×10^{14}
8	0.813	0.927	6.74×10^{4}	1.11×10^{5}	1.33×10^{14}	1.52×10^{14}
7	0.953	1.096	1.11×10^{5}	1.83×10^{5}	1.55×10^{14}	1.79×10^{14}
6	1.201	1.394	1.83×10^{5}	3.02×10^{5}	1.96×10^{14}	2.27×10^{14}
5	1.372	1.616	3.02×10^{5}	4.98×10^{5}	2.24×10^{14}	2.64×10^{14}
4	1.954	2.307	4.98×10^{5}	8.21×10^{5}	3.19×10^{14}	3.77×10^{14}
3	2.049	2.475	8.21×10^{5}	1.35×10^{6}	3.36×10^{14}	4.06×10^{14}
2	2.273	2.683	1.35×10^{6}	3.68×10^{6}	3.70×10^{14}	4.37×10^{14}
1	0.601	0.691	3.68×10^{6}	1.00×10^{7}	9.81×10^{13}	1.13×10^{14}

[a] [Cheverton and Sims 1971, Table C.5]
[b] [Cheverton and Sims 1971, Table C.2]
[c] [Cheverton and Sims 1971, Appendix C]
Group 33: Group Flux = 1.92×10^{12} x (Computer Output Group Flux) n cm^{-2} s^{-1} MW^{-1}
Groups 8-32: Group Flux = 0.96×10^{12} x (Computer Output Group Flux) n cm^{-2} s^{-1} MW^{-1}
[d] all values represent 85 MW operation, thermal fluxes converted to 2200 m/s flux at 60ºC [Lamarsh 1993, Eq. 5.63], groups 8-32 fluxes expressed per unit lethargy
[e] corresponds to the position of the Hydraulic Tube
[f] corresponds to the position of the Peripheral Target Position

2.5 Evaluation of Data

The experimental data, shown in Figure 2.4 for both thermal and epithermal flux, were fit to cosine curves, the shape of a cylindrical reactor's axial flux profile [Lamarsh 1993, Table 6.2], where the target capsule midpoints (see Section 2.1.2) were used as the x-axis values for the curve fit. As seen in Figure 2.4 and Table 2.3, the axial thermal flux profile of the peripheral target position is fairly flat, ranging from 1.1×10^{15} to 1.5×10^{15} n cm^{-2} s^{-1}, and the axial epithermal flux profile ranges from 3.5×10^{13} to 7.5×10^{13} n cm^{-2} s^{-1}. As stated in the Section 2.3.1, the epithermal flux values were based on HT thermal/epithermal flux ratios, as the 24 day HFIR operating cycle prevented direct measurement of epithermal flux using the cadmium cover technique, primarily due to significant burn out of Cd during a high-fluence irradiation. Alternative approaches such as inferring the thermal/epithermal ratio by irradiating a set of monitor foils having very different thermal and resonance cross sections or by operating the HFIR at a much lower power level are the subject of other investigations and are beyond the scope of the present work.

Calculations of neutron flux based on the HFIR core design (Table 2.5) predicted 11% lower thermal flux in the PTP than in the HT at the horizontal core midplane. The measured thermal flux of 1.49×10^{15} n cm^{-2} s^{-1} at the core midplane was, however, 26% lower than that of the HT. While the design and experimental thermal neutron flux values in the HT were rather consistent, 2.00×10^{15} n cm^{-2} s^{-1} (Table 2.5) and 2.08×10^{15}

n cm^{-2} s^{-1} [Mahmood *et al*. 1995], respectively, the design and experimental thermal neutron flux values for the PTP deviated by 16% (1.78 x 10^{15} n cm^{-2} s^{-1} and 1.5 x 10^{15} n cm^{-2} s^{-1}, respectively). The corresponding PTP epithermal flux at the core midplane was 7.5 x 10^{13} n cm^{-2} s^{-1} which was 29% lower than the design value of 1.06 x 10^{14} n cm^{-2} s^{-1} and 23% lower than the design value of 9.69 x 10^{13} n cm^{-2} s^{-1} for the HT. Since the HT and PTP flux measurements were not conducted with the same target bundle loadings, and since the metal to water ratio in the target region will result in substantial differences in neutron flux, the extrapolation of HT thermal-to-epithermal ratios to PTPs is not very accurate. As stated earlier, of thirty positions in the flux trap bundle, only 12-16 positions currently contain Cm targets and the remaining positions, with the exception to the HT, are filled with solid aluminum targets. The design neutron flux calculations of Cheverton and Sims [1971] were performed with 30 Pu targets in the flux trap. This, of course, is one major difference between the early flux calculations and the current measurements.

Due to the proximity of the PTPs to the fuel (Figure 2.1), the ratio of fast to thermal flux was expected to be higher in the PTP than the HT. Indeed, the experimental measurements indicated a value of ~6x10^{14} n cm^{-2} s^{-1} for the fast neutron flux ($E_n \geq 1$ MeV, Table 2.4) in the PTP at the core horizontal midplane, corresponding to a fast to thermal ratio of ~0.4, compared to ~0.25 reported for the HT [Mahmood *et al*. 1995]. Further, the measured fast flux value (for $E_n \geq 0.8$ MeV) is only ~10% lower than the design value of 6.8 x 10^{14} n cm^{-2} s^{-1} [Mirzadeh *et al*. 1992] and it is 20% lower than the design value of 7.5x10^{14} n cm^{-2} s^{-1} [Cheverton and Sims 1971]. In addition, the

experimental measurements indicated a relatively flat gradient for the fast neutron flux over $E_n \geq 0.3$ MeV (Table 2.4). Obviously, the fast flux measurements based on fission-neutron-averaged cross sections primarily result in integrated flux values above the reaction thresholds with an added uncertainty arising from the flux spectra differences between HFIR and other reactors used to determine the cross sections.

2.6 Uncertainties in Data

An uncertainty arises from the fact that the design neutron flux calculations derived from Cheverton and Sims [1971] do not exactly represent the conditions of HFIR operating Cycle 362, in which the measurements were performed. The design calculations were performed at 1100 megawatt-days (approximately mid-cycle at the current 85 MW operation level), whereas the experimentally determined values represent time-averaged fluxes over an entire operating cycle. Further, calculations were based on the flux trap loaded with a standard transplutonium target bundle containing 300 g of ^{242}Pu; the current loading of 12-16 Cm and 15-19 solid Al targets will produce a different flux spectrum. In addition, the calculations were performed at the core midplane and application of a cosine function over the axial length of the active core does not adequately account for the relative axial variation of thermal and epithermal fluxes due to perturbation related to the finite fuel length and heavily moderated ends of the fuel elements. Finally, the design values are adversely affected by the fact that the target bundle placed in the flux trap was assumed to have a radius of 5.00 cm whereas the current target bundle is slightly larger and the current position of the PTPs (5.38 cm from

the reactor axial centerline) is located in what was considered to be a water-filled gap in the design analysis.

With respect to the fast neutron fluxes, the flux measurements based on fission-neutron-averaged cross sections merely result in the integrated flux values above the reaction thresholds. Since fluxes and cross sections are not unfolded, these measurements do not account for differences in flux spectra between HFIR and the reactors used to determine the cross sections. Nevertheless the measured fast flux values are useful parameters in radioisotope production calculations.

Another significant source of uncertainty is the validity of the cross sections used in the calculations. Cross sections were primarily obtained from the NNDC [2002a], BNL325 [Mughabghab *et al*. 1984], or more recent measurements if available. Table 2.2 indicates the source of all cross sections used in the calculations.

2.7 Recommended Values for Flux Data

Measurements of the neutron flux at the HFIR peripheral target position indicated thermal and epithermal flux values of 1.5 x 10^{15} and 7.5 x 10^{13} n cm^{-2} s^{-1}, respectively, at the horizontal core midplane. The axial thermal flux profile of the peripheral target position were found to be fairly flat, ranging from 1.1 x 10^{15} to 1.5 x 10^{15} n cm^{-2} s^{-1}. The fast neutron flux ($E_n \geq 1$ MeV) in the PTP was ~6x10^{14} n cm^{-2} s^{-1} at the core horizontal midplane, corresponding to a fast-to-thermal ratio of ~0.4, and the profile for $E_n \geq 0.3$

MeV was rather flat. The measurements represent a reliable characterization of the PTP flux spectra since consistent results were obtained with a variety of flux monitors, which include single and double radiative capture reactions, inelastic scattering and threshold reactions. The results are also generally consistent with many years of experience in radioisotope production at the HFIR and are fairly consistent with other published data [Mirzadeh *et al*. 1992; Mahmood *et al*. 1995]. As stated earlier in the discussion of uncertainties, the deviation of the measurements from design values [Cheverton and Sims 1971] can be attributed to differences in core loadings and the different design of the flux trap target bundle.

Based on the results of analyses in this chapter, recommended flux data for isotope production calculations are provided in Table 2.6.

Table 2.6 PTP and HT Flux Data

Position	Peripheral Target Position		Hydraulic Tube	
	ϕ_0 (n cm^{-2} s^{-1})	ϕ_0/ϕ_{ep}	ϕ_0 (n cm^{-2} s^{-1})	ϕ_0/ϕ_{ep}
1	1.1×10^{15}	33	1.0×10^{15}	40
2	1.25×10^{15}	28	1.45×10^{15}	35
3	1.35×10^{15}	24	1.8×10^{15}	30
4	1.4×10^{15}	20	2.0×10^{15}	25
5	1.4×10^{15}	18	2.05×10^{15}	20
6	1.35×10^{15}	23	1.95×10^{15}	25
7	1.2×10^{15}	27	1.65×10^{15}	30
8	1.05×10^{15}	31	1.2×10^{15}	35

3 Tungsten Cross Section Measurements

Tungsten-188 yields lower than predicted values could be the result of inaccurate neutron cross sections and resonance integrals. Production calculations had historically been based upon cross section measurements made at the High Flux Isotope Reactor (HFIR) in 1996. While those measurements yielded results that were more consistent with large-scale ^{188}W production experience than calculations using published neutron data, production yields were still approximately a factor of two lower than theoretical predictions.

Data from the previous HFIR measurements and all relevant data in the literature were reviewed to determine reliable values for use in production calculations. In addition, experiments were conducted at HFIR to further validate cross sections.

3.1 Cross Section Measurement

To evaluate previous cross section measurements and evaluations, it is imperative to define the quantities being measured and reported. This has not always been done in the literature and may account, in part, for discrepancies in reported values for many nuclide cross sections.

While many publications provide comprehensive theoretical analyses of neutron cross sections [e.g., Beckurts and Wirtz 1964; Hughes 1957; Curtiss 1965; Gryntakis and Kim

1976; Krane 1988], a two-group approach is commonly used for reactor isotope production calculations [Stoughton and Halperin 1959; Gryntakis *et al*. 1987]. Using Stoughton and Halperin's [1959] methodology, thermal cross sections and resonance integrals are measured and reported such that reaction rates can be calculated by:

$$\begin{aligned} R &= \phi_0 \left(g\sigma_0 \right) + \phi_{ep} I_0' \\ &= \phi_0 \sigma_{th} + \phi_{ep} I_0 \end{aligned} \tag{3.1}$$

where

$$\begin{aligned} \sigma_{th} &= g\sigma_0 + \frac{\phi_{ep}}{\phi_0} \int_{5E_{kT}}^{E_C} \sigma(E) \frac{dE}{E} \\ &= g\sigma_0 + \frac{\phi_{ep}}{\phi_0} \left(I_0' - I_0 \right) \end{aligned}$$

In these equations, ϕ_0 is the 2200 m/s flux, ϕ_{ep} is the epithermal flux, σ_0 is the 2200 m/s cross section, I_0 is the resonance integral from neutron energies E_C (cadmium cutoff energy) to infinity, I'_0 is the resonance integral from neutron energies $5E_{kT}$ (assumed lower bound of epithermal flux) to infinity, and g is the Westcott [1955] factor (g is unity for a nuclide with a cross section that varies as $1/v$ in the thermal region). The crucial distinction between the two alternate formulations for total reaction rate has to do with the treatment of the reaction rate for neutrons with energies between $5E_{kT}$ and E_C. In the first formulation, these reactions are incorporated in the second term since I'_0 is defined as the integrated cross section from $5E_{kT}$ to infinity. In the second formulation, these reactions are incorporated in the first term (in σ_{th}) since I_0 is defined as the integrated cross section from E_C to infinity.

Graphical representations of neutron flux and cross section spectra clarify the distinction between the alternate forms for reaction rate calculations. Figure 3.1 shows a neutron population with a Maxwellian distribution (at 293.6 K) which is a representation of the thermal neutron population and a neutron population with a $1/E$ distribution which is the epithermal neutron distribution in a well-moderated reactor. It is obvious that just above the thermal neutron range ($5E_{kT}$ = 0.127 eV) the neutron population consists of both thermal neutrons (i.e., those in thermal equilibrium) and epithermal neutrons (i.e., neutrons slowing down from fission energies to thermal energy via scattering reactions). It is also apparent that the cadmium cutoff energy (E_C = 0.5 eV) is above the point where the epithermal flux is assumed to go to zero ($5E_{kT}$). Thus, the alternate formulations differ in their treatment of neutron between $5E_{kT}$ and E_C.

The first formulation is based on a resonance integral, I'_0, defined with a lower limit of integration of $5E_{kT}$. Thus, the product of I'_0 and the epithermal flux (ϕ_{ep}) yields the reaction rate above $5E_{kT}$. The total reaction rate is obtained by adding to this the product of the 2200 m/s flux (ϕ_0) and the 2200 m/s cross section (σ_0), which is the reaction rate below $5E_{kT}$.

The second formulation, on the other hand, is based on a resonance integral, I_0, defined with a lower limit of integration of E_C. In this case, the product of I_0 and ϕ_{ep} yields only the reaction rate above E_C. Since the product of ϕ_0 and σ_0 gives only the reaction rate below $5E_{kT}$, the reaction rate for neutrons between $5E_{kT}$ and E_C must be addressed. This

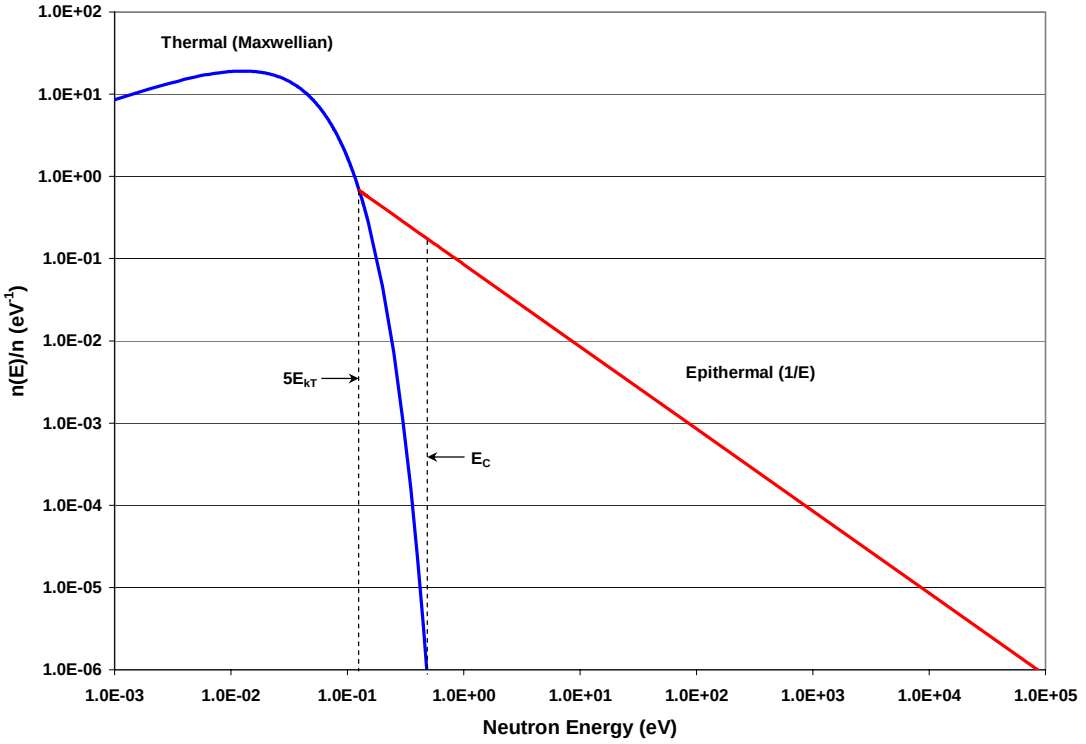

Figure 3.1 Thermal and Epithermal Neutron Flux Distributions

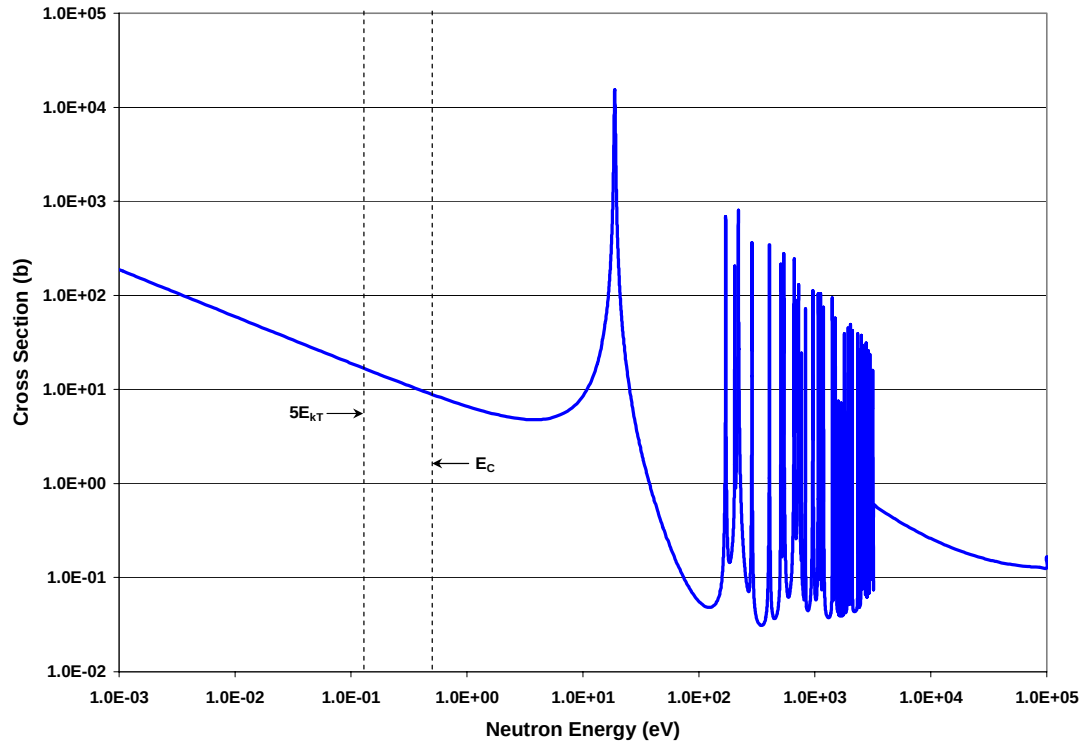

Figure 3.2 Neutron Cross Section as a Function of Neutron Energy

is done by defining σ_{th} (see Appendix C.1) which incorporates both σ_0 and the cross section between $5E_{kT}$ and E_C.

Thus, it is important to understand the cross sections one is dealing with so that appropriate pairs (either σ_0 and I'_0 or σ_{th} and I_0) are used in calculations. Unfortunately, these distinctions are not always clear in the literature and it is occasionally not possible to determine which quantities are being reported. Most thermal cross sections are reported as the 2200 m/s cross section (σ_0) since this cross section is either determined differentially or integrally in comparison with a known standard. Resonance integrals, however, may be reported without specifying whether they represent the cross section above $5E_{kT}$ or E_C. One would presume that resonance integrals measured using cadmium covers represent the cross section above E_C, but resonance integrals derived theoretically (e.g., using a Breit-Wigner calculation) or from non-cadmium cover experiments may represent the cross section above $5E_{kT}$. (As will be seen in Section 3.3, this lack of specificity is indeed the case for tungsten isotopes.)

While use of an appropriate combination of thermal cross section and resonance integral is required for scientific rigor, errors associated with misuse of cross sections tend to be small. This may explain how problems with cross sections may not be readily apparent when calculations and experimental data are compared. Figure 3.2, a plot of the evaluated nuclear data file for ^{186}W neutron capture, provides illustration of this point. The cross section for ^{186}W varies as $1/v$ ($1/\sqrt{E}$) over the thermal neutron range. As a result, the cross section between $5E_{kT}$ and E_C is much lower than the cross section at

lower neutron energies. This, in combination with the lower neutron flux between $5E_{kT}$ and E_C compared to the flux at lower energies (see Figure 3.1), clearly shows that use of σ_0 rather than σ_{th} in the second formulation will not result in a significant error. Also, since the resonance integral is essentially the superposition of resonance capture upon the $1/v$ cross section tail, for nuclides with significant resonance capture peaks the resonance capture contribution to the resonance integral will dominate the $1/v$ contribution in the $5E_{kT}$ to E_C region. Thus, use of I_0 rather than I'_0 in the first formulation may not result in a significant error.

Regardless of the possible magnitude of error, this chapter will maintain a rigorous approach to cross section definitions and measurements in order to reduce the possibility that cross section discrepancies are responsible for differences between theoretical and experimental ^{188}W yields.

3.2 Previous High Flux Isotope Reactor Measurements

Discrepancies between theoretical and large-scale production ^{188}W yields [Callahan *et al*. 1992] prompted a series of experiments to measure ^{186}W and ^{187}W cross sections at HFIR in 1996. These unpublished measurements were made by D. Marsh, a graduate student under the direction of S. Mirzadeh at ORNL.

Table 3.1 clearly demonstrates that use of these HFIR measurements in theoretical calculations would give results more consistent with ^{188}W production experience since all

cross sections are smaller than the values recommended by the National Nuclear Data Center [NNDC 2002a]. Smaller cross sections produce smaller predicted values for ^{188}W production which reduces the discrepancy between theoretical calculations and actual experience. Actual yields, however, were still a factor of two smaller than calculations based on these cross sections.

Table 3.1 HFIR Cross Section Measurements and NNDC Recommended Values

	HFIR		NNDC	
Nuclide	σ_0 (b)	I_0 (b)	σ_0 (b)	I_0 (b)
^{186}W	36.48	290.3	37.9	485
^{187}W	14.5	398	64	2760

Evaluation of a report on the 1996 measurements identified that the cross sections were based on neutron fluxes determined by averaging values obtained from three flux monitors: cobalt, silver and gold. Different nuclides can produce substantially different values for thermal and epithermal fluxes based on their resonant properties [Stoughton and Halperin 1959]. Recalling that the resonance integral is fundamentally the superposition of a resonance capture upon a 1/v curve (Section 3.1), it is helpful to note that the 1/v contribution to I_0 (resonance integral above the cadmium cutoff) is $0.45\sigma_0$, while its contribution to I'_0 (resonance integral above $5E_{kT}$) is $0.9\sigma_0$. Therefore, for a pure 1/v absorber (i.e., no resonance absorption), resonance integral measurements are extremely sensitive to the specific cutoff energy since lower cutoff energies (e.g., resulting from cadmium covers that are too thin) will cause the measured resonance integral to double as the cutoff energy goes from E_C to $5E_{kT}$. To reduce this sensitivity a nuclide with significant resonance capture is preferable; in such a case resonance capture

dominates in the resonance integral. Gold (^{197}Au), with its large resonance integral (I_0 = 1550 b) is an ideal flux monitor. With its relatively low thermal cross section (σ_0 = 98.65 b), the 1/v contribution (0.45 x 98.65 = 44 b) is a small part (2.8%) of the overall resonance integral and thus epithermal flux measurements will be fairly insensitive to the exact cadmium cutoff energy. Silver (^{109}Ag) has a moderate resonance integral (I_0 to ^{110m}Ag = 72.3 b) and while its 1/v component ($0.45\sigma_0$ = 2.1 b) is similarly small (2.9%), gold is preferentially used as a flux monitor because of its very large resonance integral (large flux monitors are not required) and its shorter half-life (^{198}Au $t_{1/2}$ = 2.7 d, ^{110m}Ag $t_{1/2}$ = 250 d) which facilitates more accurate calculations. Cobalt (^{59}Co), on the other hand, is a poor monitor for epithermal flux. While its resonance integral is similar to ^{109}Ag (I_0 = 74 b), the 1/v contribution ($0.45\sigma_0$ = 16.7 b) is significant (23% of the total resonance integral). Thus epithermal flux measurements using cobalt monitors are very sensitive to the cadmium cutoff energy. Indeed, fluxes presented in one section of the report for the three different monitors were substantially different, with the cobalt monitor producing the most discrepant value.

An attempt was made to reanalyze the data from the 1996 report to derive more reliable cross sections (using only the gold flux monitor data), but it was found that insufficient original data remained to perform all necessary calculations. Additionally, the thickness of the cadmium covers used was not specified so a valid cadmium cutoff energy could not be verified. Finally, there was concern regarding the elemental composition of the flux monitors reported by the manufacturers (this will be addressed in Section 3.4). Consequently, it was decided to review the cross section literature for validity (Section

3.3) and perform cross section measurements (Section 3.4) to confirm or replace published values.

3.3 Published Cross Section Measurements

Tungsten cross section measurements and evaluations published in the literature are summarized in Table 3.2.

Table 3.2 Tungsten Cross Section Measurements and Evaluations

Nuclide	σ_0 (b)	I_0 (b)	Reference
^{186}W	34.2 ± 7		Seren *et al*. 1947
		320	Harris *et al*. 1950
	34.1 ± 3		Pomerance 1952
	35 ± 3		Hughes and Schwartz 1958 [a]
		355	Koch 1960
	41.3		Lyon 1960
		490 ± 80	Scoville *et al*. 1962
		476 ± 50	Baumann 1963
	33	318	Gillette *et al*. 1966
	37.8 ± 1.2		Friesenhahn *et al*. 1966
		484	Baumgartner 1967
		450 ± 36	Beller *et al*. 1967
		380 ± 84	Borchardt 1967
	35.4 ± 0.8	534 ± 50	Damle *et al*. 1967
		345	Hayodom *et al*. 1967
	30.57		Cook and Wall 1968 [b]
		441 ± 22	Pierce and Shook 1968
		355	Aliev *et al*. 1970 [a]
	40 ± 1.5		Hogg and Wilson 1970
		290	DeCorte *et al*. 1971
		562	Mazlov and Lubnickij 1971
		486 ± 50	Rahn *et al*. 1972 [b]
	38 ± 2	441 ± 22	Zijp 1973 [a]
		410 ± 47	Van der Linden *et al*. 1974
	37.0 ± 1.5	490 ± 15	Gleason 1978
	36.6 ± 0.8	426 ± 32	Heft 1978

Nuclide	σ_0 (b)	I_0 (b)	Reference
	37 ± 3		Anufriev 1981
	37.4 ± 1.1	470 ± 10	Jefferies *et al*. 1982 [a]
	37.9 ± 0.6	485 ± 15	Mughabghab *et al*. 1984 [a]
	37 ± 2	507 ± 27	Simonits *et al*. 1984
	37.0 ± 1.5	490 ± 15	Gryntakis *et al*. 1987 [a]
	38.5 ± 0.8		Knopf and Waschkowski 1987
	38.7 ± 2	530 ± 28	DeCorte and Simonits 1989
		510.7 ± 24.3	Kimura *et al*. 1989
	37.89 ± 0.85	481.6	Zolotarev 2002 [b]
	39.45	528.5	JAERI 2002 [b]
	38.5 ± 0.5		Mughabghab 2003 [a]
	37.9 ± 0.6	485 ± 15	NNDC 2004b [a]
^{187}W	80		Lindner 1951
	64	2760	Gillette *et al*. 1966
	64 ± 10	2760 ± 550	Mughabghab *et al*. 1984 [a]
	64 ± 10	2670 ± 550	Gryntakis *et al*. 1987 [a]
	64 ± 10	2760 ± 550	NNDC 2004b [a]
^{188}W	12.0 ± 2.5		Mirzadeh *et al*. 1997

[a] evaluation
[b] calculation

Clearly, there is much uncertainty in tungsten cross sections. Reported vales for the ^{186}W 2200 m/s cross section range from 30.57 – 41.3 b, the largest value being 35% greater than the smallest value. An even larger variation exists in reported values for the resonance integral which ranges from 290 – 562 b, the largest value being 94% greater than the smallest value. Cross section compilations and databases provide values for ^{187}W that are based exclusively on one measurement (Gillette) (reference lists associated with cross section compilations and databases do not include the measurement by Lindner). For ^{188}W, only one measurement has been made and that measurement only determined the 2200 m/s cross section, not the resonance integral.

There are many factors responsible for discrepancies between reported values:

- Many measurements were made before the advent of highly accurate gamma ray detectors so post-irradiation analysis of targets could yield inaccurate data.
- Calculations of cross sections based on measured activity must rely upon previously measured data such as flux monitor cross sections, target material isotopic abundances, and activation product half-lives. Some of the references specified the values used in calculations and it was evident that these values have been refined over the years.
- As discussed in Section 3.2, the choice of a flux monitor has an impact on the measured flux. Gold was the most widely used monitor, although several measurements employed other monitors and many papers did not specify the monitor used.
- Cd cutoff energy is a function of (among other things) thickness of the Cd used in the Cd cover technique of cross section measurement [Stoughton and Halperin 1959, Table II]. Also, overall neutron transmission is a function of Cd thickness, decreasing as $e^{-N\sigma t}$, where N is the atom density of Cd, σ is the Cd cross section, and t is the thickness of Cd. Thus, cross section measurements (both 2200 m/s cross sections and resonance integrals) will be sensitive to the thickness of Cd covers used in the experiments. Most papers did not specify the thickness of Cd used and those that did demonstrated the use of different thickness.
- Section 3.1 identified that the epithermal flux in a well-moderated reactor has a $1/E$ distribution. Measurements of resonance integrals assume a $1/E$ epithermal

flux; if the epithermal flux at the location of the measurement deviates from a $1/E$ distribution then the calculated resonance integral will be in error [DeCorte *et al*. 1989]. Non-$1/E$ epithermal flux distributions have been demonstrated to produce inaccuracies in cross section data [*ibid*]; a detailed knowledge of the irradiation facilities (usually not provided) used to make the measurements summarized in Table 3.2 would be required to assess the epithermal flux distribution.

A reasonable estimation of the 2200 m/s cross section and resonance integral for ^{186}W could be obtained by treating the data in Table 3.2 as independent measurements of particular parameters. The resultant mean values and standard deviations are: $\sigma_0 = 37.0 \pm 2.3$ b and $I_0 = 438 \pm 80$ b. These values are close to those recommended by the National Nuclear Data Center (the last entry under ^{186}W in Table 3.2), which is to be expected since the value recommended by the National Nuclear Data Center is an evaluation of experimental and theoretical values. Experiments described in Section 3.4 will attempt to confirm these values.

Realistic values for the 2200 m/s cross section and resonance integral for ^{187}W are more difficult to derive. As mentioned previously, recommended values are based on only one measurement [Gillette *et al*. 1966], with the other measurement [Lindner 1951] not used, most likely because it did not measure both the 2200 m/s cross section and the resonance integral and due to the experiment design actually represents an effective cross section rather than a purely thermal (2200 m/s) cross section. (Note that the second value for the resonance integral, 2670 b, is nothing more than a typographical error in Gryntakis *et al*.

[1987], transposing two digits from the single measurement of 2760 b – this is obviously the case since their work is an evaluation of existing information and in an earlier compilation, the same authors recommended the 2760 b value.)

Unfortunately, it is not possible to evaluate the experimentally-derived values for the ^{187}W 2200 m/s cross section and resonance integral. The only published reference for this measurement [Gillette *et al*. 1966] is not a technical paper, but an annual report of the activities of the Oak Ridge National Laboratory Radioisotopes Program. As such, it merely reports the measured cross sections and provides insufficient detail on their derivation. Moreover, the uncertainty reported in all references since Mughabghab [1984] is not specified in the original reference [Gillette *et al*. 1966], nor is it included in the National Nuclear Data Center's online database of cross section data [NNDC 2002b]. The source of the uncertainty values can't be determined so the reported uncertainties are of questionable value.

The reported values for the ^{187}W 2200 m/s cross section and resonance integral could be at least partially responsible for the discrepancy between ^{188}W production calculations and actual experience. Results of ^{188}W production at Oak Ridge [Callahan *et al*. 1992] showed that theoretical production of ^{187}W was approximately 1.5 times actual production, while theoretical production of ^{188}W was approximately 10 times actual production. Since actual ^{188}W production is much more inconsistent with theoretical predictions than ^{187}W, a reasonable conclusion is that the ^{187}W cross section and resonance integral are suspect. A similar concern regarding the ^{187}W resonance integral

was expressed by Wootan *et al*. [1991], in which the authors identified a five-fold difference between theoretical and actual production of ^{188}W in the Fast Flux Test Facility at the Hanford Site near Richland, WA.

Given the questionable reliability of the ^{187}W thermal cross section and resonance integral, a goal of the experiments described in Section 3.4 is to validate these values.

Finally, the cross section for ^{188}W is not well understood. One measurement has been made [Mirzadeh *et al*. 1997] and the value reported was the burnup cross section of ^{188}W. The burnup cross section is actually an effective cross section, representing the contributions of both thermal and epithermal neutron reactions (in this case the thermal cross section and effective cross section will most likely not be substantially different because the experimental irradiation was performed in a location in which the epithermal flux is substantially lower than the thermal flux). The reported value, 12.0 ± 2.5 b, is a "conventional" thermal cross section since it is based on the thermal (Maxwellian) flux rather than the 2200 m/s flux. Using Equations (11) and (12) from Stoughton and Halperin [1959], one can derive an equation to convert the thermal (Maxwellian) cross section to a 2200 m/s cross section (and knowing the High Flux Australian Reactor operating temperature to be 50 °C):

$$\sigma_0 = \frac{2}{\sqrt{\pi}}\left(\frac{T}{T_0}\right)^{\frac{1}{2}}\sigma_{mxw} \tag{3.2}$$

$$= \frac{2}{\sqrt{\pi}}\left(\frac{323.15\ \mathrm{K}}{293.61\ \mathrm{K}}\right)^{\frac{1}{2}}\sigma_{mxw}$$

$$= 1.18\ \sigma_{mxw}$$

Using this conversion factor, the 2200 m/s cross section is 14.2 ± 3.0 b. It is reasonable to use this value in calculations; however, the resonance integral is completely unknown. Also, this value represents only a lower limit for the burnup cross section because the absolute intensities of ^{189}W γ-rays are not known (the two predominant γ-rays were assumed to have intensities of 100%; actual intensities less than 100% would result in higher calculated cross sections).

Thus, the best available information from the literature suggests the use of the following cross sections for isotope production calculations:

Table 3.3 Tungsten Cross Sections for Production Calculations

Nuclide	σ_0 (b)	I_0 (b)	Reference
^{186}W	37.0 ± 2.3	438 ± 80	average of experiments
^{187}W	64 ± 10	2760 ± 550	Gillette *et al*. 1966, NNDC 2004b
^{188}W	14.2 ± 3.0		Mirzadeh *et al*. 1997, this work

Experiments to confirm these cross sections are described in Section 3.4.

3.4 High Flux Isotope Reactor Cross Section Measurements

Experiments were designed to measure tungsten cross sections, using High Flux Isotope Reactor pneumatic tube #1 to measure the 2200 m/s cross section and resonance integral for ^{186}W and the HFIR hydraulic tube to measure the 2200 m/s cross section and resonance integral for ^{187}W. The hydraulic tube, located in the flux trap region of the reactor (Figure 3.3), has a higher neutron flux than the pneumatic tube which is located in

the beryllium reflector (Figure 3.3). The higher flux is necessary to produce sufficient ^{188}W for analysis. The cadmium cover technique was used to measure both the 2200 m/s cross sections and the resonance integrals.

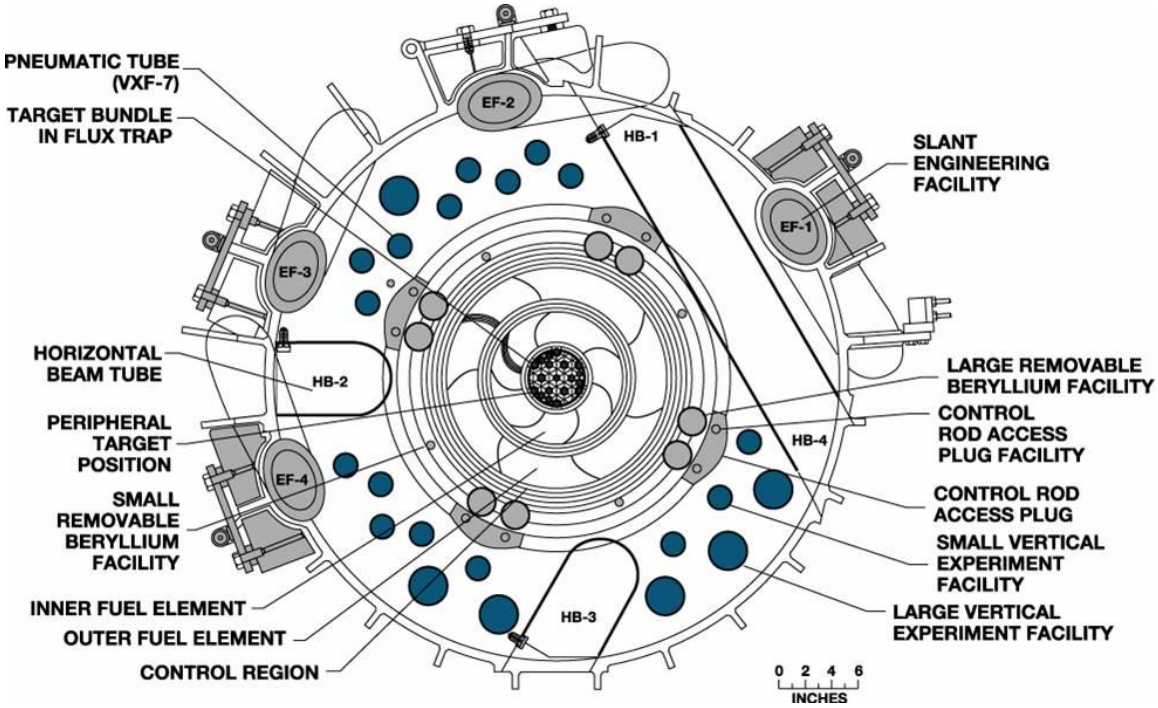

Figure 3.3 High Flux Isotope Reactor Horizontal Cross Section

3.4.1 Cadmium Cover Design

Cadmium was available in the form of 10 mil (0.0254 cm) foil. Calculations were performed to determine the number of layers of foil required to provide an adequate thermal neutron filter and also ensure the cadmium would not burn out during irradiation.

For the pneumatic tube, LAURA [Mirzadeh and Walsh 1998] was used to calculate burnup of ^{113}Cd (the cadmium isotope responsible for thermal neutron filtration) using the following data:

σ_0	20,600 b	[NNDC 2004b]
I_0	390 b	[NNDC 2004b]
ϕ_0	2.8 x 10^{14} n cm^{-2} s^{-1}	[RRD 2004]
ϕ_0/ϕ_{ep}	40	[RRD 2004]
t_{irr}	120 s	planned irradiation duration
target	1 g ^{113}Cd	

The result of this calculation was 0.9993 g of ^{113}Cd remaining at EOB, thus burnup is only 0.07%.

Calculations were also performed to assess neutron transmission through the cadmium. Taking the density of cadmium to be 8.64 g cm^{-3} [Weast 1973] and the natural abundance of ^{113}Cd to be 12.24% [NNDC 2004b], the density of ^{113}Cd in natural cadmium foil is 1.06 g cm^{-3}. The atom density of ^{113}Cd is thus:

$$N_{\text{Cd}-113} = \frac{1.06\ \text{g/cm}^3}{113\ \text{g/g}-\text{mol}} \times 6.02\times10^{23}\ \frac{\text{atoms}}{\text{g}-\text{mol}} = 5.63\times10^{21}\ \frac{\text{atoms}}{\text{cm}^3}$$

A general equation for thermal neutron transmission through cadmium and values for one, two and three layers of 10 mil cadmium foil are:

$$\begin{aligned}
\phi_x &= \phi_0 e^{-N\sigma x} \qquad (3.3)\\
&= \phi_0 e^{-(5.63\times10^{21}\ \text{atoms/cm}^3)(20{,}600\times10^{-24}\ \text{cm}^2)x}\\
&= \phi_0 e^{-116x} \quad x \text{ in cm}\\
\phi_{0.0254\,\text{cm}} &= \phi_0 e^{-116(0.0254)} = 5.25\times10^{-2}\phi_0\\
\phi_{0.0508\,\text{cm}} &= \phi_0 e^{-116(0.0508)} = 2.76\times10^{-3}\phi_0\\
\phi_{0.0762\,\text{cm}} &= \phi_0 e^{-116(0.0762)} = 1.45\times10^{-4}\phi_0
\end{aligned}$$

While two layers of 10 mil cadmium foil reduce thermal flux to 0.28% of its intensity outside the cadmium, Stoughton and Halperin [1959, Table II] show that 30 mil cadmium provide a better filter, having a cutoff energy of 0.503 eV (at room temperature and a thermal to epithermal flux ratio of 12). This is closer to a 0.5 eV filter than 20 mil cadmium which has a cutoff energy of 0.431 eV. Further, the authors state that at 30 mil or more, the cutoff energy is relatively insensitive to temperature and the thermal to epithermal flux ratio. Consequently, the cadmium covers fabricated for flux measurements consisted of three layers of 10 mil foil. The thermal flux intensity is reduced to 0.015% of its original intensity by this thickness of cadmium.

Similar calculations were performed for the hydraulic tube. Burnup of ^{113}Cd was calculated using the following data:

σ_0	20,600 b	[NNDC 2004b]
I_0	390 b	[NNDC 2004b]
ϕ_0	2.05 x 10^{15} n cm^{-2} s^{-1}	[Table 2.6]
ϕ_0/ϕ_{ep}	20	[Table 2.6]
t_{irr}	2 h	planned irradiation duration
target	1 g ^{113}Cd	

The result of this calculation was 0.7376 g of ^{113}Cd remaining at EOB, thus burnup is 26%. This burnup will be accounted for in the calculation of neutron transmission, below.

Neutron transmission calculations are the same as presented for the pneumatic tube, with the exception of an additional term to account for the burnup of cadmium. While the burnup of cadmium takes place over the course of the irradiation, the final atom density

of the cadmium filter (rather than a time-dependent atom density) will be used to simplify the calculation; this is reasonable since it provides a conservative assessment of thermal neutron transmission.

$$\begin{aligned}
\phi_x &= \phi_0 e^{-N\sigma x} \\
&= \phi_0 e^{-(0.7376)(5.63\times10^{21}\ \text{atoms/cm}^3)(20{,}600\times10^{-24}\ \text{cm}^2)x} \\
&= \phi_0 e^{-85.5x} \quad x \text{ in cm} \\
\phi_{0.0254\,\text{cm}} &= \phi_0 e^{-85.5(0.0254)} = 1.14\times10^{-1}\phi_0 \\
\phi_{0.0508\,\text{cm}} &= \phi_0 e^{-85.5(0.0508)} = 1.30\times10^{-2}\phi_0 \\
\phi_{0.0762\,\text{cm}} &= \phi_0 e^{-85.5(0.0762)} = 1.48\times10^{-3}\phi_0
\end{aligned} \tag{3.4}$$

As for the pneumatic tube, three layers of 10 mil cadmium foil will be used for the hydraulic tube cadmium covers, providing a reduction in thermal neutron intensity to 0.15% of its original intensity.

Calculations were also performed to assess the impact of 30 mil cadmium filters on epithermal neutron transmission. Using the same methodology as for thermal neutron transmission, epithermal neutron transmission is (Eq. 3.3):

$$\begin{aligned}
\phi_{0.0762\,\text{cm}} &= \phi_{ep} e^{-(5.63\times10^{21}\ \text{atoms/cm}^3)(390\times10^{-24}\ \text{cm}^2)(0.0762\ \text{cm})} \\
&= 0.846\ \phi_{ep}
\end{aligned}$$

This shows that 85% of the epithermal neutrons will pass through the cadmium filter. In the hydraulic tube irradiation, the transmission will be even greater since burnup of the cadmium will result in greater transmission over the course of irradiation. It should be recognized that the reduction in epithermal flux will not result in a measured resonance integral that is lower than its actual value; since the flux monitors will be irradiated along

with the tungsten samples, the tungsten resonance integral will be based on the resonance integrals of the flux monitors and the epithermal flux "seen" by the tungsten and the flux monitors. In the cadmium cover method of cross section measurement, the cadmium cover's only purpose is to provide a neutron flux with thermal neutrons filtered out; the effect of the cadmium on epithermal neutrons has no effect on measured resonance integrals.

Cadmium covers for the pneumatic tube irradiations were made by cutting strips of 10 mil cadmium foil 1.5 cm wide by 5.3 cm long (the length of the cadmium foil available). The strips were wrapped three times around a 0.5 cm diameter rod to make cylinders with 30 mil walls (the length of the foil was sufficient to reach nearly three complete layers, less than 20° of the cylinders was covered by only two layers). Four slits were cut in both ends of the cylinders. The four flaps (created by the slits) at one end of each cylinder were folded over to seal the bottom of each cylinder (see Figure 3.4 for a photograph of a cadmium cylinder). The bottom of one cylinder (to be used in pneumatic tube sample set #3) had a small opening so three small pieces of cadmium foil were cut and placed in the bottom to ensure 30 mil cadmium would filter neutrons entering the cylinder from below.

A cadmium cover was made for use in the hydraulic tube using the same technique, but the cadmium foil strip was 1.2 cm wide by 5.3 cm long and it was wrapped around a 0.4 cm diameter rod to produce a cylinder small enough to fit in a hydraulic tube irradiation

capsule. For this cylinder the cadmium was more than long enough for three complete wraps and approximately 0.5 cm excess was trimmed after fashioning the cylinder.

Figure 3.4 Tungsten Experiment Components (Clockwise from Lower Left): Tungsten Foils (Self-Shielding Experiments), Hydraulic Tube Irradiation Capsule, Pneumatic Tube Irradiation Capsule/Cover, Cadmium Cover for Hydraulic Tube, Tungsten Cross Section Sample Packages (2), Flux Monitor Wires (3), Quartz Vial with WO_3 Deposition

3.4.2 First Tungsten Cross Section Measurement Experiment

Flux monitors were prepared for four pneumatic tube irradiations (two with cadmium covers, two without cadmium covers) and two hydraulic tube irradiations (one with a cadmium cover, one without a cadmium cover). In addition to the standard gold flux monitor, cobalt and silver monitors were also used to investigate differences in flux as measured by different monitors (see Section 3.2). Flux monitors were wires consisting of gold, silver, and cobalt in aluminum. Pieces of wire were cut to produce sufficient activation such that post-irradiation gamma spectroscopy counting times were reasonable (desired activation would result in >10,000 counts in five minutes). However, there was insufficient cobalt/aluminum wire to make monitors of that size so smaller pieces were used. Also, very large pieces of silver/aluminum wire would have to be used to produce that level of activation so smaller pieces were used to limit the size of the flux monitor packages.

In addition to the flux monitors identified above, the HFIR Neutron Activation Analysis Laboratory had a NIST cobalt/aluminum standard wire that was used in these experiments to evaluate the composition of the cobalt/aluminum wire we (the Nuclear Medicine Group) had available and which was most likely used in the inconclusive experiment described in Section 3.2.

Masses of flux monitors for cross section measurement experiment #1 are presented in Table 3.4. Flux monitor compositions are:

Au Reactor Experiments, Inc.
0.058% Au in Al
Specified diameter 0.010 inches (0.0254 cm)
Purity 99.981%

Ag Reactor Experiments, Inc.
0.092% Ag in Al (package marked 0.145% Ag per F. Kam)
Specified diameter 0.020 inches (0.0508 cm)
Purity 99.988%

Co1 unknown manufacturer
0.66% Co in Al
Measured diameter 0.075 cm (0.03 inches)

Co2 National Institute of Standards and Technology SRM No. 953
0.116 ± 0.002% Co in Al
Specified diameter 0.05 cm (0.02 inches)

Table 3.4 Flux Monitors for Cross Section Experiment #1

	Mass (g)					
	Hydraulic Tube		Pneumatic Tube			
Monitor	Set #1	Set #2	Set #1	Set #2	Set #3	Set #4
Au	0.0020	0.0018	0.0025	0.0023	0.0027	0.0026
Ag	0.0050	0.0049	0.0420	0.0439	0.0437	0.0438
Co1	0.0022	0.0025	0.0098	0.0095	0.0097	0.0095
Co2	0.00481	0.00520	0.00523			0.00462

Enriched ^{186}W was used to make targets for tungsten cross section measurements. The ^{186}W was in a bottle labeled ^{186}W metal, batch 146642, isotope order 54-0046-5. The isotopic analysis for batch 146642 gave a ^{186}W content of 97.66%. However, the metal had obviously been oxidized to WO_3 because it was a yellow powder [Weast 1973].

To produce sufficient ^{187}W activity, 100 μg samples of ^{186}W were desired. A 6.3 mg sample of $^{186}WO_3$ was placed in a glass vial and 10 drops of NaOH were added. On a hotplate, distilled H_2O and H_2O_2 were added repeatedly until all the $^{186}WO_3$ went into solution. The solution was reduced to approximately 0.2 mL and was then transferred to

a calibrated 1 mL vial. The first vial was rinsed several times with distilled H_2O, each time pouring the solution into the calibrated vial to ensure that all the ^{186}W was transferred to the calibrated vial. Distilled water was added to the 1 mL mark of the calibrated vial, producing a solution of 6.3 mg $^{186}WO_3$ per mL. The ^{186}W content of this solution is:

$$\frac{186}{186+3(16)} \times 6.3 \frac{\text{mg } ^{186}WO_3}{\text{mL}} = 5.0 \frac{\text{mg } ^{186}W}{\text{mL}}$$

Therefore, 20 μL samples contain 100 μg of ^{186}W (correction for the actual enrichment, 97.66%, will be made in cross section calculations).

High purity (99.99%) 0.1 mm Al foil (Alfa Aesar, Ward Hill, MA) was cut into twelve 1.5 cm x 1.5 cm squares, 20 μL samples of the tungsten solution were deposited on each and allowed to dry overnight. The foil targets were folded in thirds to reduce their size to fit inside the irradiation capsules and then were wrapped with commercial aluminum foil to contain the samples.

Four pneumatic tube graphite irradiation capsules (Figure 3.4) were loaded with flux monitors and tungsten samples as follows:

PT1	two W foil packages, pneumatic tube flux monitor set #1 (Table 3.4)
PT2	two W foil packages, pneumatic tube flux monitor set #2 (Table 3.4)
PT3	one W foil package, pneumatic tube flux monitor set #3 (Table 3.4) inside a cadmium cover
PT4	one W foil package, pneumatic tube flux monitor set #4 (Table 3.4) inside a cadmium cover

The flux monitors and tungsten foil packages for PT3 and PT4 were placed inside cadmium cylinders described in Section 3.4.1 and the flaps at the tops of the cylinders were folded over to completely close the cylinders. All four samples were wrapped in commercial aluminum foil, placed in graphite irradiation capsules and graphite covers were screwed tightly in place.

Irradiations were performed in pneumatic tube facility #1 on November 2, 2003. The duration of each irradiation was set to 120 seconds with a 20 minute in-pool decay period to allow the decay of short-lived activation products before removal to the Neutron Activation Analysis Laboratory hot cell. Irradiation times for the four capsules were:

Table 3.5 Cross Section Experiment #1 Irradiations

Capsule	Insertion Time	Removal Time
PT1	17:53:12	17:55:12
PT2	18:50:19	18:52:19
PT3	18:20:53	18:22:53
PT4	19:13:22	19:15:22

All four capsules indicated "IN" the reactor as soon as the insert button was pushed. David Glasgow of the Neutron Activation Analysis Laboratory said that was a problem with a pneumatic tube facility #1 pressure switch and that target travel time to the reactor is approximately one second. Therefore, all calculations will be based on irradiation times of 119 seconds.

Upon removal of samples from the graphite capsules, it was apparent that the cadmium covers in PT3 and PT4 had melted. PT3 appeared to be covered in aluminum foil and some cadmium, but some cadmium had also melted and relocated to the bottom of the aluminum foil-covered package (the cadmium cover for PT3 was the one that had an opening in the bottom that had been blocked by three small pieces of cadmium so there was more room in the PT3 sample for cadmium to relocate than in PT4). All samples were recovered from PT3 by peeling away aluminum foil and breaking away the cadmium.

PT4 appeared to be a solid piece of cadmium; i.e., the cadmium foil had melted and solidified, encasing the samples. The hard cadmium shell was cut apart and the Ag and two Co wires were retrieved. Further cutting revealed what appeared to be a piece of the aluminum upon which the tungsten was deposited, but the Au wire was not found. Subsequent analysis of the tungsten piece showed that it contained some tungsten and gold, but not nearly as much as PT3. Obviously, only parts of those samples were recovered so no further analysis of the tungsten and gold was performed.

PT1 – PT4 samples were transported to the Nuclear Medicine Group laboratory in building 4701 for analysis using the HPGe system described in Section 2.2. Appendix A provides a summary of detector efficiencies for gamma rays associated with tungsten and all flux monitors.

In preparation for data analysis, gamma ray self-absorption factors were calculated for the flux monitor wires and the aluminum foil upon which the tungsten samples were deposited. Details of self-absorption factor derivation are provided in Appendix B.

All samples were mounted on cards for gamma ray analysis (Figure 3.5).

Figure 3.5 Cross Section Experiment #1 Samples

Gamma ray spectroscopy data and data processing for the flux monitors and tungsten samples are presented in Appendix C.1 and the results are summarized in Table 3.6.

Table 3.6 Cross Section Experiment #1 Sample Activities

Sample	A^0 (Bq mg^{-1}) [a]	σ_{A^0} (Bq mg^{-1}) [a]
W Unshielded	2.57×10^{7}	4.02×10^{5}
W Shielded	6.03×10^{6}	1.89×10^{5}
Au Unshielded	4.08×10^{4}	1.45×10^{3}
Au Shielded	1.81×10^{4}	9.11×10^{2}
Ag Unshielded	3.36×10^{1}	1.21×10^{0}
Ag Shielded	1.54×10^{1}	6.99×10^{-1}
Co1 Unshielded	4.10×10^{2}	9.82×10^{0}
Co1 Shielded	1.10×10^{2}	2.97×10^{0}
Co2 Unshielded	8.92×10^{1}	2.27×10^{0}
Co2 Shielded	2.71×10^{1}	6.88×10^{-1}

[a] per mg target material

The gold, silver and cobalt activities, along with published nuclide data, were used to calculate thermal and epithermal neutron fluxes. Details of these calculations are provided in Appendix C.1 and the results are summarized in Table 3.7.

Table 3.7 Cross Section Experiment #1 Flux Measurements

Flux Monitor	ϕ_0 (n cm^{-2} s^{-1})	ϕ_{ep} (n cm^{-2} s^{-1})
Au	3.60×10^{14}	1.86×10^{13}
Ag (0.092%)	4.06×10^{14}	2.27×10^{13}
Ag (0.145%)	2.57×10^{14}	1.44×10^{13}
Co1	2.37×10^{14}	4.45×10^{13}
Co2	2.79×10^{14}	6.23×10^{13}

Flux data from the gold flux monitors was used to calculate ^{186}W cross sections, which were determined to be σ_0 = 17.58 b and I_0 = 106.2 b (see Appendix C.1 for details of these calculations). The value for σ_0 is approximately half of what had been expected based on published values (Section 3.3). While the melting of the cadmium covers may have affected these measurements, it is very likely that the samples were covered by the cadmium for most of the irradiation and so the discrepancy should not have been that great. The results suggested that the enriched tungsten used for the tungsten targets was not in fact 97.66% enriched $^{186}WO_3$. Consequently, it was decided to re-perform these experiments using a known tungsten standard to check the composition of the $^{186}WO_3$.

Also, differences in the flux results from different monitors (Table 3.7) were expected in light of the previous discussion on flux measurement (Section 3.3); however, the disparity between values for thermal flux measured by the gold and cobalt monitors (cobalt should be a reliable monitor for thermal flux) raises a concern about the actual gold content in the gold-aluminum flux monitor wire. ORNL personnel experienced in flux measurement subsequently mentioned that flux monitors, particularly those manufactured by Reactor Experiments, Inc., are often of questionable reliability. Since the values for thermal and epithermal fluxes derived from the gold flux monitors are between the values derived using the two different compositional analyses of the silver monitors, it is likely that the actual composition of the silver wire is between 0.092% and 0.145%. Thus, it was also decided to use known standards for flux monitors in the second set of experiments.

Data from the two sets of cobalt flux monitors also highlights the uncertainty in flux monitor compositions. The actual composition of Co1 can be calculated by multiplying the composition of Co2 (the monitor certified by the National Institute of Standards and Technology) by the ratio of their unshielded activities in terms of Bq mg^{-1} of target material from Table 3.6. This results in a composition of 0.533% for Co1; the value of 0.66% marked on the package was off by 24%.

The targets made for hydraulic tube experiments to determine the 2200 m/s cross section and resonance integral for ^{187}W were not irradiated due to concerns about the melting of cadmium in the hydraulic tube facility. Since the cadmium covers melted during irradiation in the pneumatic tube, which has a neutron flux almost an order of magnitude lower than that in the hydraulic tube, approval to irradiate the targets in the hydraulic tube would be difficult to obtain. However, even with greater heat generation, cadmium melting in the hydraulic tube is probably less likely than in the pneumatic tube because target heat removal is much greater. Targets in the pneumatic tube are cooled by a stream of air that passes between the irradiation capsule and the walls of the pneumatic tube. Heat removal in the hydraulic tube, on the other hand, is provided by forced-flow of reactor cooling water. Further, capsules used for pneumatic tube irradiations are amorphous graphite which has a thermal conductivity of 1.6 W m^{-1} K^{-1} (at 300 K) [Incropera and DeWitt 1996] which is two orders of magnitude less than the thermal conductivity of 6061-T6 aluminum alloy (167 W m^{-1} K^{-1} at 300 K) [MatWeb 2003], the material used to fabricate hydraulic tube rabbit capsules.

3.4.3 Second Tungsten Cross Section Measurement Experiment

Atomic Absorption Spectrometry (AAS) standard solutions (Alfa Aesar, Ward Hill, MA) were purchased to provide known compositions for the flux monitor and tungsten samples for the second cross section measurement experiment. The AAS standards used for target preparation were:

Au	Alfa Aesar stock #88068 1 mg/mL Au in 20% HCl
Ag	Alfa Aesar stock #88096 1 mg/mL Ag in 5% HNO_3
W	Alfa Aesar stock #35760 1 mg/mL W in 5% HNO_3/tr. HF

Au and Ag wires and the enriched tungsten solution used to make targets for cross section experiment #1 were also used in this experiment to check the compositions of the flux monitor wires and the enriched tungsten solution.

AAS standard targets were prepared by depositing the solutions on 99.999% pure, 0.025 mm Al foil (Alfa Aesar stock #44233) and allowing them to dry. Au AAS solutions were dried under a heat lamp because the HCl standard solution dissolved through the Al foil when allowed to dry in air. The solutions were deposited on one half of 1 cm x 2 cm pieces of Al foil which were then folded in half and the edges crimped to seal the targets. For the two large W standard samples used for cadmium-covered irradiations, 2 cm x 4 cm pieces of Al foil were used to contain the solutions.

Four sets of targets were made as shown in Table 3.8. Physical properties used in calculating target masses are taken from Section 3.4.2 and the AAS standard specifications above. Targets of differing sizes were made to reduce the potential for systematic measurement errors to influence experimental results.

Table 3.8 Cross Section Experiment #2 Targets

Sample	Target	Sample Mass (mg)	Sample Volume (μL)	Sample Conc. (μg/μL)	Target Natural Abundance	Target Enrich-ment	Target $^{w}/_{o}$	Target Mass (μg)
PT5								
W standard	^{186}W		25	1	0.2843			7.11
W enriched	^{186}W		2	6.3		0.9766	0.7948	9.78
Au standard	^{197}Au		2	1	1			2.00
Au wire	^{197}Au	4.0			1		0.00058	2.32
PT6								
W standard	^{186}W		15	1	0.2843			4.26
W enriched	^{186}W		5	6.3		0.9766	0.7948	24.5
Au wire	^{197}Au	5.5			1		0.00058	3.19
Ag standard	^{109}Ag		5	1	0.48161			2.41
Ag wire	^{109}Ag	10.3			0.48161		0.00145	7.19
PT7 (Cd cover)								
W standard	^{186}W		700	1	0.2843			199
W enriched	^{186}W		40	6.3		0.9766	0.7948	196
Au standard	^{197}Au		10	1	1			10.0
Au wire	^{197}Au	10.4			1		0.00058	6.03
Ag standard	^{109}Ag		40	1	0.48161			19.3
PT8 (Cd cover)								
W standard	^{186}W		1000	1	0.2843			284
W enriched	^{186}W		60	6.3		0.9766	0.7948	293
Au standard	^{197}Au		15	1	1			15.0
Au wire	^{197}Au	16.4			1		0.00058	9.51
Ag standard	^{109}Ag		60	1	0.48161			28.9

Cadmium tubes were made as described in Section 3.4.2, wrapping six layers of 5 mil cadmium foil around a 0.5 mm diameter rod (30 mil wall thickness). To prevent cadmium contamination of the flux monitor foils and wires, tubes were made from

several layers of commercial aluminum foil into which were placed the gold wires with the sample foils inserted above the wires. These aluminum foil tubes were crimped at both ends before placing them in the cadmium tubes which were then sealed for use in the cadmium-covered experiments, PT7 and PT8.

Commercial aluminum foil tubes were also made to contain the samples in the non-cadmium-covered experiments, PT5 and PT6.

All samples were loaded in graphite irradiation capsules. The cadmium experiments (PT7 and PT8) were wrapped in commercial aluminum foil to improve heat transfer from the cadmium to the graphite.

Irradiations were performed in pneumatic tube facility #1 on December 15, 2003. Irradiation times shorter than experiment #1 (PT1 – PT4 were irradiated for two minutes each) were used for the cadmium-covered experiments to reduce the possibility of cadmium melting. Irradiation times for the non-cadmium-covered samples were much longer than experiment #1 to limit the amount of AAS solution that had to be deposited and dried on the foils and to reduce the counting times required to obtain a sufficient number of counts for gamma ray analysis. The duration of each irradiation is specified in Table 3.9. A technique to mitigate the control system timing problem encountered in previous irradiations (Section 3.4.2) had been developed and the expected 1 second delay between initiation of insertion and receipt of the "IN" indication occurred for all irradiations except PT8; an irradiation time of 44 seconds (rather than the control system

setpoint of 45 seconds) will be used in all PT8 calculations. As in cross section experiment #1, a 20 minute in-pool post-irradiation decay period allowed the decay of short-lived activation products before removal to the Neutron Activation Analysis Laboratory hot cell.

Table 3.9 Cross Section Experiment #2 Irradiations

Capsule	Removal Time	Irradiation Duration
PT5	13:25:45	20 m
PT6	14:22:53	20 m
PT7	11:04:45	60 s
PT8	12:22:00	44 s

The graphite capsules were opened and as had been experienced in cross section experiment #1, the cadmium covers had melted, but not to as great an extent. PT7 still had cadmium on top and the upper walls had thinned due to melting, but since the cadmium tubes had a larger diameter than experiment #1 and were filled with aluminum foil sample tubes and were wrapped with aluminum foil, the cadmium did not melt down to the bottom of the capsule as in experiment #1. PT8 was entirely encased in cadmium, although it had melted and formed a hard casing which made it difficult to retrieve the targets from the tube. The sample foils were retrieved, but they were torn (the consequences of this are addressed in the data analysis in Appendix C.2).

In both PT7 and PT8 (the cadmium-covered samples), it was noticed that there was a dark residue on portions of the sample foil package exteriors, possibly compounds that were formed inside the packages at high temperatures that leaked through the crimped

edges of the foil packages. All samples had been air-dried before sealing the packages, but were evidently not completely anhydrous since vaporization of the water molecules would have driven material out of the package. Data in Appendix C.2 shows that the residue contained tungsten, which is taken into account in data analyses.

As in cross section experiment #1, all samples were mounted on cards for gamma ray analysis. Gamma ray spectroscopy data and data processing for the flux monitors and tungsten samples are presented in Appendix C.2 and the results are summarized in Table 3.10.

Table 3.10 Cross Section Experiment #2 Sample Activities

Sample	A^0 (Bq mg^{-1}) [a]	σ_{A^0} (Bq mg^{-1}) [a]
W Standard Unshielded	7.06×10^8	1.55×10^7
W Enriched Unshielded	2.73×10^8	1.17×10^7
W Standard Shielded	6.07×10^6	1.90×10^5
W Enriched Shielded	3.92×10^6	1.23×10^5
Au Standard Unshielded	6.19×10^8	3.11×10^7
Au Wire Unshielded	6.80×10^8	2.41×10^7
Au Standard Shielded (PT7)	8.56×10^6	4.31×10^5
Au Wire Shielded (PT7)	1.14×10^7	5.72×10^4
Au Standard Shielded (PT8)	5.81×10^6	2.92×10^5
Au Wire Shielded (PT8)	8.21×10^6	4.13×10^5
Ag Wire Unshielded	5.03×10^5	2.59×10^4
Ag Standard Unshielded	5.17×10^5	2.68×10^4
Ag Standard Shielded (PT7)	8.50×10^3	4.62×10^2
Ag Standard Shielded (PT8)	5.88×10^3	3.33×10^2

[a] per mg target isotope

The activities calculated for the gold AAS standard and the gold wire can be used to calculate the actual composition of the gold wire, which had been reported to be 0.058%

by the manufacturer. Since the activities per unit mass of the gold wires are all greater than the associated AAS standard samples, the reported composition of the gold wire is low (i.e., there is a higher gold content which would decrease the calculated activities per unit mass). The ratios (gold wire to AAS standard) of the three sets of gold data in Table 3.10 are 1.10, 1.33 and 1.41. This variability, and the variability of the activities of the two gold wires that are averaged to produce the value for "Au Wire Unshielded" (see Table C.18), are indications of the inconsistency that can occur in composition along the length of a flux monitor wire due to the manufacturing process. A weighted average using the masses of the four flux monitor wires (PT5 and PT6 activities having been averaged as noted above) can be used to correct the reported composition of 0.058%:

$$\frac{(2.32+3.19\,\mu g)\left(\frac{6.80\times10^{8}}{6.19\times10^{8}}\right)+(6.03\,\mu g)\left(\frac{1.14\times10^{7}}{8.56\times10^{6}}\right)+(9.51\,\mu g)\left(\frac{8.21\times10^{6}}{5.81\times10^{6}}\right)}{2.32+3.19+6.03+9.51\,\mu g}\times 0.058\% = 0.076\%$$

Similarly, since the activity of the silver wire is less than the associated silver AAS standard, the composition used to calculate the mass of silver in the wire is high. The composition marked on the package by F. Kam (0.145%) can be corrected using activities from Table 3.10:

$$\frac{5.03\times10^{5}}{5.17\times10^{5}}\times 0.145\% = 0.141\%$$

This result confirms the conclusion drawn in Section 3.4.2 that the actual silver content of the wire was between the value reported by the manufacturer (0.092%) and the value reported by F. Kam (0.145%).

Activities of the gold and silver flux monitors, along with published nuclide data, were used to calculate thermal and epithermal neutron fluxes. Details of these calculations are provided in Appendix C.2 and the results are summarized in Table 3.11.

Table 3.11 Cross Section Experiment #2 Flux Measurements

Flux Monitor	ϕ_0 (n cm^{-2} s^{-1})	σ_{ϕ_0} (n cm^{-2} s^{-1})	ϕ_{ep} (n cm^{-2} s^{-1})	$\sigma_{\phi_{ep}}$ (n cm^{-2} s^{-1})
Au	4.21×10^{14}	3.67×10^{13}	9.73×10^{12}	17.14×10^{11}
Ag	3.48×10^{14}	3.58×10^{13}	1.07×10^{13}	1.03×10^{12}

The thermal flux and flux ratio ($\phi_0/\phi_{ep} = 43$) determined from the gold flux monitors are consistent with a measurement made by the Neutron Activation Analysis Laboratory prior to PT5 – PT8 irradiations using a different technique involving gold and manganese foils (NAA results were $\phi_0 = 4.21 \times 10^{14}$ and $\phi_0/\phi_{ep} = 36$ [David Glasgow, e-mail message to the author, January 7, 2004]). The thermal flux determined from the silver flux monitors is 17% lower than the value from the gold monitor and the value epithermal flux is 10% greater (for the silver flux monitors, $\phi_0/\phi_{ep} = 33$). While there was some concern that previously noted discrepancies between flux monitors (e.g., the large differences between gold, silver, and cobalt derived fluxes discussed in Section 3.2) could be an indication that the epithermal flux in the pneumatic tube does not have a $1/E$ distribution, it is more likely that the variations in flux values derived using gold, silver and cobalt monitors in the cross section experiments #1 and #2 are the result of the fact that different materials are better flux monitors than others – as mentioned in Section 3.2, resonance properties of the various nuclei have a significant impact on their utility as flux

monitors. In the case of gold and silver, ^{197}Au and ^{109}Ag have first resonances at almost identical energies (4.9 eV and 5.2 eV, respectively). Therefore, deviation from a 1/*E* spectrum wouldn't result in significant differences in epithermal flux measurements. Also, since the pneumatic tube is located in the beryllium reflector and not in close proximity to the fuel, the neutron flux should be well-moderated and close to 1/*E* in distribution. As specified in Stoughton and Halperin [1959], the properties of gold make it an ideal flux monitor and as such, flux data from the gold monitors was used to calculate ^{186}W cross sections.

Cross sections for ^{186}W were determined to be $\sigma_0 = 43.5 \pm 4.0$ b and $I_0 = 395 \pm 32$ b using data from the tungsten AAS standard samples (see Appendix C.2 for details of these calculations). The use of an AAS standard confirmed that the enriched tungsten that was assumed to be 97.66% enriched $^{186}WO_3$ in cross section experiment #1 (Section 3.4.2) had a different composition. The ratio of unshielded activities for the AAS standard and enriched tungsten from Table 3.10 is 2.59. This is consistent with the observation in Section 3.4.2 that the calculated value of 17.6 b for the ^{186}W thermal cross section was approximately half of what would be expected based on published values. The ratio of shielded activities from Table 3.10 is 1.55; the difference between this value and the unshielded value is most likely due to error associated with leakage of samples in the shielded experiments.

These measured cross sections are fairly consistent with published values as reported in Section 3.3. The thermal cross section is greater than that calculated in Section 3.3 (43.5

± 4.0 b vs. 37.0 ± 2.3 b), while the resonance integral is smaller (395 ± 32 b vs. 438 ± 80 b). This could be the result of the leakage from the cadmium-covered tungsten samples. Any leakage from the cadmium-covered tungsten sample foil packages would lower the measured activity and result in a lower calculated value for the resonance integral. It would also result in a greater value for the thermal cross section since the cadmium-covered tungsten activity is subtracted from the uncovered tungsten activity to calculate the thermal cross section.

3.5 Cross Section Conclusions

This chapter demonstrates that commonly used values and measured values for ^{186}W are consistent and as such could not account for significant deviations in theoretical and experimental ^{188}W yields. This is particularly true since the effective cross sections, σ_{eff}, are very similar, with the Section 3.4.3 measured value differing from the National Nuclear Data Center recommended value [NNDC 2004b] by less than 2% (σ_{eff} values were calculated using Equation 2.4 with a flux ratio of 20, the flux ratio in the irradiation location for the experiments in Chapter 5). Table 3.12 summarizes these values.

Table 3.12 ^{186}W Cross Sections

Source	σ_0 (b)	I_0 (b)	σ_{eff} [a] (b)
Section 3.3 Analysis	37.0 ± 2.3	438 ± 80	58.9
Section 3.4.3 Measurement	43.5 ± 4.0	395 ± 32	63.3
NNDC 2004b	37.9 ± 2.3	485 ± 15	62.2
JAERI 2002	39.45	528.5	65.88

[a] for $\phi_0/\phi_{ep} = 20$

On the other hand, cross sections for ^{187}W are suspect, as discussed in Section 3.3. Future work should be done to resolve the irradiation of cadmium in the hydraulic tube so that measurements of the ^{187}W thermal cross section and resonance integral can be made.

4 Temperature Effects on Cross Sections and Neutron Energies

Production of ^{188}W at ORNL has demonstrated to the Nuclear Medicine Group that the tungsten targets experience very high temperatures during irradiation. Metallic and oxide powders have formed compounds that were found to be insoluble during post-irradiation chemical processing. Since the chemical reactions occur at elevated temperatures, an assessment of target temperature is necessary to determine what effects, if any, temperature may have on radiative capture by tungsten. Elevated temperatures could impact production by affecting radiative capture cross sections and the energy distribution of the neutron flux.

This chapter first analyzes tungsten temperatures during HFIR irradiation and then assesses the impact of those temperatures on radiative capture by tungsten.

4.1 Tungsten Temperature Analysis

Calculations were performed to determine temperatures in an experiment designed to study neutron self-shielding by irradiating five concentric tungsten cylinders (the experiment is addressed in Chapter 5). The cylinders were placed in an aluminum holder that fit into a thin-walled aluminum irradiation capsule which was irradiated in the High Flux Isotope Reactor hydraulic tube facility located in the flux trap (Figures 2.1 and 3.3). In addition to determining the temperature profile throughout the tungsten cylinders, these calculations ensured compliance with the safety bases of HFIR by determining

maximum temperatures in the aluminum components to ensure structural integrity and determining the maximum surface temperature of the capsule to ensure that net vapor generation does not occur (experiments are not allowed to be irradiated if boiling can occur in the hydraulic tube facility).

HEATING7.3 (H7) [HEATING7 1999], a multidimensional, finite-difference heat transfer code was used to perform the two-dimensional heat transport calculations necessary to obtain a temperature profile of the experiment components.

A summary of the methods and results of these calculations will be presented in this chapter. Details can be found in ORNL Research Reactors Division Calculation C-HFIR-2002-035 [Garland 2003].

4.1.1 Component Descriptions

The experiment consisted of essentially three components: the set of tungsten cylinders, the aluminum holder, and the aluminum hydraulic tube irradiation capsule. Figure 4.1 is the fabrication drawing for the tungsten cylinders, Figure 4.2 is the fabrication drawing for the aluminum holder, and Figure 4.3 is the fabrication drawing for the irradiation capsule (photograph in Figure 3.4). Dimensions from these drawings were used to develop the H7 model used for calculations; the model is shown in Figure 4.4.

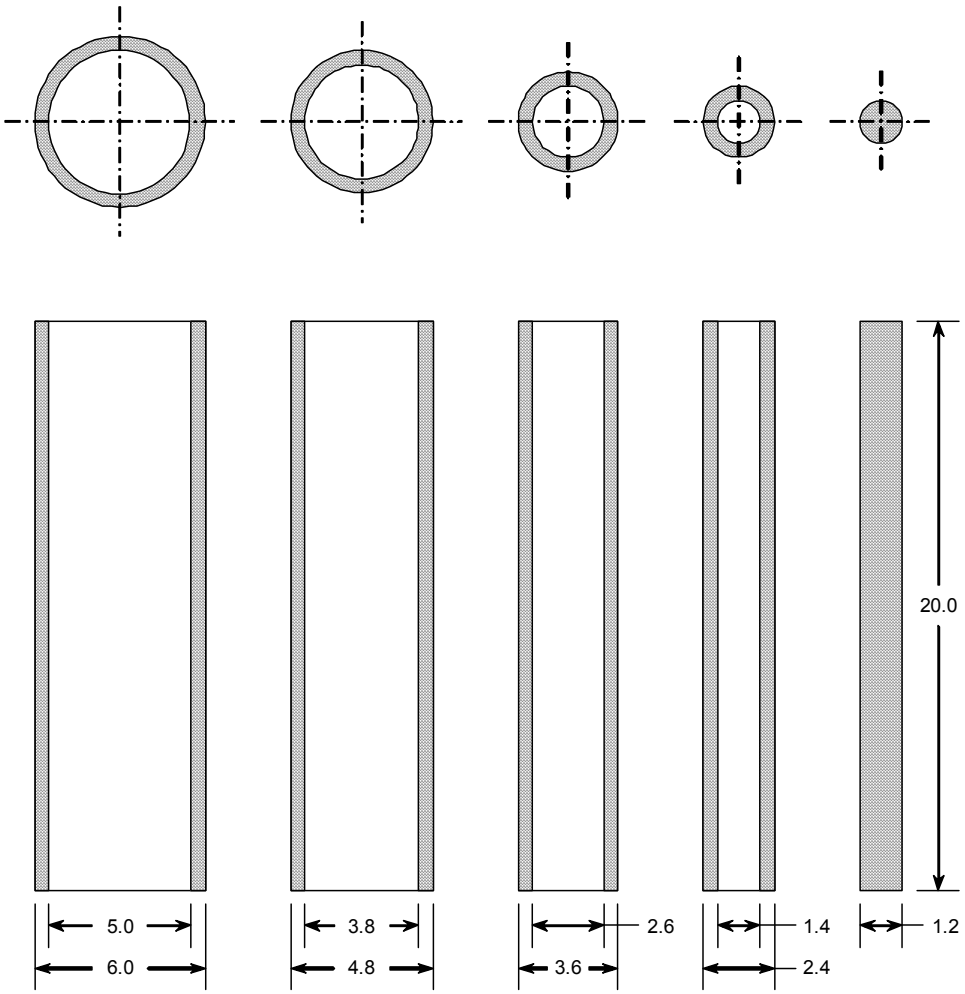

Prepared by: M. A. Garland			
QAS: W. G. Askew			
RRD: R. W. Hobbs			
RRD QAS: L. C. Smith			
Lead Experimenter: S. Mirzadeh	Drawing: MG100302-1 Rev: 0	Material: natural tungsten	
	TUNGSTEN CYLINDER TARGETS		Dimensions: mm

Figure 4.1 Tungsten Cylinder Targets

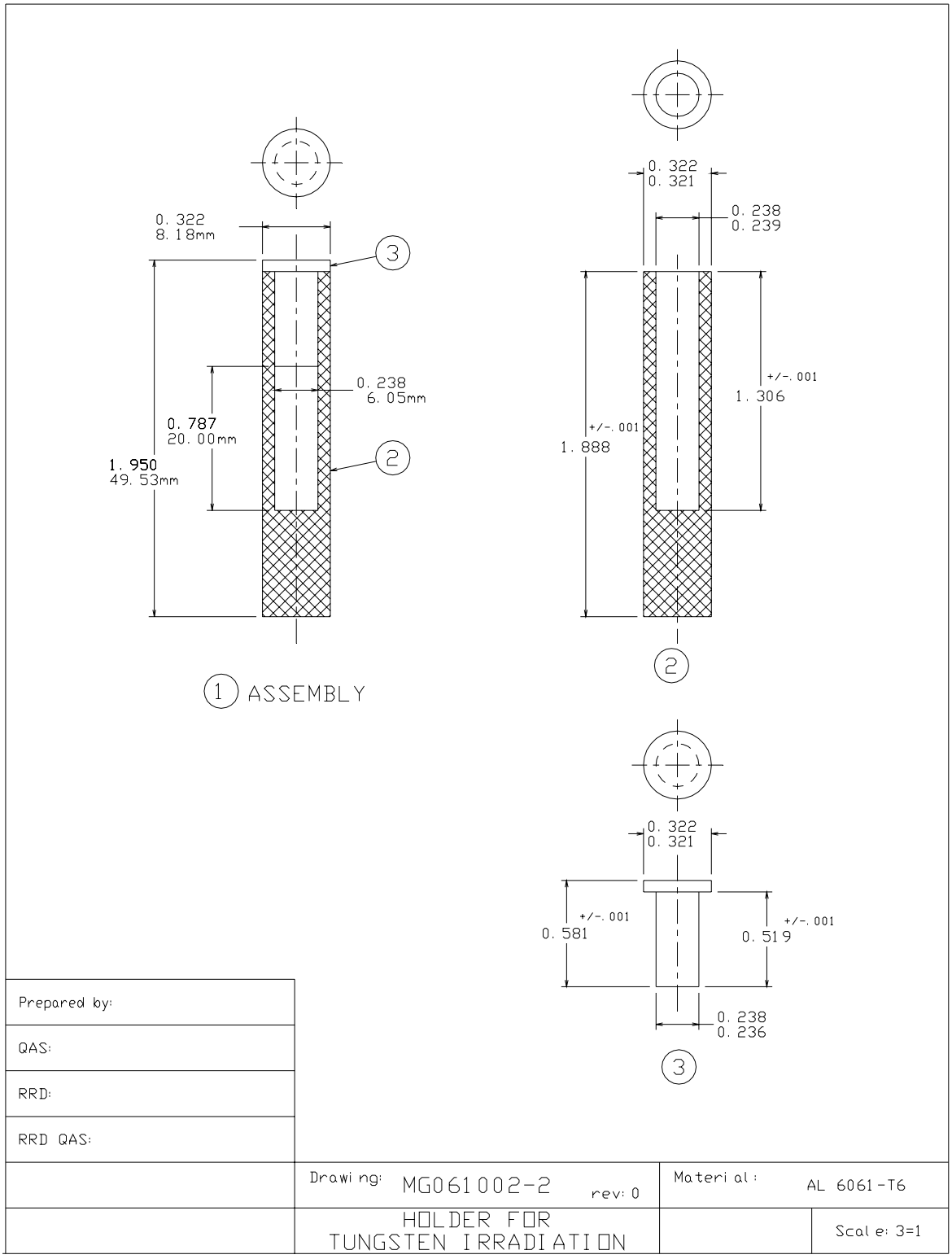

Figure 4.2 Aluminum Holder for Tungsten Cylinder Targets

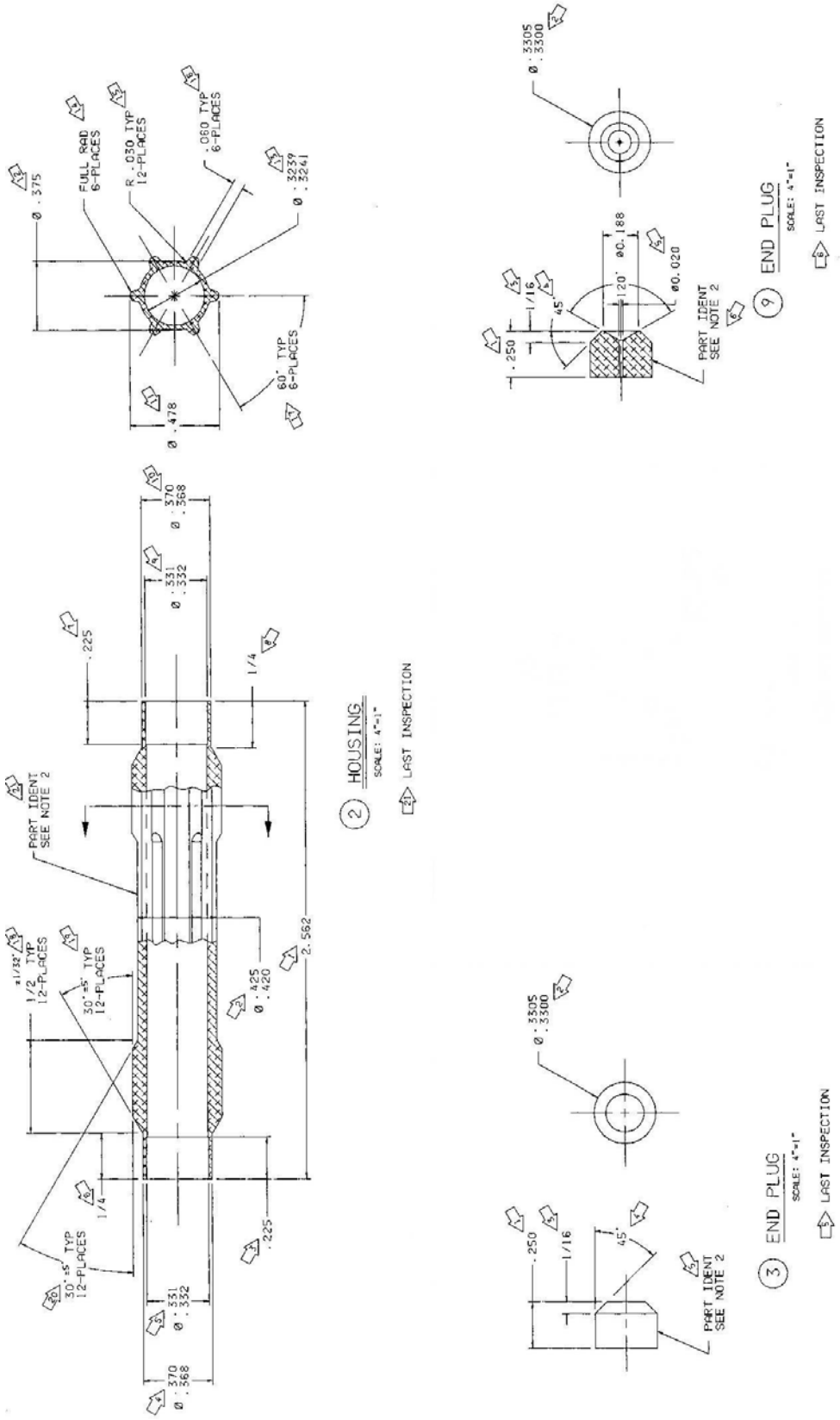

Figure 4.3 Aluminum Hydraulic Tube Irradiation Capsule

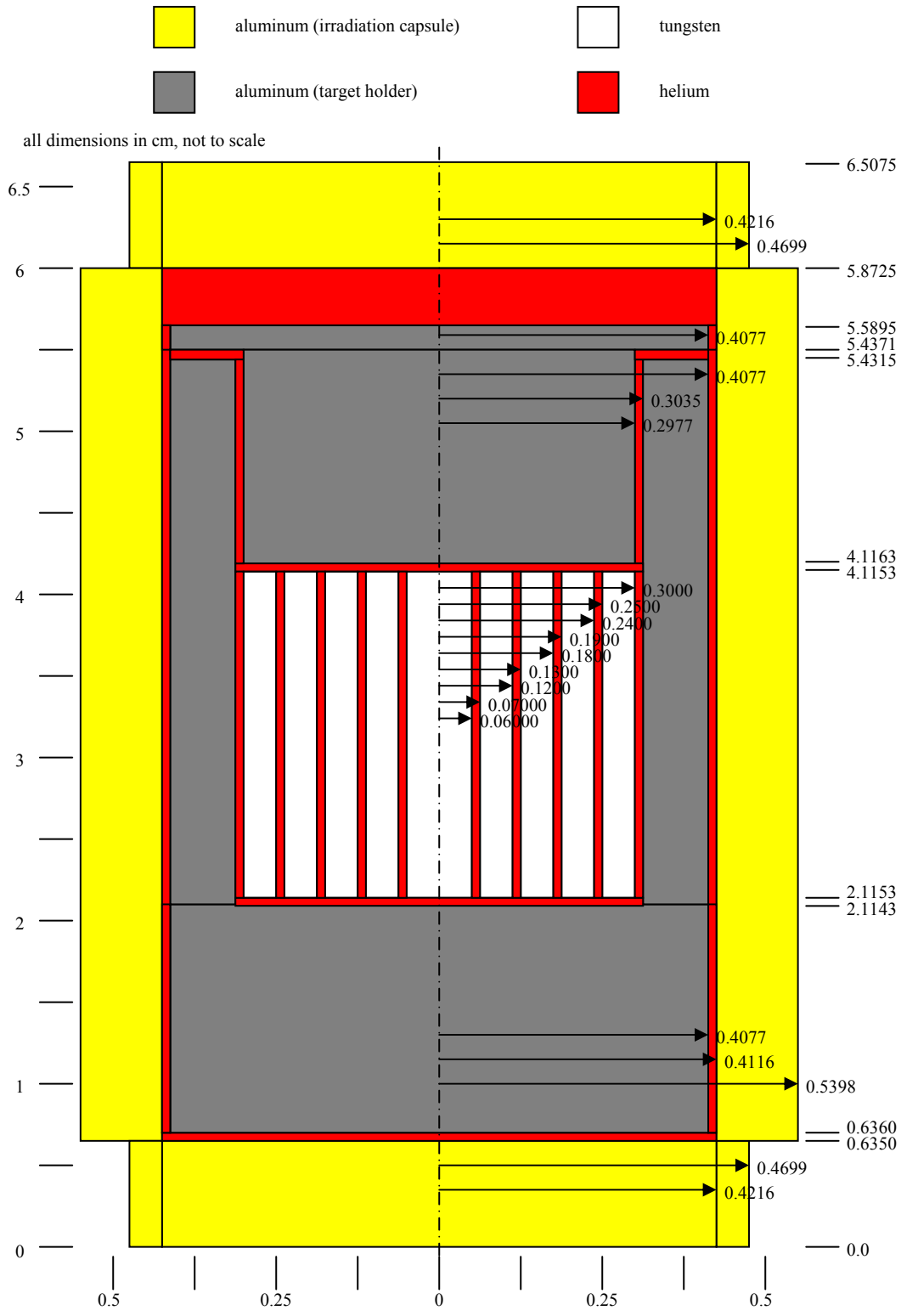

Figure 4.4 Tungsten Cylinder Experiment Geometric Model

4.1.2 Assumptions

In order to simplify the analysis, while maintaining conservatism with respect to maximum temperature predictions, a number of assumptions were made.

Adiabatic Heat Transfer. In the H7 model, heat transfer from the irradiation capsule to the coolant occurs on the outer radial surfaces of the capsule only. The top and bottom of the capsule are assumed to be adiabatic surfaces and thus no credit is taken for axial heat transfer to the coolant. Assuming that the top and bottom of the irradiation capsule are adiabatic surfaces leads to a conservative prediction of temperatures since no credit is taken for axial heat transfer; i.e., from these surfaces to the coolant. Heat transfer from these surfaces will indeed occur, increasing total heat transfer from the irradiation capsule to the coolant and thus lowering predicted temperatures relative to assuming that these surfaces are adiabatic. However, heat transfer coefficients for these surfaces are not known so the assumption of zero heat transfer simplifies the calculations.

Simplified Geometrical Model. The aluminum irradiation capsule housings are primarily cylindrical, but have six fins on the outer surface to increase heat transfer to the coolant. Modeling the housings for the input to H7 is simplified by ignoring the fins. Not incorporating the irradiation capsule housing fins in the H7 model adds conservatism to the prediction of temperatures because credit is not taken for the additional heat transfer from the capsule to the coolant provided by the fins.

Contact Resistances. For all parts that are in direct physical contact (such as the tungsten cylinders resting upon the aluminum holder), a contact resistance was modeled in H7 by creating a 0.001 cm helium gas gap between parts (the irradiation capsules was evacuated and backfilled with helium prior to being welded closed). Further, parts were assumed to maintain maximum distances from one another rather than coming into physical contact (e.g., 0.1 mm gaps being maintained around tungsten cylinders). Even though parts will come into physical contact with one another, modeling helium gas gaps between all different parts produces conservative results since credit is not taken for direct thermal conduction between parts.

Heat Generation Rates. Heat generation rates for all components (tungsten and aluminum) represent the heat generation rates at the end of a full cycle of reactor operation. Using heat generation rates corresponding to the end of a full cycle of reactor operation produces conservative results since heat generation rates are greatest at that point. In reality, the experiment was irradiated for approximately two hours and heat generation rates were lower since activation products hadn't reached equilibrium levels (i.e., decay heat associated with the activation products hadn't built up to end-of-cycle levels).

4.1.3 Calculation Input

This section describes the development of the initial input file for H7. After running the initial input (Run 1), an iterative process was performed to incorporate thermal expansion

effects since H7 does not provide the capability to account for thermal expansion. Section 6 presents the details of the iterative process (including the initial input run) to arrive at a steady-state temperature profile that accounts for thermal expansion of all components.

Geometry. Geometries of the components used in this experiment are defined in the design drawings (Figures 4.1 – 4.3). A simplified geometric model of the experiment is shown in Figure 4.4; actual geometric modeling of these components is defined in the H7 input files. Where ranges for dimensions are shown on drawings, the most conservative value for a dimension was selected to produce the most conservative temperature profile. The "conservative value" was selected by choosing the value that maximizes gas gaps between components and/or maximizes component thickness, both of which maximize thermal resistance.

Material Properties. Thermal conductivities used in H7 input files and the sources of the data are:

Table 4.1 Tungsten Cylinder Experiment Thermal Conductivities

Material	Thermal Conductivity ($W\ cm^{-1}\ K^{-1}$)	Reference
Tungsten	1.633	MatWeb 2003
Aluminum (6061-T6)	1.67	MatWeb 2003
Helium	$0.001487 + 2.835 \times 10^{-6}\ T$	Touloukian *et al*. 1970

Initial Temperatures. All components were assumed to be in thermal equilibrium with the reactor coolant at the beginning of irradiation. To be conservative, this temperature was taken to be the worst-case limiting control setting (LCS) condition of 57.2 °C.

Heat Generation. Heat generation rates were calculated at the worst-case LCS reactor power of 110.5 MW as follows:

Tungsten

heating rate due to γ-rays and neutrons from core fissions = 45.108 W g^{-1} [Hobbs 2002]
heating rate due to γ-rays from fission product decay = 15.04 W g^{-1} [Hobbs 2002]
heating rate due to γ- and β-rays from tungsten decay = 7.85 W g^{-1} (Table 4.2)
total heating rate = 67.998 W g^{-1}

Table 4.2 Tungsten Target Heating due to Radioactive Decay [a]

Radio-nuclide	Half-life	Decay Energy (MeV/Dis)	Radioactivity (Ci) [e]	Radioactivity (dps)	Ave. β [b] $<E_\beta>$ (keV)	Ave. γ [c] $<E_\gamma>$ (keV)	Heat [d] (MeV/sec)	Heat [d] (Watt)
Target: 1.0 g of natural tungsten								
^{187}W	24 h	1.313	9.7×10^{2}	3.59×10^{13}	274	430	1.75×10^{13}	2.81
^{188}W	69 d	0.349	1.8	6.66×10^{10}	99	1.9	6.66×10^{9}	1.07×10^{-3}
^{188}Re	17 h	2.120	1.1×10^{3}	3.92×10^{13}	765	57.4	3.11×10^{13}	4.99
	69 d	2.120	1.8	6.66×10^{10}	765	57.4	5.29×10^{10}	8.47×10^{-3}
^{191}Os	15 d	0.310	9.8×10^{-1}	3.64×10^{10}	37.5	74.9	2.73×10^{9}	4.37×10^{-4}
^{192}Ir	75 d	1.457	3.2	1.18×10^{11}	171	813	6.83×10^{10}	1.0×10^{-2}
^{185}W	75 d	0.433	2.2×10^{1}	8.10×10^{11}	127	0.05	1.03×10^{11}	2.0×10^{-2}
^{186}Re	3.7 d	1.075	3.8	1.40×10^{11}	323	19.3	4.65×10^{10}	7.45×10^{-3}
						Total	4.89×10^{13}	7.85

[a] $\phi_0 = 2.0 \times 10^{15}$ n cm^{-2} s^{-1}, $(\phi_0/\phi_{ep}) = 25$, end of one cycle irradiation
[b] average energy of β-particles, $<E_\beta> = (1/3)\Sigma E_\beta I_\beta / \Sigma I_\beta$, i.e., 2/3 of the energy is carried away by neutrinos
[c] average energy of γ-rays, $<E_\gamma> = \Sigma E_\gamma I_\gamma / \Sigma I_\gamma$
[d] heat is calculated based on averaged β energy plus 50% of the averaged γ energy, i.e. all the β-particles and 50% of the γ-rays deposit their energies in the target
[e] experimental and calculational yields

ρ_W = 19.3 g/cm^3 [MatWeb 2003]

$$67.998\frac{\text{W}}{\text{g}}\times 19.3\frac{\text{g}}{\text{cm}^3}\times\frac{110.5\text{ MW}}{87.6\text{ MW}}=1655\frac{\text{W}}{\text{cm}^3}$$

Aluminum (6061-T6)

total heating rate = 35.71 W/g [Hobbs 2002]

$\rho_{6061\text{-}T6}$ = 2.7 g/cm^3 [MatWeb 2003]

$$35.71\frac{\text{W}}{\text{g}}\times 2.7\frac{\text{g}}{\text{cm}^3}\times\frac{110.5\text{ MW}}{87.6\text{ MW}}=121.6\frac{\text{W}}{\text{cm}^3}$$

Helium

Heat generation in helium is assumed to be zero. Since heat generation is related to mass and density, the low mass and density of helium result in negligible heat generation.

Boundary Conditions. Heat transfer to the reactor coolant is assumed to occur only at the outer radial surface of the irradiation capsule. In the H7 input files, this was accomplished by establishing a type 1 (surface-to-environment) boundary condition with a boundary temperature of 57.2 °C (LCS worst-case) and a forced convection heat transfer coefficient of 1.92 W cm^{-2} K^{-1}. The heat transfer coefficient was calculated as follows (equations are from [Hobbs 2002]):

$$\Omega = 0.4115 \ln T_b - 2.12232 \qquad T_b \text{ in } °C$$
$$= 0.4115 \ln(57.2) - 2.12232$$
$$= -0.4572$$
$$h_c = e^{\Omega} \times \text{flow}^{0.8} \frac{W}{cm^2 \cdot K} \qquad \text{flow in gpm}$$
$$= e^{-0.4572} \times (4.0)^{0.8}$$
$$= 1.92 \frac{W}{cm^2 \cdot K}$$

4.1.4 Computations and Analyses

This section describes the iterative process used to calculate temperature profiles. The process involved the use of H7 to carry out the temperature calculations, and manual calculations to determine thermal expansion associated with the H7 temperature data. After each H7 run, thermal expansion effects were calculated and incorporated into a new H7 input geometry. This process was repeated until H7 output converged to a steady temperature profile.

After convergence of the thermal expansion iteration process, a check of the adequacy of the result was performed by running the final dimensions with a very fine grid structure and a tightened convergence criterion for the H7 determination of convergence of the steady-state temperature solution. Adequacy of this solution was verified by running the H7 direct solution method.

In response to a comment received from the independent review required for safety-related calculations, a final calculation was performed in which the thermal conductivity

of helium was reduced by 20% to conservatively model reduced thermal conductance associated with small gaps.

The iterative process was as follows:

1. develop an H7 input file
2. run H7
3. run the H7 program H7MAP to create a temperature map
4. import the temperature map into Excel©
5. use Excel© to calculate average temperatures for all components
6. calculate coefficients of thermal expansion for all components based on curves of temperature vs. linear thermal expansion for tungsten [Goldsmith *et al*. 1961a] and aluminum [Goldsmith *et al*. 1961b]
7. use Excel© to calculate revised dimensions for all components based on the coefficients of thermal expansion
8. develop an H7 input file based on the revised dimensions

Run 1. Used the initial input presented in Section 4.1.3 and Figure 4.4.

Runs 2 – 6. Carried out the iterative process described above.

Runs 7 and 8. After the iterative thermal expansion process converged to a set of final dimensions for all components, a run was performed to check the adequacy of the solution. Runs 1 through 6 used a coarse grid structure to facilitate calculation of thermal expansion. For Run 7, a very fine grid structure (using the same component dimensions as Run 6) and a tightened convergence criterion were used to obtain a more accurate calculation of the steady-state temperature profile. Run 8 also used the same component dimensions as Run 6, but used the direct solution method (an exact solution of the heat

balance equations) rather than the SOR iterative solution method which was used for Runs 1 – 7.

Run 9. A final calculation was performed in which the reduced thermal conductance of small gas gaps [Garnier and Begej 1979] was conservatively modeled by reducing the thermal conductivity of helium by 20%. Other than the equation for helium thermal conductivity ($0.001190 + 2.268 \times 10^{-6}$ T W cm^{-1} K^{-1}), the input for this run was identical to Run 8.

4.1.5 Summary of Results

Results from Runs 1 – 6 show that the iterative process for incorporating thermal expansion effects converges on a final solution.

Table 4.3 presents maximum temperatures in the tungsten targets, the aluminum components, and the surface of the irradiation capsule for each of the six runs. The columns marked "Change" represent the absolute value of the difference between successive runs. The table shows that the change in temperatures between runs decreases in successive iterations and at the end of six iterations, temperature changes are negligible. Thus, the solution is convergent.

Table 4.3 Tungsten Cylinder Experiment Component Temperatures

	Tungsten		Aluminum		Capsule Surface	
Run	Max. Temp. (°C)	Change	Max. Temp. (°C)	Change	Max. Temp. (°C)	Change
1	1054.36		448.17		104.20	
2	1020.63	33.7	388.67	59.5	105.09	0.9
3	1032.24	11.6	407.83	19.2	104.49	0.6
4	1027.74	4.5	400.33	7.5	104.91	0.4
5	1030.41	2.7	405.19	4.9	104.56	0.3
6	1029.59	0.8	403.18	2.0	104.64	0.1

A graphical display of convergence is presented in Figure 4.5 which shows temperature profiles for each of the six runs. The entire temperature profile is shown, from the experiment centerline to the outer surface of the irradiation capsule at a height corresponding to the horizontal center of the tungsten targets. Convergence can best be seen in the region from 0.3 – 0.4 cm where Run 1 has the highest temperature, Run 2 the lowest temperature, and the subsequent runs have alternately higher and lower temperatures with Runs 5 and 6 being nearly identical.

Run 7 was performed to check the adequacy of the Run 6 solution by using a very fine grid structure and a tightened convergence criterion (the convergence criterion is used by the H7 iterative SOR method of solution to terminate the iterative process). Convergence of the solution was demonstrated by the fact that the calculated steady-state heat generation rate and boundary heat flow rate were identical (six significant figures displayed).

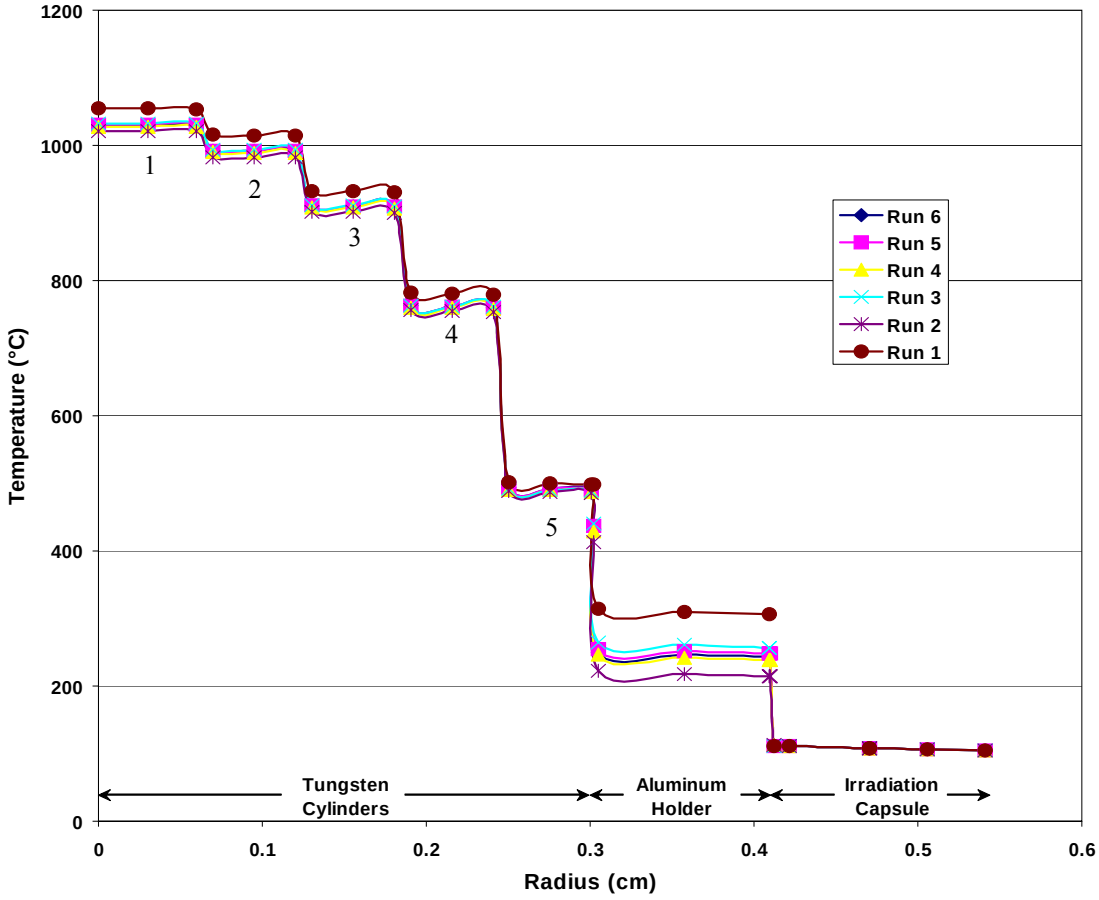

Figure 4.5 Tungsten Cylinder Experiment Temperature Profile

Run 8 provided a further check of the adequacy of the solution by using the direct solution method of H7. (Also, Runs 7 and 8 were run in two dimensions – Runs 1-6 had been run in three dimensions – to allow for increasing the number of nodes in Run 7 and enable the use of the exact solution method in Run 8.) As in Run 7, the heat generation rate and boundary heat flow rate were identical. Temperatures were the same as Run 7. In Run 8 the maximum tungsten temperature changed from 1029.59 °C (Run 6) to 1057.26 °C (Δ = 28 °C), the maximum internal aluminum temperature changed from 403.18 °C (Run 6) to 438.96 °C (Δ = 36 °C), and the maximum external aluminum

temperature (capsule surface temperature) changed from 104.64 °C (Run 6) to 105.20 °C (Δ = 0.6 °C).

Run 9 was subsequently performed to address a concern regarding a report [Garnier and Begej 1979] that investigated non-linearities in heat conduction across small gas gaps. ORNL Research Reactors Division determined that the effective thermal conductivity of helium in the tungsten cylinder model was 80% of the actual thermal conductivity. Run 9 used the same input as Run 8 with the helium thermal conductivity equation multiplied by 0.8. Peak internal temperatures increased, but were still within acceptable limits. The maximum tungsten temperature increased from 1057.26 °C (Run 8) to 1177.81 °C and the maximum aluminum temperature increased from 438.96 °C (Run 8) to 488.81 °C. The maximum external temperature decreased from 105.20 °C to 104.27 °C.

Thus, Run 9 provides a reliable, conservative estimate of the temperature profile of the tungsten cylinder experiment under LCS conditions and postulated reductions in heat transfer across gas gaps. Maximum tungsten temperature is 1178 °C, well below the melting point of 3370 °C [MatWeb 2003]. Maximum aluminum temperature is 489 °C, below the melting point of 582 – 652 °C for 6061-T6 [MatWeb 2003]. Peak irradiation capsule surface temperature is 104 °C, well below the point of net vapor generation of > 200 °C at the hydraulic tube horizontal midplane.

Figure 4.5 shows that under worst-case LCS conditions (130% reactor power), peak temperatures in the tungsten cylinder experiment can exceed 1000 °C. The following sections will assess the impact of such temperatures on radiative capture by tungsten.

4.2 Temperature Effects on Neutron Flux Distribution

Temperature of the environment to which neutrons are exposed has an impact on their energy distribution at the lower end of the spectrum. Neutron distribution at higher energies in a nuclear reactor is essentially independent of reactor temperature since atomic vibration has negligible impact on neutron energy distribution as neutrons slow down from fission energies to thermal energies, primarily through a series of elastic collisions [Stacey 2001]. At lower energies, however, neutrons eventually reach thermal equilibrium with their surroundings, exhibiting a Maxwellian distribution with respect to energy [*ibid*]. The equation that describes thermal neutron distribution is:

$$\frac{n(E)}{n} = \frac{2\pi}{(\pi kT)^{3/2}} E^{1/2} e^{-E/kT} \tag{4.1}$$

where $n(E)/n$ is the normalized neutron density per unit energy, T is the absolute temperature of the system, E is neutron energy, and k is Boltzmann's constant. A graph of Equation 4.1 for various values of T is shown in Figure 4.6.

With this distribution, only approximately 1.9% of the Maxwellian neutrons have energies above $5E_{kT}$ [Stoughton and Halperin 1959]. Therefore, at standard temperature

(293.6 K), most thermal neutrons have energies below 0.127 eV. At a temperature 1000 K above standard temperature, neutron distribution broadens and $5E_{kT}$ becomes 0.56 eV.

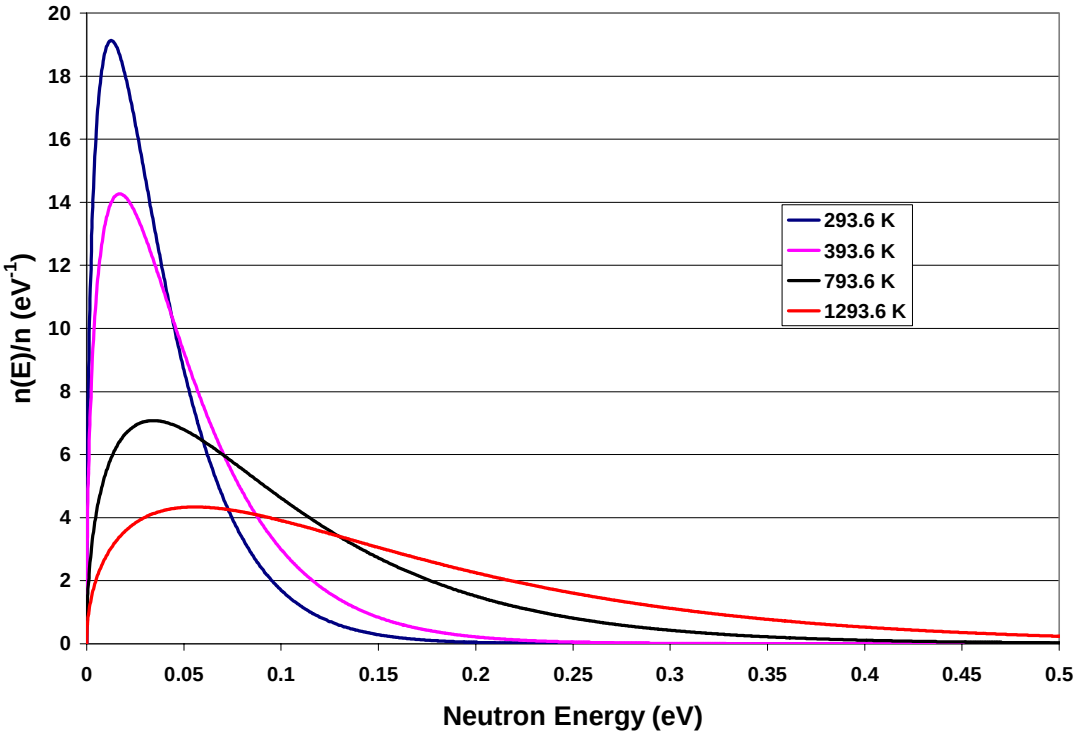

Figure 4.6 Thermal Neutron Flux Distributions

Thus, temperature can have a significant impact on neutron energy distribution in the thermal range of the neutron spectrum, but not in the epithermal and higher energy regions. Figure 3.1 shows the thermal and epithermal contributions to total neutron flux; the discussion above shows that a shift in the Maxwellian component occurs as temperature changes, but the epithermal component retains a $1/E$ distribution.

With regard to the temperatures determined in Section 4.1 for the tungsten cylinder self-shielding experiment, a graph of Equation 4.1 with T = 60 °C (approximate coolant

temperature at the HFIR horizontal midplane) and 1000 °C is shown in Figure 4.7. While the flux distribution flattens at the higher temperature, the majority of Maxwellian neutrons have energies below 0.55 eV (at 1000 °C, $5E_{kT}$ = 0.549 eV).

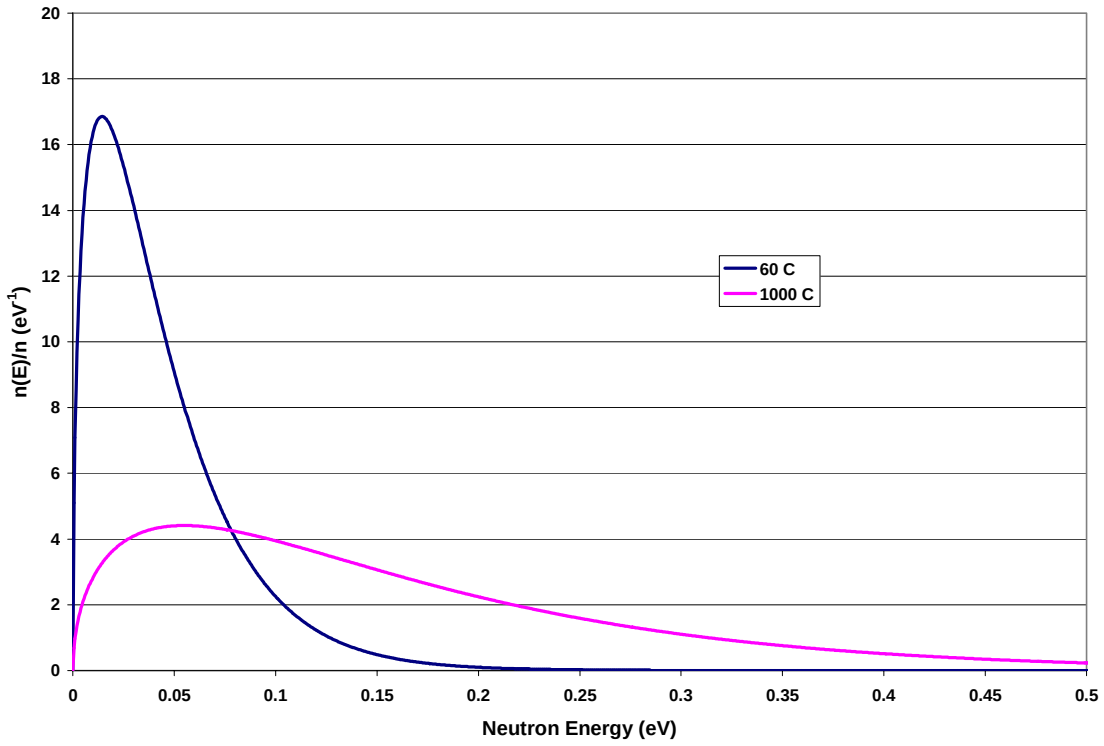

Figure 4.7 Thermal Neutron Flux Distributions at 60 °C and 1000 °C

The consequences of temperature effects on flux distribution with respect to radiative capture will be addressed in Section 4.4.

4.3 Temperature Effects on Radiative Capture Cross Sections

Temperature affects the radiative capture cross section through Doppler broadening of the resonance peaks, with the peaks broadening and decreasing in magnitude as

temperature of the target nuclei increases. Figure 4.8 demonstrates this effect by plotting the first resonance peak (18.81 eV) of ^{186}W neutron capture at temperatures of 0 K and 1000 K. Figure 4.8 was generated from SAMMY-M6 output files, run by Nancy M. Larson of the Oak Ridge National Laboratory using ENDF [NNDC 2004a] ^{186}W resonance parameters.

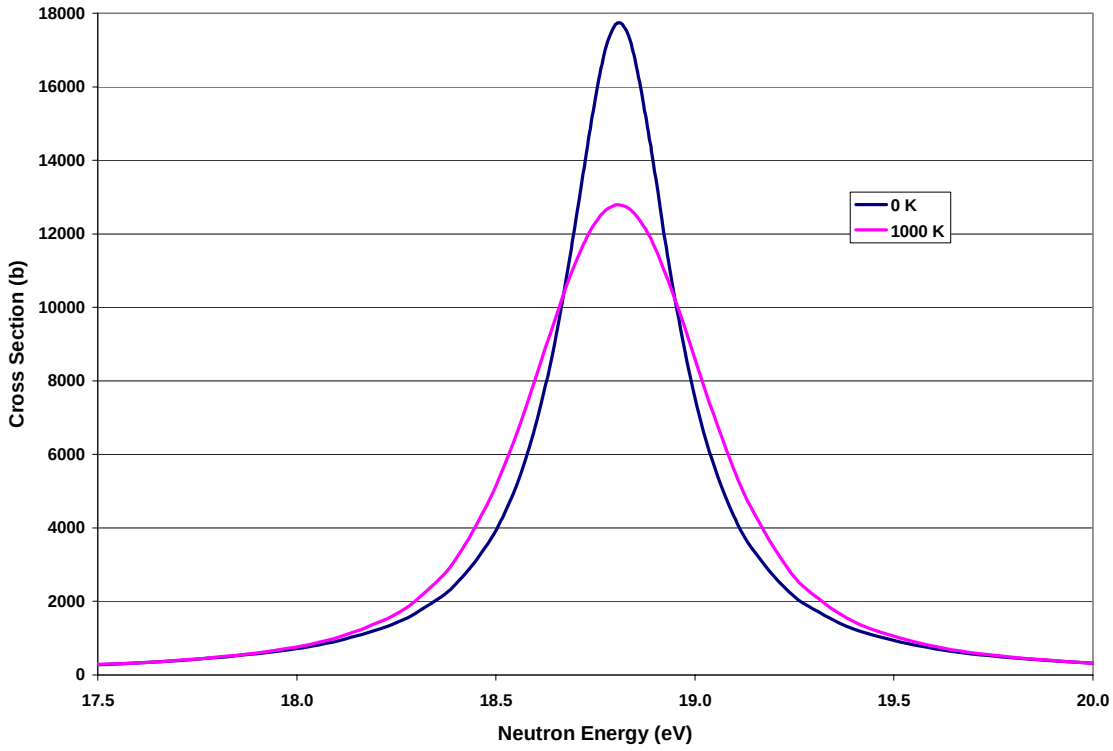

Figure 4.8 Doppler Broadening of ^{186}W Radiative Capture First Resonance Peak

Figure 4.9 shows the effects of Doppler broadening over the range of neutron energy in a nuclear reactor (using the same data files as Figure 4.8). With a logarithmic scale, resonance peak broadening is not very pronounced, although decreases in peak magnitudes are observable.

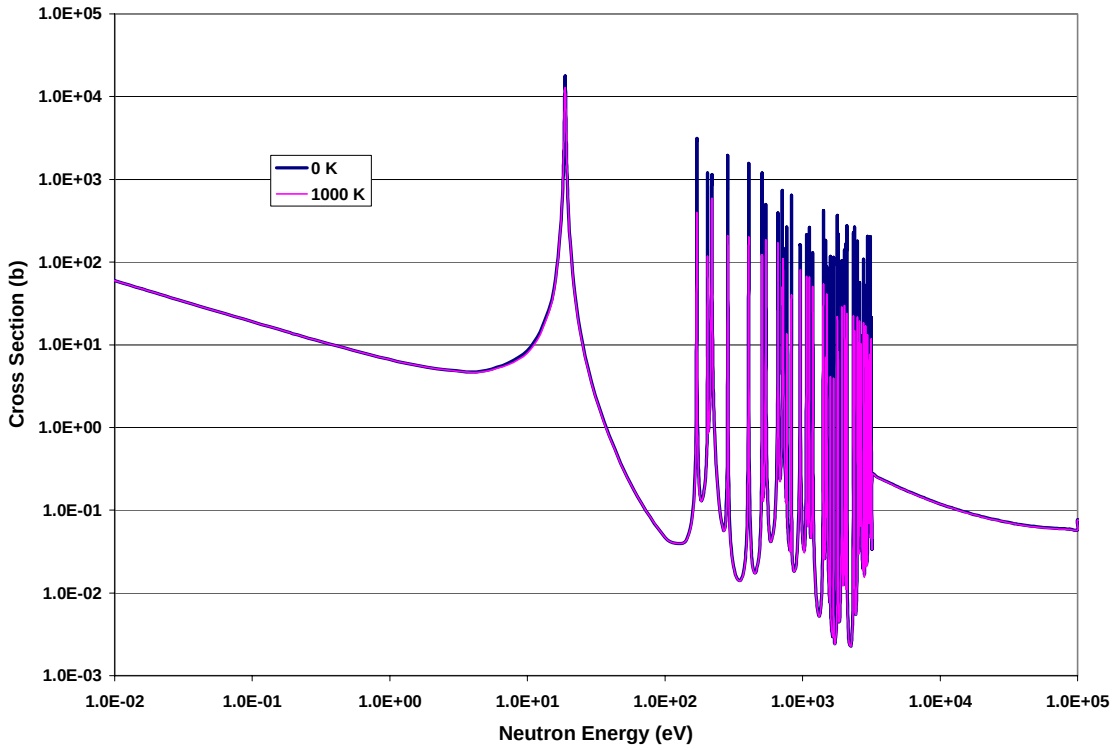

Figure 4.9 ^{186}W Radiative Capture Cross Section as a Function of Neutron Energy

While the area under the curve of a resonance peak does not change due to Doppler broadening, the overall reaction rate increases because flux depletion at resonant energies becomes less significant. For very sharp peaks, the neutron flux becomes depleted at the resonant energy and neutrons slowing down by elastic scattering can pass over the resonant energy range as they change energy. With a broadened peak, more neutrons will fall in the resonant range as they scatter through the epithermal region.

4.4 Temperature Effects on Radiative Capture Reaction Rates

Section 4.2 identified that elevated temperature has an effect on the Maxwellian distribution of thermal neutrons while epithermal neutron distribution is unaffected by temperature. Section 4.3 showed that Doppler broadening flattens resonance peaks at elevated temperature. To demonstrate the effect these phenomena have on ^{186}W radiative capture, thermal neutron flux distributions at 60 °C and 1000 °C are plotted on the same graph as the radiative capture cross section at 0 K and 1000 K (Figure 4.10).

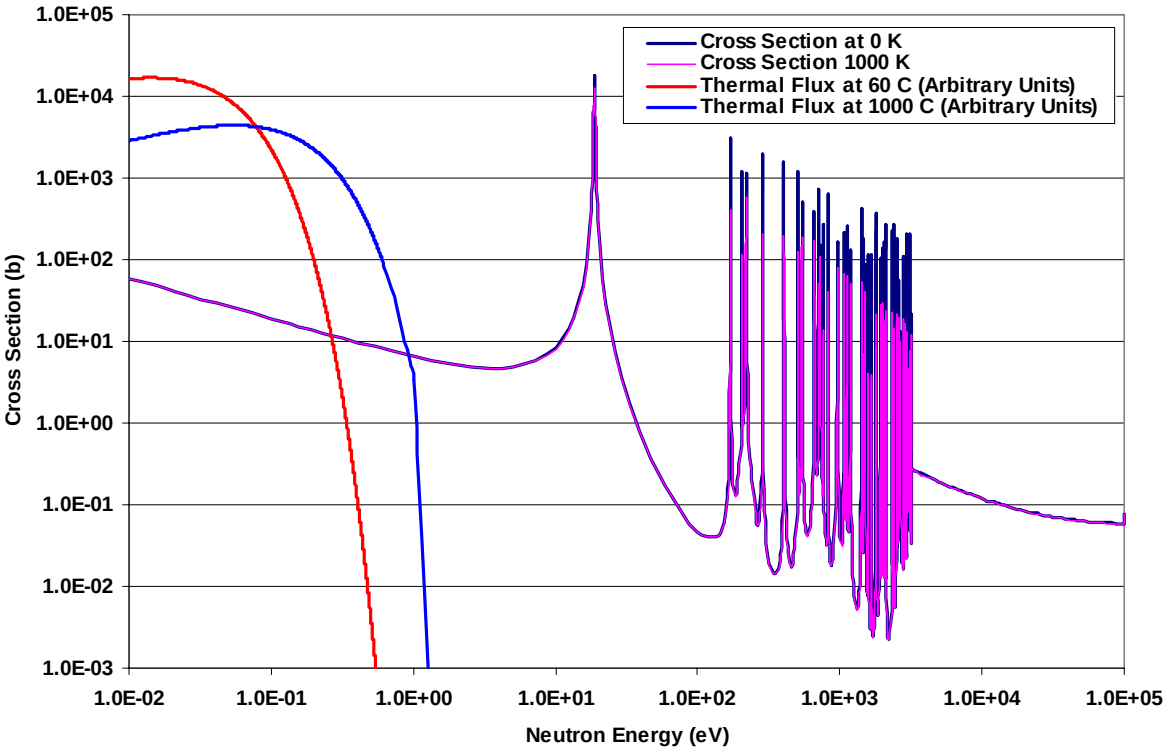

Figure 4.10 ^{186}W Radiative Capture Cross Section and Thermal Neutron Flux

Figure 4.10 clearly shows that the Maxwellian temperature distribution shift does not result in the thermal neutron population reaching the first resonance peak and thus the temperature effect on neutron energies cannot significantly increase radiative capture rates. In fact, radiative capture would tend to decrease in response to increasing neutron temperature because the distribution shifts to higher energies in the region where the radiative capture cross section decreases as $1/\sqrt{E}$ [Lamarsh 1993].

However, as identified in Section 4.3, Doppler broadening at elevated temperatures can increase radiative capture reaction rates. Experiments described in Chapter 5 give some indication that an overall increase in reaction rates does occur at elevated temperatures.

5 Neutron Self-Shielding Experiments

Two concepts were employed to investigate neutron self-shielding experimentally: a set of concentric tungsten cylinders and packages of stacked tungsten foils. Product activities (in terms of Bq per unit mass) of the components of each experiment would reveal the effects of neutron self-shielding and temperature as functions of the distance of the components from the surface of the experiments.

5.1 Self-Shielding Experiment Target Descriptions

Three sets of five concentric natural tungsten cylinders were manufactured by Goodfellow Corporation (Berwyn, PA, order #G0054A) per the fabrication drawing shown in Figure 4.1. One set was sent to the Oregon State University Department of Nuclear Engineering, two HFIR hydraulic tube targets were assembled using the other two sets. After receipt inspection by ORNL Quality Assurance to verify compliance with the design drawing, both sets of targets were weighed using a calibrated Mettler AE240 balance. Specifications for the tungsten cylinders are provided in Table 5.1. A graphical representation of the cylinders is provided in Figure 5.1

Target holders for the cylinders were manufactured by Iverson Engineering Corporation (Clyde, NC, order #101802) per the fabrication drawing shown in Figure 4.2. The target holders were designed to fit into thin-walled hydraulic tube irradiation capsules, which

were manufactured under the same order according to the fabrication drawing shown in Figure 4.3.

Table 5.1 Tungsten Cylinder Specifications

Cylinder Number	Set Number	OD (mm)	ID (mm)	Mass (g)
1	1	1.2	N/A [a]	0.4444
	2	1.2	N/A [a]	0.4478
2	1	2.4	1.4	1.1597
	2	2.4	1.4	1.1594
3	1	3.6	2.6	1.8730
	2	3.6	2.6	1.8777
4	1	4.8	3.8	2.6523
	2	4.8	3.8	2.6427
5	1	6.0	5.0	3.3271
	2	6.0	5.0	3.3228

[a] solid

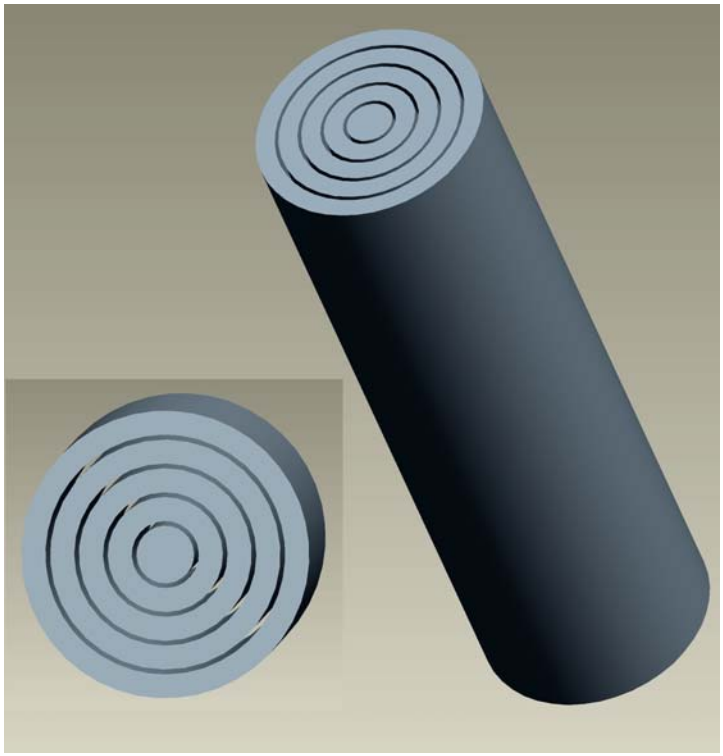

Figure 5.1 Tungsten Cylinders

Two thicknesses of natural tungsten foil (Alfa Aesar, Ward Hill, MA) were used to fabricate the foil self-shielding experiments:

0.1 mm thick	Alfa Aesar stock #10416, lot #F21K08
0.25 mm thick	Alfa Aesar stock #10415, lot #F27K02

Each foil was cut into 4.0 mm x 6.25 mm pieces. Masses of the foil pieces are specified in Tables in Appendix D in which activities per unit mass are calculated. Typical foil pieces are shown in Figure 3.4.

Target holders for the foils were also manufactured by Iverson Engineering Corporation (Clyde, NC, order #101802), per the fabrication drawing shown in Figure 5.2. The target holders were designed to fit into thin-walled hydraulic tube irradiation capsules, as described above. This design accommodated a stack of eighteen 0.1 mm foils (producing a 4.0 mm x 6.25 mm x 1.8 mm package) and eleven 0.25 mm foils (producing a 4.0 mm x 6.25 mm x 2.75 mm package).

The tungsten cylinders were placed in their target holders, the target holder caps were put in place, and the assemblies were inserted in irradiation capsules.

The tungsten foil packages were placed in the slots in parts 3 and 4 of the fabrication drawing (Figure 5.2), those parts were inserted in part 2, and the assemblies were inserted in irradiation capsules.

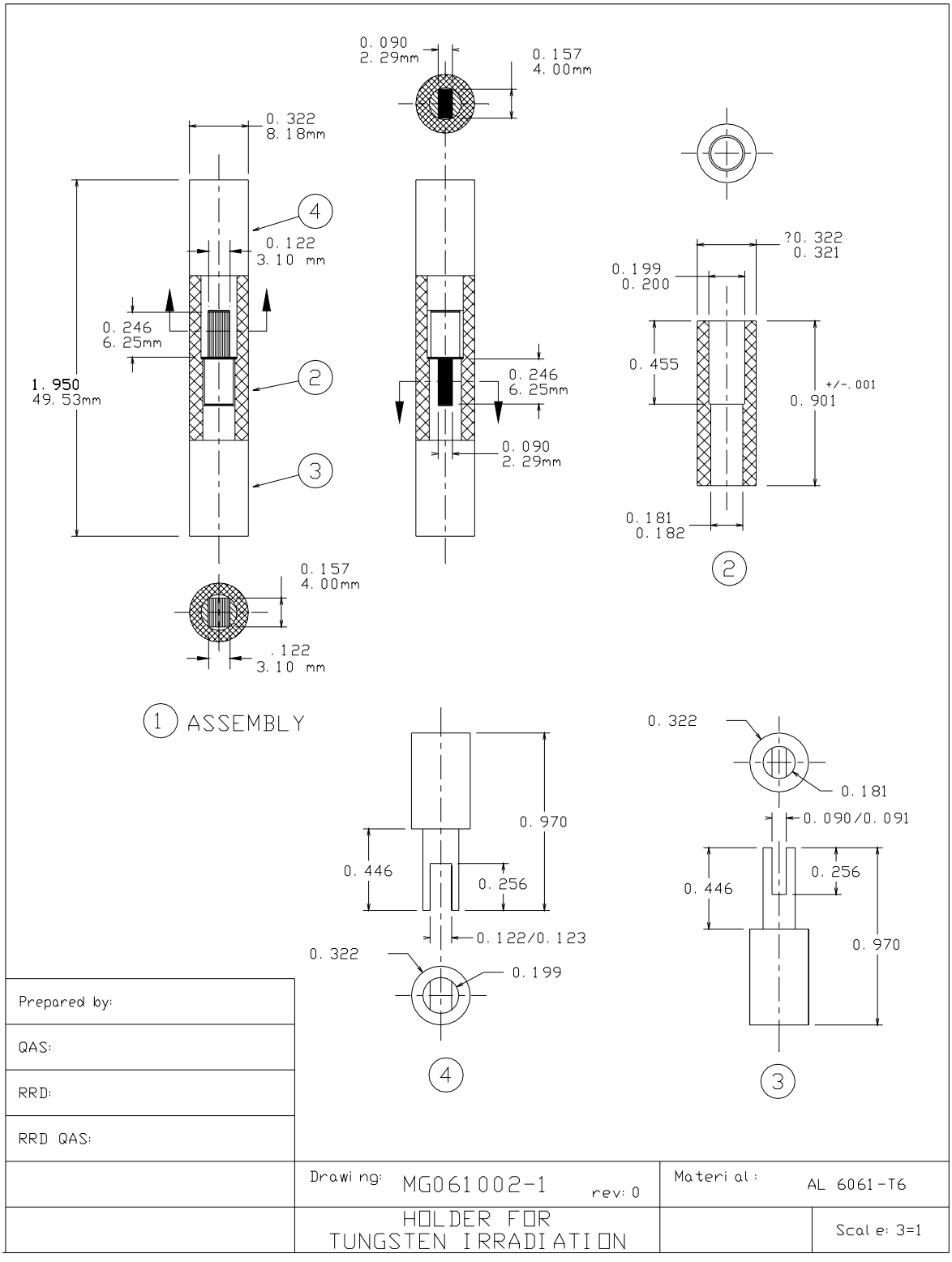

Figure 5.2 Aluminum Holder for Tungsten Foil Targets

Irradiation capsule end plugs (Figure 4.3) were put in place, the irradiation capsules were evacuated, backfilled with helium (~ 1 atm), and welded closed by the ORNL experiment fabrication shop. All four targets (two irradiation capsules containing tungsten cylinder experiments and two containing tungsten foil experiments) were fully certified by ORNL Quality Assurance for irradiation in HFIR.

5.2 Target Irradiation and Processing

The self-shielding experiments were irradiated in the High Flux Isotope Reactor hydraulic tube facility located in the flux trap (Figures 2.1 and 3.3). Irradiations were performed in the hydraulic tube because its high flux is necessary to produce sufficient ^{188}W activity for analysis and because targets can be inserted and removed from the reactor at any time (irradiation for a full reactor cycle, typically 21 – 24 days, would have resulted in significant target and product isotope burnup, which would obscure the effects being studied). Irradiations were performed in position #5 of the hydraulic tube which, as identified in Chapter 2, has a thermal neutron flux of 2.05×10^{15} n cm^{-2} s^{-1} and a thermal to epithermal flux ratio of 20.

The target containing set #1 of the tungsten cylinders was irradiated for 30 minutes with EOB at 1329 on June 12, 2003. The target containing set #1 of the tungsten foils was irradiated for 60 minutes with EOB at 1442 on June 12, 2003.

Both targets were transported to the Nuclear Medicine Group laboratory in building 4701 for analysis using the HPGe system described in Section 2.2. All samples were mounted on cards for gamma ray analysis as shown in Figure 5.3. The tungsten cylinders are shown mounted on cards in the foreground labeled 1 – 5, the 0.25 mm foils are shown mounted on cards labeled 1 – 11, and the 0.1 mm foils are shown on cards labeled A – R.

Figure 5.3 Tungsten Self-Shielding Experiment Cylinders and Foils

5.3 Data Analysis

As in Chapter 3, gamma ray spectra were obtained for all samples and CLSQ [Cumming 1963] was used to determine activities at EOB in counts per second. Gamma ray detector

efficiencies (Appendix A), intensities [NNDC 2003], and self-absorption factors (Appendix B) were used to calculate activities at EOB in Bq. Finally, target masses were used to calculate activities at EOB in Bq mg^{-1} tungsten. Gamma ray spectroscopy data and data processing for the tungsten foils and cylinders are presented in Appendix D.

Figure 5.4 shows the ^{187}W and ^{188}W activities induced in the tungsten cylinder experiment. Activities of each cylinder are plotted with the *x*-axis representing the distance from the outer surface of the outer cylinder to the midpoint of the cylinder (in this representation, the data points approximate average values for each cylinder).

In a similar fashion, ^{187}W and ^{188}W activities induced in the 0.25 mm tungsten foils are plotted in Figure 5.5. Data points at 0.125 mm are the middle of the two outer foils in the package and the data point at 1.375 mm is the central foil. Using the same method, data from the 0.1 mm foils is plotted in Figure 5.6.

As is seen in Figures 5.4 – 5.6, induced activities drop rapidly with distance to the surface of the target. After the rapid drop in induced activity near the outer surface of the targets, the activity in the central regions tends to become somewhat level. A decrease in activity is to be expected due to neutron self-shielding and these results demonstrate that the phenomenon occurs over a very short range. The "leveling off" of the induced activities toward the centers of the targets is due (at least in part) to flux depletion at the energies of the resonance peaks [Stacey 2001], particularly the first resonance peak of ^{186}W which has a very large cross section (Figure 4.9).

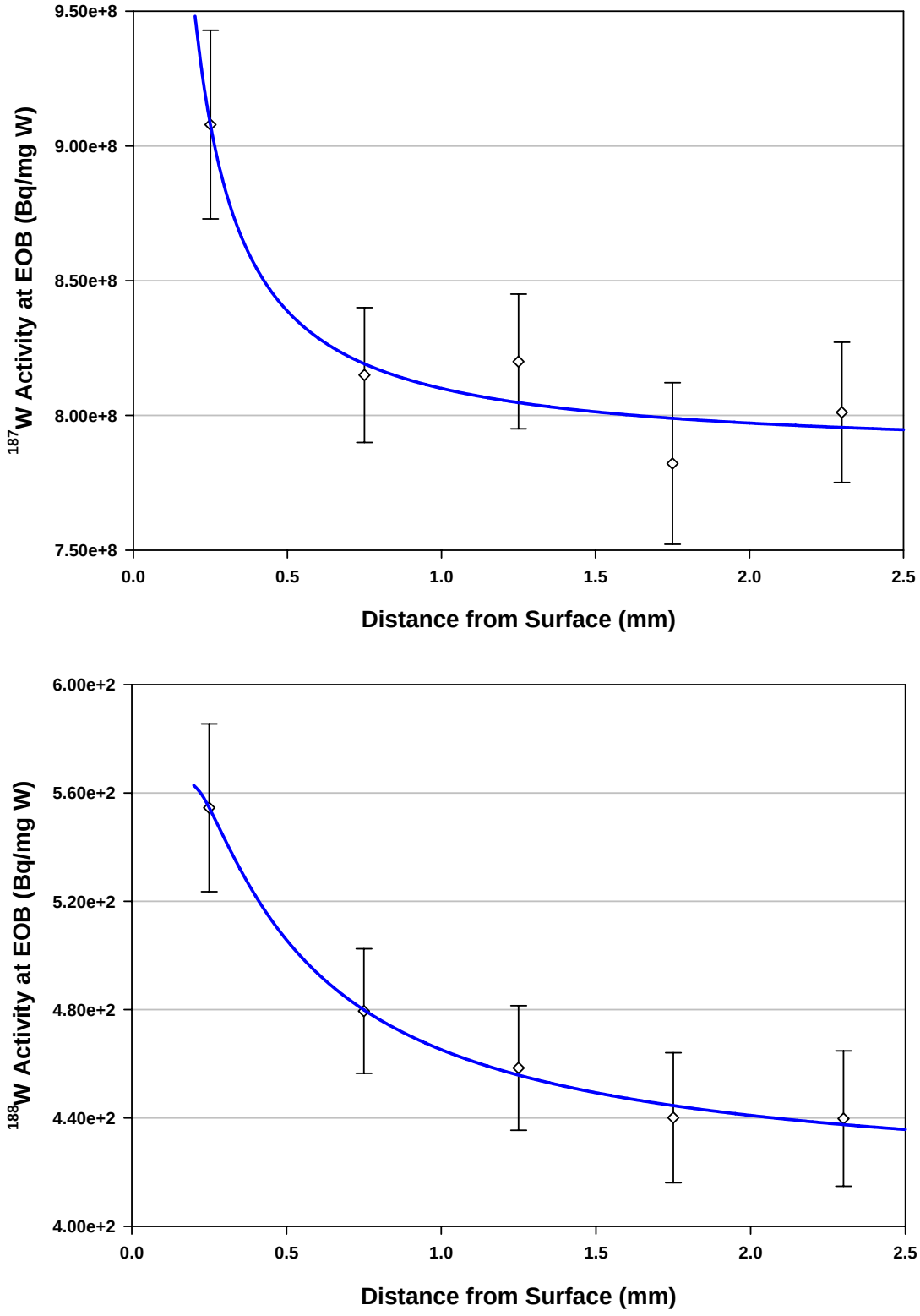

Figure 5.4 Cylinder Self-Shielding Experiment Tungsten Activities

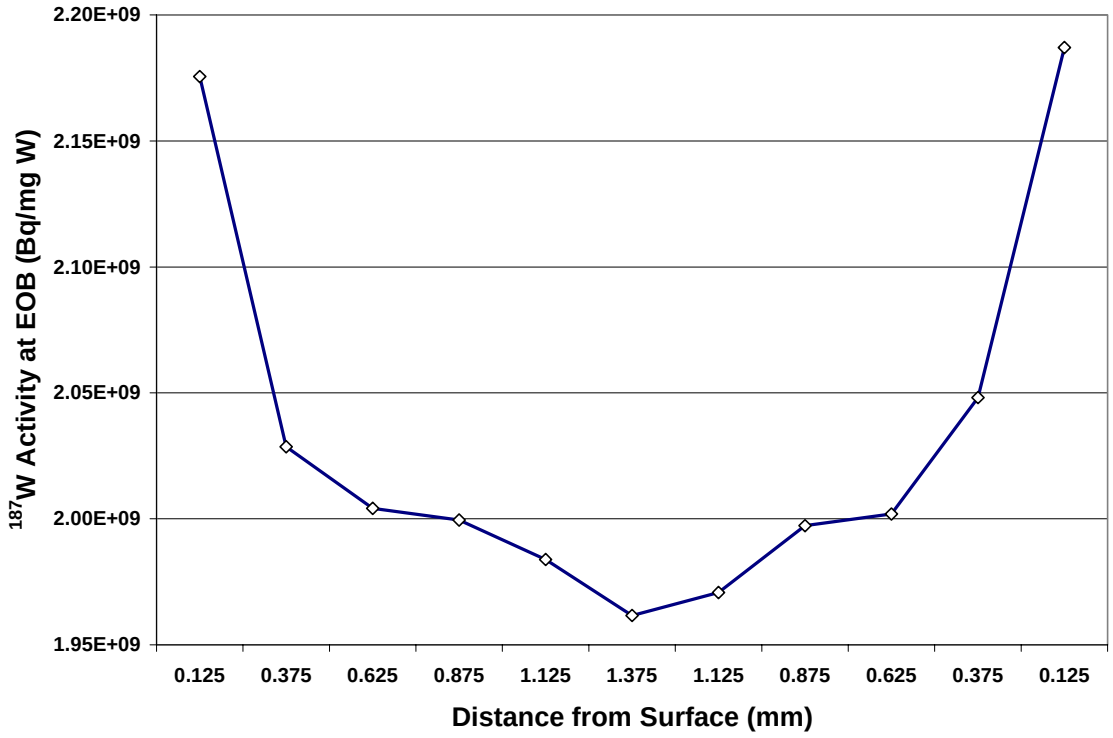

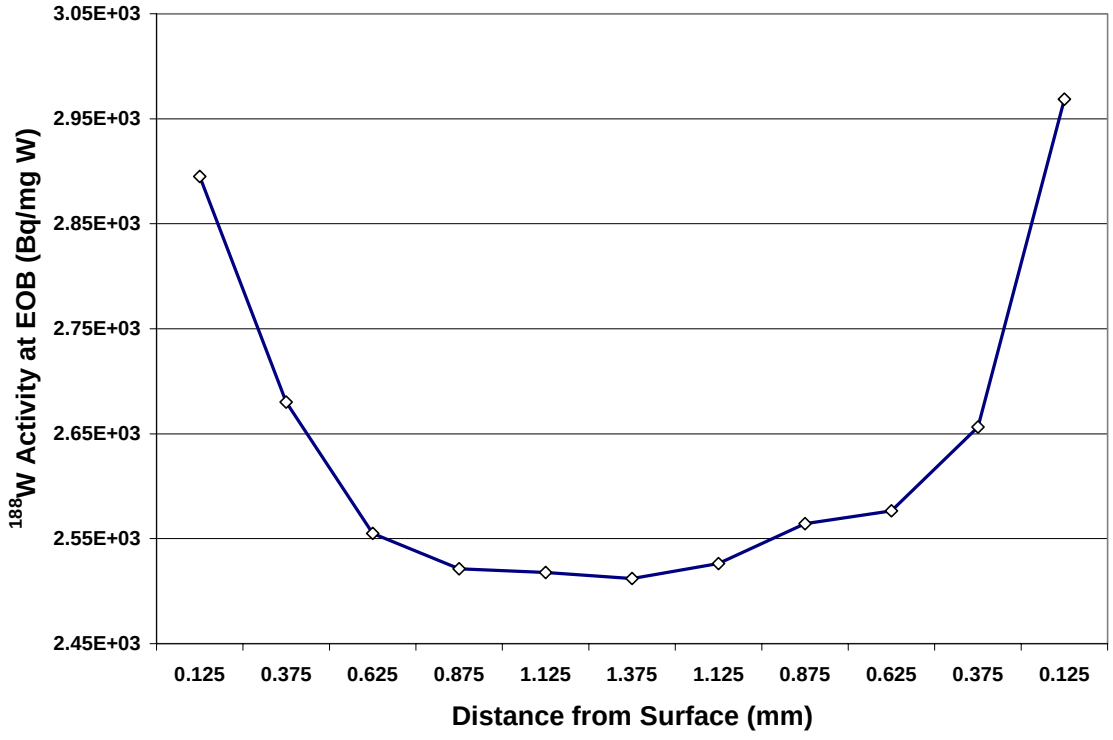

Figure 5.5 0.25 mm Foil Self-Shielding Experiment Tungsten Activities

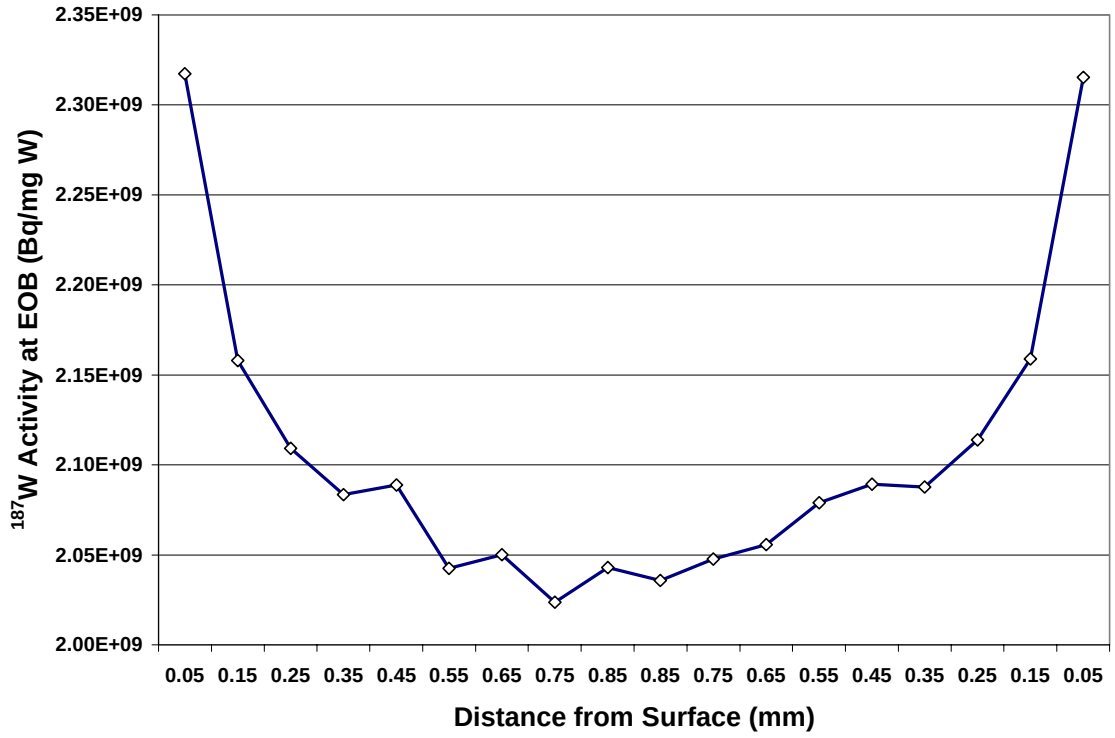

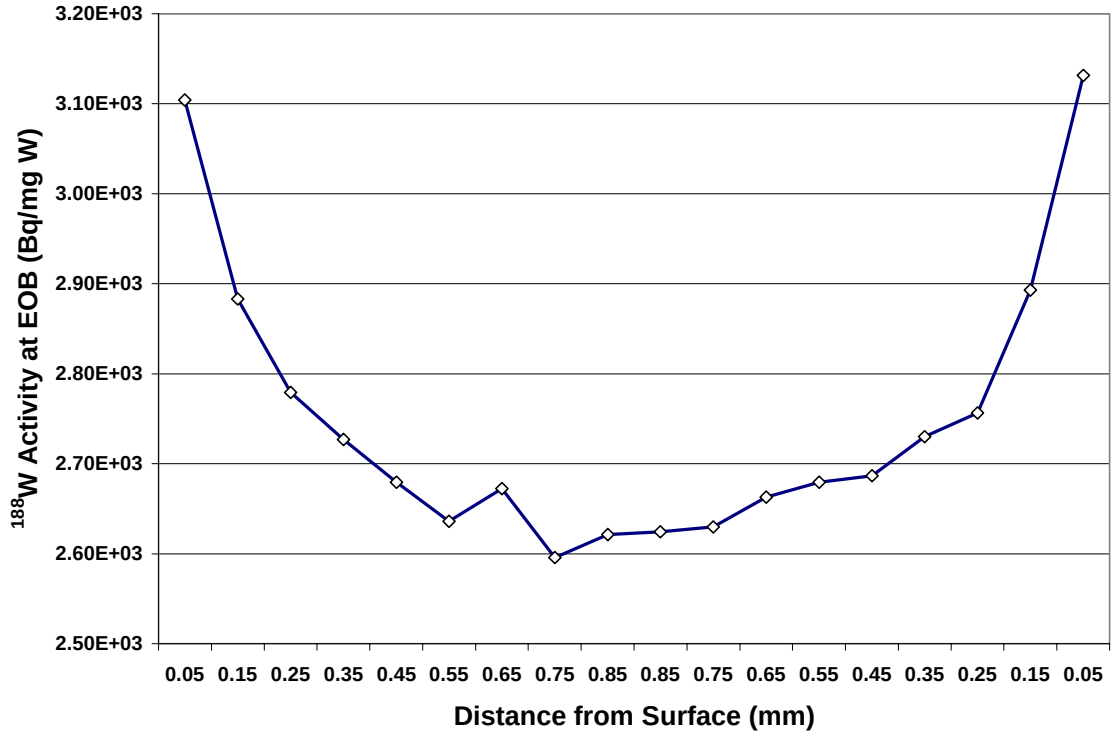

Figure 5.6 0.1 mm Foil Self-Shielding Experiment Tungsten Activities

Figure 5.7 combines the 0.25 mm and 0.1 mm foil data and uses the symmetry of the foil packages to produce two curves comparing that facilitate data analysis. The symmetry of both curves (0.25 mm foil and 0.1 mm foil) is an indication that the neutron flux in this region of the hydraulic tube is very isotropic since nearly identical activities are induced in both halves of each package. It is interesting to note that induced activities in both foil packages are consistent to approximately 0.3 mm from the surface. Along with the decrease in the rate of decline in activity at approximately 0.4 mm, this indicates that self-shielding effects can be expected to have maximum impact in the first 0.3 – 0.4 mm of target depth.

Figure 5.7 also reveals that the decrease in induced activity through the 0.1 mm foil package is not as pronounced as in the 0.25 mm package. The analysis of temperature effects (Chapter 4) would suggest that the reverse should be true; i.e., the thicker 0.25 mm foil package should have greater levels of activity due to the greater temperatures induced in the thicker package. However, the greater activity in the 0.1 mm foil is possibly due to the fact that a foil in the central part of the 0.1 mm foil package is closer to the far side of the package than one in the 0.25 mm foil package. Essentially, the combined flux on both sides of a 0.1 mm foil is greater than that for a 0.25 mm foil due not only to lessened flux depletion, but more so to lessened thermal neutron attenuation which will be addressed later in this chapter.

As mentioned earlier, the "leveling off" of the curves in Figures 5.4 – 5.7 is certainly due in part to the diminishing effects of neutron self-shielding due to flux depletion.

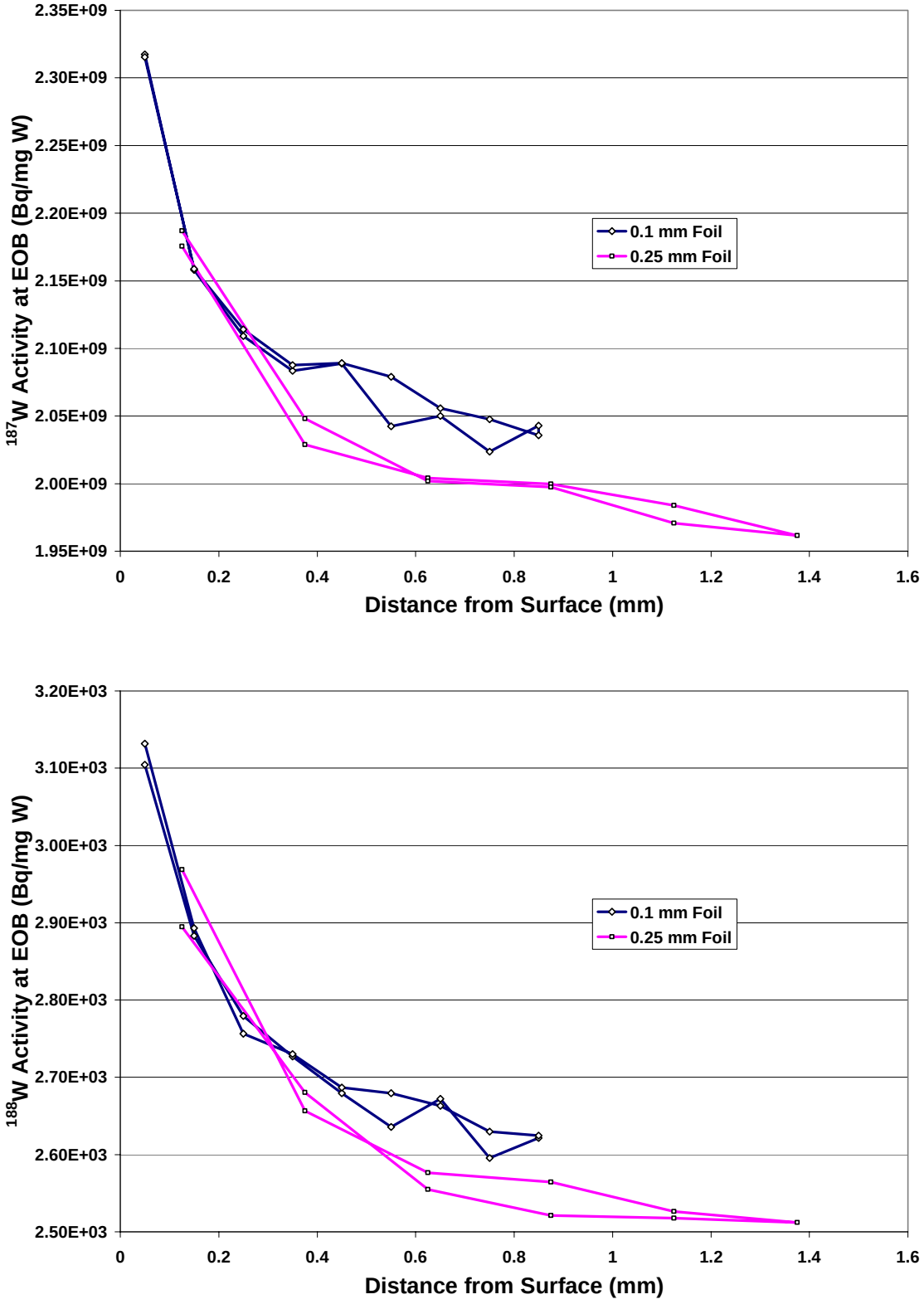

Figure 5.7 0.25 mm and 0.1 mm Foil Self-Shielding Experiment Tungsten Activities

However, even with the depletion of neutrons at resonant energies in the epithermal region, induced activities would be expected to continue to decrease as the result of the attenuation of thermal neutrons. Neutron attenuation through a target can be calculated using the following equation [Lamarsh 1993]:

$$\begin{aligned} \phi_x &= \phi_{initial} e^{-N\sigma x} \\ &= \phi_{initial} e^{-\left(6.32\times10^{22}\right)\left(35.7\times10^{-24}\right)x} \\ &= \phi_{initial} e^{-2.26x} \qquad x \text{ in cm} \end{aligned} \tag{5.1}$$

where N is the atom density of tungsten, 6.32 x 10^{22} atoms cm^{-3} (using ρ_W = 19.3 g cm^{-3}, M_W = 183.84 g g-mol^{-1}, and N_A = 6.022 x 10^{23} atoms g-mol^{-1}), and σ is an effective cross section of 35.7 b (using σ_a = 18.2 b, I_a = 350 b and r = 20 in Equation 2.4 where the subscript "a" means the absorption cross section) (all data from Parrington *et al*. [1996]).

An estimate of the induced ^{187}W activity at the surface of a target (i.e., no neutron self-shielding) was made by running LAURA [Mirzadeh and Walsh 1998] with the tungsten cross sections derived in Chapter 3 and the hydraulic tube flux derived in Chapter 2. The actual induced activity varies since neutron flux varies with core loading and the time of irradiation during a reactor cycle. This estimate, 3.37 x 10^9 Bq mg^{-1}, was used for $\phi_{initial}$ in Equation 5.1 and plotted along with the 0.25 mm and 0.1 mm foil data in Figure 5.8.

Figure 5.8 demonstrates that overall neutron flux decreases linearly through the target as the result of neutron attenuation, the dashed line showing the decrease in induced activity that would be experienced if neutron attenuation were the only phenomenon involved. Since the induced activities in the center of the target do not decline in such a manner, it

is likely that the radiative capture rate is increasing as the result of temperature-induced Doppler broadening.

Figure 5.8 also suggests that if the estimate of induced tungsten activity is accurate, the effects of neutron self-shielding are even more dramatic than suggested by Figures 5.4 – 5.6 since the decrease in activity from the surface to the first data point is striking:

$$\frac{3.37\times10^{9}-2.32\times10^{9}}{3.37\times10^{9}}\times100=31\%$$

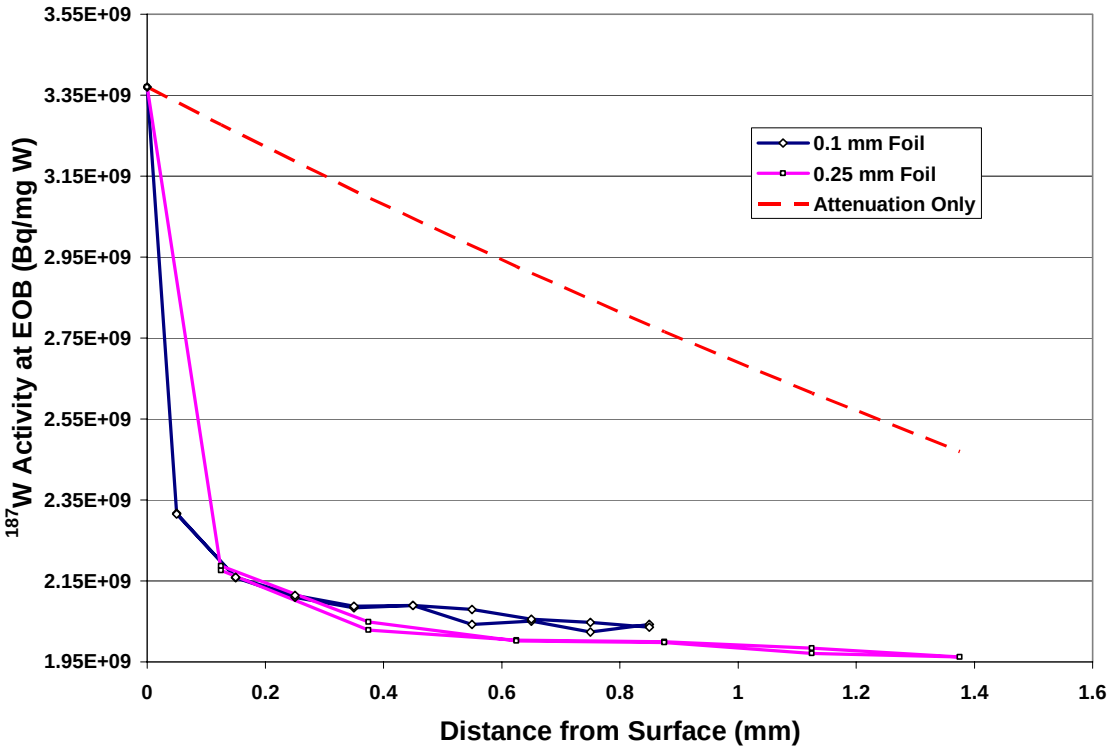

Figure 5.8 0.25 mm and 0.1 mm Foil Self-Shielding Experiment Tungsten Activities Relative to the Effect of Neutron Attenuation in the Targets

6 Conclusions and Future Work

6.1 Conclusions

Neutron self-shielding has a significant impact on induced target activity, particularly within the initial 0.3 mm to 0.4 mm depth of the target. It is possible that the effect could be even greater in light of the sharp decrease in activity of the outer most foils with respect to a theoretical calculation of induced activity in the absence of neutron self-shielding. A realistic experiment to investigate this possibility would be to use thinner foils. However, the results would be unlikely to have practical value with regard to ^{188}W production since targets with a depth of less than a few tenths of a millimeter would be extremely inefficient in producing large quantities of ^{188}W.

Temperature also appears to have an impact on production yields as the yields seen in the central portions of the cylinder and foil targets do not decrease at a rate as high as would be expected due to neutron absorption in the target.

The thermal cross section and resonance integral for ^{186}W appear to be fairly well characterized given the values reported in the literature and results from experiments presented in Chapter 3. However, there is significant concern that the single measurement of the ^{187}W thermal cross section and resonance integral is invalid.

6.2 Future Work

Future experiments are anticipated to resolve these issues. Hollow cylindrical targets of various thicknesses will be irradiated to further study yield as a function of thickness. The results may demonstrate that an optimal thickness is too small for practical manufacturing (e.g., less than 0.5 mm), but a production-scale target should be able to be identified based on the results of this work to limit the amount of target material that is essentially wasted due to low production in the central part of a target. Another option to be pursued is the design of a wire or similar geometry (such as by drilling thin holes in a material in which metallic tungsten powder can be inserted) that could minimize target depth.

To assess the impact of temperature, the experiments mentioned above will be irradiated bare and inside synthetic quartz ampoules. The targets in the quartz ampoules will experience greater temperatures than the bare targets and any difference in production yields will be due to the increased temperatures.

Cross section measurements will be made in the hydraulic tube facility to determine values for the questionable ^{187}W thermal cross section and resonance integral. This will require resolution of the concern regarding the possibility of cadmium melting, but in light of prior cadmium irradiations in the hydraulic tube, approval should be obtainable.

Appendix A Gamma Ray Spectrometer Efficiencies

The Nuclear Medicine Group gamma ray detector in ORNL building 4701 was recalibrated August 11, 2003 to ensure that calibration problems were not contributing to discrepancies between isotope production calculations and actual production yields. Sources with a variety of radionuclides were used to assure adequate calibration over a wide range of energy:

Table A.1 Gamma Ray Spectrometer Calibration Sources

Source	Radionuclides	Manufacturer
SRM 4275C-78	^{154}Eu, ^{155}Eu, ^{125}Sb	National Institute of Standards and Technology, Gaithersburg, MD
1Q453	^{241}Am	Amersham plc, Buckinghamshire, UK
1Q859	^{241}Am	Amersham plc, Buckinghamshire, UK
1R416	^{133}Ba	Amersham plc, Buckinghamshire, UK
1R792	^{133}Ba	Amersham plc, Buckinghamshire, UK
SRS 62615-198	^{109}Cd	Analytics, Inc., Atlanta, GA
SRS 62616-198	^{57}Co	Analytics, Inc., Atlanta, GA

All spectra for Sections 3 and 4 were acquired after this calibration.

Detector efficiencies referenced in Sections 3 and 4 were obtained from the GENIE2K software (Canberra Industries, Inc., Meriden, CT) used with this detector. Efficiencies for tungsten and flux monitor gamma rays used for analysis are presented in Table A.2 (shelf numbers indicate the distance between the source and the detector in cm).

Table A.2 Gamma Ray Spectrometer Efficiencies

Energy (keV)	Isotope	Efficiency			
		Shelf 5	Shelf 10	Shelf 30	Shelf 60
134.25	^{187}W	2.118×10^{-2}	7.737×10^{-3}	1.096×10^{-3}	3.407×10^{-4}
155.04	^{188}Re	1.194×10^{-2}	7.043×10^{-3}	1.014×10^{-3}	3.131×10^{-4}
290.67	^{188}W	1.074×10^{-2}	4.135×10^{-3}	6.492×10^{-4}	1.925×10^{-4}
411.09	^{198}Au	7.459×10^{-3}	2.928×10^{-3}	4.737×10^{-4}	1.797×10^{-4}
477.99	^{188}Re	6.380×10^{-3}	2.515×10^{-3}	4.089×10^{-4}	1.193×10^{-4}
479.55	^{187}W	6.367×10^{-3}	2.510×10^{-3}	4.080×10^{-4}	1.191×10^{-4}
632.98	^{188}Re	4.827×10^{-3}	1.905×10^{-3}	3.081×10^{-4}	9.029×10^{-5}
656.62	^{110m}Ag	4.659×10^{-3}	1.839×10^{-3}	2.967×10^{-4}	8.707×10^{-5}
685.73	^{187}W	4.447×10^{-3}	1.766×10^{-3}	2.842×10^{-4}	8.354×10^{-5}
1173.23	^{60}Co	2.834×10^{-3}	1.114×10^{-3}	1.740×10^{-4}	5.230×10^{-5}
1332.49	^{60}Co	2.565×10^{-3}	1.015×10^{-3}	1.592×10^{-4}	4.789×10^{-5}

Appendix B Gamma Ray Self-Absorption Factors

Gamma ray self-absorption can be significant, particularly in the analysis of thick samples. To account for gamma ray self-absorption, correction factors were derived for all samples analyzed.

B.1 Linear Attenuation

Linear attenuation of gamma rays emitted by sources deposited on foils can be represented one-dimensionally by [Lamarsh 1993; Tsoulfanidis 1995]:

$$I = I_0 e^{-\frac{\mu}{\rho}t} \tag{B.1}$$

where I_0 is the un-attenuated gamma ray intensity, μ/ρ is the mass attenuation coefficient ($cm^2\ g^{-1}$) of the material through which the gamma rays travel, and t is the mass thickness ($g\ cm^{-2}$) of the material. This model assumes a mono-directional beam with no absorption in the source.

This approach is a good approximation of gamma ray attenuation for tungsten deposited on aluminum foil for cross section measurements in Section 3.4.2 and tungsten, gold and silver deposited on aluminum foil for cross section measurements in Section 3.4.3 (when these samples were counted, there was one layer of aluminum foil between the sample and the detector). Attenuation factors (the exponential term above) for use in Sections

3.4.2 and 3.4.3 are derived in Table B.1. These factors are used to correct the observed source strength using the relation:

$$S_{\text{actual}} = \frac{S_{\text{observed}}}{e^{-\frac{\mu}{\rho}t}} \tag{B.2}$$

Table B.1 Aluminum Foil Gamma Ray Attenuation Factors

	Energy (keV)	Isotope	Mass Attenuation Coefficient, μ/ρ [a] ($cm^2\ g^{-1}$)	Attenuation Factor, $e^{-t(\mu/\rho)}$
$\rho_{Al} = 2.6989\ g\ cm^{-3}$ [MatWeb 2003]				
Section 3.4.2				
foil thickness, $T = 0.01$ cm mass thickness, $t = T\rho_{Al} = (0.01\ cm)(2.6989\ g\ cm^{-3}) = 0.026989\ g\ cm^{-2}$				
	134.25	^{187}W	0.1481	0.9960
	155.04	^{188}Re	0.1362	0.9963
	479.55	^{187}W	0.08615	0.9977
	685.73	^{187}W	0.07390	0.9980
Section 3.4.3				
foil thickness, $T = 0.0025$ cm mass thickness, $t = T\rho_{Al} = (0.0025\ cm)(2.6989\ g\ cm^{-3}) = 0.0067473\ g\ cm^{-2}$				
	134.25	^{187}W	0.1481	0.9990
	155.04	^{188}Re	0.1362	0.9991
	411.09	^{198}Au	0.08256	0.9994
	479.55	^{187}W	0.08615	0.9994
	656.62	^{110m}Ag	0.07528	0.9995
	685.73	^{187}W	0.07390	0.9995

[a] linear interpolation of NIST [2003] data

B.2 Solid Slab Source

As sample size increases, gamma ray self-absorption becomes more significant. Since the source is distributed throughout the sample, a linear attenuation model does not adequately represent self-absorption (i.e., gamma rays do not traverse the entire thickness of the sample, they originate throughout the sample). A one-dimensional approach [Tsoulfanidis 1995] provides an accurate approximation of self-absorption in samples with slab geometry such as the tungsten foils used in self-shielding experiments (Chapter 5). Figure B.1 depicts the geometry of this approach.

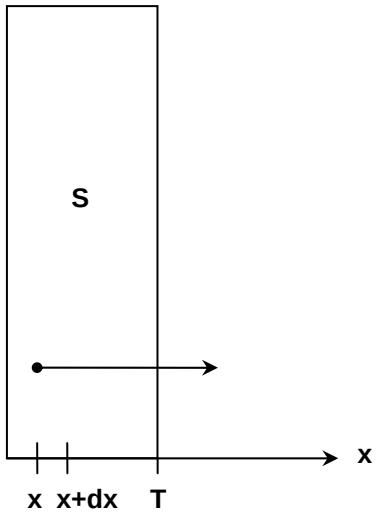

Figure B.1 One-Dimensional Slab Geometry Model for Gamma Ray Self-Absorption

The probability of escape of a gamma ray from the slab source shown in Figure 3.1 is $e^{-\mu(T-x)}$, where μ is the attenuation coefficient of the material in which the source is uniformly distributed [Tsoulfanidis 1995]. Assuming that the source emits S gamma rays

per second in the positive x-direction, the total number of gamma rays escaping the sample is:

$$\begin{aligned}\text{total } \gamma\text{ - ray escape} &= \int_0^T \frac{dx}{T} S e^{-\mu(T-x)} \\ &= \frac{S}{T}\int_0^T e^{\mu x-\mu T}\,dx \\ &= \frac{S}{Te^{\mu T}}\int_0^T e^{\mu x}\,dx \\ &= \frac{S}{\mu T e^{\mu T}} e^{\mu x}\Big|_0^T \\ &= \frac{S}{\mu T e^{\mu T}} e^{\mu T} - \frac{S}{\mu T e^{\mu T}} \\ &= \frac{S}{\mu T}\left(1-e^{\mu T}\right)\end{aligned} \tag{B.3}$$

A self-absorption factor, f_a, can be defined as [*ibid*]:

$$\begin{aligned}f_a &= \frac{\text{number of } \gamma\text{ - rays leaving source with self - absorption}}{\text{number of } \gamma\text{ - rays leaving source without self - absorption}} \\ &= \frac{\frac{S}{\mu T}\left(1-e^{-\mu T}\right)}{S} \\ &= \frac{1}{\mu T}\left(1-e^{-\mu T}\right)\end{aligned} \tag{B.4}$$

This equation can also be written in terms of mass attenuation coefficients, μ/ρ, and mass thicknesses, t (g cm^{-2}):

$$f_a = \frac{1}{\frac{\mu}{\rho}t}\left(1-e^{-\frac{\mu}{\rho}t}\right) \tag{B.5}$$

where $T = t/\rho$ and ρ = density (g cm^{-3}).

Self-absorption factors for the tungsten foil experiments (Chapter 5) are derived in Table B.2. These factors are used to correct the observed countrates according to the relation:

$$S_{\text{actual}} = \frac{S_{\text{observed}}}{f_a} \tag{B.6}$$

Table B.2 Tungsten Foil Gamma Ray Self-Absorption Factors

	Energy (keV)	Isotope	Mass Attenuation Coefficient, μ/ρ [a] ($cm^2\ g^{-1}$)	Self-Absorption Factor, f_a
ρ_W = 19.3 g cm^{-3} [MatWeb 2003]				
Chapter 5				
foil thickness, T = 0.01 cm mass thickness, $t = T\rho_W$ = (0.01 cm)(19.3 g cm^{-3}) = 0.193 g cm^{-2}				
	134.25	^{187}W	2.08	0.824
	155.04	^{188}Re	1.45	0.872
	479.55	^{187}W	0.143	0.986
	685.73	^{187}W	0.0926	0.991
Chapter 5				
foil thickness, T = 0.025 cm mass thickness, $t = T\rho_W$ = (0.025 cm)(19.3 g cm^{-3}) = 0.483 g cm^{-2}				
	134.25	^{187}W	2.08	0.631
	155.04	^{188}Re	1.45	0.719
	479.55	^{187}W	0.143	0.966
	685.73	^{187}W	0.0926	0.978

[a] polynomial fit of NIST [2003] data

In Table B.2, mass attenuation coefficients were derived by using SigmaPlot (SPSS Inc., Chicago, IL) to fit NIST [2003] data to an inverse third order polynomial:

$$y = y_0 + \left(\frac{a}{x}\right) + \left(\frac{b}{x^2}\right) + \left(\frac{c}{x^3}\right) \tag{B.7}$$

$$y_0 = 5.334 \times 10^{-2}$$

$$a = -1.956$$

$$b = 1.564 \times 10^{4}$$

$$c = 2.841 \times 10^{6}$$

where x is the photon energy and y is the mass attenuation coefficient. Figure B.2 shows the NIST data (data points) and a plot of Equation B.7 (solid curve).

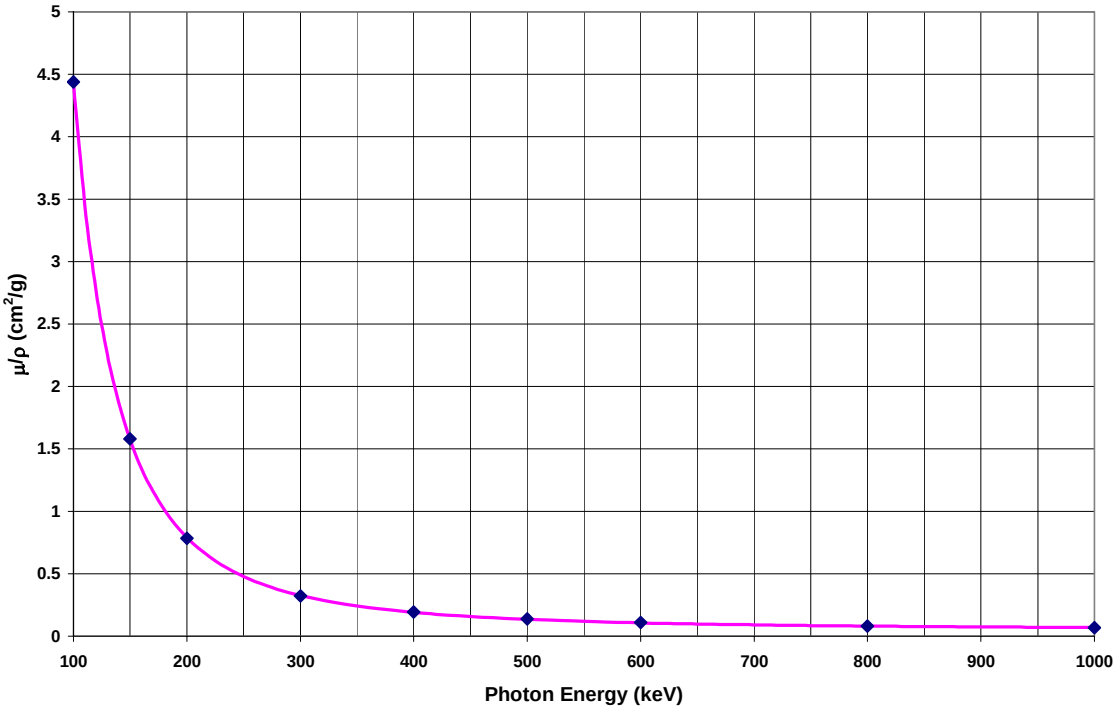

Figure B.2 Tungsten Mass Attenuation Coefficient

B.3 Solid Cylinder Source

Cylindrical source geometries are more complicated than the slab geometry addressed in Section B.2 because the "thickness" of the source is not constant.

Some attempts have been made to provide useful methods for deriving self-absorption factors. Tian *et al*. [2000] develop a method using two gamma rays; however, the method makes the assumption that detector efficiency is independent of energy. Given that assumption, the method would only be reliable to derive self-absorption factors at energies for which there are two distinct gamma rays with similar energies. Dickens' [1972] method applies to large sources with a large source-to-detector distance and works well for energies greater than 500 keV; for lower energies, Monte Carlo calculations must be employed. Rzama *et al*. [1994] use Monte Carlo calculations that simulate experimental conditions to derive self-absorption coefficients.

A simpler approach, based on the method developed in Section B.2, will be used to derive gamma ray self-absorption factors for cylindrical geometries in this work. Solid cylindrical geometries are encountered in the analysis of flux monitor wires (Chapter 3) and the central cylinder in the tungsten cylinder self-shielding experiment (Chapter 5).

A method for calculating gamma ray self-absorption in samples with a solid cylindrical geometry would be to extend the slab geometry approach by considering the cylinder to be an infinite stack of slabs and integrating the one-dimensional self-absorption equation (Section B.2) from the bottom of the stack to the top (see Figure B.3). As in Section B.2, assuming that the source emits S gamma rays per second in the positive x-direction, the total number of gamma rays escaping the sample is:

$$\text{total } \gamma\text{ - ray escape} = 2\int_{-\sqrt{b^2-y^2}}^{\sqrt{b^2-y^2}} \int_0^b \frac{dx}{2\sqrt{b^2-y^2}} \frac{S}{2} e^{-\mu\left(\sqrt{b^2-y^2}-x\right)} dy \qquad \text{(B.8)}$$

Unfortunately, evaluation of Equation B.8 leads to an integral for which there is no analytic solution. Thus, an exact equation for gamma ray self-absorption for cylindrical geometry cannot be derived as in Section B.2.

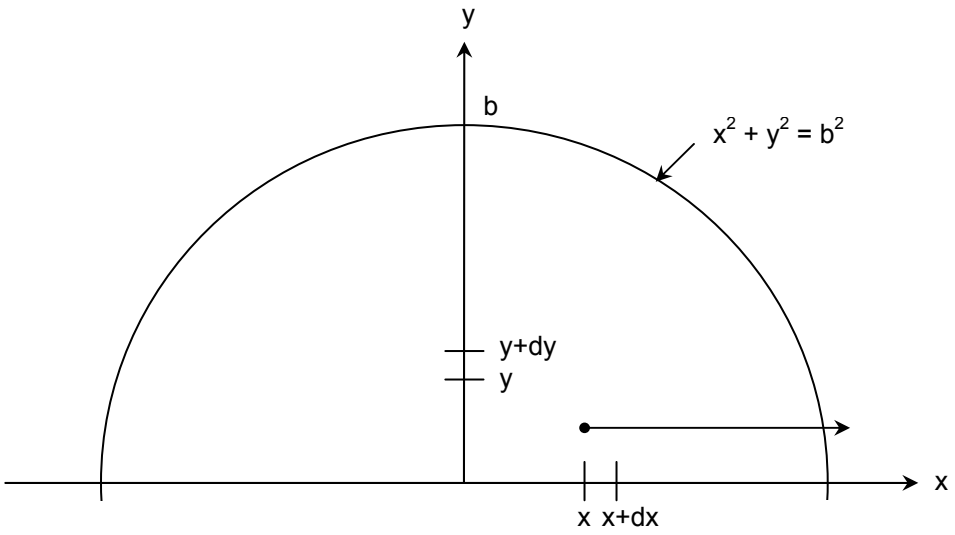

Figure B.3 Model for Calculating Cylindrical Geometry Gamma Ray Self-Absorption Factors

A solution to this problem is to approximate the infinite stack with a finite number of slabs, evaluating the probability of escape from each slab, and calculating a weighted average probability of escape. Figure B.4 depicts the model used for this approach, with the gray area representing a typical slab of a solid cylindrical source emitting *S* gamma rays per second in the positive *x*-direction (the direction of the detector). An Excel© spreadsheet was used to perform the calculations, with 200 slabs approximating the infinite stack for each cylinder.

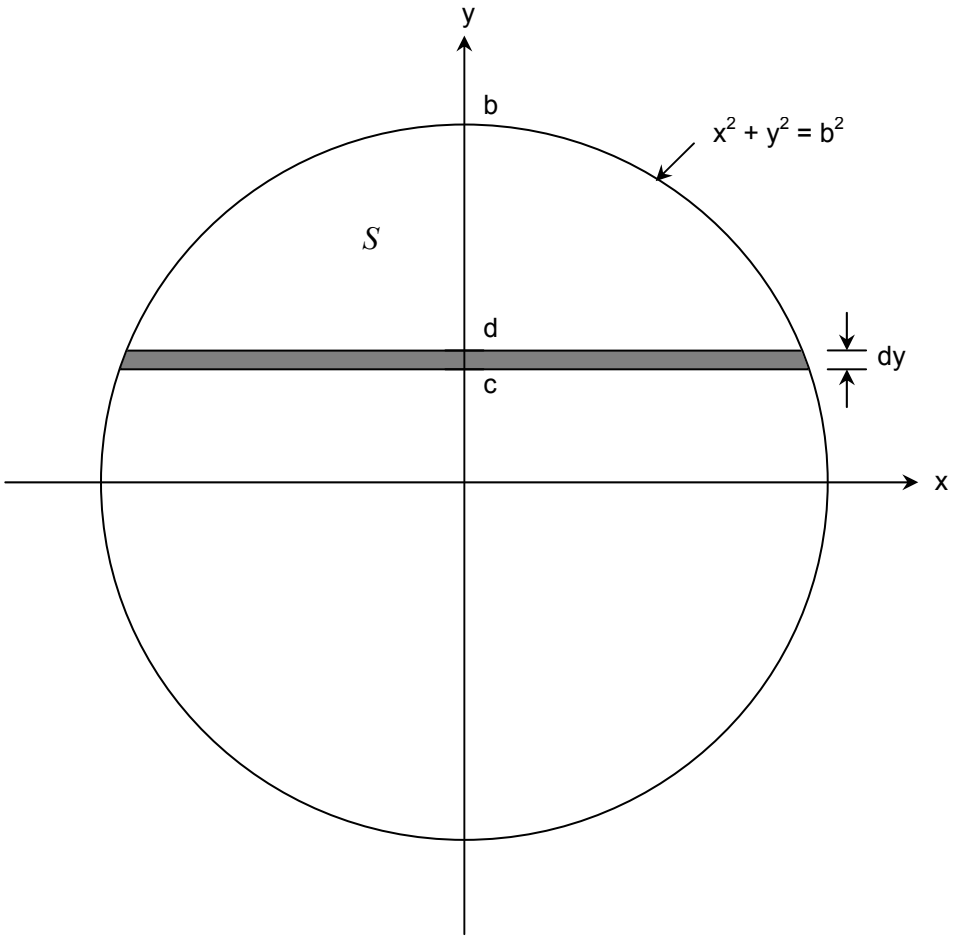

Figure B.4 Gamma Ray Self-Absorption – Differential Slab in Solid Cylinder

The area of each slab is:

$$
\begin{aligned}
A &= 2\int_0^{\sqrt{b^2-y^2}} \int_c^d dxdy \qquad \text{(B.9)} \\
&= 2\int_c^d xdy \Big|_0^{\sqrt{b^2-y^2}} \\
&= 2\int_c^d \sqrt{b^2-y^2}\,dy \\
&= \left(y\sqrt{b^2-y^2} + b^2 \sin^{-1}\frac{y}{b} \right)\Big|_c^d \\
&= \left(d\sqrt{b^2-d^2} + b^2 \sin^{-1}\frac{d}{b} \right) - \left(c\sqrt{b^2-c^2} + b^2 \sin^{-1}\frac{c}{b} \right) \\
&= d\sqrt{b^2-d^2} - c\sqrt{b^2-c^2} + b^2\left(\sin^{-1}\frac{d}{b} - \sin^{-1}\frac{c}{b} \right)
\end{aligned}
$$

The length of each slab is:

$$L = \frac{A}{dy} \tag{B.10}$$

The source strength in each slab is:

$$S = \frac{A}{A_{total}} \tag{B.11}$$

The number of gamma rays escaping from each slab in the *x*-direction is:

$$\gamma \text{ - ray escape} = \frac{S}{\frac{\mu}{\rho} L\rho}\left(1 - e^{-\frac{\mu}{\rho}L\rho}\right) \tag{B.12}$$

Spreadsheets calculated gamma ray escape from each slab and summed the results to produce a total self-absorption factor, f_a, as in Section B.2:

$$f_a = \frac{1}{\frac{\mu}{\rho} L\rho}\left(1 - e^{-\frac{\mu}{\rho}L\rho}\right) \tag{B.13}$$

Self-absorption factors for solid cylindrical geometries are derived in Table B.3. As identified in Section B.2, these factors are used to correct the observed countrates according to Equation B.6.

In the case of the flux monitor wires, self-absorption is assumed to occur in the aluminum and not the monitor material which is present in very dilute quantities.

Table B.3 Gamma Ray Self-Absorption Factors for Solid Cylinders

	Energy (keV)	Isotope	Mass Attenuation Coefficient, μ/ρ [a] ($cm^2\ g^{-1}$)	Self-Absorption Factor, f_a
1.2 mm Tungsten Cylinder (Chapter 5)				
ρ_W = 19.3 g cm^{-3} [MatWeb 2003] radius, b = 0.06 cm				
	134.25	^{187}W	2.08	0.251
	155.04	^{188}Re	1.45	0.340
	290.67	^{188}W	0.347	0.727
	477.99	^{188}Re	0.144	0.871
	479.55	^{187}W	0.143	0.872
	632.98	^{188}Re	0.101	0.907
	685.73	^{187}W	0.0926	0.914
Au Flux Monitor (Sections 3.4.2 and 3.4.3)				
ρ_{Al} = 2.6989 g cm^{-3} [MatWeb 2003] radius, b = 0.0127 cm				
	411.09	^{198}Au	0.08256	0.9976
Ag Flux Monitor (Sections 3.4.2 and 3.4.3)				
ρ_{Al} = 2.6989 g cm^{-3} [MatWeb 2003] radius, b = 0.0254 cm				
	656.62	^{110m}Ag	0.07528	0.9956
Co1 Flux Monitor (Section 3.4.2)				
ρ_{Al} = 2.6989 g cm^{-3} [MatWeb 2003] radius, b = 0.0375 cm				
	1173.23	^{60}Co	0.05699	0.9950
	1332.49	^{60}Co	0.05337	0.9953
Co2 Flux Monitor (Section 3.4.2)				
ρ_{Al} = 2.6989 g cm^{-3} [MatWeb 2003] radius, b = 0.025 cm				
	1173.23	^{60}Co	0.05699	0.9967
	1332.49	^{60}Co	0.05337	0.9969

[a] NIST [2003]: polynomial fit of data for W, linear interpolation of data for Al

B.4 Hollow Cylinder Source

Gamma ray self-absorption factors for hollow cylinders were calculated using a method similar to that for solid cylinders, with a modification to account for the central void. Figure B.5 depicts the model used for this approach, with the gray area representing a typical slab of a solid cylindrical source emitting *S* gamma rays per second in the positive *x*-direction (the direction of the detector). As in Section B.3, a spreadsheet was used to perform the calculations, with at least 240 slabs approximating the infinite stack for each cylinder.

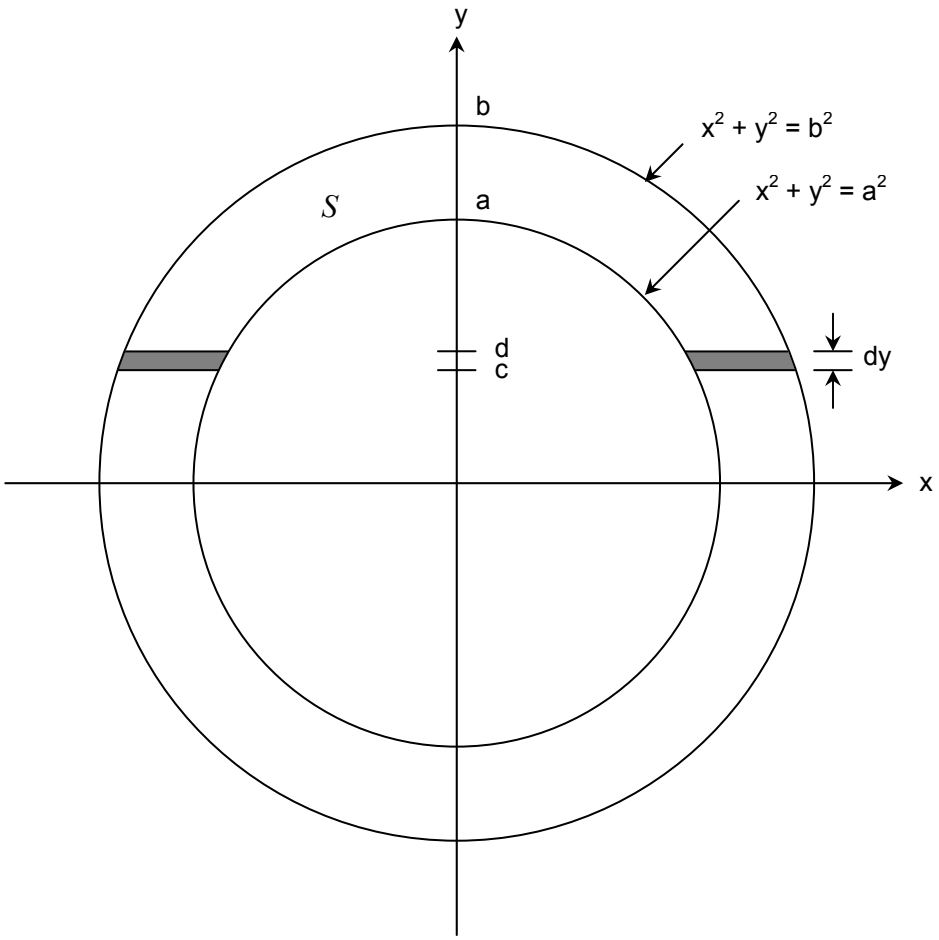

Figure B.5 Gamma Ray Self-Absorption – Differential Slab in Hollow Cylinder

In this model, the area of slabs for which c > a or d < -a is calculated using the formula for A derived in Section B.3 since in these regions the slabs do not have a central void.

The area of each slab where d ≤ a and c ≥ -a is:

$$
\begin{aligned}
A &= 2\int_{\sqrt{a^2-y^2}}^{\sqrt{b^2-y^2}}\int_c^d dxdy \\
&= 2\int_c^d xdy\Bigg|_{\sqrt{a^2-y^2}}^{\sqrt{b^2-y^2}} \\
&= 2\int_c^d \sqrt{b^2-y^2}-\sqrt{a^2-y^2}\,dy \\
&= \left(y\sqrt{b^2-y^2}+b^2\sin^{-1}\frac{y}{b}\right)-\left(y\sqrt{a^2-y^2}+a^2\sin^{-1}\frac{y}{a}\right)\Bigg|_c^d \\
&= \left(d\sqrt{b^2-d^2}+b^2\sin^{-1}\frac{d}{b}\right)-\left(d\sqrt{a^2-d^2}+a^2\sin^{-1}\frac{d}{a}\right) \\
&\quad -\left(c\sqrt{b^2-c^2}+b^2\sin^{-1}\frac{c}{b}\right)+\left(c\sqrt{a^2-c^2}+a^2\sin^{-1}\frac{c}{a}\right) \\
&= d\left(\sqrt{b^2-d^2}-\sqrt{a^2-d^2}\right)-c\left(\sqrt{b^2-c^2}-\sqrt{a^2-c^2}\right) \\
&\quad +b^2\left(\sin^{-1}\frac{d}{b}-\sin^{-1}\frac{c}{b}\right)+a^2\left(\sin^{-1}\frac{c}{a}-\sin^{-1}\frac{d}{a}\right)
\end{aligned}
\tag{B.14}
$$

Equations for slab length (L), source strength (S), γ-ray escape and total self-absorption factor (f_a) are the same as presented in Section B.3 (Equations B.10 – B.13).

Gamma ray self-absorption factors for the hollow tungsten cylinders used for the cylindrical self-shielding experiment in Chapter 5 are summarized in Table B.4. As identified in Section B.2, these factors are used to correct the countrates observed in the tungsten cylinders using Equation B.6.

Table B.4 Gamma Ray Self-Absorption Factors for Hollow Cylinders

ρ_W = 19.3 g cm^{-3} [MatWeb 2003]

Cylinder	a (cm)	b (cm)
2.4 mm	0.07	0.12
3.6 mm	0.13	0.18
4.8 mm	0.19	0.24
6.0 mm	0.25	0.30

Energy (keV)	Isotope	Mass Attenuation Coefficient, μ/ρ [a] (cm^2 g^{-1})	Self-Absorption Factor, f_a 2.4 mm	3.6 mm	4.8 mm	6.0 mm
134.25	^{187}W	2.08	0.197	0.182	0.175	0.171
155.04	^{188}Re	1.45	0.273	0.254	0.245	0.239
290.67	^{188}W	0.347	0.665	0.640	0.625	0.616
477.99	^{188}Re	0.144	0.836	0.820	0.810	0.803
479.55	^{187}W	0.143	0.837	0.821	0.812	0.805
632.98	^{188}Re	0.101	0.881	0.869	0.861	0.855
685.73	^{187}W	0.0926	0.890	0.878	0.871	0.866

[a] polynomial fit of NIST [2003] data

Obviously, this method of deriving gamma ray self-absorption factors for solid and hollow cylinders approximates actual gamma ray self-absorption with increasing accuracy as the distance between the source and the detector increases because gamma rays emitted from the source will increasingly only interact with the detector if they travel with decreasing deviation from the *x*-direction (i.e., the solid angle from a point in the source to the detector decreases as the distance between the source and the detector increases). The reliability of this method is affirmed by the very good agreement between activities calculated (Chapter 5) using different gamma rays with self-absorption factors differing by as much as a factor of 5.1. For example, ^{188}Re activities determined from the 155 keV and 633 keV gamma rays for each cylinder were within 3% of each

other, even though the self-absorption factors differ by a factor of as much as 3.6 (in the 6.0 mm cylinder f_a is 0.855 at 633 keV and 0.239 at 155 keV).

Appendix C Cross Section Measurement Data

C.1 Cross Section Experiment #1

A summary of gamma ray spectroscopy data for all tungsten samples is provided in Table C.1. Tungsten samples were recovered from three pneumatic tube irradiations, which are identified as PT1, PT2 and PT3 (the tungsten sample in PT4 was not recovered). PT1 and PT2 both contained two tungsten samples, which are identified as W1 and W2. Five analyses were obtained for each sample. Total Counts and Absolute Uncertainty data were taken from the output of each analysis. The data in this table was used to create input files for the CLSQ [Cumming 1962] calculations of sample countrates at the end of bombardment. In this, and subsequent analyses, data points were not used in calculations if they had large dead times or uncertainties or if they were rejected by CLSQ due to excessive variation from a fit of all data points. For error propagation, an error of the mean, $\bar{\sigma}/\bar{x}$, was calculated using total counts and uncertainties for all non-rejected data points, n. The error of the mean was calculated as:

$$\frac{\bar{\sigma}}{\bar{x}} = \frac{100\sqrt{\sum\left(\frac{\sigma_i}{x_i}\right)^2}}{n} \qquad \text{(C.1)}$$

Countrates at EOB and their associated uncertainties calculated by CLSQ for each of the three gamma rays for each tungsten sample are given in Table C.2. The error of the

mean, $\overline{\sigma}/\overline{x}$, was carried forward from Table C.1. Activities at end of bombardment in counts per unit time, $\boldsymbol{A^0}$, were converted to disintegrations per unit time, A^0, by dividing by gamma ray intensity, I_γ, detector efficiency, ε, and the self-absorption factor, f_a:

$$A^0 = \frac{\boldsymbol{A^0}}{I_\gamma \varepsilon f_a} \tag{C.2}$$

Uncertainty in A^0 was calculated using the uncertainties in $\boldsymbol{A^0}$ (the greater of the CLSQ uncertainty or error of the mean was selected to produce a conservative value for uncertainty; in each case, the error of the mean was greater than the CLSQ uncertainty), gamma ray intensity, and detector efficiency (5%) using the following equation [Bevington and Robinson 1992]:

$$\sigma_{A^0} = A^0 \sqrt{\left(\frac{\overline{\sigma}/\overline{x}}{100}\right)^2 + \left(\frac{\sigma_{I_\gamma}}{I_\gamma}\right)^2 + (\sigma_\varepsilon)^2} \tag{C.3}$$

Activities derived from the three gamma rays for each sample were averaged to produce a value for the activity of each sample (Table C.3). As in Table C.1, an error of the mean, $\overline{\sigma_{A^0}}$, was calculated using the activities and uncertainties for each of the three gamma rays. Standard deviation from the mean [Bevington and Robinson 1992], σ, was also calculated and the greater of the two uncertainties was used in error propagation.

Data from the four tungsten samples irradiated without cadmium covers were combined to produce a single value for unshielded tungsten activity (Table C.4). As in Table C.3, $\overline{\sigma_{A^0}}$ and σ were calculated. Finally, A^0 and its associated uncertainty were expressed in terms of activity per unit mass for both the shielded and unshielded tungsten samples.

Table C.1 Cross Section Experiment #1 Gamma Ray Spectroscopy Data for Tungsten

Sample	Shelf (cm)	Count Time (s)	Dead Time (%)	Time Since EOB (d:h:m)	134 keV γ-ray			479 keV γ-ray			685 keV γ-ray		
					Total Counts	Absolute Uncert.	Rel.Unc. (%)	Total Counts	Absolute Uncert.	Rel.Unc. (%)	Total Counts	Absolute Uncert.	Rel.Unc. (%)
PT1 W1	30	300	10.3	1:15:19	2.24×10^4	2.61×10^2	1.2 [a]	2.06×10^4	2.07×10^2	1.0 [a]	1.82×10^4	1.62×10^2	0.9 [a]
	30	600	4.5	2:13:48	2.46×10^4	2.47×10^2	1.0	2.24×10^4	2.06×10^2	0.9	1.91×10^4	1.57×10^2	0.8
	30	900	3.2	2:23:27	2.76×10^4	2.34×10^2	0.8	2.49×10^4	2.14×10^2	0.9	2.17×10^4	1.72×10^2	0.8
	30	900	2.0	3:13:05	1.92×10^4	2.13×10^2	1.1	1.68×10^4	1.80×10^2	1.1	1.49×10^4	1.36×10^2	0.9
	30	900	1.5	3:21:06	1.46×10^4	1.51×10^2	1.0	1.33×10^4	1.53×10^2	1.1	1.19×10^4	1.20×10^2	1.0
$\bar{\sigma}/\bar{x}$							0.50			0.50			0.44
PT1 W2	30	300	10.3	1:15:28	2.25×10^4	2.37×10^2	1.1 [a]	2.10×10^4	2.09×10^2	1.0 [a]	1.81×10^4	1.59×10^2	0.9 [a]
	30	600	4.5	2:14:01	2.44×10^4	2.23×10^2	0.9	2.20×10^4	2.04×10^2	0.9	1.93×10^4	1.65×10^2	0.9
	30	900	3.2	2:23:52	2.79×10^4	2.68×10^2	1.0	2.47×10^4	2.23×10^2	0.9	2.19×10^4	1.74×10^2	0.8
	30	900	2.0	3:13:22	1.89×10^4	1.83×10^2	1.0	1.70×10^4	1.60×10^2	0.9	1.48×10^4	1.37×10^2	0.9
	30	900	1.5	3:21:23	1.49×10^4	1.83×10^2	1.2	1.33×10^4	1.56×10^2	1.2	1.16×10^4	1.15×10^2	1.0
$\bar{\sigma}/\bar{x}$							0.51			0.50			0.45
PT2 W1	30	300	10.6	1:14:39	2.31×10^4	2.47×10^2	1.1 [a]	2.09×10^4	2.02×10^2	1.0 [a]	1.88×10^4	1.80×10^2	1.0 [a]
	30	600	4.6	2:13:16	2.49×10^4	2.17×10^2	0.9	2.21×10^4	1.87×10^2	0.8	1.95×10^4	1.66×10^2	0.9
	30	600	3.2	2:23:14	1.88×10^4	2.05×10^2	1.1	1.66×10^4	1.53×10^2	0.9	1.46×10^4	1.38×10^2	0.9
	30	900	2.0	3:12:42	1.89×10^4	1.78×10^2	0.9	1.68×10^4	1.68×10^2	1.0	1.50×10^4	1.39×10^2	0.9
	30	900	1.5	3:20:43	1.49×10^4	1.63×10^2	1.1	1.37×10^4	1.37×10^2	1.0	1.18×10^4	1.15×10^2	1.0
$\bar{\sigma}/\bar{x}$							0.50			0.47			0.46
PT2 W2	30	300	10.6	1:14:46	2.35×10^4	2.66×10^2	1.1 [a]	2.08×10^4	2.07×10^2	1.0 [a]	1.84×10^4	1.73×10^2	0.9 [a]
	30	600	4.6	2:13:28	2.45×10^4	2.56×10^2	1.0	2.23×10^4	2.23×10^2	1.0	1.94×10^4	1.68×10^2	0.9
	30	600	3.2	2:23:25	1.84×10^4	2.11×10^2	1.1	1.68×10^4	1.89×10^2	1.1	1.48×10^4	1.42×10^2	1.0
	30	900	2.0	3:12:58	1.89×10^4	1.77×10^2	0.9	1.68×10^4	1.63×10^2	1.0	1.48×10^4	1.32×10^2	0.9
	30	900	1.5	3:21:00	1.54×10^4	1.72×10^2	1.1	1.38×10^4	1.56×10^2	1.1	1.19×10^4	1.17×10^2	1.0
$\bar{\sigma}/\bar{x}$							0.53			0.53			0.46

Sample	Shelf (cm)	Count Time (s)	Dead Time (%)	Time Since EOB (d:h:m)	134 keV γ-ray			479 keV γ-ray			685 keV γ-ray		
					Total Counts	Absolute Uncert.	Rel.Unc. (%)	Total Counts	Absolute Uncert.	Rel.Unc. (%)	Total Counts	Absolute Uncert.	Rel.Unc. (%)
PT3 W	30	900	1.8	1:15:30	1.65×10^4	2.00×10^2	1.2 [a]	1.48×10^4	1.52×10^2	1.0 [a]	1.32×10^4	1.28×10^2	1.0 [a]
	30	1800	0.8	2:14:12	1.73×10^4	1.74×10^2	1.0	1.54×10^4	1.63×10^2	1.1	1.34×10^4	1.25×10^2	0.9
	30	2700	0.6	3:0:07	1.93×10^4	1.89×10^2	1.0	1.72×10^4	1.57×10^2	0.9	1.49×10^4	1.29×10^2	0.9
	30	3600	0.4	3:13:45	1.70×10^4	2.05×10^2	1.2	1.53×10^4	1.59×10^2	1.0	1.36×10^4	1.22×10^2	0.9
	30	5400	0.3	3:21:46	2.01×10^4	2.03×10^2	1.0	1.81×10^4	1.58×10^2	0.9	1.58×10^4	1.35×10^2	0.9
$\overline{\sigma}/\overline{x}$							0.53			0.49			0.44

[a] data point not used in calculations of A^0 and uncertainty

Table C.2 Cross Section Experiment #1 Tungsten Sample Activities for Each Gamma Ray

γ-ray/ Sample	Count Rate at EOB			Absolute Gamma Intensity [c]	Absolute Detector Efficiency [d]	Self-Absorption Factor [e]	A^0 (Bq)	σ_{A^0} (Bq)
	Counts per Second [a]	CLSQ Rel.Unc.[a] (%)	$\overline{\sigma}/\overline{x}$ Rel.Unc.[b] (%)					
134 keV								
PT1 W1	2.51×10^2	0.34	0.50	0.0885 ± 0.00164	1.10×10^{-3}	0.9960	2.59×10^6	1.39×10^5
PT1 W2	2.53×10^2	0.34	0.51	0.0885 ± 0.00164	1.10×10^{-3}	0.9960	2.62×10^6	1.40×10^5
PT2 W1	2.50×10^2	0.36	0.50	0.0885 ± 0.00164	1.10×10^{-3}	0.9960	2.59×10^6	1.39×10^5
PT2 W2	2.51×10^2	0.36	0.53	0.0885 ± 0.00164	1.10×10^{-3}	0.9960	2.60×10^6	1.39×10^5
PT3 W	5.92×10^1	0.37	0.53	0.0885 ± 0.00164	1.10×10^{-3}	0.9960	6.12×10^5	3.28×10^4
479 keV								
PT1 W1	2.26×10^2	0.36	0.50	0.218 ± 0.00437	4.08×10^{-4}	0.9977	2.54×10^6	1.37×10^5
PT1 W2	2.27×10^2	0.36	0.50	0.218 ± 0.00437	4.08×10^{-4}	0.9977	2.55×10^6	1.38×10^5
PT2 W1	2.23×10^2	0.38	0.47	0.218 ± 0.00437	4.08×10^{-4}	0.9977	2.52×10^6	1.36×10^5
PT2 W2	2.27×10^2	0.38	0.53	0.218 ± 0.00437	4.08×10^{-4}	0.9977	2.55×10^6	1.38×10^5
PT3 W	5.30×10^1	0.39	0.49	0.218 ± 0.00437	4.08×10^{-4}	0.9977	5.97×10^5	3.23×10^4

γ-ray/ Sample	Count Rate at EOB: Counts per Second [a]	CLSQ Rel.Unc.[a] (%)	$\overline{\sigma}/\overline{x}$ Rel.Unc.[b] (%)	Absolute Gamma Intensity [c]	Absolute Detector Efficiency [d]	Self-Absorption Factor [e]	A^0 (Bq)	σ_{A^0} (Bq)
685 keV								
PT1 W1	1.97×10^2	0.38	0.44	0.273 ± 0.00601	2.84×10^{-4}	0.9980	2.54×10^6	1.39×10^5
PT1 W2	1.99×10^2	0.38	0.45	0.273 ± 0.00601	2.84×10^{-4}	0.9980	2.57×10^6	1.41×10^5
PT2 W1	1.97×10^2	0.41	0.46	0.273 ± 0.00601	2.84×10^{-4}	0.9980	2.54×10^6	1.39×10^5
PT2 W2	1.98×10^2	0.41	0.46	0.273 ± 0.00601	2.84×10^{-4}	0.9980	2.56×10^6	1.40×10^5
PT3 W	4.63×10^1	0.42	0.44	0.273 ± 0.00601	2.84×10^{-4}	0.9980	5.98×10^6	3.28×10^4

[a] CLSQ output
[b] Table C.1
[c] [NNDC 2003]
[d] Table A.2
[e] Table B.1

Table C.3 Cross Section Experiment #1 Tungsten Sample Activities

Sample	Gamma Ray Energy [a]: 134 keV A^0 (Bq)	134 keV σ_{A^0} (Bq)	479 keV A^0 (Bq)	479 keV σ_{A^0} (Bq)	685 keV A^0 (Bq)	685 keV σ_{A^0} (Bq)	$\overline{A^0}$ (Bq)	$\overline{\sigma_{A^0}}$ (Bq)	σ (Bq)
PT1 W1	2.59×10^6	1.39×10^5	2.54×10^6	1.37×10^5	2.54×10^6	1.39×10^5	2.56×10^6	8.00×10^4	2.45×10^4
PT1 W2	2.62×10^6	1.40×10^5	2.55×10^6	1.38×10^5	2.57×10^6	1.41×10^5	2.58×10^6	8.06×10^4	2.92×10^4
PT2 W1	2.59×10^6	1.39×10^5	2.52×10^6	1.36×10^5	2.54×10^6	1.39×10^5	2.55×10^6	7.97×10^4	3.11×10^4
PT2 W2	2.60×10^6	1.39×10^5	2.55×10^6	1.38×10^5	2.56×10^6	1.40×10^5	2.57×10^6	8.03×10^4	1.97×10^4
PT3 W	6.12×10^5	3.28×10^4	5.97×10^5	3.23×10^4	5.98×10^6	3.28×10^4	6.03×10^5	1.89×10^4	6.91×10^3

[a] Table C.2

Table C.4 Cross Section Experiment #1 Tungsten Activities

Sample	Mass (mg)	A^{0} [a] (Bq)	σ_{A^0} [a] (Bq)	$\overline{A^0}$ (Bq)	$\overline{\sigma_{A^0}}$ (Bq)	σ (Bq)	A^0 (Bq mg^{-1})	σ_{A^0} (Bq mg^{-1})
PT1 W1	0.1	2.56×10^6	8.00×10^4	2.57×10^6	4.02×10^4	1.12×10^4	2.57×10^7	4.02×10^5
PT1 W2	0.1	2.58×10^6	8.06×10^4					
PT2 W1	0.1	2.55×10^6	7.97×10^4					
PT2 W2	0.1	2.57×10^6	8.03×10^4					
PT3 W	0.1	6.03×10^5	1.89×10^4				6.03×10^6	1.89×10^5

[a] Table C.3

A summary of gamma ray spectroscopy data for the gold flux monitor wires is provided in Table C.5. Gold flux monitors were recovered from three pneumatic tube irradiations (the gold flux monitor in PT4 was not recovered). Four gamma ray analyses were obtained for each monitor. The data in this table was used to create input files for the CLSQ [Cumming 1962] calculations of sample countrates at EOB. As in the analysis of the tungsten samples, an error of the mean, $\overline{\sigma}/\overline{x}$, was calculated for use in error propagation.

Table C.5 Cross Section Experiment #1 Gamma Ray Spectroscopy Data for Gold

					411 keV γ-ray		
Sample	Shelf (cm)	Count Time (s)	Dead Time (%)	Time Since EOB (d:h:m)	Total Counts	Absolute Uncert.	Rel.Unc. (%)
PT1 Au	30	900	0.39	1:16:31	2.63×10^4	1.64×10^2	0.6
	30	1200	0.23	3:15:16	2.09×10^4	1.46×10^2	0.7
	30	2700	0.10	7:14:22	1.72×10^4	1.34×10^2	0.8
	30	3600	0.06	10:14:30	1.08×10^4	1.06×10^2	1.0
$\overline{\sigma}/\overline{x}$							0.39
PT2 Au	30	600	0.37	1:15:57	1.72×10^4	1.33×10^2	0.8
	30	1200	0.22	3:14:41	2.04×10^4	1.45×10^2	0.7
	30	2700	0.10	7:14:11	1.64×10^4	1.31×10^2	0.8
	30	3600	0.05	10:14:49	9.92×10^3	1.02×10^2	1.0
$\overline{\sigma}/\overline{x}$							0.42
PT3 Au	30	5400	0.21	1:16:38	7.74×10^4	2.84×10^2	0.4
	30	1800	0.13	3:15:36	1.54×10^4	1.25×10^2	0.8
	30	5400	0.06	7:15:53	1.64×10^4	1.31×10^2	0.8
	30	7200	0.04	10:16:21	1.00×10^4	1.04×10^2	1.0
$\overline{\sigma}/\overline{x}$							0.40

Countrates at EOB and their associated uncertainties calculated by CLSQ for the 411 keV ^{198}Au gamma ray for each flux monitor are given in Table C.6. The error of the

Table C.6 Cross Section Experiment #1 Gold Sample Activities

Sample	Count Rate at EOB: Counts per Second [a]	Count Rate at EOB: CLSQ Rel.Unc.[a] (%)	Count Rate at EOB: $\overline{\sigma}/\overline{x}$ Rel.Unc.[b] (%)	Absolute Gamma Intensity [c]	Absolute Detector Efficiency [d]	Self-Absorption Factor [e]	A^0 (Bq)	σ_{A^0} (Bq)
PT1 Au	4.51×10^{1}	0.36	0.39	0.9558 ± 0.0012	4.74×10^{-4}	0.9976	9.98×10^{4}	5.01×10^{3}
PT2 Au	4.32×10^{1}	0.40	0.42	0.9558 ± 0.0012	4.74×10^{-4}	0.9976	9.57×10^{4}	4.80×10^{3}
PT3 Au	2.21×10^{1}	0.35	0.40	0.9558 ± 0.0012	4.74×10^{-4}	0.9976	4.90×10^{4}	2.46×10^{3}

[a] CLSQ output
[b] Table C.1
[c] [NNDC 2003]
[d] Table A.2
[e] Table B.3

Table C.7 Cross Section Experiment #1 Gold Activities

Sample	Mass (mg)	A^0 [a] (Bq mg^{-1})	σ_{A^0} [a] (Bq mg^{-1})	$\overline{A^0}$ (Bq mg^{-1})	$\overline{\sigma_{A^0}}$ (Bq mg^{-1})	σ (Bq mg^{-1})	A^0 (Bq mg^{-1})	σ_{A^0} (Bq mg^{-1})
PT1 Au	2.5	3.99×10^{4}	2.00×10^{3}	4.08×10^{4}	1.45×10^{3}	8.37×10^{2}	4.08×10^{4}	1.45×10^{3}
PT2 Au	2.3	4.16×10^{4}	2.09×10^{3}					
PT3 Au	2.7	1.81×10^{4}	9.11×10^{2}				1.81×10^{4}	9.11×10^{2}

[a] A^0 in and uncertainty Bq from Table C.6

mean, $\overline{\sigma}/\overline{x}$, was carried forward from Table C.5. Countrates were converted to activities at EOB, A^0, and uncertainties were calculated as they were for the tungsten samples.

Activities from Table C.6 were converted from Bq to Bq mg^{-1} in Table C.7 prior to taking an average since unlike the tungsten samples, the masses of the gold monitors were not identical. Data from the two gold monitors irradiated without cadmium covers were combined to produce a single value for unshielded gold activity. As in Table C.4, $\overline{\sigma_{A^0}}$ and σ were calculated. Finally, A^0 and its associated uncertainty were expressed using the average value and the uncertainty with the greatest magnitude.

A summary of gamma ray spectroscopy data for the silver flux monitor wires is provided in Table C.8. Silver flux monitors were recovered from all four pneumatic tube irradiations. Since ^{110m}Ag has a half-life of 249.76 d, only one measurement was used to calculate activity at EOB. Countrates at the time of measurement were calculated by dividing Total Counts by Count Times. These countrates were converted to activities at the time of measurement, A, by dividing by gamma intensity, detector efficiency, and the gamma ray self-absorption factor. Activities at EOB, A^0, were calculated using the equation:

$$A^0 = Ae^{-\lambda t} \tag{C.4}$$

where λ is the decay constant for ^{110m}Ag and t is the Time Since EOB. Uncertainty in A^0 was calculated as the square root of the sum of the squares of the uncertainties in counts, gamma ray intensity, and detector efficiency.

Table C.8 Cross Section Experiment #1 Gamma Ray Spectroscopy Data for Silver

Sample	Shelf (cm)	Count Time (s)	Dead Time (%)	Time Since EOB (d:h:m)	Total Counts	Absolute Uncert.	Counts per Second	Absolute Gamma Intensity [a]	Absolute Detector Efficiency [b]	Self-Absorption Factor [c]	A (Bq)	A^0 (Bq)	σ_{A^0} (Bq)
PT1 Ag	30	36000	0.06	3:1:30	1.40×10^4	1.40×10^2	3.89×10^{-1}	0.943 ± 0.003	2.97×10^{-4}	0.9956	1.40×10^3	1.41×10^3	7.20×10^1
PT2 Ag	30	29500.5	0.04	9:14:33	1.18×10^4	1.32×10^2	4.00×10^{-1}	0.943 ± 0.003	2.97×10^{-4}	0.9956	1.44×10^3	1.47×10^3	7.55×10^1
PT3 Ag	30	52000.4	0.05	1:22:50	9.25×10^3	1.47×10^2	1.78×10^{-1}	0.943 ± 0.003	2.97×10^{-4}	0.9956	6.39×10^2	6.42×10^2	3.37×10^1
PT4 Ag	30	52000.5	0.03	9:22:40	9.93×10^3	1.28×10^2	1.91×10^{-1}	0.943 ± 0.003	2.97×10^{-4}	0.9956	6.86×10^2	7.05×10^2	3.65×10^1

[a] [NNDC 2003]
[b] Table A.2
[c] Table B.3

Table C.9 Cross Section Experiment #1 Silver Activities

Sample	Mass (mg)	A^0 [a] (Bq mg^{-1})	σ_{A^0} [a] (Bq mg^{-1})	$\overline{A^0}$ (Bq mg^{-1})	$\overline{\sigma_{A^0}}$ (Bq mg^{-1})	σ (Bq mg^{-1})	A^0 (Bq mg^{-1})	σ_{A^0} (Bq mg^{-1})
PT1 Ag	42.0	3.35×10^1	1.71×10^0	3.36×10^1	1.21×10^0	3.47×10^{-2}	3.36×10^1	1.21×10^0
PT2 Ag	43.9	3.36×10^1	1.72×10^0					
PT3 Ag	43.7	1.47×10^1	7.71×10^{-1}	1.54×10^1	5.67×10^{-1}	6.99×10^{-1}	1.54×10^1	6.99×10^{-1}
PT4 Ag	43.8	1.61×10^1	8.33×10^{-1}					

[a] A^0 and uncertainty in Bq from Table C.8

Activities at EOB and their uncertainties from Table C.8 were converted from Bq to Bq mg^{-1} in Table C.9 prior to calculating averages and error propagation since the masses of the silver monitors were not identical. Data from the two silver monitors irradiated with and without cadmium covers were combined to produce single values for shielded and unshielded gold activity. As in Table C.4, $\overline{\sigma_{A^0}}$ and σ were calculated. Finally, activities at EOB, A^0, and their associated uncertainties were expressed using the average values and the uncertainties of greatest magnitude.

A summary of gamma ray spectroscopy data for the cobalt flux monitor wires is provided in Table C.10. Cobalt flux monitors were recovered from all four pneumatic tube irradiations. As identified in Section 3.4.2, cobalt wires from the Nuclear Medicine Group (Co1) were irradiated in all four pneumatic tube capsules and cobalt wires from the Neutron Activation Analysis Laboratory (Co2) were irradiated in capsules PT1 and PT4. Since ^{60}Co has a half-life of 1925.3 d, activities at EOB and their uncertainties were calculated as described for ^{110m}Ag. Both prominent ^{60}Co gamma rays were analyzed.

Activities of the Co2 wires were too low to be counted on the 30 cm shelf as all previous samples had been to eliminate any errors associated with differing accuracies in detector efficiencies. An assessment of the 5 cm and 10 cm shelves was performed by analyzing Co1 samples and comparing the results with data from the 30 cm shelf. Table C.10 shows very good agreement between data and consequently data from all three shelves was used in calculating average cobalt activities.

Activities at EOB and their uncertainties from Table C.10 were converted from Bq to Bq mg^{-1} in Table C.11 prior to calculating averages and error propagation since the masses of the cobalt monitors were not identical. Data from monitors irradiated with and without cadmium covers were combined to produce single values for shielded and unshielded cobalt activity. As in Table C.4, $\overline{\sigma_{A^0}}$ and σ were calculated. Finally, activities at EOB, A^0, and their associated uncertainties were expressed using the average values and the uncertainties of greatest magnitude.

Gold, silver and cobalt activities derived in Tables C.7, C.9 and C.11, respectively, were used along with published nuclide data to calculate thermal and epithermal fluxes according to equations derived from a generalized radioactive decay and transmutation equation that was developed from the Bateman [1910] equations and extended by Friedlander [1981] to include reactor transmutations (this generalized form extends the work of Friedlander to allow for initial quantities of any material in the transmutation and decay chain). For a transmutation and decay chain,

$$N_1 \xrightarrow{\Lambda_1^*} N_2 \xrightarrow{\Lambda_2^*} \cdots N_{n-1} \xrightarrow{\Lambda_{n-1}^*} N_n \xrightarrow{\Lambda_n^*} \cdots N_m$$

the quantity of the n^{th} nuclide can be calculated:

$$N_n(t) = \sum_{k=1}^{n}\left(\prod_{i=k}^{n-1}\Lambda_i^*\right)N_k^0 \sum_{i=k}^{n} a_i e^{-\Lambda_i t} \qquad \text{(C.5)}$$

$$a_i = \prod_{j\neq i}\left(\Lambda_j - \Lambda_i\right)^{-1} \quad (j = k, k+1, ..., n)$$

where Λ_{n-1}^* is the formation rate constant (λ_{n-1} or $\sigma_{n-1}\phi$) of the n^{th} nuclide from the $(n\text{-}1)^{\text{th}}$ nuclide and Λ_n is the total depletion rate constant ($\lambda_n + \sigma_n\phi$) of the n^{th} nuclide.

Table C.10 Cross Section Experiment #1 Gamma Ray Spectroscopy Data for Cobalt

Sample	Shelf (cm)	Count Time (s)	Dead Time (%)	Time Since EOB (d:h:m)	γ-ray	Total Counts	Absolute Uncert.	Counts per Second	Absolute Gamma Intensity [a]	Absolute Detector Efficiency [b]	Self-Absorp. Factor [c]	A (Bq)	A^0 (Bq)	σ_{A^0} (Bq)
PT1 Co1	30	14000.4	0.06	7:19:36	1173	9.84×10^{3}	1.12×10^{2}	7.03×10^{-1}	0.9985 ± 0.0003	1.74×10^{-4}	0.9950	4.07×10^{3}	4.08×10^{3}	2.09×10^{2}
					1332	8.91×10^{3}	9.78×10^{1}	6.36×10^{-1}	0.9998	1.59×10^{-4}	0.9953	4.02×10^{3}	4.03×10^{3}	2.06×10^{2}
PT1 Co1	10	7200	0.23	8:17:36	1173	3.16×10^{4}	1.92×10^{2}	4.39×10^{0}	0.9985 ± 0.0003	1.11×10^{-3}	0.9950	3.97×10^{3}	3.98×10^{3}	2.00×10^{2}
					1332	2.87×10^{4}	1.73×10^{2}	3.99×10^{0}	0.9998	1.02×10^{-3}	0.9953	3.95×10^{3}	3.96×10^{3}	1.99×10^{2}
PT1 Co1	5	1800	0.84	2:22:53	1173	2.04×10^{4}	1.55×10^{2}	1.13×10^{1}	0.9985 ± 0.0003	2.83×10^{-3}	0.9950	4.03×10^{3}	4.03×10^{3}	2.04×10^{2}
					1332	1.81×10^{4}	1.38×10^{2}	1.01×10^{1}	0.9998	2.57×10^{-3}	0.9953	3.94×10^{3}	3.94×10^{3}	1.99×10^{2}
PT2 Co1	30	13900.4	0.06	8:12:33	1173	9.42×10^{3}	1.09×10^{2}	6.78×10^{-1}	0.9985 ± 0.0003	1.74×10^{-4}	0.9950	3.92×10^{3}	3.93×10^{3}	2.02×10^{2}
					1332	8.60×10^{3}	9.59×10^{1}	6.19×10^{-1}	0.9998	1.59×10^{-4}	0.9953	3.91×10^{3}	3.92×10^{3}	2.01×10^{2}
PT3 Co1	30	50100.4	0.03	7:23:04	1173	9.35×10^{3}	1.15×10^{2}	1.87×10^{-1}	0.9985 ± 0.0003	1.74×10^{-4}	0.9950	1.08×10^{3}	1.08×10^{3}	5.56×10^{1}
					1332	8.33×10^{3}	9.98×10^{1}	1.66×10^{-1}	0.9998	1.59×10^{-4}	0.9953	1.05×10^{3}	1.05×10^{3}	5.41×10^{1}
PT3 Co1	5	5400	0.24	3:18:50	1173	1.63×10^{4}	1.38×10^{2}	3.02×10^{0}	0.9985 ± 0.0003	2.83×10^{-3}	0.9950	1.07×10^{3}	1.07×10^{3}	5.43×10^{1}
					1332	1.43×10^{4}	1.23×10^{2}	2.65×10^{0}	0.9998	2.57×10^{-3}	0.9953	1.04×10^{3}	1.04×10^{3}	5.27×10^{1}
PT4 Co1	30	54000	0.03	10:18:09	1173	1.03×10^{4}	1.14×10^{2}	1.91×10^{-1}	0.9985 ± 0.0003	1.74×10^{-4}	0.9950	1.10×10^{3}	1.11×10^{3}	5.68×10^{1}
					1332	9.08×10^{3}	1.07×10^{2}	1.68×10^{-1}	0.9998	1.59×10^{-4}	0.9953	1.06×10^{3}	1.07×10^{3}	5.47×10^{1}
PT4 Co1	10	18000	0.07	21:13:02	1173	2.07×10^{4}	1.65×10^{2}	1.15×10^{0}	0.9985 ± 0.0003	1.11×10^{-3}	0.9950	1.04×10^{3}	1.05×10^{3}	5.32×10^{1}
					1332	1.84×10^{4}	1.40×10^{2}	1.02×10^{0}	0.9998	1.02×10^{-3}	0.9953	1.01×10^{3}	1.02×10^{3}	5.16×10^{1}
PT4 Co1	5	5400	0.25	3:15:18	1173	1.61×10^{4}	1.46×10^{2}	2.98×10^{0}	0.9985 ± 0.0003	2.83×10^{-3}	0.9950	1.06×10^{3}	1.06×10^{3}	5.39×10^{1}
					1332	1.42×10^{4}	1.22×10^{2}	2.63×10^{0}	0.9998	2.57×10^{-3}	0.9953	1.03×10^{3}	1.03×10^{3}	5.23×10^{1}
PT1 Co2	10	36000	0.05	12:14:58	1173	1.84×10^{4}	1.51×10^{2}	5.11×10^{-1}	0.9985 ± 0.0003	1.11×10^{-3}	0.9967	4.61×10^{2}	4.63×10^{2}	2.35×10^{1}
					1332	1.68×10^{4}	1.37×10^{2}	4.67×10^{-1}	0.9998	1.02×10^{-3}	0.9969	4.61×10^{2}	4.63×10^{2}	2.35×10^{1}
PT1 Co2	5	10800	0.14	2:19:51	1173	1.44×10^{4}	1.37×10^{2}	1.33×10^{0}	0.9985 ± 0.0003	2.83×10^{-3}	0.9967	4.73×10^{2}	4.73×10^{2}	2.41×10^{1}
					1332	1.29×10^{4}	1.18×10^{2}	1.19×10^{0}	0.9998	2.57×10^{-3}	0.9969	4.67×10^{2}	4.68×10^{2}	2.38×10^{1}
PT4 Co2	10	129600	0.03	18:21:26	1173	1.79×10^{4}	1.67×10^{2}	1.38×10^{-1}	0.9985 ± 0.0003	1.11×10^{-3}	0.9967	1.25×10^{2}	1.25×10^{2}	6.36×10^{1}
					1332	1.65×10^{4}	1.45×10^{2}	1.27×10^{-1}	0.9998	1.02×10^{-3}	0.9969	1.26×10^{2}	1.27×10^{2}	6.43×10^{1}
PT4 Co2	5	54000	0.04	11:22:09	1173	1.88×10^{4}	1.61×10^{2}	3.48×10^{-1}	0.9985 ± 0.0003	2.83×10^{-3}	0.9967	1.23×10^{2}	1.24×10^{2}	6.29×10^{1}
					1332	1.72×10^{4}	1.42×10^{2}	3.19×10^{-1}	0.9998	2.57×10^{-3}	0.9969	1.25×10^{2}	1.25×10^{2}	6.34×10^{1}

[a] [NNDC 2003]; no uncertainty specified in this table for the 1332 keV γ-ray because the intensity is known to greater precision than shown (0.999826 ± 0.000006)
[b] Table A.2
[c] Table B.3

Table C.11 Cross Section Experiment #1 Cobalt Activities

Sample	Mass (mg)	A^0 [a] (Bq mg^{-1})	σ_{A^0} [a] (Bq mg^{-1})	$\overline{A^0}$ (Bq mg^{-1})	$\overline{\sigma_{A^0}}$ (Bq mg^{-1})	σ (Bq mg^{-1})	A^0 (Bq mg^{-1})	σ_{A^0} (Bq mg^{-1})
PT1 Co1	9.8	4.16×10^2	2.13×10^1					
		4.11×10^2	2.11×10^1					
		4.06×10^2	2.05×10^1					
		4.04×10^2	2.03×10^1	4.10×10^2	9.82×10^0	4.61×10^0	4.10×10^2	9.82×10^0
		4.11×10^2	2.08×10^1					
		4.02×10^2	2.04×10^1					
PT2 Co1	9.5	4.14×10^2	2.12×10^1					
		4.12×10^2	2.11×10^1					
PT3 Co1	9.7	1.11×10^2	5.73×10^0					
		1.09×10^2	5.58×10^0					
		1.10×10^2	5.59×10^0					
		1.07×10^2	5.43×10^0					
PT4 Co1	9.5	1.17×10^2	5.98×10^0	1.10×10^2	2.97×10^0	2.72×10^0	1.10×10^2	2.97×10^0
		1.12×10^2	5.76×10^0					
		1.11×10^2	5.60×10^0					
		1.07×10^2	5.43×10^0					
		1.12×10^2	5.67×10^0					
		1.09×10^2	5.51×10^0					
PT1 Co2	5.23	8.85×10^1	4.49×10^0					
		8.86×10^1	4.49×10^0	8.92×10^1	2.27×10^0	7.73×10^{-1}	8.92×10^1	2.27×10^0
		9.04×10^1	4.60×10^0					
		8.94×10^1	4.54×10^0					
PT4 Co2	4.62	2.71×10^1	1.38×10^0					
		2.74×10^1	1.39×10^0	2.71×10^1	6.88×10^{-1}	2.10×10^{-1}	2.71×10^1	6.88×10^{-1}
		2.68×10^1	1.36×10^0					
		2.71×10^1	1.37×10^0					

[a] A^0 and uncertainty in Bq from Table C.10

A two nuclide chain can be used to represent the radiative capture reactions involved in these flux monitors:

$$N_2(t) = \frac{\Lambda_1^*}{\Lambda_2 - \Lambda_1} N_1^0 \left(e^{-\Lambda_1 t} - e^{-\Lambda_2 t} \right) + N_2^0 e^{-\Lambda_2 t} \tag{C.6}$$

In terms of activity, this can be expressed:

$$A_2(t) = \lambda_2 N_2(t) = \frac{\lambda_2 \Lambda_1^*}{\Lambda_2 - \Lambda_1} N_1^0 \left(e^{-\Lambda_1 t} - e^{-\Lambda_2 t} \right) \tag{C.7}$$

where the final term has been dropped because there is no initial quantity of the radioactive product nuclide, N_2. For all three monitors (gold, silver and cobalt), the rate constants are:

$$\begin{aligned} \Lambda_1^* &= \Lambda_1 = \sigma\phi \\ \Lambda_2 &= \sigma\phi + \lambda_2 \end{aligned} \tag{C.8}$$

To determine thermal and epithermal fluxes Equation C.7 must be solved, with the cadmium-covered (shielded) data yielding the epithermal flux and the difference between the unshielded and shielded activities yielding the thermal flux. Since neutron flux appears in all rate constants, Λ, a solution for Equation C.7 in terms of flux is not possible. Instead, Equation C.7 was implemented in Excel© spreadsheets and neutron flux was varied until calculated activities matched measured activities.

As identified in Section 3.1, when performing cross section measurements using the cadmium cover technique, it is necessary to use a thermal cross section, σ_{th}, rather than σ_0 to account for reactions with neutrons with energies between $5E_{kT}$ and E_C. Since

thermal cross sections reported for the flux monitors were 2200 m/s cross sections, σ_0, it was necessary to convert them to σ_{th} for flux calculations using the following correction factor [Stoughton and Halperin 1959, Eq. 22]:

$$\sigma_{th} = \sigma_0 \left\{ 1 + 2 \left[\left(\frac{E_0}{5E_{kT}} \right)^{\frac{1}{2}} - \left(\frac{E_0}{E_C} \right)^{\frac{1}{2}} \right] \frac{\phi_{ep}}{\phi_0} \right\} \tag{C.9}$$

$$= \sigma_0 \left\{ 1 + 2 \left[\left(\frac{0.0253}{5 \times 0.0287} \right)^{\frac{1}{2}} - \left(\frac{0.0253}{0.5} \right)^{\frac{1}{2}} \right] \frac{1}{20} \right\}$$

$$= 1.02\ \sigma_0$$

where E_0 = 0.0253 eV, k = 8.6173 x 10^{-5} eV K^{-1}, T = 60°C = 333.15 K (HFIR coolant temperature), and ϕ_0/ϕ_{ep} = 20. The flux ratio of 20 was based on an initial analysis of the gold flux monitor data. Subsequently, calculations of neutron fluxes using the gold flux monitor data and a flux ratio of 40 to calculate σ_{th} cross sections showed that the results changed by less than 1% so the precision of the flux ratio is not critical.

The spreadsheet used to calculate neutron fluxes using data from the gold flux monitors is shown in Figure C.1. The upper portion of the spreadsheet contains nuclear data used in calculations performed by the spreadsheet. The equation displayed below the nuclear data (A_{198}) is the application of Equation C.7 to the activation of ^{198}Au. Shielded and unshielded activities for the gold monitors, A^0_{198}, are taken from Table C.7. These activities are expressed in terms of Bq/mg of target material (i.e., the mass of the gold wire) and so they are converted to Bq/mg of ^{197}Au by dividing by the gold content of the wire and the natural abundance of ^{197}Au.

t_{irr}	119	s								
σ_0^{197}	98.65	b	σ_{th}^{197}	100.6	I_0^{197}	1550	b	M_{197}	196.9666	g
σ_0^{198}	25100	b	σ_{th}^{198}	25602	I_0^{198}	1	b	M_{198}	197.9682	g
λ_{198}	2.977E-06	s^{-1}	$t_{1/2}^{198}$	2.33E+05	s					
$A_{198} = \lambda_{198}N_{198} = \lambda_{198}(\Lambda^*_{197}/\Lambda_{198}-\Lambda_{197})N^o_{197}(e^{-\Lambda_{197}t}-e^{-\Lambda_{198}t})$										
					Epithermal Flux Determination					
Sample	Au Content	^{197}Au Natural Abundance	A^0_{198} (Bq/mg target)	A^0_{198} (Bq/mg ^{197}Au)	ϕ_{ep} (n cm^{-2} s^{-1})	Λ^*_{197} (s^{-1})	Λ_{197} (s^{-1})	Λ_{198} (s^{-1})	A_{198} RHS (Bq/mg)	
Unshielded	0.00058	1.000	4.08E+04	7.03E+07						
Shielded	0.00058	1.000	1.81E+04	3.12E+07	1.86E+13	2.88E-08	2.88E-08	2.98E-06	3.12E+07	
				Thermal Flux Determination						
				A_{198} Unshielded-Shielded (Bq/mg)	ϕ_0 (n cm^{-2} s^{-1})	Λ^*_{197} (s^{-1})	Λ_{197} (s^{-1})	Λ_{198} (s^{-1})	A_{198} RHS (Bq/mg)	
				3.91E+07	3.60E+14	3.62E-08	3.62E-08	1.22E-05	3.91E+07	
				ϕ_0/ϕ_{ep}	19.3					

Figure C.1 Cross Section Experiment #1 Calculation of Neutron Flux from Gold Flux Monitor Data

The activity induced in the shielded sample is due solely to epithermal neutrons and can thus be used to calculate epithermal flux. This is done by using a cell in the Epithermal Flux Determination section of the spreadsheet to implement the right-hand-side of the equation for A_{198} (the cell is in the column labeled A_{198} RHS) and varying the epithermal flux (in the column ϕ_{ep}) until A_{198} RHS equals the experimentally derived activity, A^0_{198}. As mentioned previously, this "numerical" solution is necessary because all the rate constants, Λ, are functions of the epithermal flux (as seen in the spreadsheet, the rate constants are calculated and used as inputs to the equation for A_{198} RHS). In the calculations of the rate constants, the $\sigma\phi$ terms (see Equation C.2) use ϕ_{ep} for ϕ and I_0 for σ because, as stated previously, activation of the shielded sample is due to epithermal neutrons.

The activity induced in the unshielded sample is due to both thermal and epithermal neutrons. Thus, subtracting the activity induced in the shielded sample yields the activity induced by thermal neutrons. The spreadsheet performs this subtraction and the result is in a cell under the heading A_{198} Unshielded-Shielded. As described in the discussion of epithermal flux determination, the thermal flux, ϕ_0, is varied in the Thermal Flux Determination section of the spreadsheet until A_{198} RHS equals the experimentally derived activity, A_{198} Unshielded-Shielded. In the calculations of the rate constants in this section, the $\sigma\phi$ terms (Equation C.8) use ϕ_0 for ϕ and σ_{th} for σ because A_{198} Unshielded-Shielded represents activity induced by thermal neutrons.

Data from the silver flux monitors was processed in the same manner as the gold flux monitor data; the results are presented in Figure C.2. The data was analyzed using both values for silver content of the flux monitors (the value reported by the manufacturer and the value written on the package; see Section 3.4.2).

Data from both sets of cobalt flux monitors were processed and the spreadsheet used for these calculations is shown in Figure C.3.

A similar method was used to calculate cross sections for ^{186}W. Figure C.4 is the spreadsheet used for these calculations. In this spreadsheet, ϕ_0 and ϕ_{ep} are taken from the gold flux monitor data and σ_{th} (Thermal Cross Section Determination section) and I_0 (Resonance Integral Determination section) are varied until the calculated activities, A_{187} RHS, equal the measured activities. The value for σ_0^{186} is calculated in the upper left portion of the spreadsheet by dividing σ_{th}^{186} by 1.02, the conversion factor derived by Equation C.9.

t_{irr}	119	s								
$\sigma_0^{109\text{-}110m}$	4.7	b	$\sigma_{th}^{109\text{-}110m}$	4.79	$I_0^{109\text{-}110m}$	72.3	b	M_{109}	108.9048	g
$\sigma_0^{109\text{-}110m+g}$	91	b	$\sigma_{th}^{109\text{-}110m+g}$	92.8	$I_0^{109\text{-}110m+g}$	1400	b			
σ_0^{110m}	82	b	σ_{th}^{110m}	83.6	I_0^{110m}	93.88	b	M_{110m}	109.90624	g
λ_{110m}	3.212E-08	s^{-1}	$t_{1/2}^{110m}$	2.16E+07	s					
$A_{110m} = \lambda_{110m}N_{110m} = \lambda_{110m}(\Lambda^*_{109}/\Lambda_{110m}-\Lambda_{109})N^o_{109}(e^{-\Lambda_{109}t}-e^{-\Lambda_{110m}t})$										
					Epithermal Flux Determination					
Sample	Ag Content	^{109}Ag Natural Abundance	A^0_{110m} (Bq/mg target)	A^0_{110m} (Bq/mg ^{109}Ag)	ϕ_{ep} (n cm^{-2} s^{-1})	Λ^*_{109} (s^{-1})	Λ_{109} (s^{-1})	Λ_{110m} (s^{-1})	A_{110m} RHS (Bq/mg)	
using F. Kam's analysis										
Unshielded	0.00145	0.48161	3.36E+01	4.81E+04						
Shielded	0.00145	0.48161	1.54E+01	2.21E+04	1.44E+13	1.04E-09	2.02E-08	3.35E-08	2.21E+04	
using Reactor Experiment's analysis										
Unshielded	0.00092	0.48161	3.36E+01	7.58E+04						
Shielded	0.00092	0.48161	1.54E+01	3.48E+04	2.27E+13	1.64E-09	3.18E-08	3.43E-08	3.48E+04	
				Thermal Flux Determination						
				A_{110m} Unshielded-Shielded (Bq/mg)	ϕ_0 (n cm^{-2} s^{-1})	Λ^*_{109} (s^{-1})	Λ_{109} (s^{-1})	Λ_{110m} (s^{-1})	A_{110m} RHS (Bq/mg)	
using F. Kam's analysis				2.61E+04	2.57E+14	1.23E-09	2.39E-08	5.36E-08	2.61E+04	
using Reactor Experiment's analysis				4.11E+04	4.06E+14	1.94E-09	3.77E-08	6.60E-08	4.11E+04	
				ϕ_0/ϕ_{ep} (Kam)	17.8					
				ϕ_0/ϕ_{ep} (RE)	17.8					

Figure C.2 Cross Section Experiment #1 Calculation of Neutron Flux from Silver Flux Monitor Data

t_{irr}	119	s								
σ_0^{59}	37.18	b	σ_{th}^{59}	37.92	I_0^{59}	74	b	M_{59}	58.93319	g
σ_0^{60}	2	b	σ_{th}^{60}	2.04	I_0^{60}	4.3	b	M_{60}	59.93382	g
λ_{60}	4.167E-09	s^{-1}	$t_{1/2}^{60}$	1.66E+08	s					
$A_{60} = \lambda_{60}N_{60} = \lambda_{60}(\Lambda^*_{59}/\Lambda_{60}-\Lambda_{59})N^o_{59}(e^{-\Lambda_{59}t}-e^{-\Lambda_{60}t})$										
					Epithermal Flux Determination					
Sample	Co Content	^{59}Co Natural Abundance	A^0_{60} (Bq/mg target)	A^0_{60} (Bq/mg ^{59}Co)	ϕ_{ep} (n cm^{-2} s^{-1})	Λ^*_{59} (s^{-1})	Λ_{59} (s^{-1})	Λ_{60} (s^{-1})	A_{60} RHS (Bq/mg)	
Co1 Unshielded	0.0066	1.000	4.10E+02	6.21E+04						
Co1 Shielded	0.0066	1.000	1.10E+02	1.67E+04	4.45E+13	3.29E-09	3.29E-09	4.36E-09	1.67E+04	
Co2 Unshielded	0.00116	1.000	8.92E+01	7.69E+04						
Co2 Shielded	0.00116	1.000	2.71E+01	2.34E+04	6.23E+13	4.61E-09	4.61E-09	4.43E-09	2.34E+04	
				Thermal Flux Determination						
				A_{60} Unshielded-Shielded (Bq/mg)	ϕ_0 (n cm^{-2} s^{-1})	Λ^*_{59} (s^{-1})	Λ_{59} (s^{-1})	Λ_{60} (s^{-1})	A_{60} RHS (Bq/mg)	
Co1				4.55E+04	2.37E+14	8.97E-09	8.97E-09	4.65E-09	4.55E+04	
Co2				5.35E+04	2.79E+14	1.06E-08	1.06E-08	4.74E-09	5.35E+04	
				ϕ_0/ϕ_{ep} Co1	5.3					
				ϕ_0/ϕ_{ep} Co2	4.5					

Figure C.3 Cross Section Experiment #1 Calculation of Neutron Flux from Cobalt Flux Monitor Data

σ_0^{186}	17.58	b	σ_{th}^{186}	17.93	I_0^{186}	106.2	b	M_{186}	185.9544	g
σ_0^{187}	64	b	σ_{th}^{187}	65.28	I_0^{187}	2760	b	M_{187}	186.9572	g
λ_{187}	8.117E-06	s^{-1}	$t_{1/2}^{187}$	85392	s					
$A_{187} = \lambda_{187}N_{187} = \lambda_{187}(\Lambda^*_{186}/\Lambda_{187}-\Lambda_{186})N^o_{186}(e^{-\Lambda_{186}t}-e^{-\Lambda_{187}t})$										
					Resonance Integral Determination					
Sample	W Content	^{186}W Enrichment	A^0_{187} (Bq/mg target)	A^0_{187} (Bq/mg ^{186}W)	ϕ_{ep} (n cm^{-2} s^{-1})	I_0^{186} (b)	Λ^*_{186} (s^{-1})	Λ_{186} (s^{-1})	Λ_{187} (s^{-1})	A_{187} RHS (Bq/mg)
Unshielded	1.0000	0.9766	2.57E+07	2.63E+07						
Shielded	1.0000	0.9766	6.03E+06	6.17E+06	1.86E+13	106.2	1.97E-09	1.97E-09	8.17E-06	6.17E+06
				Thermal Cross Section Determination						
				A_{187} Unshielded-Shielded (Bq/mg)	ϕ_0 (n cm^{-2} s^{-1})	σ_{th}^{186} (b)	Λ^*_{186} (s^{-1})	Λ_{186} (s^{-1})	Λ_{187} (s^{-1})	A_{187} RHS (Bq/mg)
				2.01E+07	3.59E+14	17.93	6.44E-09	6.44E-09	8.14E-06	2.01E+07

Figure C.4 Cross Section Experiment #1 Calculation of Tungsten Cross Sections

C.2 Cross Section Experiment #2

Data for cross section experiment #2 was processed using the same methods described for cross section experiment #1 (Appendix C.1). Only the variations from previous methods (such as a modification to accommodate the different irradiation times of the capsules – in cross section experiment #1 all capsules were irradiated for the same duration) will be described in this section.

A summary of gamma ray spectroscopy data for all tungsten samples is provided in Table C.12. PT5 and PT6 (unshielded samples) both contained AAS standard and enriched tungsten samples. PT7 and PT8 also contained AAS standard and enriched tungsten samples, but as discussed in Section 3.4.3, material from these samples leaked from the foil packages and contaminated other samples. Therefore, there are entries in Table C.12 for the tungsten activity found on the gold and silver flux monitor packages in PT7 and PT8. The AAS standard and enriched tungsten samples in PT8 were damaged when targets were extracted from the cadmium casing (see Section 3.4.3) and are noted to be "partial" in this section.

An analysis of the gamma ray spectra of the PT5 and PT6 samples (no leakage from tungsten sample packages) and the samples in PT7 and PT8 was performed to identify the material that had leaked. To do this, the ratio of 134 keV (^{187}W) to 1369 keV (^{24}Na) was calculated for each sample. A small amount of ^{24}Na is present in all samples due to the ^{27}Al(n,α)^{24}Na reaction that takes place in the aluminum foil. However, there is a much

larger amount of ^{24}Na in the enriched tungsten samples due to activation of the sodium in the NaOH that was used to dissolve the enriched tungsten during sample preparation. For the PT5 and PT6 samples, this ratio was two orders of magnitude greater for the AAS standard samples compared to the enriched tungsten samples. While it is not possible to draw conclusions about the identity of the material on the gold and silver flux monitor packages (since the ratio of the tungsten signal to sodium signal depends on the unknown amount of material deposited), it was found that the ratios for the AAS standard and enriched tungsten samples differed from what would be expected based on the PT5 and PT6 ratios, indicating that both the AAS standard and enriched tungsten samples had leaked and contaminated other foil packages. It is understandable that leakage only occurred in the PT7 and PT8 tungsten samples and not those in PT5 and PT6 since the amount of solution evaporated and material deposited for the PT7 and PT8 targets was far greater than for the PT5 and PT6 targets (Table 3.8).

Table C.13 is a calculation of activities for each tungsten gamma ray as described in Appendix C.1 for Table C.2. As noted above, tungsten counts from gold and silver flux monitor samples are included and a sum of all "miscellaneous" counts is calculated. The uncertainties for the summations represent the total uncertainty of all samples included in the summation (the square root of the sum of the squares of the addends).

Table C.14 is a calculation of activities for each tungsten sample based on all three tungsten gamma rays as described in Appendix C.1 for Table C.3. The "miscellaneous"

activities from deposits on flux monitors for PT7 and PT8 are now shown as totals rather than identifying the activities associated with each individual monitor.

Table C.15 is a calculation of activities per unit mass as described in Appendix C.1 for Table C.4. Results from PT5 and PT6 AAS standard and enriched tungsten samples were averaged to provide single values for unshielded activities. Activities for PT7 and PT8 AAS standard and enriched tungsten samples are shown, along with the "miscellaneous" activities added to each sample. Absolute uncertainties for the combined sample and miscellaneous activities (identified as std+misc and enr+misc in Table C.15) were calculated by multiplying the total activities by the percent uncertainty associated with the main sample (i.e., neglecting the uncertainties in all the "miscellaneous" counts). This is reasonable since the main sample represents the majority of the combined counts.

Analyses of PT8 sample activities with respect to those of PT7 accounting for the differences between irradiation times (PT8 was 44 s, PT7 was 60s) and sample masses (PT8 samples were larger as identified in Table C.15) demonstrated that PT8 activities were approximately half of what would be expected and thus the "partial" PT8 samples have no value and will not be analyzed further.

Table C.12 Cross Section Experiment #2 Gamma Ray Spectroscopy Data for Tungsten

Sample	Shelf (cm)	Count Time (s)	Dead Time (%)	Time Since EOB (d:h:m)	134 keV γ-ray			479 keV γ-ray			685 keV γ-ray		
					Total Counts	Absolute Uncert.	Rel.Unc. (%)	Total Counts	Absolute Uncert.	Rel.Unc. (%)	Total Counts	Absolute Uncert.	Rel.Unc. (%)
PT5 W std	30	300	12.9	1:2:44	6.48×10^4	3.55×10^2	0.5 [a]	5.72×10^4	3.22×10^2	0.6 [a]	4.96E+04	2.41×10^2	0.5 [a]
	30	300	8.5	1:17:32	4.23×10^4	2.57×10^2	0.6 [a]	3.83×10^4	2.61×10^2	0.7 [a]	3.32E+04	1.91×10^2	0.6 [a]
	30	300	7.0	2:0:42	3.48×10^4	2.26×10^2	0.6 [a]	3.10×10^4	2.05×10^2	0.7 [a]	2.73E+04	1.72×10^2	0.6
	30	300	4.3	2:18:08	2.15×10^4	1.77×10^2	0.8	1.90×10^4	1.62×10^2	0.9	1.64E+04	1.31×10^2	0.8
	30	300	3.0	3:6:00	1.50×10^4	1.56×10^2	1.0	1.32×10^4	1.30×10^2	1.0	1.19E+04	1.12×10^2	0.9
	30	600	1.8	4:1:24	1.73×10^4	1.55×10^2	0.9	1.55×10^4	1.42×10^2	0.9	1.35E+04	1.19×10^2	0.9
	30	1200	0.9	4:22:05	1.88×10^4	1.79×10^2	1.0	1.70×10^4	1.67×10^2	1.0	1.47E+04	1.24×10^2	0.8
$\bar{\sigma}/\bar{x}$							0.47			0.47			0.37
PT5 W enr	30	300	17.9	1:2:26	3.57×10^4	3.36×10^2	0.9 [a]	3.16×10^4	2.68×10^2	0.8 [a]	2.75×10^4	2.29×10^2	0.8 [a]
	30	300	10.2	1:17:41	2.30×10^4	2.63×10^2	1.1 [a]	2.07×10^4	2.05×10^2	1.0 [a]	1.83×10^4	1.73×10^2	0.9 [a]
	30	300	7.9	2:0:49	1.91×10^4	2.31×10^2	1.2 [a]	1.73×10^4	1.85×10^2	1.1	1.51×10^4	1.39×10^2	0.9
	30	600	4.2	2:18:15	2.41×10^4	2.38×10^2	1.0	2.11×10^4	1.90×10^2	0.9	1.81×10^4	1.57×10^2	0.9
	30	600	2.7	3:6:33	1.63×10^4	1.66×10^2	1.0	1.48×10^4	1.57×10^2	1.1	1.27×10^4	1.23×10^2	1.0
	30	1200	1.4	4:1:35	1.91×10^4	1.87×10^2	1.0	1.65×10^4	1.50×10^2	0.9	1.50×10^4	1.32×10^2	0.9
	30	1800	0.7	4:21:33	1.59×10^4	1.55×10^2	1.0	1.42×10^4	1.51×10^2	1.1	1.24×10^4	1.18×10^2	1.0
$\bar{\sigma}/\bar{x}$							0.50			0.45			0.41
PT6 W std	30	300	8.3	1:2:01	4.08×10^4	2.80×10^2	0.7 [a]	3.60×10^4	2.27×10^2	0.6 [a]	3.21×10^4	1.88×10^2	0.6 [a]
	30	300	5.4	1:17:00	2.66×10^4	2.27×10^2	0.9	2.39×10^4	1.84×10^2	0.8	2.10×10^4	1.51×10^2	0.7
	30	300	4.2	2:1:51	2.06×10^4	1.79×10^2	0.9	1.82×10^4	1.58×10^2	0.9	1.63×10^4	1.31×10^2	0.8
	30	420	2.6	2:18:05	1.80×10^4	1.59×10^2	0.9	1.63×10^4	1.49×10^2	0.9	1.44×10^4	1.23×10^2	0.9
	30	600	1.9	3:5:48	1.84×10^4	1.92×10^2	1.0	1.64×10^4	1.48×10^2	0.9	1.46×10^4	1.24×10^2	0.9
	30	900	1.1	4:1:00	1.61×10^4	1.74×10^2	1.1	1.41×10^4	1.44×10^2	1.0	1.24×10^4	1.13×10^2	0.9
$\bar{\sigma}/\bar{x}$							0.42			0.40			0.37
PT6 W enr	30	120.4	36.0	1:2:15	2.82×10^4	3.25×10^2	1.2 [a]	2.59×10^4	2.91×10^2	1.1 [a]	2.29×10^4	2.32×10^2	1.0 [a]
	30	300	22.3	1:16:52	5.05×10^4	4.08×10^2	0.8 [a]	4.60×10^4	3.34×10^2	0.7 [a]	4.02×10^4	2.77×10^2	0.7 [a]
	30	300	16.6	2:1:44	4.06×10^4	3.42×10^2	0.8 [a]	3.68×10^4	2.89×10^2	0.8 [a]	3.22×10^4	2.21×10^2	0.7 [a]
	30	300	9.5	2:17:53	2.65×10^4	2.40×10^2	0.9 [a]	2.40×10^4	2.11×10^2	0.9 [a]	2.09×10^4	1.75×10^2	0.8 [a]

Sample	Shelf (cm)	Count Time (s)	Dead Time (%)	Time Since EOB (d:h:m)	134 keV γ-ray			479 keV γ-ray			685 keV γ-ray		
					Total Counts	Absolute Uncert.	Rel.Unc. (%)	Total Counts	Absolute Uncert.	Rel.Unc. (%)	Total Counts	Absolute Uncert.	Rel.Unc. (%)
PT6 W enr	30	300	6.2	3:6:00	1.90×10^{4}	2.11×10^{2}	1.1	1.67×10^{4}	1.57×10^{2}	0.9 [a]	1.49×10^{4}	1.44×10^{2}	1.0
	30	600	3.2	4:1:17	2.17×10^{4}	2.21×10^{2}	1.0	1.94×10^{4}	1.93×10^{2}	1.0	1.70×10^{4}	1.42×10^{2}	0.8
	30	900	1.6	4:21:31	1.85×10^{4}	1.85×10^{2}	1.0	1.65×10^{4}	1.60×10^{2}	1.0	1.43×10^{4}	1.29×10^{2}	0.9
	30	900	1.4	5:0:45	1.65×10^{4}	1.61×10^{2}	1.0	1.49×10^{4}	1.38×10^{2}	0.9	1.30×10^{4}	1.23×10^{2}	0.9
	30	1800	0.8	5:21:10	1.82×10^{4}	1.94×10^{2}	1.1	1.64×10^{4}	1.58×10^{2}	1.0	1.44×10^{4}	1.28×10^{2}	0.9
$\bar{\sigma}/\bar{x}$							0.46			0.48			0.41
PT7 W std	30	900	2.8	1:5:59	4.18×10^{4}	2.39×10^{2}	0.6	3.70×10^{4}	2.11×10^{2}	0.6	3.26×10^{4}	1.86×10^{2}	0.6
	30	420	1.8	1:20:27	1.26×10^{4}	1.40×10^{2}	1.1	1.15×10^{4}	1.19×10^{2}	1.0	9.93×10^{3}	1.02×10^{2}	1.0
	30	600	1.4	2:5:17	1.43×10^{4}	1.47×10^{2}	1.0	1.28×10^{4}	1.37×10^{2}	1.1	1.10×10^{4}	1.07×10^{2}	1.0
	30	900	0.9	2:21:32	1.32×10^{4}	1.35×10^{2}	1.0	1.16×10^{4}	1.33×10^{2}	1.1	1.03×10^{4}	1.04×10^{2}	1.0
	30	1200	0.7	3:8:33	1.30×10^{4}	1.45×10^{2}	1.1	1.15×10^{4}	1.22×10^{2}	1.1	9.88×10^{3}	1.02×10^{2}	1.0
$\bar{\sigma}/\bar{x}$							0.44			0.45			0.42
PT7 W enr	30	71780.5	0.1	5:4:27	9.79×10^{4}	4.17×10^{2}	0.4	8.64×10^{3}	3.56×10^{2}	0.4	7.63×10^{4}	2.91×10^{2}	0.4
	30	14899.7	0.05	6:23:21	7.19×10^{3}	1.20×10^{2}	1.7	6.38×10^{3}	1.06×10^{2}	1.7	5.72×10^{3}	8.62×10^{1}	1.5
	30	45915.4	0.04	7:7:26	1.52×10^{4}	2.02×10^{2}	1.3	1.38×10^{4}	1.40×10^{2}	1.0	1.22×10^{4}	1.30×10^{2}	1.1
	30	54000	0.03	8:4:30	9.46×10^{3}	1.74×10^{2}	1.8	8.43×10^{3}	1.26×10^{2}	1.5	7.51×10^{3}	1.05×10^{2}	1.4
$\bar{\sigma}/\bar{x}$							0.71			0.62			0.59
PT7 Ag std	30	18000	0.1	1:8:08	1.68×10^{4}	1.78×10^{2}	1.1	1.49×10^{4}	1.45×10^{2}	1.0	1.31E+04	1.24×10^{2}	0.9
(W)	30	25600	0.05	2:13:09	9.91×10^{3}	1.54×10^{2}	1.6	8.76×10^{3}	1.15×10^{2}	1.3	7.91×10^{3}	9.60×10^{1}	1.2
	30	42510.5	0.04	3:10:04	8.13×10^{3}	1.52×10^{2}	1.9	7.42×10^{3}	1.12×10^{2}	1.5	6.43×10^{3}	1.14×10^{2}	1.8
	30	59000.3	0.03	4:7:28	5.73×10^{3}	2.12×10^{2}	3.7	5.24×10^{3}	1.07×10^{2}	2.0	4.82×10^{3}	9.53×10^{1}	2.0
$\bar{\sigma}/\bar{x}$							1.14			0.75			0.77
PT7 Au std	30	420	0.45	1:6:47	4.94×10^{2}	5.30×10^{1}	10.7	4.52×10^{2}	2.43×10^{1}	5.4	4.28×10^{2}	2.13×10^{1}	5.0
(W)	30	900	0.19	4:6:22	1.24×10^{2}	5.08×10^{1}	40.9	1.10×10^{2}	1.47×10^{1}	13.3	1.34×10^{2}	1.26×10^{1}	9.4
$\bar{\sigma}/\bar{x}$							21.16			7.18			5.33
PT7 Au	30	600	0.33	1:5:46	3.06×10^{2}	5.26×10^{1}	17.2	3.20×10^{2}	2.34×10^{1}	7.3	2.91×10^{2}	1.81×10^{1}	6.2
wire (W)	30	1200	0.15	4:6:00				9.69×10^{1}	1.13×10^{1}	11.7	7.21×10^{1}	1.05×10^{1}	14.5
$\bar{\sigma}/\bar{x}$										6.88			7.89

Sample	Shelf (cm)	Count Time (s)	Dead Time (%)	Time Since EOB (d:h:m)	134 keV γ-ray			479 keV γ-ray			685 keV γ-ray		
					Total Counts	Absolute Uncert.	Rel.Unc. (%)	Total Counts	Absolute Uncert.	Rel.Unc. (%)	Total Counts	Absolute Uncert.	Rel.Unc. (%)
PT8 W std	30	600	1.8	1:5:40	1.75×10^{4}	1.85×10^{2}	1.1	1.56×10^{4}	1.51×10^{2}	1.0	1.37×10^{4}	1.19×10^{2}	0.9
(partial)	30	900	1.2	1:19:19	1.79×10^{4}	1.79×10^{2}	1.0	1.57×10^{4}	1.52×10^{2}	1.0	1.39×10^{4}	1.20×10^{2}	0.9
	30	900	0.9	2:4:33	1.34×10^{4}	1.47×10^{2}	1.1	1.20×10^{4}	1.30×10^{2}	1.1	1.04×10^{4}	1.04×10^{2}	1.0
	30	1200	0.6	2:19:31	1.14×10^{4}	1.30×10^{2}	1.1	1.04×10^{4}	1.26×10^{2}	1.2	9.15×10^{3}	9.82×10^{1}	1.1
	30	1800	0.4	3:8:09	1.21×10^{4}	1.40×10^{2}	1.2	1.11×10^{4}	1.33×10^{2}	1.2	9.41×10^{3}	9.91×10^{1}	1.1
$\overline{\sigma}/\overline{x}$							0.49			0.49			0.44
PT8 W enr	30	600	1.6	1:6:06	1.49×10^{4}	1.72×10^{2}	1.2	1.32×10^{4}	1.37×10^{2}	1.0	1.15×10^{4}	1.11×10^{2}	1.0
(partial)	30	900	1.1	1:19:50	1.48×10^{4}	1.64×10^{2}	1.1	1.35×10^{4}	1.40×10^{2}	1.0	1.17×10^{4}	1.13×10^{2}	1.0
	30	1200	0.8	2:4:50	1.51×10^{4}	1.57×10^{2}	1.0	1.39×10^{4}	1.46×10^{2}	1.0	1.22×10^{4}	1.13×10^{2}	0.9
	30	2700	0.4	3:6:16	1.65×10^{4}	1.49×10^{2}	0.9	1.44×10^{4}	1.33×10^{2}	0.9	1.29×10^{4}	1.18×10^{2}	0.9
	30	3600	0.2	4:3:30	1.17×10^{4}	1.29×10^{2}	1.1	1.05×10^{4}	1.25×10^{2}	1.2	9.15×10^{3}	9.80×10^{1}	1.1
$\overline{\sigma}/\overline{x}$							0.48			0.47			0.43
PT8 Ag std	30	1813.3	0.1	1:17:07	1.64×10^{3}	5.99×10^{1}	3.7	1.31×10^{3}	4.26×10^{1}	3.3	1.14×10^{3}	3.62×10^{1}	3.2
(partial)	30	2496.1	0.1	1:20:07	1.73×10^{3}	5.73×10^{1}	3.3	1.62×10^{3}	4.58×10^{1}	2.8	1.45×10^{3}	4.22×10^{1}	2.9
(W)	30	9000.4	0.1	1:21:04	6.29×10^{3}	9.98×10^{1}	1.6	5.60×10^{3}	8.64×10^{1}	1.5	4.87×10^{3}	7.80×10^{1}	1.6
	30	13444.7	0.05	2:20:32	4.54×10^{3}	1.26×10^{1}	2.8	4.19×10^{3}	7.89×10^{1}	1.9	3.57×10^{3}	7.31×10^{1}	2.0
	30	11000.6	0.03	3:23:21	1.62×10^{3}	7.95×10^{1}	4.9	1.50×10^{3}	5.92×10^{1}	3.9	1.37×10^{3}	4.74×10^{1}	3.5
	30	56073.4	0.02	6:3:17	1.74×10^{3}	1.58×10^{2}	9.1	1.50×10^{3}	7.73×10^{1}	5.2	1.49×10^{3}	6.20×10^{1}	4.2 [a]
$\overline{\sigma}/\overline{x}$							1.98			1.36			1.22
PT8 Au std	30	420	0.52	1:6:21	8.57×10^{2}	6.34×10^{1}	7.4	7.58×10^{2}	3.37×10^{1}	4.4	6.16×10^{2}	2.61×10^{1}	4.2
(W)	30	900	0.20	4:5:42	2.33×10^{2}	5.91×10^{1}	25.4	1.79×10^{2}	1.69×10^{1}	9.4	1.69×10^{2}	1.40×10^{1}	8.3
$\overline{\sigma}/\overline{x}$							13.21			5.21			4.64
PT8 Au	30	600	0.38	1:5:18	4.04×10^{2}	6.01×10^{1}	14.9	3.56×10^{2}	2.26×10^{1}	6.4	3.59×10^{2}	2.04×10^{1}	5.7
wire (W)	30	1200	0.17	4:5:21				8.89E+01	1.31×10^{1}	14.7	9.13×10^{1}	1.15×10^{1}	12.6
$\overline{\sigma}/\overline{x}$										8.02			6.89

[a] data point not used in calculations of A^0 and uncertainty

Table C.13 Cross Section Experiment #2 Tungsten Sample Activities for Each Gamma Ray

γ-ray/ Sample	Count Rate at EOB: Counts per Second [a]	Count Rate at EOB: CLSQ Rel.Unc.[a] (%)	Count Rate at EOB: $\overline{\sigma}/\overline{x}$ Rel.Unc.[b] (%)	Absolute Gamma Intensity [c]	Absolute Detector Efficiency [d]	Self-Absorption Factor [e]	A^0 (Bq)	σ_{A^0} (Bq)
134 keV								
PT5 W std	4.95×10^{2}	0.37	0.47	0.0885 ± 0.00164	1.10×10^{-3}	0.9990	5.11×10^{6}	2.74×10^{5}
PT5 W enr	2.78×10^{2}	0.41	0.50	0.0885 ± 0.00164	1.10×10^{-3}	0.9990	2.87×10^{6}	1.54×10^{5}
PT6 W std	2.96×10^{2}	0.35	0.42	0.0885 ± 0.00164	1.10×10^{-3}	0.9990	3.05×10^{6}	1.63×10^{5}
PT6 W enr	6.28×10^{2}	0.33	0.46	0.0885 ± 0.00164	1.10×10^{-3}	0.9990	6.48×10^{6}	3.47×10^{5}
PT7 W std	1.12×10^{2}	0.33	0.44	0.0885 ± 0.00164	1.10×10^{-3}	0.9990	1.16×10^{6}	6.21×10^{4}
PT7 W enr	6.86×10^{1}	0.37	0.71	0.0885 ± 0.00164	1.10×10^{-3}	0.9990	7.07×10^{5}	3.80×10^{4}
PT7 Ag std (W)	2.55×10^{0}	0.50	1.14	0.0885 ± 0.00164	1.10×10^{-3}	1.0000 [g]	2.63×10^{4}	1.43×10^{3}
PT7 Au std (W)	2.87×10^{0}	4.03	21.2	0.0885 ± 0.00164	1.10×10^{-3}	1.0000 [g]	2.95×10^{4}	6.45×10^{3}
PT7 Au wire (W)	1.22×10^{0}	5.73	17.2	0.0885 ± 0.00164	1.10×10^{-3}	1.0000 [g]	1.26×10^{4}	2.27×10^{3}
PT7 misc (W) (sum)	6.64×10^{0}	7.02 [f]	27.3 [f]	0.0885 ± 0.00164	1.10×10^{-3}	1.0000 [g]	6.82×10^{4}	1.90×10^{4}
PT8 W std (partial)	6.98×10^{1}	0.37	0.49	0.0885 ± 0.00164	1.10×10^{-3}	0.9990	7.21×10^{5}	3.86×10^{4}
PT8 W enr (partial)	6.00×10^{1}	0.37	0.48	0.0885 ± 0.00164	1.10×10^{-3}	0.9990	6.19×10^{5}	3.31×10^{4}
PT8 Ag std (partial) (W)	2.69×10^{0}	0.76	1.98	0.0885 ± 0.00164	1.10×10^{-3}	1.0000 [g]	2.77×10^{4}	1.48×10^{3}
PT8 Au std (W)	4.99×10^{0}	3.03	13.2	0.0885 ± 0.00164	1.10×10^{-3}	1.0000 [g]	5.14×10^{4}	7.32×10^{3}
PT8 Au wire (W)	1.59×10^{0}	4.98	14.9	0.0885 ± 0.00164	1.10×10^{-3}	1.0000 [g]	1.64×10^{4}	2.60×10^{3}
PT8 misc (W) (sum)	9.27×10^{0}	5.88 [f]	20.0 [f]	0.0885 ± 0.00164	1.10×10^{-3}	1.0000 [g]	9.52×10^{4}	1.97×10^{4}

γ-ray/ Sample	Count Rate at EOB: Counts per Second [a]	CLSQ Rel.Unc.[a] (%)	$\overline{\sigma}/\overline{x}$ Rel.Unc.[b] (%)	Absolute Gamma Intensity [c]	Absolute Detector Efficiency [d]	Self-Absorption Factor [e]	A^0 (Bq)	σ_{A^0} (Bq)
479 keV								
PT5 W std	4.41×10^{2}	0.39	0.47	0.218 ± 0.00437	4.08×10^{-4}	0.9994	4.96×10^{6}	2.68×10^{5}
PT5 W enr	2.43×10^{2}	0.35	0.45	0.218 ± 0.00437	4.08×10^{-4}	0.9994	2.74×10^{6}	1.48×10^{5}
PT6 W std	2.65×10^{2}	0.34	0.40	0.218 ± 0.00437	4.08×10^{-4}	0.9994	2.98×10^{6}	1.61×10^{5}
PT6 W enr	5.65×10^{2}	0.39	0.48	0.218 ± 0.00437	4.08×10^{-4}	0.9994	6.35×10^{6}	3.43×10^{5}
PT7 W std	9.99×10^{1}	0.34	0.45	0.218 ± 0.00437	4.08×10^{-4}	0.9994	1.12×10^{6}	6.05×10^{4}
PT7 W enr	6.10×10^{1}	0.38	0.62	0.218 ± 0.00437	4.08×10^{-4}	0.9994	6.86×10^{5}	3.72×10^{4}
PT7 Ag std (W)	2.28×10^{0}	0.52	0.75	0.218 ± 0.00437	4.08×10^{-4}	1.0000 [g]	2.57×10^{4}	1.40×10^{3}
PT7 Au std (W)	2.61×10^{0}	4.23	7.18	0.218 ± 0.00437	4.08×10^{-4}	1.0000 [g]	2.93×10^{4}	2.63×10^{3}
PT7 Au wire (W)	1.33×10^{0}	4.93	6.88	0.218 ± 0.00437	4.08×10^{-4}	1.0000 [g]	1.49×10^{4}	1.30×10^{3}
PT7 misc (W) (sum)	6.22×10^{0}	6.52 [f]	9.97 [f]	0.218 ± 0.00437	4.08×10^{-4}	1.0000 [g]	6.99×10^{4}	7.92×10^{3}
PT8 W std (partial)	6.26×10^{1}	0.39	0.49	0.218 ± 0.00437	4.08×10^{-4}	0.9994	7.04×10^{5}	3.81×10^{4}
PT8 W enr (partial)	5.38×10^{1}	0.39	0.47	0.218 ± 0.00437	4.08×10^{-4}	0.9994	6.05×10^{5}	3.27×10^{4}
PT8 Ag std (partial) (W)	2.41×10^{0}	0.80	1.36	0.218 ± 0.00437	4.08×10^{-4}	1.0000 [g]	2.71×10^{4}	1.51×10^{3}
PT8 Au std (W)	4.28×10^{0}	3.27	5.21	0.218 ± 0.00437	4.08×10^{-4}	1.0000 [g]	4.81×10^{4}	3.60×10^{3}
PT8 Au wire (W)	1.41×10^{0}	4.75	8.02	0.218 ± 0.00437	4.08×10^{-4}	1.0000 [g]	1.58×10^{4}	1.53×10^{3}
PT8 misc (W) (sum)	8.10×10^{0}	5.82 [f]	9.66 [f]	0.218 ± 0.00437	4.08×10^{-4}	1.0000 [g]	9.11×10^{4}	1.01×10^{4}

γ-ray/ Sample	Count Rate at EOB: Counts per Second [a]	CLSQ Rel.Unc.[a] (%)	$\overline{\sigma}/\overline{x}$ Rel.Unc.[b] (%)	Absolute Gamma Intensity [c]	Absolute Detector Efficiency [d]	Self-Absorption Factor [e]	A^0 (Bq)	σ_{A^0} (Bq)
685 keV								
PT5 W std	3.86×10^{2}	0.35	0.37	0.273 ± 0.00601	2.84×10^{-4}	0.9995	4.94×10^{6}	2.70×10^{5}
PT5 W enr	2.12×10^{2}	0.37	0.41	0.273 ± 0.00601	2.84×10^{-4}	0.9995	2.74×10^{6}	1.50×10^{5}
PT6 W std	2.35×10^{2}	0.36	0.37	0.273 ± 0.00601	2.84×10^{-4}	0.9995	3.03×10^{6}	1.66×10^{5}
PT6 W enr	4.92×10^{2}	0.37	0.41	0.273 ± 0.00601	2.84×10^{-4}	0.9995	6.34×10^{6}	3.47×10^{5}
PT7 W std	8.73×10^{1}	0.37	0.42	0.273 ± 0.00601	2.84×10^{-4}	0.9995	1.13×10^{6}	6.19×10^{4}
PT7 W enr	5.40×10^{1}	0.39	0.59	0.273 ± 0.00601	2.84×10^{-4}	0.9995	6.96×10^{5}	3.82×10^{4}
PT7 Ag std (W)	2.01×10^{0}	0.60	0.77	0.273 ± 0.00601	2.84×10^{-4}	1.0000 [g]	2.59×10^{4}	1.43×10^{3}
PT7 Au std (W)	2.59×10^{0}	4.24	5.33	0.273 ± 0.00601	2.84×10^{-4}	1.0000 [g]	3.34×10^{4}	2.55×10^{3}
PT7 Au wire (W)	1.17×10^{0}	5.26	7.89	0.273 ± 0.00601	2.84×10^{-4}	1.0000 [g]	1.50×10^{4}	1.44×10^{3}
PT7 misc (W) (sum)	5.77×10^{0}	6.78 [f]	9.55 [f]	0.273 ± 0.00601	2.84×10^{-4}	1.0000 [g]	7.44×10^{4}	8.19×10^{3}
PT8 W std (partial)	5.46×10^{1}	0.42	0.44	0.273 ± 0.00601	2.84×10^{-4}	0.9995	7.05×10^{5}	3.86×10^{4}
PT8 W enr (partial)	4.72×10^{1}	0.42	0.43	0.273 ± 0.00601	2.84×10^{-4}	0.9995	6.08×10^{5}	3.33×10^{4}
PT8 Ag std (partial) (W)	2.10×10^{0}	0.90	1.22	0.273 ± 0.00601	2.84×10^{-4}	1.0000 [g]	2.70×10^{4}	1.51×10^{3}
PT8 Au std (W)	3.59×10^{0}	3.57	4.64	0.273 ± 0.00601	2.84×10^{-4}	1.0000 [g]	4.63×10^{4}	3.32×10^{3}
PT8 Au wire (W)	1.42×10^{0}	4.72	6.89	0.273 ± 0.00601	2.84×10^{-4}	1.0000 [g]	1.84×10^{4}	1.62×10^{3}
PT8 misc (W) (sum)	7.11×10^{0}	5.82 [f]	8.40 [f]	0.273 ± 0.00601	2.84×10^{-4}	1.0000 [g]	9.17×10^{4}	9.19×10^{3}

[a] CLSQ output
[b] Table C.12
[c] [NNDC 2003]
[d] Table A.2
[e] Table B.1
[f] uncertainties of sums are total uncertainties (square root of the sum of the squares of the addends)
[g] self-absorption for samples with external deposits of W is assumed to be negligible

Table C.14 Cross Section Experiment #2 Tungsten Sample Activities

	Gamma Ray Energy [a]								
	134 keV		479 keV		685 keV				
Sample	A^0 (Bq)	σ_{A^0} (Bq)	A^0 (Bq)	σ_{A^0} (Bq)	A^0 (Bq)	σ_{A^0} (Bq)	$\overline{A^0}$ (Bq)	$\overline{\sigma_{A^0}}$ (Bq)	σ (Bq)
PT5 W std	5.11×10^6	2.74×10^5	4.96×10^6	2.68×10^5	4.94×10^6	2.70×10^5	5.00×10^6	1.56×10^5	7.58×10^4
PT6 W std	3.05×10^6	1.63×10^5	2.98×10^6	1.61×10^5	3.03×10^6	1.66×10^5	3.02×10^6	9.43×10^4	2.88×10^4
PT5 W enr	2.87×10^6	1.54×10^5	2.74×10^6	1.48×10^5	2.74×10^6	1.50×10^5	2.78×10^6	8.69×10^4	6.07×10^4
PT6 W enr	6.48×10^6	3.47×10^5	6.35×10^6	3.43×10^5	6.34×10^6	3.47×10^5	6.39×10^6	2.00×10^5	6.03×10^4
PT7 W std	1.16×10^6	6.21×10^4	1.12×10^6	6.05×10^4	1.13×10^6	6.19×10^4	1.14×10^6	3.56×10^4	1.64×10^4
PT7 W enr	7.07×10^5	3.80×10^4	6.86×10^5	3.72×10^4	6.96×10^5	3.82×10^4	6.97×10^5	2.18×10^4	8.73×10^3
PT7 W misc	6.82×10^4	1.90×10^4	6.99×10^4	7.92×10^3	7.44×10^4	8.19×10^3	7.09×10^4	7.57×10^3	2.52×10^3
PT8 W std (partial)	7.21×10^5	3.86×10^4	7.04×10^5	3.81×10^4	7.05×10^5	3.86×10^4	7.10×10^5	2.22×10^4	7.73×10^3
PT8 W enr (partial)	6.19×10^5	3.31×10^4	6.05×10^5	3.27×10^4	6.08×10^5	3.33×10^4	6.11×10^5	1.91×10^4	5.81×10^3
PT8 W misc	9.52×10^4	1.97×10^4	9.11×10^4	1.01×10^4	9.17×10^4	9.19×10^3	9.27×10^4	7.89×10^3	1.97×10^3

[a] Table C.13

Table C.15 Cross Section Experiment #2 Tungsten Activities

Sample	Mass (μg)	A^0 [a] (Bq μg^{-1})	σ_{A^0} [a] (Bq μg^{-1})	$\overline{A^0}$ (Bq μg^{-1})	$\overline{\sigma_{A^0}}$ (Bq μg^{-1})	σ (Bq μg^{-1})	A^0 (Bq mg^{-1})	σ_{A^0} (Bq mg^{-1})
PT5 W std	7.11	7.04 x 10^5	2.19 x 10^4	7.06 x 10^5	1.55 x 10^4	2.78 x 10^3	7.06 x 10^8	1.55 x 10^7
PT6 W std	4.26	7.09 x 10^5	2.21 x 10^4					
PT5 W enr	9.78	2.84 x 10^5	8.89 x 10^3	2.73 x 10^5	6.04 x 10^3	1.17 x 10^4	2.73 x 10^8	1.17 x 10^7
PT6 W enr	24.5	2.61 x 10^5	8.16 x 10^3					
PT7 W std	199	5.71 x 10^3	1.79 x 10^2				5.71 x 10^6	1.79 x 10^5
PT7 W std+misc	199	6.07 x 10^3	1.90 x 10^2 [b]				6.07 x 10^6	1.90 x 10^5
PT8 W std (partial)	284	2.50 x 10^3	7.82 x 10^1				–	–
PT8 W std+misc	284	2.83 x 10^3	8.85 x 10^1 [b]				–	–
PT7 W enr	196	3.55 x 10^3	1.11 x 10^2				3.55 x 10^6	1.11 x 10^5
PT7 W enr+misc	196	3.92 x 10^3	1.23 x 10^2 [b]				3.92 x 10^6	1.23 x 10^5
PT8 W enr (partial)	293	2.08 x 10^3	6.52 x 10^1				–	–
PT8 W enr+misc	293	2.40 x 10^3	7.52 x 10^1 [b]				–	–

[a] A^0 and uncertainty in Bq from Table C.14

[b] same % uncertainty as std or enr main sample

A summary of gamma ray spectroscopy data for all gold flux monitors is provided in Table C.16. All capsules contained gold wires and all but PT6 contained gold AAS standard samples.

Table C.17 is a calculation of gold flux monitor sample activities as described in Appendix C.1 for Table C.6.

Table C.18 is a calculation of shielded and unshielded gold AAS standard and wire activities as described in Appendix C.1 for Table C.7. At this point, average shielded values cannot be calculated because PT7 and PT8 had different irradiation durations.

Table C.19 is a calculation of silver flux monitor sample activities as described in Appendix C.1 for Table C.8. Unlike the first cross section experiment, the silver flux monitor samples were counted on the 5 cm shelf as well as the 30 cm shelf. This was done because of the low activity levels in the shielded samples. Samples were counted on both shelves to verify consistency of results (see the discussion of cobalt analysis on different shelves associated with Table C.10). A weighted average of all analyses for each sample was calculated because the different analyses had greatly different total counts.

Table C.20 is a calculation of silver flux monitor activities in units of activity per unit mass. As with the gold flux monitors, an average value for shielded activity (PT7 and PT8) is not appropriate because of the different irradiation durations.

Table C.16 Cross Section Experiment #2 Gamma Ray Spectroscopy Data for Gold

Sample	Shelf (cm)	Count Time (s)	Dead Time (%)	Time Since EOB (d:h:m)	411 keV γ-ray Total Counts	411 keV γ-ray Absolute Uncert.	411 keV γ-ray Rel.Unc. (%)
PT5 Au	30	180	5.31	1:2:21	7.45×10^4	2.80×10^2	0.4 [a]
std	30	120	4.15	2:0:00	3.94×10^4	2.02×10^2	0.5 [a]
	30	120	2.36	4:3:29	2.30×10^4	1.54×10^2	0.7
	30	120	1.48	6:2:04	1.41×10^4	1.20×10^2	0.8
	30	120	1.15	7:1:19	1.10×10^4	1.06×10^2	1.0
$\bar{\sigma}/\bar{x}$							0.32
PT5 Au	30	180	6.59	1:2:15	9.53×10^4	3.16×10^2	0.3 [a]
wire	30	120	5.14	2:0:04	5.06×10^4	2.28×10^2	0.5 [a]
	30	120	2.99	4:3:32	2.99×10^4	1.76×10^2	0.6
	30	120	1.80	6:2:07	1.82×10^4	1.36×10^2	0.7
	30	120	1.48	7:1:22	1.40×10^4	1.20×10^2	0.9
$\bar{\sigma}/\bar{x}$							0.28
PT6 Au	30	120	8.75	1:2:22	8.53×10^4	3.00×10^2	0.4 [a]
wire	30	120	6.98	1:23:30	6.87×10^4	2.67×10^2	0.4 [a]
	30	180	5.01	3:6:41	7.43×10^4	2.77×10^2	0.4
	30	120	4.08	4:2:38	4.01×10^4	2.03×10^2	0.5
	30	120	2.52	6:1:13	2.48×10^4	1.60×10^2	0.6
	30	120	1.96	7:0:28	1.91×10^4	1.40×10^2	0.7
$\bar{\sigma}/\bar{x}$							0.24
PT7 Au	30	420	0.45	1:6:47	1.18×10^4	1.11×10^2	0.9
std	30	900	0.19	4:6:22	1.15×10^4	1.08×10^2	0.9
	30	1800	0.09	7:4:57	1.09×10^4	1.07×10^2	1.0
$\bar{\sigma}/\bar{x}$							0.55
PT7 Au	30	600	0.33	1:5:46	1.35×10^4	1.18×10^2	0.9
wire	30	1200	0.15	4:6:00	1.25×10^4	1.14×10^2	0.9
	30	2700	0.08	7:4:10	1.31×10^4	1.16×10^2	0.9
$\bar{\sigma}/\bar{x}$							0.51
PT8 Au	30	420	0.52	1:6:21	1.22×10^4	1.14×10^2	0.9
std	30	900	0.20	4:5:42	1.19×10^4	1.11×10^2	0.9
	30	1800	0.10	7:4:10	1.12×10^4	1.08×10^2	1.0
$\bar{\sigma}/\bar{x}$							0.55
PT8 Au	30	600	0.38	1:5:18	1.55×10^4	1.26×10^2	0.8
wire	30	1200	0.17	4:5:21	1.42×10^4	1.22×10^2	0.9
	30	1800	0.09	7:4:42	9.70×10^3	1.00×10^2	1.0
$\bar{\sigma}/\bar{x}$							0.52

[a] data point not used in calculations of A^0 and uncertainty

Table C.17 Cross Section Experiment #2 Gold Sample Activities

	Count Rate at EOB							
Sample	Counts per Second [a]	CLSQ Rel.Unc.[a] (%)	$\bar{\sigma}/\bar{x}$ Rel.Unc.[b] (%)	Absolute Gamma Intensity [c]	Absolute Detector Efficiency [d]	Self-Absorption Factor [e]	A^0 (Bq)	σ_{A^0} (Bq)
PT5 Au std	5.60×10^{2}	0.46	0.32	0.9558 ± 0.0012	4.74×10^{-4}	0.9994	1.24×10^{6}	6.21×10^{4}
PT5 Au wire	7.24×10^{2}	0.40	0.28	0.9558 ± 0.0012	4.74×10^{-4}	0.9976	1.60×10^{6}	8.02×10^{4}
PT6 Au wire	9.64×10^{2}	0.32	0.24	0.9558 ± 0.0012	4.74×10^{-4}	0.9976	2.13×10^{6}	1.07×10^{5}
PT7 Au std	3.87×10^{1}	0.54	0.55	0.9558 ± 0.0012	4.74×10^{-4}	0.9994	8.56×10^{4}	4.31×10^{3}
PT7 Au wire	3.10×10^{1}	0.51	0.51	0.9558 ± 0.0012	4.74×10^{-4}	0.9976	6.86×10^{4}	3.45×10^{3}
PT8 Au std	3.94×10^{1}	0.66	0.55	0.9558 ± 0.0012	4.74×10^{-4}	0.9994	8.71×10^{4}	4.38×10^{3}
PT8 Au wire	3.53×10^{1}	0.58	0.52	0.9558 ± 0.0012	4.74×10^{-4}	0.9976	7.81×10^{4}	3.93×10^{3}

[a] CLSQ output
[b] Table C.16
[c] [NNDC 2003]
[d] Table A.2
[e] Table B.1 (std), Table B.3 (wire)

Table C.18 Cross Section Experiment #2 Gold Activities

Sample	Mass (μg)	A^0 [a] (Bq μg^{-1})	σ_{A^0} [a] (Bq μg^{-1})	$\overline{A^0}$ (Bq μg^{-1})	$\overline{\sigma_{A^0}}$ (Bq μg^{-1})	σ (Bq μg^{-1})	A^0 (Bq mg^{-1})	σ_{A^0} (Bq mg^{-1})
PT5 Au std	2.00	6.19 x 10^5	3.11 x 10^4				6.19 x 10^8	3.11 x 10^7
PT5 Au wire	2.32	6.91 x 10^5	3.46 x 10^4	6.80 x 10^5	2.41 x 10^4	1.09 x 10^4	6.80 x 10^8	2.41 x 10^7
PT6 Au wire	3.19	6.69 x 10^5	3.35 x 10^4					
PT7 Au std	10.0	8.56 x 10^3	4.31 x 10^2				8.56 x 10^6	4.31 x 10^5
PT7 Au wire	6.03	1.14 x 10^4	5.72 x 10^2				1.14 x 10^7	5.72 x 10^4
PT8 Au std	15.0	5.81 x 10^3	2.92 x 10^2				5.81 x 10^6	2.92 x 10^5
PT8 Au wire	9.51	8.21 x 10^3	4.13 x 10^2				8.21 x 10^6	4.13 x 10^5

[a] A^0 and uncertainty in Bq from Table C.17

Table C.19 Cross Section Experiment #2 Gamma Ray Spectroscopy Data for Silver

Sample	Shelf (cm)	Count Time (s)	Dead Time (%)	Time Since EOB (d:h:m)	Total Counts	Absolute Uncert.	Counts per Second	Absolute Gamma Intensity [a]	Absolute Detector Efficiency [b]	Self-Absorption Factor [c]	A (Bq)	A^0 (Bq)	σ_{A^0} (Bq)
PT6 Ag	30	9600.2	0.09	4:22:02	9.55×10^{3}	1.25×10^{2}	9.95×10^{-1}	0.9430 ± 0.003	2.97×10^{-4}	0.9956	3.57×10^{3}	3.62×10^{3}	1.87×10^{2}
wire	5	900	0.76	7:3:16	1.40×10^{4}	1.37×10^{2}	1.56×10^{1}	0.9430 ± 0.003	4.66×10^{-3}	0.9956	3.56×10^{3}	3.63×10^{3}	1.85×10^{2}
weighted average												3.62×10^{3}	1.86×10^{2}
PT6 Ag	30	10800.3	0.04	5:21:59	3.67×10^{3}	7.76×10^{1}	3.40×10^{-1}	0.9430 ± 0.003	2.97×10^{-4}	0.9995	1.22×10^{3}	1.24×10^{3}	6.74×10^{1}
std	30	54000	0.04	21:2:48	1.78×10^{4}	1.70×10^{2}	3.30×10^{-1}	0.9430 ± 0.003	2.97×10^{-4}	0.9995	1.18×10^{3}	1.25×10^{3}	6.38×10^{1}
	5	1800	0.30	6:15:33	9.77×10^{3}	1.19×10^{2}	5.43×10^{0}	0.9430 ± 0.003	4.66×10^{-3}	0.9995	1.24×10^{3}	1.26×10^{3}	6.50×10^{1}
weighted average												1.25×10^{3}	6.46×10^{1}
PT7 Ag	30	25600	0.05	2:13:09	1.19×10^{3}	4.85×10^{1}	4.65×10^{-2}	0.9430 ± 0.003	2.97×10^{-4}	0.9995	1.66×10^{2}	1.67×10^{2}	1.08×10^{1}
std	30	42510.5	0.04	3:10:04	1.93×10^{3}	6.22×10^{1}	4.54×10^{-2}	0.9430 ± 0.003	2.97×10^{-4}	0.9995	1.62×10^{2}	1.64×10^{2}	9.77×10^{0}
	30	59000.3	0.03	4:7:28	2.61×10^{3}	6.92×10^{1}	4.42×10^{-2}	0.9430 ± 0.003	2.97×10^{-4}	0.9995	1.58×10^{2}	1.60×10^{2}	9.07×10^{0}
	5	14400	0.06	7:20:16	1.02×10^{4}	1.16×10^{2}	7.08×10^{-1}	0.9430 ± 0.003	4.66×10^{-3}	0.9995	1.61×10^{2}	1.65×10^{2}	8.48×10^{0}
weighted average												1.64×10^{2}	8.91×10^{0}
PT8 Ag	30	9000.4	0.08	1:21:04	4.10×10^{2}	3.27×10^{1}	4.56×10^{-2}	0.9430 ± 0.003	2.97×10^{-4}	0.9995	1.63×10^{2}	1.64×10^{2}	1.54×10^{1}
std	30	13444.7	0.05	2:20:32	5.86×10^{2}	3.72×10^{1}	4.36×10^{-2}	0.9430 ± 0.003	2.97×10^{-4}	0.9995	1.56×10^{2}	1.57×10^{2}	1.27×10^{1}
	30	11000.6	0.03	3:23:21	5.48×10^{2}	3.58×10^{1}	4.98×10^{-2}	0.9430 ± 0.003	2.97×10^{-4}	0.9995	1.78×10^{2}	1.80×10^{2}	1.48×10^{1}
	30	56073.4	0.02	6:3:17	2.72×10^{3}	9.60×10^{1}	4.85×10^{-2}	0.9430 ± 0.003	2.97×10^{-4}	0.9995	1.73×10^{2}	1.76×10^{2}	1.08×10^{1}
	5	14700.2	0.06	7:23:04	1.07×10^{4}	1.20×10^{2}	7.28×10^{-1}	0.9430 ± 0.003	4.66×10^{-3}	0.9995	1.66×10^{2}	1.69×10^{2}	8.68×10^{0}
weighted average												1.70×10^{2}	9.63×10^{0}

[a] [NNDC 2003]
[b] Table A.2
[c] Table B.1 (std), Table B.3 (wire)

Table C.20 Cross Section Experiment #2 Silver Activities

Sample	Mass (μg)	$A^{0\,a}$ (Bq)	$\sigma_{A^0}{}^{a}$ (Bq)	A^0 (Bq mg^{-1})	σ_{A^0} (Bq mg^{-1})
PT6 Ag wire	7.19	3.62 x 10^3	1.86 x 10^2	5.03 x 10^5	2.59 x 10^4
PT6 Ag std	2.41	1.25 x 10^3	6.46 x 10^1	5.17 x 10^5	2.68 x 10^4
PT7 Ag std	19.3	1.64 x 10^2	8.91 x 10^0	8.50 x 10^3	4.62 x 10^2
PT8 Ag std	28.9	1.70 x 10^2	9.63 x 10^0	5.88 x 10^3	3.33 x 10^2

[a] Table C.19

An initial analysis of the gold flux monitor data indicated that the thermal-to-epithermal flux ratio was 40, as opposed to the value of approximately 20 found in cross section experiment #1. Consequently, the conversion factor between σ_0 and σ_{th} was recalculated using a ratio of 40 in Equation C.9 and the new value, 1.01, was incorporated in the flux and cross section calculation spreadsheets, Figures C.5 – C.7.

Figure C.5 is the spreadsheet used to calculate thermal and epithermal flux from the gold flux monitor data using the same method described for cross section experiment #1 in Appendix C.1 for Figure C.1. In cross section experiment #2, however, an average value for epithermal flux is calculated based on the results from gold flux monitors in PT7 and PT8. As mentioned previously, activities for PT7 and PT8 gold flux monitor samples (8.56 x 10^6 and 5.81 x 10^6 n cm^{-2} s^{-1}, respectively) could not be averaged because of their different irradiation durations. The spreadsheet accounts for the different values (t_{irr}) in the calculations under the heading "A_{198} RHS." Uncertainty in the value of epithermal flux is due primarily to the uncertainties in sample activities and the resonance integral for ^{197}Au:

$$\sigma_{\phi_{ep}} = \sqrt{\left(\frac{4.31\times10^5}{8.56\times10^6}\right)^2 + \left(\frac{2.92\times10^5}{5.81\times10^6}\right)^2 + \left(\frac{28}{1550}\right)^2} = 7.34\%$$

t_{irr} (s)	PT5, PT6	1200	PT7	60	PT8	44				
σ_0^{197}	98.65	b	σ_{th}^{197}	99.64	I_0^{197}	1550	b	M_{197}	196.9666	g
σ_0^{198}	25100	b	σ_{th}^{198}	25351	I_0^{198}	1	b	M_{198}	197.9682	g
λ_{198}	2.977E-06	s^{-1}	$t_{1/2}^{198}$	2.33E+05	s					
$A_{198} = \lambda_{198}N_{198} = \lambda_{198}(\Lambda^*_{197}/\Lambda_{198}-\Lambda_{197})N^o_{197}(e^{-\Lambda_{197}t}-e^{-\Lambda_{198}t})$										
					Epithermal Flux Determination					
Sample				A^0_{198} (Bq/mg ^{197}Au)	ϕ_{ep} (n cm^{-2} s^{-1})	Λ^*_{197} (s^{-1})	Λ_{197} (s^{-1})	Λ_{198} (s^{-1})	A_{198} RHS (Bq/mg)	
Unshielded (PT5 std)				6.19E+08						
Shielded (PT7 std)				8.56E+06	1.01E+13	1.57E-08	1.57E-08	2.98E-06	8.56E+06	
Shielded (PT8 std)				5.81E+06	9.36E+12	1.45E-08	1.45E-08	2.98E-06	5.81E+06	
				average	9.73E+12					
calculated activity induced by a 20 minute irradiation of Au under a Cd cover (using epithermal flux from PT7 and PT8 std average):										
$A_{198} = \lambda_{198}N_{198} = \lambda_{198}(\Lambda^*_{197}/\Lambda_{198}-\Lambda_{197})N^o_{197}(e^{-\Lambda_{197}t}-e^{-\Lambda_{198}t})/M^0_{197}$					9.73E+12	1.51E-08	1.51E-08	2.98E-06	1.64E+08	
				Thermal Flux Determination						
				A_{198} Unshielded-Shielded (Bq/mg)	ϕ_0 (n cm^{-2} s^{-1})	Λ^*_{197} (s^{-1})	Λ_{197} (s^{-1})	Λ_{198} (s^{-1})	A_{198} RHS (Bq/mg)	
Unshielded (PT5 std) - calculated shielded				4.54E+08	4.21E+14	4.19E-08	4.19E-08	1.36E-05	4.54E+08	
				ϕ_0/ϕ_{ep}	43.2					

Figure C.5 Cross Section Experiment #2 Calculation of Neutron Flux from Gold Flux Monitor Data

t_{irr}	PT6	1200	PT7	60	PT8	44				
$\sigma_0^{109\text{-}110m}$	4.7	b	$\sigma_{th}^{109\text{-}110m}$	4.7	$I_0^{109\text{-}110m}$	72.3	b	M_{109}	108.9048	g
$\sigma_0^{109\text{-}110m+g}$	91	b	$\sigma_{th}^{109\text{-}110m+g}$	91.9	$I_0^{109\text{-}110m+g}$	1400	b			
σ_0^{110m}	82	b	σ_{th}^{110m}	82.8	I_0^{110m}	93.88	b	M_{110m}	109.90624	g
λ_{110m}	3.212E-08	s^{-1}	$t_{1/2}^{110m}$	2.16E+07	s					
$A_{110m} = \lambda_{110m}N_{110m} = \lambda_{110m}(\Lambda^*_{109}/\Lambda_{110m}-\Lambda_{109})N^o_{109}(e^{-\Lambda_{109}t}-e^{-\Lambda_{110m}t})$										
					Epithermal Flux Determination					
Sample				A^0_{110m} (Bq/mg ^{109}Ag)	ϕ_{ep} (n cm^{-2} s^{-1})	Λ^*_{109} (s^{-1})	Λ_{109} (s^{-1})	Λ_{110m} (s^{-1})	A_{110m} RHS (Bq/mg)	
Unshielded				5.17E+05						
Shielded (PT7)				8.50E+03	1.10E+13	7.98E-10	1.54E-08	3.32E-08	8.50E+03	
Shielded (PT8)				5.88E+03	1.04E+13	7.52E-10	1.46E-08	3.31E-08	5.88E+03	
				average	1.07E+13					
calculated activity induced by a 20 minute irradiation of Ag under a Cd cover (using epithermal flux from PT7 and PT8 average):										
$A_{110m} = \lambda_{110m}N_{110m} = \lambda_{110m}(\Lambda^*_{109}/\Lambda_{110m}-\Lambda_{109})N^o_{109}(e^{-\Lambda_{109}t}-e^{-\Lambda_{110m}t})/M^0_{109}$					1.07E+13	7.75E-10	1.50E-08	3.31E-08	1.65E+05	
					Thermal Flux Determination					
				A_{110m} Unshielded-Shielded (Bq/mg)	ϕ_0 (n cm^{-2} s^{-1})	Λ^*_{109} (s^{-1})	Λ_{109} (s^{-1})	Λ_{110m} (s^{-1})	A_{110m} RHS (Bq/mg)	
Unshielded - calculated shielded				3.52E+05	3.48E+14	1.65E-09	3.20E-08	6.09E-08	3.52E+05	
				ϕ_0/ϕ_{ep}	32.4					

Figure C.6 Cross Section Experiment #2 Calculation of Neutron Flux from Silver Flux Monitor Data

t_{irr}	PT5, PT6	1200	PT7	60	PT8	43				
σ_0^{186}	43.45	b	σ_{th}^{186}	44.31	I_0^{186}	395.15	b	M_{186}	185.9544	g
σ_0^{187}	64	b	σ_{th}^{187}	64.64	I_0^{187}	2760	b	M_{187}	186.9572	g
λ_{187}	8.117E-06	s^{-1}	$t_{1/2}^{187}$	85392	s					
$A_{187} = \lambda_{187}N_{187} = \lambda_{187}(\Lambda^*_{186}/\Lambda_{187}-\Lambda_{186})N^o_{186}(e^{-\Lambda_{186}t}-e^{-\Lambda_{187}t})$										
					Resonance Integral Determination					
Sample				A^0_{187} (Bq/mg ^{186}W)	ϕ_{ep} (n cm^{-2} s^{-1})	I_0^{186} (b)	Λ^*_{186} (s^{-1})	Λ_{186} (s^{-1})	Λ_{187} (s^{-1})	A_{187} RHS (Bq/mg)
Unshielded				7.06E+08						
Shielded (PT7 std)				5.71E+06	9.73E+12	371.95	3.62E-09	3.62E-09	8.14E-06	5.71E+06
Shielded (PT7 std+misc)				6.07E+06	9.73E+12	395.15	3.85E-09	3.85E-09	8.14E-06	6.06E+06
activity induced by a 20 minute irradiation of W under a Cd cover (using epithermal flux from Au std and I_0 from PT7 std+misc):										
$A_{187} = \lambda_{187}N_{187} = \lambda_{187}(\Lambda^*_{186}/\Lambda_{187}-\Lambda_{186})N^o_{186}(e^{-\Lambda_{186}t}-e^{-\Lambda_{187}t})/M^o_{186}$					9.73E+12	395.15	3.85E-09	3.85E-09	8.14E-06	1.21E+08
				Thermal Cross Section Determination						
				A_{187} Unshielded-Shielded (Bq/mg)	ϕ_0 (n cm^{-2} s^{-1})	σ_{th}^{186} (b)	Λ^*_{186} (s^{-1})	Λ_{186} (s^{-1})	Λ_{187} (s^{-1})	A_{187} RHS (Bq/mg)
Unshielded - calculated shielded				5.86E+08	4.21E+14	44.31	1.87E-08	1.87E-08	8.14E-06	5.86E+08

Figure C.7 Cross Section Experiment #2 Calculation of Tungsten Cross Sections

Thermal flux is calculated as in Figure C.1 except that the shielded activities (PT7 and PT8) can't be directly subtracted from the unshielded activity (PT5) because of the different irradiation durations. Instead, a calculation is performed to determine the activity that would be induced in gold irradiated 20 minutes (PT5 irradiation time) under a cadmium cover, using the epithermal flux determined from PT7 and PT8 activities. That activity (1.64×10^8 Bq mg^{-1}) is subtracted from the unshielded activity (6.19×10^8 Bq mg^{-1}) to derive the activity induced by thermal neutrons in the unshielded sample. Uncertainty in the value of thermal flux is due primarily to the uncertainties in sample activities and the resonance integral for ^{197}Au:

$$\sigma_{\phi_0} = \sqrt{\left(\frac{4.31\times10^5}{8.56\times10^6}\right)^2 + \left(\frac{2.92\times10^5}{5.81\times10^6}\right)^2 + \left(\frac{3.11\times10^7}{6.19\times10^8}\right)^2 + \left(\frac{0.09}{98.65}\right)^2} = 8.71\%$$

Thermal and epithermal fluxes are calculated from the silver flux monitor data using the same method (Figure C). Uncertainties in the calculated fluxes are:

$$\sigma_{\phi_{ep}} = \sqrt{\left(\frac{4.62\times10^2}{8.50\times10^3}\right)^2 + \left(\frac{3.33\times10^2}{5.88\times10^3}\right)^2 + \left(\frac{4.0}{72.3}\right)^2} = 9.60\%$$

$$\sigma_{\phi_0} = \sqrt{\left(\frac{4.62\times10^2}{8.50\times10^3}\right)^2 + \left(\frac{3.33\times10^2}{5.88\times10^3}\right)^2 + \left(\frac{2.68\times10^4}{5.17\times10^5}\right)^2 + \left(\frac{0.2}{4.7}\right)^2} = 10.3\%$$

Figure C.7 presents the spreadsheet used to calculate the thermal cross section and resonance integral for ^{187}W based on the gold flux monitor data using the method described for Figure C.4 in Appendix C.1. As in Figures C.5 and C.6, a modification was

made to calculate shielded activity due to the different irradiation times for the shielded and unshielded samples. The resonance integral was calculated using both the activity from the PT7 tungsten sample alone and with the "miscellaneous" tungsten activity added to the PT7 activity. The combined activity results in a resonance integral (395 b) that is 6% greater than that from the PT7 activity alone (372 b). It is reasonable to use the combined activity value since it was earlier shown that some of the PT7 standard sample leaked from its foil package and while the "miscellaneous" activity is also due to the PT7 enriched tungsten sample, it is unlikely that all the leaked material is accounted for in the "miscellaneous" activity. The value of 395 b was used to calculate the induced activity for the thermal cross section calculation (using 395 b resulted in a 2200 m/s cross section of 43.5 b; using 372 b for the resonance integral produces a 2200 m/s cross section of 44.0 b, a difference of approximately 1%).

Uncertainties in the cross sections are primarily due to uncertainties in the thermal and epithermal fluxes derived from the gold flux monitors and the tungsten sample activities:

$$\sigma_{I_0} = \sqrt{(0.0734)^2 + \left(\frac{1.90\times10^5}{6.07\times10^6}\right)^2} = 7.98\%$$

$$\sigma_{\sigma_0} = \sqrt{(0.0871)^2 + \left(\frac{1.90\times10^5}{6.07\times10^6}\right)^2 + \left(\frac{1.55\times10^7}{7.06\times10^8}\right)^2} = 9.51\%$$

Appendix D Neutron Self-Shielding Experiments Data

Table D.1 Tungsten Cylinder Self-Shielding Experiment Gamma Ray Spectroscopy Data [a]

Cylinder	Time Since EOB (d:h:m)	Count Time (m)	Dead Time (%)	Activity (Total Counts)						
				^{187}W γ-ray			^{188}Re γ-ray			^{188}W γ-ray
				134 keV	479 keV	685 keV	155 keV	478 keV	633 keV	291 keV
1	16:1:13	5.00	7.4	1.04×10^4	3.12×10^4	2.84×10^4	1.21×10^3			
	17:3:36	10.00	4.5	9.39×10^3	2.93×10^4	2.67×10^4	1.56×10^3			
	18:6:45	15.00	3.2	5.96×10^3	1.98×10^4	1.82×10^4	2.38×10^3		1.37×10^2	
	19:2:05	30.00	2.7	6.74×10^3	2.30×10^4	2.08×10^4	4.67×10^3		3.75×10^2	
	21:3:19	120.00	2.1	7.23×10^3	2.23×10^4	1.93×10^4	1.95×10^4		1.29×10^3	4.82×10^2
	22:3:46	300.00	2.1	7.91×10^3	2.81×10^4	2.27×10^4	4.78×10^4		2.62×10^3	1.34×10^3
	32:3:32	900.00	1.9				1.30×10^5	7.92×10^3	9.14×10^3	4.16×10^3
	37:6:19	1344.82	1.8				1.81×10^5	1.15×10^4	1.29×10^4	4.33×10^3
	43:4:58	2160.00	1.7				2.81×10^5	1.67×10^4	1.94×10^4	7.61×10^3
	53:2:24	1030.15	1.6				1.20×10^5	7.47×10^3	8.40×10^3	3.35×10^3
	60:0:55	1367.66	1.5				1.52×10^5	9.12×10^3	1.04×10^4	4.46×10^3
	64:23:35	2160.00	1.4				2.23×10^5	1.36×10^4	1.54×10^4	5.12×10^3
	71:2:29	2160.00	1.4				2.12×10^5	1.28×10^4	1.49×10^4	5.24×10^3
2	17:4:01	5.00	10.1	9.13×10^3	3.52×10^4	3.24×10^4	1.71×10^3			
	18:7:02	10.00	6.9	7.95×10^3	3.27×10^4	3.02×10^4	3.29×10^3		2.16×10^2	
	19:3:04	20.00	5.7	8.33×10^3	3.71×10^4	3.36×10^4	7.26×10^3		5.74×10^2	
	21:1:13	85.01	4.5	1.04×10^4	4.22×10^4	3.69×10^4	2.97×10^4		2.39×10^3	8.84×10^2
	21:21:58	120.00	4.3	7.98×10^3	3.33×10^4	2.80×10^4	3.96×10^4		3.23×10^3	1.30×10^3
	32:1:07	120.00	3.8				3.66×10^4	2.52×10^3	2.94×10^3	1.03×10^3
	33:3:58	600.00	3.8				1.81×10^5	1.33×10^4	1.49×10^4	5.77×10^3
	39:3:00	900.00	3.6				2.56×10^5	1.84×10^4	2.14×10^4	8.36×10^3
	42:4:24	855.01	3.5				2.36×10^5	1.70×10^4	1.99×10^4	7.85×10^3
	47:3:50	900.00	3.4				2.37×10^5	1.72×10^4	1.97×10^4	7.80×10^3
	56:3:01	900.00	3.2				2.14×10^5	1.57×10^4	1.80×10^4	6.53×10^3
	68:1:33	900.00	2.9				1.91×10^5	1.40×10^4	1.61×10^4	5.70×10^3

Cylinder	Time Since EOB (d:h:m)	Count Time (m)	Dead Time (%)	Activity (Total Counts)						
				^{187}W γ-ray			^{188}Re γ-ray			^{188}W γ-ray
				134 keV	479 keV	685 keV	155 keV	478 keV	633 keV	291 keV
3	17:3:54	5.00	15.7	1.46×10^4	5.63×10^4	5.23×10^4	2.91×10^3		1.66×10^2	
	18:7:14	10.00	10.7	1.39×10^4	5.21×10^4	4.85×10^4	5.64×10^3		5.10×10^2	
	19:3:27	15.00	8.8	1.31×10^4	4.44×10^4	4.04×10^4	8.30×10^3		6.74×10^2	
	20:23:24	41.67	6.9	8.45×10^3	3.52×10^4	3.13×10^4	2.27×10^4		1.94×10^3	3.36×10^2
	22:0:05	90.00	6.6	8.74×10^3	3.80×10^4	3.24×10^4	4.80×10^4		4.15×10^3	1.27×10^3
	31:19:40	300.00	5.9				1.43×10^5	1.10×10^4	1.27×10^4	4.72×10^3
	34:5:25	600.00	5.7				2.80×10^5	2.12×10^4	2.47×10^4	9.83×10^3
	40:2:17	600.00	5.5				2.64×10^5	2.03×10^4	2.32×10^4	8.36×10^3
	44:18:22	600.00	5.3				2.53×10^5	1.94×10^4	2.25×10^4	9.07×10^3
	48:19:11	491.68	5.2				1.98×10^5	1.54×10^4	1.74×10^4	6.45×10^3
	57:6:00	900.00	4.9				3.33×10^5	2.56×10^4	2.97×10^4	1.05×10^4
	69:2:06	900.00	4.4				2.95×10^5	2.29×10^4	2.57×10^4	1.14×10^4
	70:1:32	900.00	4.4				2.93×10^5	2.28×10^4	2.64×10^4	1.09×10^4
4	17:4:14	3.00	21.7	1.17×10^4	4.59×10^4	4.27×10^4	1.43×10^3			
	18:7:26	7.00	14.9	1.29×10^4	5.08×10^4	4.70×10^4	5.16×10^3		4.87×10^2	
	19:3:45	10.00	12.3	1.09×10^4	4.11×10^4	3.78×10^4	7.27×10^3		7.05×10^2	
	21:2:44	30.00	9.6	7.30×10^3	3.29×10^4	2.89×10^4	2.25×10^4		2.15×10^3	9.13×10^2
	22:1:43	60.00	9.2	7.64×10^3	3.51×10^4	2.99×10^4	4.41×10^4		3.95×10^3	1.19×10^3
	31:19:01	30.00	8.2				2.05×10^4	1.57×10^3	1.94×10^3	7.16×10^2
	32:22:26	300.00	8.1				2.01×10^5	1.58×10^4	1.82×10^4	7.17×10^3
	39:18:53	300.00	7.8				1.86×10^5	1.49×10^4	1.71×10^4	6.63×10^3
	42:19:13	275.01	7.6				1.68×10^5	1.34×10^4	1.55×10^4	6.15×10^3
	48:2:29	900.00	7.3				5.18×10^5	4.20×10^4	4.71×10^4	1.84×10^4
	58:5:50	900.00	6.9				4.70×10^5	3.74×10^4	4.28×10^4	1.54×10^4
	64:3:04	900.00	6.5				4.42×10^5	3.52×10^4	4.09×10^4	1.62×10^4

Cylinder	Time Since EOB (d:h:m)	Count Time (m)	Dead Time (%)	Activity (Total Counts)						
				^{187}W γ-ray			^{188}Re γ-ray			^{188}W γ-ray
				134 keV	479 keV	685 keV	155 keV	478 keV	633 keV	291 keV
5	17:4:19	2.00	28.4	1.06×10^4	4.02×10^4	3.74×10^4	1.08×10^3			
	17:19:35	5.00	19.8	1.25×10^4	4.84×10^4	4.39×10^4	5.28×10^3		4.86×10^2	
	19:3:58	10.00	16.3	1.43×10^4	5.40×10^4	5.03×10^4	1.05×10^4		1.03×10^3	
	20:19:56	14.25	13.2	7.74×10^3	2.51×10^4	2.25×10^4	1.56×10^4		1.40×10^3	4.69×10^2
	20:20:22	30.00	13.1	1.27×10^4	5.23×10^4	4.68×10^4	3.22×10^4		2.89×10^3	1.22×10^3
	22:2:51	45.00	12.2	7.32×10^3	3.26×10^4	2.88×10^4	4.83×10^4		4.25×10^3	1.32×10^3
	31:18:32	20.00	11.0				1.98×10^4	1.42×10^3	1.76×10^3	6.45×10^2
	32:18:55	180.00	11.0				1.75×10^5	1.38×10^4	1.56×10^4	5.35×10^3
	33:18:12	300.00	10.9				2.85×10^5	2.23×10^4	2.59×10^4	8.94×10^3
	38:18:49	300.00	10.5				2.76×10^5	2.15×10^4	2.47×10^4	9.31×10^3
	43:0:23	245.00	10.1				2.15×10^5	1.67×10^4	1.91×10^4	7.07×10^3
	47:20:47	300.00	9.8				2.52×10^5	1.99×10^4	2.24×10^4	9.15×10^3
	58:0:02	300.00	9.2				2.28×10^5	1.81×10^4	2.08×10^4	7.67×10^3
	63:21:32	300.00	8.7				2.16×10^5	1.67×10^4	1.93×10^4	7.24×10^3
	67:4:35	600.00	8.5				4.16×10^5	3.27×10^4	3.75×10^4	1.39×10^4

[a] all counts taken on shelf 60

Table D.2 Tungsten Foil Self-Shielding Experiments Gamma Ray Spectroscopy Data

Foil	Shelf (cm)	Time Since EOB (d:h:m)	Count Time (m)	Dead Time (%)	Activity (Total Counts) ^{187}W γ-ray 134 keV	^{187}W γ-ray 479 keV	^{187}W γ-ray 685 keV	^{188}Re γ-ray 155 keV
0.25 mm Foil								
1	60	15:20:43	5	9.5	2.09×10^4	2.81×10^4	2.46×10^4	2.59×10^3
	60	17:0:14	10	6.5	1.95×10^4	2.54×10^4	2.25×10^4	5.95×10^3
	60	18:3:22	10	5.2	9.16×10^3	1.19×10^4	1.04×10^4	6.02×10^3
	60	28:19:18	30	3.9				1.63×10^4
	60	36:22:53	30	3.6				1.47×10^4
	60	46:18:28	30	3.4				1.34×10^4
	60	55:17:54	30	3.2				1.26×10^4
	60	66:17:28	30	2.9				1.11×10^4
2	60	15:20:54	5	9.0	1.93×10^4	2.57×10^4	2.31×10^4	2.99×10^3
	60	17:0:25	10	6.3	1.87×10^4	2.40×10^4	2.11×10^4	5.52×10^3
	60	18:3:33	10	5.0	8.05×10^3	1.10×10^4	9.46×10^3	5.54×10^3
	60	28:20:15	30	3.7				1.53×10^4
	60	36:23:28	30	3.5				1.37×10^4
	60	46:19:02	30	3.3				1.24×10^4
	60	55:18:27	30	3.1				1.15×10^4
	60	66:18:00	30	2.8				1.03×10^4
3	60	15:21:01	5	8.3	1.86×10^4	2.41×10^4	2.15×10^4	2.46×10^3
	60	17:0:37	10	5.7	1.63×10^4	2.19×10^4	1.93×10^4	5.13×10^3
	60	18:3:45	10	4.6	7.54×10^3	9.99×10^3	8.89×10^3	4.97×10^3
	60	28:20:48	30	3.5				1.36×10^4
	60	37:0:00	30	3.2				1.28×10^4
	60	46:19:35	30	3.0				1.10×10^4
	60	55:19:08	30	2.9				1.00×10^4
	60	66:18:32	30	2.6				9.23×10^3
4	60	15:21:08	5	8.8	1.98×10^4	2.54×10^4	2.26×10^4	2.72×10^3
	60	17:0:48	10	6.0	1.74×10^4	2.31×10^4	2.03×10^4	5.59×10^3
	60	18:3:56	10	4.9	8.25×10^3	1.05×10^4	9.20×10^3	5.46×10^3
	60	28:22:25	30	3.6				1.42×10^4
	60	37:0:32	30	3.4				1.33×10^4
	60	46:20:26	30	3.2				1.16×10^4
	60	55:19:40	30	3.0				1.08×10^4
	60	66:19:04	30	2.8				9.57×10^3
5	60	15:21:15	5	8.8	1.94×10^4	2.52×10^4	2.23×10^4	3.16×10^3
	60	17:1:00	10	6.1	1.77×10^4	2.29×10^4	2.03×10^4	5.23×10^3
	60	18:4:07	10	4.9	8.08×10^3	1.05×10^4	9.27×10^3	5.16×10^3
	60	28:22:57	30	3.6				1.40×10^4
	60	37:1:04	30	3.4				1.31×10^4

Foil	Shelf (cm)	Time Since EOB (d:h:m)	Count Time (m)	Dead Time (%)	Activity (Total Counts) ^{187}W γ-ray 134 keV	^{187}W γ-ray 479 keV	^{187}W γ-ray 685 keV	^{188}Re γ-ray 155 keV
	60	46:22:04	30	3.2				1.18×10^4
	60	55:20:13	30	3.0				1.09×10^4
	60	66:19:36	30	2.8				9.97×10^3
6	60	15:21:21	5	8.6	1.86×10^4	2.45×10^4	2.19×10^4	2.77×10^3
	60	17:1:12	10	6.0	1.67×10^4	2.23×10^4	1.97×10^4	5.15×10^3
	60	18:4:19	10	4.8	7.80×10^3	1.02×10^4	9.22×10^3	5.11×10^3
	60	28:23:32	30	3.6				1.40×10^4
	60	37:1:37	30	3.4				1.30×10^4
	60	46:22:39	30	3.1				1.18×10^4
	60	55:20:45	30	3.0				1.04×10^4
	60	66:20:09	30	2.7				9.47×10^3
7	60	15:21:28	5	8.3	1.82×10^4	2.36×10^4	2.12×10^4	1.84×10^3
	60	17:1:23	10	5.7	1.64×10^4	2.15×10^4	1.89×10^4	4.96×10^3
	60	18:4:30	10	4.6	7.72×10^3	9.88×10^3	8.77×10^3	4.93×10^3
	60	29:0:08	30	3.5				1.39×10^4
	60	37:2:09	30	3.3				1.22×10^4
	60	46:23:44	30	3.1				1.13×10^4
	60	55:22:20	30	2.9				1.04×10^4
	60	66:20:42	30	2.7				9.37×10^3
8	60	15:21:34	5	8.4	1.87×10^4	2.42×10^4	2.14×10^4	3.11×10^3
	60	17:1:35	10	5.8	1.65×10^4	2.17×10^4	1.93×10^4	5.07×10^3
	60	18:4:42	10	4.7	7.71×10^3	1.00×10^4	8.88×10^3	5.02×10^3
	60	29:0:40	30	3.5				1.38×10^4
	60	37:2:41	30	3.3				1.26×10^4
	60	47:0:16	30	3.1				1.17×10^4
	60	55:23:06	30	2.9				1.08×10^4
	60	66:22:07	30	2.7				9.46×10^3
9	60	15:21:41	5	8.6	1.86×10^4	2.45×10^4	2.15×10^4	2.56×10^3
	60	17:1:47	10	5.9	1.68×10^4	2.18×10^4	1.94×10^4	4.99×10^3
	60	18:4:53	10	4.8	7.68×10^3	1.00×10^4	8.81×10^3	5.19×10^3
	60	29:1:12	30	3.6				1.41×10^4
	60	37:3:14	30	3.4				1.29×10^4
	60	47:0:49	30	3.1				1.18×10^4
	60	55:23:39	30	3.0				1.05×10^4
	60	66:22:53	30	2.7				9.74×10^3
10	60	15:21:47	5	8.5	1.87×10^4	2.41×10^4	2.13×10^4	2.21×10^3
	60	17:1:58	10	5.8	1.67×10^4	2.16×10^4	1.91×10^4	5.09×10^3
	60	18:5:06	10	4.7	7.67×10^3	9.98×10^3	8.62×10^3	5.20×10^3
	60	29:1:45	30	3.5				1.40×10^4
	60	37:3:47	30	3.3				1.27×10^4
	60	47:1:21	30	3.1				1.16×10^4

Foil	Shelf (cm)	Time Since EOB (d:h:m)	Count Time (m)	Dead Time (%)	Activity (Total Counts) ^{187}W γ-ray 134 keV	^{187}W γ-ray 479 keV	^{187}W γ-ray 685 keV	^{188}Re γ-ray 155 keV
	60	56:0:11	30	2.9				1.10×10^4
	60	66:23:25	30	2.7				9.81×10^3
11	60	15:21:54	5	9.1	2.03×10^4	2.61×10^4	2.32×10^4	3.85×10^3
	60	17:2:10	10	6.3	1.80×10^4	2.35×10^4	2.08×10^4	6.04×10^3
	60	18:5:18	10	5.1	8.35×10^3	1.09×10^4	9.46×10^3	5.70×10^3
	60	29:2:17	30	3.8				1.58×10^4
	60	37:4:19	30	3.6				1.51×10^4
	60	47:1:54	30	3.3				1.34×10^4
	60	56:0:44	30	3.1				1.22×10^4
	60	66:23:58	30	2.9				1.09×10^4
0.1 mm Foil								
A	60	15:22:07	5	5.3	1.22×10^4	1.25×10^4	1.10×10^4	1.88×10^3
	60	16:19:12	15	4.1	2.03×10^4	2.10×10^4	1.82×10^4	5.10×10^3
	60	17:19:08	20	3.4	1.32×10^4	1.39×10^4	1.21×10^4	6.68×10^3
	30	27:23:55	15	9.3				1.45×10^4
	30	41:19:02	20	8.5				1.73×10^4
	30	49:18:10	20	8.0				1.63×10^4
	30	56:20:27	20	7.7				1.49×10^4
	30	67:0:31	20	7.1				1.33×10^4
B	60	15:22:13	5	4.8	1.07×10^4	1.09×10^4	9.64×10^3	1.72×10^3
	60	16:19:29	15	3.7	1.69×10^4	1.76×10^4	1.57×10^4	4.34×10^3
	60	17:19:31	20	3.1	1.19×10^4	1.17×10^4	1.03×10^4	5.59×10^3
	30	28:0:31	15	8.5				1.25×10^4
	30	41:19:26	20	7.8				1.48×10^4
	30	49:18:34	20	7.4				1.37×10^4
	30	56:20:51	20	7.0				1.30×10^4
	30	67:0:54	20	6.5				1.18×10^4
C	60	15:22:19	5	4.9	1.10×10^4	1.16×10^4	9.90×10^3	1.40×10^3
	60	16:19:46	15	3.8	1.77×10^4	1.86×10^4	1.60×10^4	4.26×10^3
	60	17:19:53	20	3.2	1.18×10^4	1.22×10^4	1.07×10^4	5.98×10^3
	30	28:0:50	15	8.9				1.30×10^4
	30	41:19:57	20	8.1				1.53×10^4
	30	49:18:57	20	7.7				1.44×10^4
	30	56:22:14	20	7.3				1.32×10^4
	30	67:1:30	20	6.7				1.18×10^4
D	60	15:22:26	5	4.6	1.01×10^4	1.07×10^4	9.48×10^3	1.49×10^3
	60	16:20:02	15	3.6	1.63×10^4	1.71×10^4	1.52×10^4	4.14×10^3
	60	17:20:14	20	3.0	1.14×10^4	1.14×10^4	9.92×10^3	5.52×10^3
	30	28:1:07	15	8.4				1.22×10^4
	30	41:20:20	20	7.7				1.42×10^4

Foil	Shelf (cm)	Time Since EOB (d:h:m)	Count Time (m)	Dead Time (%)	Activity (Total Counts) ^{187}W γ-ray 134 keV	^{187}W γ-ray 479 keV	^{187}W γ-ray 685 keV	^{188}Re γ-ray 155 keV
	30	49:19:20	20	7.3				1.32×10^4
	30	56:22:45	20	6.9				1.23×10^4
	30	67:2:00	20	6.4				1.14×10^4
E	60	15:22:32	5	4.8	1.06×10^4	1.11×10^4	9.71×10^3	9.72×10^2
	60	16:20:18	15	3.7	1.69×10^4	1.82×10^4	1.56×10^4	4.22×10^3
	60	17:20:36	20	3.1	1.17×10^4	1.19×10^4	1.05×10^4	5.55×10^3
	30	28:1:25	15	8.7				1.25×10^4
	30	41:20:44	20	7.9				1.47×10^4
	30	49:19:43	20	7.5				1.35×10^4
	30	56:23:15	20	7.2				1.26×10^4
	30	67:2:36	20	6.6				1.17×10^4
F	60	15:22:38	5	4.5	1.01×10^4	1.06×10^4	9.23×10^3	1.39×10^3
	60	16:20:35	15	3.5	1.60×10^4	1.66×10^4	1.47×10^4	3.97×10^3
	60	17:20:57	20	3.0	1.01×10^4	1.11×10^4	9.57×10^3	5.20×10^3
	30	28:1:43	15	8.3				1.20×10^4
	30	41:22:03	20	7.6				1.36×10^4
	30	49:20:06	20	7.2				1.29×10^4
	30	56:23:38	20	6.9				1.21×10^4
	30	67:2:58	20	6.3				1.07×10^4
G	60	15:22:44	5	4.5	9.80×10^3	1.01×10^4	8.97×10^3	1.06×10^3
	60	16:20:52	15	3.4	1.54×10^4	1.58×10^4	1.39×10^4	3.98×10^3
	60	17:21:19	20	2.9	1.01×10^4	1.06×10^4	9.34×10^3	5.28×10^3
	30	28:2:01	15	8.1				1.15×10^4
	30	41:22:27	20	7.4				1.36×10^4
	30	49:20:29	20	7.0				1.25×10^4
	30	57:0:01	20	6.7				1.17×10^4
	30	67:17:10	20	6.2				1.07×10^4
H	60	15:22:50	5	4.6	1.01×10^4	1.05×10^4	9.20×10^3	1.63×10^3
	60	16:21:09	15	3.5	1.54×10^4	1.67×10^4	1.45×10^4	4.14×10^3
	60	17:21:40	20	3.0	1.02×10^4	1.10×10^4	9.40×10^3	5.09×10^3
	30	28:2:18	15	8.3				1.18×10^4
	30	41:22:51	20	7.6				1.39×10^4
	30	49:20:52	20	7.2				1.28×10^4
	30	57:0:25	20	6.9				1.18×10^4
	30	67:17:33	20	6.3				1.08×10^4
I	60	15:22:56	5	4.5	9.99×10^3	1.02×10^4	9.15×10^3	1.14×10^3
	60	16:21:25	15	3.5	1.55×10^4	1.59×10^4	1.43×10^4	3.99×10^3
	60	17:22:03	20	2.9	1.06×10^4	1.05×10^4	9.30×10^3	5.25×10^3
	30	28:2:36	15	8.3				1.20×10^4
	30	41:23:14	20	7.5				1.38×10^4
	30	49:22:20	20	7.1				1.23×10^4

Foil	Shelf (cm)	Time Since EOB (d:h:m)	Count Time (m)	Dead Time (%)	Activity (Total Counts) ^{187}W γ-ray 134 keV	^{187}W γ-ray 479 keV	^{187}W γ-ray 685 keV	^{188}Re γ-ray 155 keV
	30	57:0:48	20	6.8				1.19×10^4
	30	67:18:01	20	6.3				1.07×10^4
J	60	15:23:02	5	4.6	1.01×10^4	1.05×10^4	9.36×10^3	1.50×10^3
	60	16:21:42	15	3.6	1.58×10^4	1.65×10^4	1.47×10^4	4.07×10^3
	60	17:22:36	20	3.0	1.03×10^4	1.09×10^4	9.44×10^3	5.23×10^3
	30	28:2:54	15	8.5				1.20×10^4
	30	41:23:38	20	7.7				1.43×10^4
	30	49:22:56	20	7.4				1.32×10^4
	30	57:1:11	20	7.0				1.24×10^4
	30	67:18:24	20	6.5				1.09×10^4
K	60	15:23:09	5	4.5	1.01×10^4	1.03×10^4	9.18×10^3	1.62×10^3
	60	16:21:58	15	3.5	1.56×10^4	1.62×10^4	1.41×10^4	4.18×10^3
	60	17:22:58	20	2.9	9.96×10^3	1.03×10^4	9.09×10^3	5.32×10^3
	30	28:3:12	15	8.3				1.20×10^4
	30	42:0:01	20	7.5				1.37×10^4
	30	49:23:19	20	7.1				1.30×10^4
	30	57:1:35	20	6.8				1.20×10^4
	30	67:18:47	20	6.3				1.07×10^4
L	60	15:23:15	5	4.5	9.53×10^3	1.05×10^4	9.11×10^3	1.22×10^3
	60	16:22:14	15	3.5	1.54×10^4	1.59×10^4	1.42×10^4	4.18×10^3
	60	17:23:19	20	2.9	1.01×10^4	1.04×10^4	8.97×10^3	5.41×10^3
	30	28:3:29	15	8.4				1.20×10^4
	30	42:0:24	20	7.6				1.41×10^4
	30	49:23:42	20	7.2				1.30×10^4
	30	57:1:58	20	6.9				1.20×10^4
	30	67:19:10	20	6.4				1.08×10^4
M	60	15:23:21	5	5.0	1.08×10^4	1.19×10^4	1.03×10^4	1.42×10^3
	60	16:22:31	15	3.9	1.69×10^4	1.77×10^4	1.58×10^4	4.27×10^3
	60	18:0:13	20	3.2	1.09×10^4	1.13×10^4	9.67×10^3	5.91×10^3
	30	28:3:47	15	9.2				1.32×10^4
	30	42:0:47	20	8.3				1.55×10^4
	30	50:0:06	20	8.0				1.43×10^4
	30	57:2:21	20	7.6				1.36×10^4
	30	67:19:50	20	7.0				1.24×10^4
N	60	15:23:27	5	4.5	9.95×10^3	1.01×10^4	9.09×10^3	1.54×10^3
	60	16:22:47	15	3.4	1.48×10^4	1.57×10^4	1.36×10^4	4.07×10^3
	60	18:0:41	20	2.9	9.68×10^3	9.79×10^3	8.64×10^3	5.42×10^3
	30	28:4:06	15	8.3				1.18×10^4
	30	42:1:11	20	7.5				1.39×10^4
	30	50:0:29	20	7.1				1.27×10^4
	30	57:2:44	20	6.8				1.18×10^4

Foil	Shelf (cm)	Time Since EOB (d:h:m)	Count Time (m)	Dead Time (%)	Activity (Total Counts)			
					^{187}W γ-ray			^{188}Re γ-ray
					134 keV	479 keV	685 keV	155 keV
	30	67:20:13	20	6.3				1.08×10^4
O	60	15:23:33	5	4.8	1.05×10^4	1.11×10^4	9.51×10^3	1.50×10^3
	60	16:23:04	15	3.7	1.58×10^4	1.67×10^4	1.46×10^4	4.38×10^3
	60	18:1:02	20	3.1	1.04×10^4	1.05×10^4	8.95×10^3	5.47×10^3
	30	28:4:24	15	8.8				1.27×10^4
	30	42:1:34	20	8.0				1.53×10^4
	30	50:0:52	20	7.6				1.40×10^4
	30	57:3:07	20	7.3				1.29×10^4
	30	67:20:35	20	6.7				1.17×10^4
P	60	15:23:40	5	4.9	1.03×10^4	1.11×10^4	9.71×10^3	1.85×10^3
	60	16:23:20	15	3.7	1.59×10^4	1.70×10^4	1.47×10^4	4.47×10^3
	60	18:1:24	20	3.1	1.01×10^4	1.08×10^4	9.01×10^3	5.79×10^3
	30	28:4:41	15	8.9				1.31×10^4
	30	42:1:57	20	8.0				1.51×10^4
	30	50:1:15	20	7.7				1.41×10^4
	30	57:3:34	20	7.3				1.31×10^4
	30	67:23:08	20	6.7				1.18×10^4
Q	60	15:23:46	5	4.6	9.76×10^3	1.07×10^4	9.18×10^3	1.57×10^3
	60	16:23:37	15	3.5	1.50×10^4	1.57×10^4	1.38×10^4	4.33×10^3
	60	18:1:46	20	3.0	9.39×10^3	1.01×10^4	8.62×10^3	5.66×10^3
	30	28:5:02	15	8.5				1.27×10^4
	30	42:2:21	20	7.7				1.49×10^4
	30	50:1:40	20	7.3				1.35×10^4
	30	57:3:57	20	7.0				1.29×10^4
	30	67:23:31	20	6.4				1.15×10^4
R	60	15:23:52	5	5.3	1.18×10^4	1.25×10^4	1.10×10^4	1.94×10^3
	60	16:23:53	15	4.0	1.79×10^4	1.84×10^4	1.62×10^4	5.03×10^3
	60	18:2:08	20	3.3	1.10×10^4	1.14×10^4	1.00×10^4	6.63×10^3
	30	28:5:19	15	9.5				1.50×10^4
	30	42:2:45	20	8.6				1.74×10^4
	30	50:2:03	20	8.2				1.62×10^4
	30	57:4:19	20	7.8				1.57×10^4
	30	67:23:56	20	7.2				1.40×10^4

Table D.3 Tungsten Cylinder Self-Shielding Experiment Activities

Cylinder	Isotope	γ-ray	Counts per Second [a]	Absolute Gamma Intensity [b]	Absolute Detector Efficiency [c]	Self-Absorption Factor [d]	A^0 (Bq)	Mass (mg)	A^0 (Bq mg^{-1})
1	^{187}W	134	2.62×10^{6}	0.0885	3.41×10^{-4}	0.251	3.46×10^{11}		
		479	8.20×10^{6}	0.218	1.19×10^{-4}	0.872	3.62×10^{11}		
		685	7.50×10^{6}	0.273	8.35×10^{-5}	0.914	3.60×10^{11}		
						Average:	3.56×10^{11}	444.4	8.01×10^{8}
	^{188}W	155	3.32×10^{0}	0.1561	3.13×10^{-4}	0.340	2.00×10^{5}		
		478	2.03×10^{-1}	0.01081	1.19×10^{-4}	0.871	1.80×10^{5}		
		633	2.32×10^{-1}	0.01374	9.03×10^{-5}	0.907	2.06×10^{5}		
						Average:	1.95×10^{5}	444.4	4.40×10^{2}
2	^{187}W	134	5.10×10^{6}	0.0885	3.41×10^{-4}	0.197	8.58×10^{11}		
		479	2.04×10^{7}	0.218	1.19×10^{-4}	0.837	9.37×10^{11}		
		685	1.88×10^{7}	0.273	8.35×10^{-5}	0.890	9.26×10^{11}		
						Average:	9.07×10^{11}	1159.7	7.82×10^{8}
	^{188}W	155	7.00×10^{0}	0.1561	3.13×10^{-4}	0.273	5.24×10^{5}		
		478	5.08×10^{-1}	0.01081	1.19×10^{-4}	0.836	4.71×10^{5}		
		633	5.86×10^{-1}	0.01374	9.03×10^{-5}	0.881	5.36×10^{5}		
						Average:	5.10×10^{5}	1159.7	4.40×10^{2}
3	^{187}W	134	8.50×10^{6}	0.0885	3.41×10^{-4}	0.182	1.55×10^{12}		
		479	3.26×10^{7}	0.218	1.19×10^{-4}	0.821	1.53×10^{12}		
		685	3.07×10^{7}	0.273	8.35×10^{-5}	0.878	1.53×10^{12}		
						Average:	1.54×10^{12}	1873.0	8.20×10^{8}
	^{188}W	155	1.09×10^{1}	0.1561	3.13×10^{-4}	0.254	8.80×10^{5}		
		478	8.44×10^{-1}	0.01081	1.19×10^{-4}	0.820	7.98×10^{5}		
		633	9.68×10^{-1}	0.01374	9.03×10^{-5}	0.869	8.97×10^{5}		
						Average:	8.59×10^{5}	1873.0	4.58×10^{2}

Cylinder	Isotope	γ-ray	Counts per Second [a]	Absolute Gamma Intensity [b]	Absolute Detector Efficiency [c]	Self-Absorption Factor [d]	A^0 (Bq)	Mass (mg)	A^0 (Bq mg^{-1})
4	^{187}W	134	1.15×10^{7}	0.0885	3.41×10^{-4}	0.175	2.18×10^{12}		
		479	4.55×10^{7}	0.218	1.19×10^{-4}	0.812	2.16×10^{12}		
		685	4.26×10^{7}	0.273	8.35×10^{-5}	0.871	2.14×10^{12}		
						Average:	2.16×10^{12}	2652.3	8.15×10^{8}
	^{188}W	155	1.55×10^{1}	0.1561	3.13×10^{-4}	0.245	1.30×10^{6}		
		478	1.24×10^{0}	0.01081	1.19×10^{-4}	0.810	1.19×10^{6}		
		633	1.42×10^{0}	0.01374	9.03×10^{-5}	0.861	1.33×10^{6}		
						Average:	1.27×10^{6}	2652.3	4.79×10^{2}
5	^{187}W	134	1.64×10^{7}	0.0885	3.41×10^{-4}	0.171	3.18×10^{12}		
		479	6.11×10^{7}	0.218	1.19×10^{-4}	0.805	2.92×10^{12}		
		685	5.84×10^{7}	0.273	8.35×10^{-5}	0.866	2.96×10^{12}		
						Average:	3.02×10^{12}	3327.1	9.08×10^{8}
	^{188}W	155	2.25×10^{1}	0.1561	3.13×10^{-4}	0.239	1.93×10^{6}		
		478	1.77×10^{0}	0.01081	1.19×10^{-4}	0.803	1.70×10^{6}		
		633	2.02×10^{0}	0.01374	9.03×10^{-5}	0.855	1.90×10^{6}		
						Average:	1.84×10^{6}	3327.1	5.55×10^{2}

[a] CLSQ output divided by count time from Table D.1
[b] [NNDC 2003]
[c] Table A.2
[d] Table B.3 (Cylinder #1), Table B.4 (Cylinders 2 – 5)

Table D.4 0.25 mm Tungsten Foil Self-Shielding Experiment Activities

Foil	Isotope	γ-ray	Counts per Second [a]	Absolute Gamma Intensity [b]	Absolute Detector Efficiency [c]	Self-Absorption Factor [d]	A^0 (Bq)	Mass (mg)	A^0 (Bq mg^{-1})
1	^{187}W	134	4.88×10^{6}	0.0885	3.41×10^{-4}	0.631	2.56×10^{11}		
		479	6.45×10^{6}	0.218	1.19×10^{-4}	0.966	2.57×10^{11}		
		685	5.67×10^{6}	0.273	8.35×10^{-5}	0.978	2.54×10^{11}		
						Average:	2.56×10^{11}	117.6	2.18×10^{9}
	^{188}W	155	1.20×10^{1}	0.1561	3.13×10^{-4}	0.719	3.40×10^{5}	117.6	2.89×10^{3}
2	^{187}W	134	4.56×10^{6}	0.0885	3.41×10^{-4}	0.631	2.39×10^{11}		
		479	6.01×10^{6}	0.218	1.19×10^{-4}	0.966	2.40×10^{11}		
		685	5.32×10^{6}	0.273	8.35×10^{-5}	0.978	2.38×10^{11}		
						Average:	2.39×10^{11}	117.9	2.03×10^{9}
	^{188}W	155	1.11×10^{1}	0.1561	3.13×10^{-4}	0.719	3.16×10^{5}	117.9	2.68×10^{3}
3	^{187}W	134	4.23×10^{6}	0.0885	3.41×10^{-4}	0.631	2.22×10^{11}		
		479	5.58×10^{6}	0.218	1.19×10^{-4}	0.966	2.22×10^{11}		
		685	4.95×10^{6}	0.273	8.35×10^{-5}	0.978	2.22×10^{11}		
						Average:	2.22×10^{11}	110.8	2.00×10^{9}
	^{188}W	155	9.95×10^{0}	0.1561	3.13×10^{-4}	0.719	2.83×10^{5}	110.8	2.56×10^{3}
4	^{187}W	134	4.55×10^{6}	0.0885	3.41×10^{-4}	0.631	2.39×10^{11}		
		479	5.90×10^{6}	0.218	1.19×10^{-4}	0.966	2.35×10^{11}		
		685	5.21×10^{6}	0.273	8.35×10^{-5}	0.978	2.34×10^{11}		
						Average:	2.36×10^{11}	118.0	2.00×10^{9}
	^{188}W	155	1.05×10^{1}	0.1561	3.13×10^{-4}	0.719	2.98×10^{5}	118.0	2.52×10^{3}

Foil	Isotope	γ-ray	Counts per Second [a]	Absolute Gamma Intensity [b]	Absolute Detector Efficiency [c]	Self-Absorption Factor [d]	A^0 (Bq)	Mass (mg)	A^0 (Bq mg^{-1})
5	^{187}W	134	4.54×10^{6}	0.0885	3.41×10^{-4}	0.631	2.39×10^{11}		
		479	5.89×10^{6}	0.218	1.19×10^{-4}	0.966	2.35×10^{11}		
		685	5.21×10^{6}	0.273	8.35×10^{-5}	0.978	2.34×10^{11}		
						Average:	2.36×10^{11}	118.8	1.98×10^{9}
	^{188}W	155	1.05×10^{1}	0.1561	3.13×10^{-4}	0.719	2.99×10^{5}	118.8	2.52×10^{3}
6	^{187}W	134	4.35×10^{6}	0.0885	3.41×10^{-4}	0.631	2.29×10^{11}		
		479	5.75×10^{6}	0.218	1.19×10^{-4}	0.966	2.29×10^{11}		
		685	5.13×10^{6}	0.273	8.35×10^{-5}	0.978	2.30×10^{11}		
						Average:	2.29×10^{11}	116.9	1.96×10^{9}
	^{188}W	155	1.03×10^{1}	0.1561	3.13×10^{-4}	0.719	2.94×10^{5}	116.9	2.51×10^{3}
7	^{187}W	134	4.29×10^{6}	0.0885	3.41×10^{-4}	0.631	2.25×10^{11}		
		479	5.57×10^{6}	0.218	1.19×10^{-4}	0.966	2.22×10^{11}		
		685	4.96×10^{6}	0.273	8.35×10^{-5}	0.978	2.22×10^{11}		
						Average:	2.23×10^{11}	113.3	1.97×10^{9}
	^{188}W	155	1.01×10^{1}	0.1561	3.13×10^{-4}	0.719	2.86×10^{5}	113.3	2.53×10^{3}
8	^{187}W	134	4.37×10^{6}	0.0885	3.41×10^{-4}	0.631	2.30×10^{11}		
		479	5.69×10^{6}	0.218	1.19×10^{-4}	0.966	2.27×10^{11}		
		685	5.05×10^{6}	0.273	8.35×10^{-5}	0.978	2.26×10^{11}		
						Average:	2.28×10^{11}	114.0	2.00×10^{9}
	^{188}W	155	1.02×10^{1}	0.1561	3.13×10^{-4}	0.719	2.91×10^{5}	114.0	2.55×10^{3}
9	^{187}W	134	4.41×10^{6}	0.0885	3.41×10^{-4}	0.631	2.32×10^{11}		
		479	5.76×10^{6}	0.218	1.19×10^{-4}	0.966	2.30×10^{11}		
		685	5.09×10^{6}	0.273	8.35×10^{-5}	0.978	2.28×10^{11}		
						Average:	2.30×10^{11}	114.8	2.00×10^{9}
	^{188}W	155	1.04×10^{1}	0.1561	3.13×10^{-4}	0.719	2.96×10^{5}	114.8	2.58×10^{3}

Foil	Isotope	γ-ray	Counts per Second [a]	Absolute Gamma Intensity [b]	Absolute Detector Efficiency [c]	Self-Absorption Factor [d]	A^0 (Bq)	Mass (mg)	A^0 (Bq mg^{-1})
10	^{187}W	134	4.43×10^{6}	0.0885	3.41×10^{-4}	0.631	2.33×10^{11}		
		479	5.72×10^{6}	0.218	1.19×10^{-4}	0.966	2.28×10^{11}		
		685	5.00×10^{6}	0.273	8.35×10^{-5}	0.978	2.24×10^{11}		
						Average:	2.28×10^{11}	111.5	2.05×10^{9}
	^{188}W	155	1.04×10^{1}	0.1561	3.13×10^{-4}	0.719	2.96×10^{5}	111.5	2.66×10^{3}
11	^{187}W	134	4.82×10^{6}	0.0885	3.41×10^{-4}	0.631	2.53×10^{11}		
		479	6.25×10^{6}	0.218	1.19×10^{-4}	0.966	2.49×10^{11}		
		685	5.52×10^{6}	0.273	8.35×10^{-5}	0.978	2.48×10^{11}		
						Average:	2.50×10^{11}	114.3	2.19×10^{9}
	^{188}W	155	1.19×10^{1}	0.1561	3.13×10^{-4}	0.719	3.39×10^{5}	114.3	2.97×10^{3}

[a] CLSQ output divided by count time from Table D.1
[b] [NNDC 2003]
[c] Table A.2
[d] Table B.2

Table D.5 0.1 mm Tungsten Foil Self-Shielding Experiment Activities

Foil	Isotope	γ-ray	Counts per Second [a]	Absolute Gamma Intensity [b]	Absolute Detector Efficiency [c]	Self-Absorption Factor [d]	A^0 (Bq)	Mass (mg)	A^0 (Bq mg^{-1})
A	^{187}W	134	2.93×10^{6}	0.0885	3.41×10^{-4}	0.824	1.18×10^{11}		
		479	3.03×10^{6}	0.218	1.19×10^{-4}	0.986	1.18×10^{11}		
		685	2.64×10^{6}	0.273	8.35×10^{-5}	0.991	1.17×10^{11}		
						Average:	1.18×10^{11}	50.8	2.32×10^{9}
	^{188}W	155	2.18×10^{1}	0.1561	1.01×10^{-3}	0.872	1.58×10^{5}	50.8	3.10×10^{3}
B	^{187}W	134	2.55×10^{6}	0.0885	3.41×10^{-4}	0.824	1.03×10^{11}		
		479	2.59×10^{6}	0.218	1.19×10^{-4}	0.986	1.01×10^{11}		
		685	2.30×10^{6}	0.273	8.35×10^{-5}	0.991	1.02×10^{11}		
						Average:	1.02×10^{11}	47.2	2.16×10^{9}
	^{188}W	155	1.88×10^{1}	0.1561	1.01×10^{-3}	0.872	1.36×10^{5}	47.2	2.88×10^{3}
C	^{187}W	134	2.63×10^{6}	0.0885	3.41×10^{-4}	0.824	1.06×10^{11}		
		479	2.76×10^{6}	0.218	1.19×10^{-4}	0.986	1.08×10^{11}		
		685	2.38×10^{6}	0.273	8.35×10^{-5}	0.991	1.05×10^{11}		
						Average:	1.06×10^{11}	50.4	2.11×10^{9}
	^{188}W	155	1.93×10^{1}	0.1561	1.01×10^{-3}	0.872	1.40×10^{5}	50.4	2.78×10^{3}
D	^{187}W	134	2.47×10^{6}	0.0885	3.41×10^{-4}	0.824	9.95×10^{10}		
		479	2.57×10^{6}	0.218	1.19×10^{-4}	0.986	1.00×10^{11}		
		685	2.27×10^{6}	0.273	8.35×10^{-5}	0.991	1.00×10^{11}		
						Average:	1.00×10^{11}	48.0	2.08×10^{9}
	^{188}W	155	1.81×10^{1}	0.1561	1.01×10^{-3}	0.872	1.31×10^{5}	48.0	2.73×10^{3}

Foil	Isotope	γ-ray	Counts per Second [a]	Absolute Gamma Intensity [b]	Absolute Detector Efficiency [c]	Self-Absorption Factor [d]	A^0 (Bq)	Mass (mg)	A^0 (Bq mg^{-1})
E	^{187}W	134	2.58×10^{6}	0.0885	3.41×10^{-4}	0.824	1.04×10^{11}		
		479	2.72×10^{6}	0.218	1.19×10^{-4}	0.986	1.06×10^{11}		
		685	2.36×10^{6}	0.273	8.35×10^{-5}	0.991	1.04×10^{11}		
						Average:	1.05×10^{11}	50.2	2.09×10^{9}
	^{188}W	155	1.86×10^{1}	0.1561	1.01×10^{-3}	0.872	1.35×10^{5}	50.2	2.68×10^{3}
F	^{187}W	134	2.41×10^{6}	0.0885	3.41×10^{-4}	0.824	9.68×10^{10}		
		479	2.55×10^{6}	0.218	1.19×10^{-4}	0.986	9.94×10^{10}		
		685	2.23×10^{6}	0.273	8.35×10^{-5}	0.991	9.85×10^{10}		
						Average:	9.82×10^{10}	48.1	2.04×10^{9}
	^{188}W	155	1.75×10^{1}	0.1561	1.01×10^{-3}	0.872	1.27×10^{5}	48.1	2.64×10^{3}
G	^{187}W	134	2.36×10^{6}	0.0885	3.41×10^{-4}	0.824	9.51×10^{10}		
		479	2.44×10^{6}	0.218	1.19×10^{-4}	0.986	9.54×10^{10}		
		685	2.16×10^{6}	0.273	8.35×10^{-5}	0.991	9.54×10^{10}		
						Average:	9.53×10^{10}	46.5	2.05×10^{9}
	^{188}W	155	1.72×10^{1}	0.1561	1.01×10^{-3}	0.872	1.24×10^{5}	46.5	2.67×10^{3}
H	^{187}W	134	2.41×10^{6}	0.0885	3.41×10^{-4}	0.824	9.69×10^{10}		
		479	2.58×10^{6}	0.218	1.19×10^{-4}	0.986	1.01×10^{11}		
		685	2.23×10^{6}	0.273	8.35×10^{-5}	0.991	9.87×10^{10}		
						Average:	9.88×10^{10}	48.8	2.02×10^{9}
	^{188}W	155	1.75×10^{1}	0.1561	1.01×10^{-3}	0.872	1.27×10^{5}	48.8	2.60×10^{3}
I	^{187}W	134	2.45×10^{6}	0.0885	3.41×10^{-4}	0.824	9.86×10^{10}		
		479	2.49×10^{6}	0.218	1.19×10^{-4}	0.986	9.71×10^{10}		
		685	2.23×10^{6}	0.273	8.35×10^{-5}	0.991	9.84×10^{10}		
						Average:	9.81×10^{10}	48.0	2.04×10^{9}
	^{188}W	155	1.74×10^{1}	0.1561	1.01×10^{-3}	0.872	1.26×10^{5}	48.0	2.62×10^{3}

Foil	Isotope	γ-ray	Counts per Second [a]	Absolute Gamma Intensity [b]	Absolute Detector Efficiency [c]	Self-Absorption Factor [d]	A^0 (Bq)	Mass (mg)	A^0 (Bq mg^{-1})
J	^{187}W	134	2.48×10^{6}	0.0885	3.41×10^{-4}	0.824	9.99×10^{10}		
		479	2.60×10^{6}	0.218	1.19×10^{-4}	0.986	1.01×10^{11}		
		685	2.30×10^{6}	0.273	8.35×10^{-5}	0.991	1.02×10^{11}		
						Average:	1.01×10^{11}	49.6	2.04×10^{9}
	^{188}W	155	1.80×10^{1}	0.1561	1.01×10^{-3}	0.872	1.30×10^{5}	49.6	2.62×10^{3}
K	^{187}W	134	2.46×10^{6}	0.0885	3.41×10^{-4}	0.824	9.91×10^{10}		
		479	2.54×10^{6}	0.218	1.19×10^{-4}	0.986	9.93×10^{10}		
		685	2.24×10^{6}	0.273	8.35×10^{-5}	0.991	9.89×10^{10}		
						Average:	9.91×10^{10}	48.4	2.05×10^{9}
	^{188}W	155	1.76×10^{1}	0.1561	1.01×10^{-3}	0.872	1.27×10^{5}	48.4	2.63×10^{3}
L	^{187}W	134	2.43×10^{6}	0.0885	3.41×10^{-4}	0.824	9.79×10^{10}		
		479	2.56×10^{6}	0.218	1.19×10^{-4}	0.986	1.00×10^{11}		
		685	2.25×10^{6}	0.273	8.35×10^{-5}	0.991	9.93×10^{10}		
						Average:	9.91×10^{10}	48.2	2.06×10^{9}
	^{188}W	155	1.77×10^{1}	0.1561	1.01×10^{-3}	0.872	1.28×10^{5}	48.2	2.66×10^{3}
M	^{187}W	134	2.72×10^{6}	0.0885	3.41×10^{-4}	0.824	1.09×10^{11}		
		479	2.88×10^{6}	0.218	1.19×10^{-4}	0.986	1.12×10^{11}		
		685	2.52×10^{6}	0.273	8.35×10^{-5}	0.991	1.11×10^{11}		
						Average:	1.11×10^{11}	53.4	2.08×10^{9}
	^{188}W	155	1.98×10^{1}	0.1561	1.01×10^{-3}	0.872	1.43×10^{5}	53.4	2.68×10^{3}
N	^{187}W	134	2.44×10^{6}	0.0885	3.41×10^{-4}	0.824	9.83×10^{10}		
		479	2.53×10^{6}	0.218	1.19×10^{-4}	0.986	9.86×10^{10}		
		685	2.22×10^{6}	0.273	8.35×10^{-5}	0.991	9.83×10^{10}		
						Average:	9.84×10^{10}	47.1	2.09×10^{9}
	^{188}W	155	1.75×10^{1}	0.1561	1.01×10^{-3}	0.872	1.27×10^{5}	47.1	2.69×10^{3}

Foil	Isotope	γ-ray	Counts per Second [a]	Absolute Gamma Intensity [b]	Absolute Detector Efficiency [c]	Self-Absorption Factor [d]	A^0 (Bq)	Mass (mg)	A^0 (Bq mg^{-1})
O	^{187}W	134	2.62×10^{6}	0.0885	3.41×10^{-4}	0.824	1.06×10^{11}		
		479	2.74×10^{6}	0.218	1.19×10^{-4}	0.986	1.07×10^{11}		
		685	2.36×10^{6}	0.273	8.35×10^{-5}	0.991	1.04×10^{11}		
						Average:	1.06×10^{11}	50.6	2.09×10^{9}
	^{188}W	155	1.91×10^{1}	0.1561	1.01×10^{-3}	0.872	1.38×10^{5}	50.6	2.73×10^{3}
P	^{187}W	134	2.61×10^{6}	0.0885	3.41×10^{-4}	0.824	1.05×10^{11}		
		479	2.80×10^{6}	0.218	1.19×10^{-4}	0.986	1.09×10^{11}		
		685	2.41×10^{6}	0.273	8.35×10^{-5}	0.991	1.06×10^{11}		
						Average:	1.07×10^{11}	50.6	2.11×10^{9}
	^{188}W	155	1.93×10^{1}	0.1561	1.01×10^{-3}	0.872	1.39×10^{5}	50.6	2.76×10^{3}
Q	^{187}W	134	2.48×10^{6}	0.0885	3.41×10^{-4}	0.824	9.96×10^{10}		
		479	2.65×10^{6}	0.218	1.19×10^{-4}	0.986	1.03×10^{11}		
		685	2.29×10^{6}	0.273	8.35×10^{-5}	0.991	1.01×10^{11}		
						Average:	1.01×10^{11}	47.0	2.16×10^{9}
	^{188}W	155	1.88×10^{1}	0.1561	1.01×10^{-3}	0.872	1.36×10^{5}	47.0	2.89×10^{3}
R	^{187}W	134	2.97×10^{6}	0.0885	3.41×10^{-4}	0.824	1.20×10^{11}		
		479	3.09×10^{6}	0.218	1.19×10^{-4}	0.986	1.21×10^{11}		
		685	2.72×10^{6}	0.273	8.35×10^{-5}	0.991	1.20×10^{11}		
						Average:	1.20×10^{11}	51.9	2.32×10^{9}
	^{188}W	155	2.24×10^{1}	0.1561	1.01×10^{-3}	0.872	1.63×10^{5}	51.9	3.13×10^{3}

[a] CLSQ output divided by count time from Table D.1
[b] [NNDC 2003]
[c] Table A.2
[d] Table B.2

References

Aliev, A.I., Drynkin, V.I., Leipunskaya, D.I., Kasatkin, V.A. 1970. *Handbook of Nuclear Data for Neutron Activation Analysis*. Jerusalem: Israel Program for Scientific Translations.

Anufriev, V.A., Babich, S.I., Kolesov, A.G., Nefedov, V.N., Poruchikov, V.A. 1981. Neutron Resonance of 186W in the Energy Range up to 300 eV. Translated from the Russian by Dennis W. Wester (Pacific Northwest National Laboratory). *Atomnaia Energiia* 50:67.

Bateman, H. 1910. Solution of a System of Differential Equations Occurring in the Theory of Radio-active Transformations. *Proc. Cambridge Phil. Soc.* 15:423.

Baumann, N.P. 1963. *Resonance Integrals and Self-Shielding Factors for Detector Foils*, Savannah River Reports DP-817. Wilmington, DE: E.I. DuPont de Nemours & Co.

Baumgartner, F. 1967. *Table of Neutron Activation Constants*. Munich: Verlag Karl Thiemig.

Beckurts, K.H., Wirtz, K. 1964. *Neutron Physics*. Berlin: Springer-Verlag.

Beller, L.S., Latham, D.W., Otter, J.M. 1967. *Measurement of the Resonance Integral in ^{186}W*, NAA-SR-12500. North American Aviation, Inc.

Bevington, P.R., Robinson, D.K. 1992. Data Reduction and Error Analysis for the Physical Sciences, Second Edition. Boston, MA: WCB McGraw Hill.

Borchardt, G. 1967. *Activation Resonance Integral and Factor of the Neutron Self-Shielding*, JUEL-503. Juelich, Germany: Juelich Nuclear Research Center.

Brookhaven National Laboratory (BNL). 2002. Table of Nuclides, URL: http://www2.bnl.gov/ton/.

Callahan, A.P., Mirzadeh, S., Knapp, Jr., F.F. 1992. Large-Scale Production of Tungsten-188. *Radioactivity & Radiochemistry* 3:46.

Cheverton, R.D., Sims, T.M. 1971. *HFIR Core Nuclear Design*, ORNL-4621. Oak Ridge, TN: Oak Ridge National Laboratory.

Cook, J.L., Wall, A.L. 1968. The Statistical Estimation of Thermal-Neutron Cross Sections. *Nuclear Science and Engineering* 31:234.

Cumming, J.B. 1963. CLSQ, The Brookhaven Decay-Curve Analysis Program. In *Application of Computers to Nuclear- and Radiochemistry*, ed. G.D. O'Kelly, 25. Washington, DC: National Academy of Sciences - National Research Council.

Curtiss, L.F. 1965. *Introduction to Neutron Physics*. Cambridge, MA: Boston Technical Publishers, Inc.

Damle, P.P., Fabry, A., Jacquemin, R. 1967. *Study of the Reaction W-186(n,gamma)W-187*, EANDC(E)-76. Paris: European-American Nuclear Data Committee.

DeCorte, F., Speecke, A., Hoste, J. 1971. Activation Analysis of High-Purity Silicon. *Journal of Radioanalytical Chemistry* 9:9.

DeCorte, F., Moens, L., Simonits, A., Hoste, J. 1985. Critical Evaluation and Experimental Determination of the Nuclear Activation and Decay Parameters for the Reactions: $^{64}Zn(n,\gamma)^{65}Zn$, $^{112}Sn(n,\gamma)^{113(m)}Sn(E.C.)^{113(m)}In$, $^{174}Yb(n,\gamma)^{175(m)}Yb$. *Journal of Radioanalytical and Nuclear Chemistry* 92:183.

DeCorte, F., Simonits, A. 1989. k_0-Measurements and Related Nuclear Data Compilation for (n,γ) Reactor Neutron Activation Analysis. *Journal of Radioanalytical and Nuclear Chemistry* 133:43.

DeCorte, F., Simonits, A., DeWispelaere, A. 1989. Comparative Study of Measured and Critically Evaluated Resonance Integral to Thermal Cross Section Ratios, III. *Journal of Radioanalytical and Nuclear Chemistry* 133:131.

Dickens, J.K. 1972. Self-Absorption of Gamma Rays Produced in Large Cylindrical Samples. *Nuclear Instruments and Methods* 98:451.

Evans, R.D. 1955. *The Atomic Nucleus*. Malabar, FL: Krieger Publishing Company.

Friedlander, G., Kennedy, J.W., Macias, E.S., Miller, J.M. 1981. Nuclear and Radiochemistry, 3rd Edition. New York, NY: John Wiley & Sons.

Friesenhahn, S.J., Haddad, E., Frohner, F.H., Lopez, W.M. 1966. The Neutron Capture Cross Section of the Tungsten Isotopes from 0.01 to 10 Electron Volts. *Nuclear Science and Engineering* 26:487.

Garland, M.A. 2003. *Tungsten Cylinder Target Temperatures in the HFIR Hydraulic Tube*, C-HFIR-2002-035. Oak Ridge, TN: Research Reactors Division, Oak Ridge National Laboratory.

Garnier, J.E., Begej, S. 1979. *Ex-Reactor Determination of Thermal Gap and Contact Conductance Between Uranium Dioxide: Zircaloy-4 Interfaces, Stage I: Low Gas Pressure*, NUREG/CR-0330 PNL-2696 R3. Richland, WA: Pacific Northwest Laboratory.

Gillette, J.H., Lane, I.B., Baker, P.S., Beauchamp, E.E., Butler, T.A., Case, F.N., Robinson, R.A., Schaich, R.W. 1966. *Review of Radioisotopes Program, 1965*, ORNL-4621. Oak Ridge, TN: Oak Ridge National Laboratory.

Gleason, G.W. 1977. Thermal Neutron (n,gamma) Cross Sections and Resonance Integrals – Part 2. Private communication to Nuclear Energy Agency. Data available in EXFOR accession no. 10662 (database online, www.nndc.bnl.gov).

Goldsmith, A., Waterman, T.E., Hirschhorn, H.J. 1961a. *Handbook of Thermophysical Properties of Solid Materials: Volume I – Elements*. New York, NY: Pergamon Press.

———. 1961b. *Handbook of Thermophysical Properties of Solid Materials: Revised Edition: Volume II: Alloys*. New York, NY: The MacMillan Company.

Gryntakis, E.M., Kim, J.I. 1983. A Compilation of Resonance Integrals from Hydrogen to Fermium. *Journal of Radioanalytical Chemistry* 76:341.

Gryntakis, E.M., Cullen, D.E., Mundy, G. 1987. Thermal Neutron Cross-Sections and Infinite Dilution Resonance Integrals. Chap. 2-1 in Technical Reports Series No. 273, *Handbook on Nuclear Activation Data*. Vienna: International Atomic Energy Agency.

Harris, S.P., Muehlhause, C.O., Thomas, G.E. 1950. Low Energy Neutron Resonance Scattering and Absorption. *Physical Review* 79:11.

Hayodom, V., Boonkong, W., Mahapanyawong, S., Chaimonkon, C. 1967. Resonance Integral Measurements. In *Certain Accounts on the Utilization of the THAI Research Reactor Bangkok Conference*, THAI-AEC-10. Bangkok: Office of Atomic Energy for Peace.

HEATING7. 1999. *HEATING7: Multidimensional, Finite-Difference Heat Conduction Analysis Code System Versions 7.2i and 7.3*, PSR-199. Oak Ridge, TN: Oak Ridge National Laboratory.

Heft, R.E. 1978. A Consistent Set of Nuclear Parameter Values for Absolute Instrumental Neutron Activation Analysis. In *Proceedings of the American Nuclear Society Topical Conference on Computers in Activation Analysis and Gamma-Ray Spectroscopy, Mayaguez, Puerto Rico*, CONF-780421. La Grange Park, IL: American Nuclear Society.

Hobbs, R.W. 2002. *Tungsten Rabbit Irradiations in the HFIR B-3 Hydraulic Tube*, C-HFIR-2001-039, Rev. 0. Oak Ridge, TN: Research Reactors Division, Oak Ridge National Laboratory.

Hogg, C.H., Wilson, W.L. 1970. *Reactor Thermal-Neutron Cross Sections of 64-Zn, 68-Zn, 121-Sb, 123-Sb, 55-Mn, and 186-W*, IN-1317. Idaho Falls, ID: Idaho Nuclear Corporation.

Hughes, D.J. 1957. *Neutron Cross Sections*. London: Pergamon Press.

Hughes, D.J., Schwartz, R.B. 1958. *Neutron Cross Sections,* BNL-325, 2nd Edition. Upton, NY: Brookhaven National Laboratory.

IAEA. 1974. Technical Reports Series No. 156, *Handbook on Nuclear Activation Cross Sections*. Vienna: International Atomic Energy Agency.

Incropera, F.P., DeWitt, D.P. 1996. *Introduction to Heat Transfer, Third Edition*. New York, NY: John Wiley & Sons.

Japan Atomic Energy Research Institute (JAERI). 2002. Japanese Evaluated Nuclear Data Library, JENDL-3.3. URL: http://wwwndc.tokai.jaeri.go.jp/jendl/j33/j33.html.

Jefferies, S.M., MacMahon, T.D., Williams, J.G., Ahmad, A., Ryves, T.B. 1983. Analysis and Evaluation of Thermal and Resonance Neutron Activation Data. In *Nuclear Data for Science and Technology, Proceedings of the International Conference Antwerp 6 – 10 September 1982*, ed. K.H. Bockhoff, 681 – 684. Dordrecht, Holland: D. Reidel Publishing Company.

Kimura, I., Kobayashi, K., Yamamoto, S., Miki, R., Itoh, T. 1989. Resonance Integral Measurement with the Standard 1/E Neutron Spectrum Field. Chap. 3.3 in *Proceedings of the 1988 Seminar on Nuclear Data*, JAERI-M 89-026, eds. T. Nakagawa and A. Zukeran. Tokai-mura, Japan: Japan Atomic Energy Research Institute.

Knopf, K., Waschkowski, W. 1987. Wechselwirkung von Neutronen mit Wolfram und seinen Isotopen. *Z. Naturforsch* 42a:909.

Koch, R.C. 1960. *Activation Analysis Handbook*. New York, NY: Academic Press.

Krane, K.S. 1988. *Introductory Nuclear Physics*. New York, NY: John Wiley & Sons.

Lamarsh, J.R. 1993. *Introduction to Nuclear Engineering, 2nd Edition*. Reading, MA: Addison-Wesley Pub. Co.

Lindner, M. 1951. Characteristics of Some Radionuclides of Tungsten, Rhenium, and Osmium Formed by Second-Order Thermal Neutron Capture. *Physical Review* 84:240.

Lyon, W.S. 1960. Reactor Neutron Activation Cross Sections for a Number of Elements. *Nuclear Science and Engineering* 8:378.

Mahmood, S.T., Mirzadeh, S., Farrell, K., Pace, J.V., Oliver, B.M. 1995. *Neutron Dosimetry of the HFIR Hydraulic Facility*, ORNL/TM-12831. Oak Ridge, TN: Oak Ridge National Laboratory.

MatWeb. 2003. MatWeb Material Property Data. URL: http://www.matweb.com.

Mazlov, I.A., Lubnickij, V.A. 1971. *Handbook of Neutron Activation Analysis*. Leningrad: Izd. Nauka.

Mirzadeh, S., Knapp Jr., F.F., Alexander, C.W., Mausner, L.F. 1997a. Evaluation of Neutron Inelastic Scattering for Radioisotope Production. *Appl. Radiat. Isot.* 48:441.

Mirzadeh, S., Knapp, Jr., F.F. (Russ), Lambrecht, R.M. 1997b. Burn-up Cross Section of ^{188}W. *Radiochimica Acta* 77:99.

Mirzadeh, S., Schenter, R.E., Callahan, A.P., Knapp Jr., F.F. 1992. *Production Capabilities in U.S. Nuclear Reactors for Medical Radioisotopes*, ORNL/TM-12010. Oak Ridge, TN: Oak Ridge National Laboratory.

Mirzadeh, S., Walsh, P. 1998. Numerical Evaluation of the Production of Radionuclides in a Nuclear Reactor (Parts I and II). *Appl. Radiat. Isot.* 49:379, 383.

Mughabghab, S.F., Divadeenam, M., Holden, N.E. 1984. *Neutron Cross Sections, Volume 1 Neutron Resonance Parameters and Thermal Cross Sections, Parts A (Z=1-60) and B (Z=61-100)*. San Diego, CA: Academic Press, Inc.

Mughabghab, S.F. 2003. *Thermal Neutron Capture Cross Sections Resonance Integrals and G-Factors*, INDC(NDS)-440. Vienna: IAEA Nuclear Data Section.

National Institute of Standards and Technology (NIST). 2003. X-Ray Mass Attenuation Coefficients. URL: http://physics.nist.gov/PhysRefData/XrayMassCoef/tab3.html.

National Nuclear Data Center (NNDC). 2002a. Nuclear Data from NuDat. URL: http://www.nndc.bnl.gov/nndc/nudat/.

———. 2002b. Experimental Nuclear Reaction Data File (EXFOR [CSISRS]). URL: http://www.nndc.bnl.gov/nndc/exfor/.

———. 2003. Evaluated Nuclear Structure Data File (ENSDF). URL: http://www.nndc.bnl.gov/nndc/ensdf/.

———. 2004a. Evaluated Nuclear Data File (ENDF). URL: http://www.nndc.bnl.gov/nndc/endf/.

———. 2004b. Nuclear Data from NuDat. URL: http://www-original.nndc.bnl.gov/nndc/nudat/.

Parrington, J.R., Knox, H.D., Breneman, S.L., Baum, E.M., Feiner, F. 1996. *Nuclides and Isotopes Chart of the Nuclides 15th Edition*. San Jose, CA: General Electric Co. and KAPL, Inc.

Pierce, C.R., Shook, D.F. 1968. Determination of Dilute ^{186}W and ^{184}W Resonance Integrals by Activation. *Nuclear Science and Engineering* 31:431.

Pomerance, H. 1952. Thermal Neutron Cross Sections. *Physical Review* 88:412.

Rahn, F., Camarda, H.S., Hacken, G., Havens, Jr., W.W., Liou, H.I., Rainwater, J., Slagowitz, M., Wynchank, S. 1972. Values of the Neutron Resonance Capture Integral for Some Rare Earth Isotopes. *Nuclear Science and Engineering* 48:219.

Research Reactors Division (RRD). 2004. Oak Ridge National Laboratory Research Reactors Division Website: Neutron Activation Analysis (NAA) Laboratory and Pneumatic Tube Facilities. URL: http://www.ornl.gov/sci/rrd/pages/experiment.html.

Rzama, A., Misdaq, M.A., Erramli, H., Blondiaux, G., Isabelle, D.B., Bajard, J.C. 1994. Study of Gamma-Photon Self-Absorption in Stainless Steel Samples by Experimental and Calculational Methods. *Journal of Radioanalytical and Nuclear Chemistry* 183:409.

SAMMY-M6. 2003. *Code System for Multilevel R-Matrix Fits to Neutron and Charged-Particle Cross-Section Data Using Bayes' Equations*, PSR-1589. Oak Ridge, TN: Oak Ridge National Laboratory.

Scoville, J.J., Knight, D.F., Fast, E. 1962. Resonance Absorption Integrals of Dysprosium and Tungsten. *Trans. Am. Nucl. Soc.* 5:377.

Seren, L., Friedlander, H.N., Turkel, S.H. 1947. Thermal Neutron Activation Cross Sections. *Physical Review* 72:888.

Simonits, A., DeCorte, F., El Nimr, T., Moens, L., Hoste, J. 1984. Comparative Study of Measured and Critically Evaluated Resonance Integrals to Thermal Cross-Section Ratios, Part II. *Journal of Radioanalytical and Nuclear Chemistry* 81:397.

Stacey, W.M. 2001. *Nuclear Reactor Physics*. New York, NY: John Wiley & Sons.

Stoughton, R.W., Halperin, J. 1959. Heavy Nuclide Cross Sections of Particular Interest to Thermal Reactor Operation: Conventions, Measurements and Preferred Values. *Nuclear Science and Engineering* 6:100.

Tian, D., Xie, D., Ho, Y., Yang, F. 2000. Fissile Material Isotopic Composition by γ-ray Spectra. *Nuclear Instruments and Methods in Physics Research A* 449:500.

Touloukian, Y.S., Liley, P.E., Saxena, S.C. 1970. *Thermophysical Properties of Matter Volume 3; Thermal Conductivity; Nonmetallic Liquids and Gases*. New York, NY: IFI/Plenum Data Corporation.

Tsoulfanidis, N. 1995. *Measurement and Detection of Radiation, Second Edition*. Washington, DC: Taylor & Francis.

Van der Linden, R., DeCorte, F., Hoste, J. 1974. A Compilation of Infinite Dilution Resonance Integrals, II. *Journal of Radioanalytical Chemistry* 20:695.

Weast, R.C. 1973. *CRC Handbook of Chemistry and Physics, 54th Edition*. Cleveland, OH: CRC Press.

Westcott, C.H. 1955. The Specification of Neutron Flux and Nuclear Cross-Sections in Reactor Calculations. *J. Nuclear Energy* 2:59.

Wootan, D.W., Caggiano, J.A., Carter, L.L., Jordheim, D.P., Lu, A.H., Mann, F.M., Rawlins, J.A., Schenter, R.E., Schmittroth, F.A., Schwarz, R.A., Simons, R.L., Matsumoto, W.Y. 1991. Isotope Production Test in the Fast Flux Test Facility. In *LMR: A Decade of LMR Progress and Promise, ANS Winter Meeting, November 11 – 15, 1990, Washington, D.C.* La Grange Park, IL: American Nuclear Society.

Zijp, W.L. 1973. Nuclear Data for Neutron Metrology, IAEA-SM-170/73. In *Nuclear Data in Science and Technology Vol. II: Proceedings of the Symposium on Applications of Nuclear Data in Science and Technology Held by the International Atomic Energy Agency in Paris, 12-16 March 1973*. Vienna: International Atomic Energy Agency.

Zolotarev, K.I. 2002. *Evaluation and Improvement of Cross Section Accuracy for Most Important Dosimetry Reactions Including Covariance Data*, INDC(CCP)-431. Vienna: IAEA Nuclear Data Section.